2

RL

②

Annual Scientific Report

on

ADVANCED DIAGNOSTICS FOR REACTING FLOWS

Grant AFOSR 89-0067

Prepared for

AIR FORCE OFFICE OF SCIENTIFIC RESEARCH

For the Period

November 1, 1992 to October 31, 1993

Submitted by

R. K. Hanson, Principal Investigator

HIGH TEMPERATURE GASDYNAMICS LABORATORY
Mechanical Engineering Department
Stanford University

REPORT DOCUMENTATION PAGE

Form Approved
OMB No. 0704-0188

1. AGENCY USE ONLY *(Leave blank)*

2. REPORT DATE
1993 November 24

3. REPORT TYPE AND DATES COVERED
Annual Technical 11/1/92 - 10/31/93

4. TITLE AND SUBTITLE
(U)Advanced Diagnostics for Reacting Flows

5. FUNDING NUMBERS
PE - 61102F
PR - 2308
SA - BS
G - AFOSR 89-0067

6. AUTHOR(S)
R. K. Hanson

7. PERFORMING ORGANIZATION NAME(S) AND ADDRESS(ES)
Stanford University
Mechanical Engineering Department
Stanford, CA 94305-3032

8. PERFORMING ORGANIZATION REPORT NUMBER

9. SPONSORING/MONITORING AGENCY NAME(S) AND ADDRESS(ES)
AFOSR/NA
110 Duncan Avenue, Suite B115
Bolling AFB DC 20332-0001

10. SPONSORING/MONITORING AGENCY REPORT NUMBER

11. SUPPLEMENTARY NOTES

12a. DISTRIBUTION/AVAILABILITY STATEMENT
Approved for public release; distribution is unlimited

12b. DISTRIBUTION CODE

13. ABSTRACT *(Maximum 200 words)*

Progress is reported for the past year of an interdisciplinary program aimed at establishing advanced optical diagnostic techniques applicable to combustion gases and plasmas, with some emphasis on high speed flows. The primary parameters of interest are species concentrations (including electrons), temperature, mass density, pressure, velocity, and quantities derivable from these parameters such as mass flow rate (from the product of density and velocity). The techniques under study are based on laser spectroscopy, particularly laser absorption and laser-induced fluorescence, with the latter capable of providing both single-point and multi-point (2-D and 3-D) measurements. Laser sources include tunable cw lasers (ring dye and semiconductor diode lasers) and tunable pulsed lasers (excimer-pumped dye and narrow-linewidth excimer). The cw lasers are spectrally narrow, allowing study of a new class of techniques based on spectral lineshapes and shifts, while the pulsed lasers provide intense bursts of photons needed for techniques based on light-scattering phenomena. Accomplishments of note include: development of a new plasma diagnostic based on saturated LIF measurements with a diode laser source; development of a novel multiple-laser absorption diagnostic which enables simultaneous monitoring of multiple species (or other quantities) along a common optical path; development of spectrally-resolved diagnostic methods suitable for quantitative measurements in very high enthalpy flows; the first quantitative single-shot velocity imaging via PLIF in a hypersonic flow; the first use of PLIF to monitor multiple temperatures in nonequilibrium hypersonic flows; the development of a novel PLIF imaging scheme, based on the use of acetone, which allows simultaneous imaging of two species (acetone and OH) in a flowfield using only one laser source; and exploration of various aspects of degenerate four-wave mixing diagnostics.

14. SUBJECT TERMS
Laser, Imaging, Combustion, Velocity, Pressure, Absorption Temperature, Fluorescence, Reacting, Flow, Plasma, Diagnostics

15. NUMBER OF PAGES
124

16. PRICE CODE

17. SECURITY CLASSIFICATION OF REPORT	**18. SECURITY CLASSIFICATION OF THIS PAGE**	**19. SECURITY CLASSIFICATION OF ABSTRACT**	**20. LIMITATION OF ABSTRACT**
Unclassified	Unclassified	Unclassified	UL

Annual Scientific Report

on

ADVANCED DIAGNOSTICS FOR REACTING FLOWS

Grant AFOSR 89-0067

Prepared for

AIR FORCE OFFICE OF SCIENTIFIC RESEARCH

For the Period

November 1, 1992 to October 31, 1993

Submitted by

R. K. Hanson, Principal Investigator

TABLE OF CONTENTS

1.0 INTRODUCTION

Progress is reported for the past year of an interdisciplinary program aimed at establishing advanced optical diagnostic techniques applicable to combustion gases and plasmas, with some emphasis on high speed flows. The primary parameters of interest are species concentrations (including electrons), temperature, mass density, pressure, velocity, and quantities derivable from these parameters such as mass flow rate (from the product of density and velocity). The techniques under study are based on laser spectroscopy, particularly laser absorption and laser-induced fluorescence, with the latter capable of providing both single-point and multi-point (2-D and 3-D) measurements. Laser sources include tunable cw lasers (ring dye and semiconductor diode lasers) and tunable pulsed lasers (excimer-pumped dye and narrow-linewidth excimer). The cw lasers are spectrally narrow, allowing study of a new class of techniques based on spectral lineshapes and shifts, while the pulsed lasers provide intense bursts of photons needed for techniques based on light-scattering phenomena. Accomplishments of note include: development of a new plasma diagnostic based on saturated LIF measurements with a diode laser source; development of a novel multiple-laser absorption diagnostic which enables simultaneous monitoring of multiple species (or other quantities) along a common optical path; development of spectrally-resolved diagnostic methods suitable for quantitative measurements in very high enthalpy flows; the first quantitative single-shot velocity imaging via PLIF in a hypersonic flow; the first use of PLIF to monitor multiple temperatures in nonequilibrium hypersonic flows; the development of a novel PLIF imaging scheme, based on the use of acetone, which allows simultaneous imaging of two species (acetone and OH) in a flowfield using only one laser source; and exploration of various aspects of degenerate four-wave mixing diagnostics.

2.0 PROJECT SUMMARIES

Included in this section are summaries of progress in each of seven project areas. Additional descriptions of this work may be found in the publications listed in Sections 3.2 and 3.3. Reprints of these papers are available on request. Personnel involved in these projects are listed in Section 4.0. Copies of key publications are included as Sec. 6.0.

2.1 Plasma Diagnostics

During the past year we have continued to explore the use of cw semiconductor diode lasers (GaAlAs) as light sources for absorption and fluorescence diagnostics of temperature, species concentration, collisional transfer rates, and electron number density in laboratory plasmas. These low-cost lasers are evolving rapidly owing to their numerous practical applications (compact disc players, supermarket scanners, etc.), but they also offer exciting prospects for use in scientific applications. With regard to spectroscopic diagnostics, these lasers can be viewed as economical, rugged and compact sources of low power, cw, tunable wavelength light with relatively narrow spectral linewidths. Thus they represent possible replacements for currently employed cw dye lasers. Unfortunately, diode lasers have been developed primarily for use at near-infrared wavelengths (especially 1.3 and 1.5 microns), and only in the past few years have lasers become readily available at wavelengths below 1 micron where most electronic transitions of interest in atoms and molecules are located. At the present time, diode lasers are available for use in selected wavelength bands down to about 650 nm. In our recent work we have utilized diode lasers which operate in the 770-850 nm range. This has allowed studies of excited-state transitions of three species: (a) the strong $4s^3P \rightarrow 4p^3D$ transitions of argon linking the first excited state of argon (4s) with the second excited state (4p); (b) the $3s^5S^0 \rightarrow 3p^5P_3$ excited-state transition of O-atoms; and (c) the $6s[3/2]_2^0 - 6p[3/2]_2$ transition of xenon. These species and the spectroscopic diagnostics under development are relevant to electric propulsion and to basic studies of plasmadynamics.

Particular accomplishments of our recent research include: the first application of diode lasers for single-point fluorescence measurements in atmospheric pressure plasmas, and the first studies of partially-saturated fluorescence as a possible method of measuring electronic quench rates in plasmas, both of which were conducted in an RF-excited argon plasma. Details of this work are available in the publications cited in Sec. 3.2 (see papers 1 and 2). Here we summarize our approach and illustrate the type of information obtained.

A simplified form of the experimental arrangement used to extend diode laser techniques to fluorescence is indicated in Fig. 1, together with a sketch of representative data

Spectrally-Resolved Plasma Diagnostics using Tunable Diode Lasers

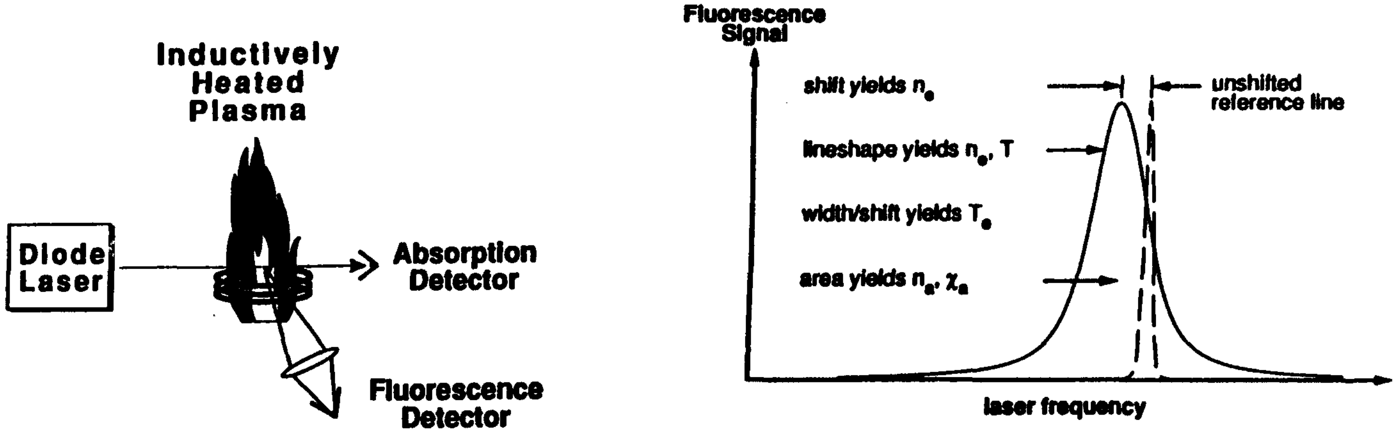

- Spatially-resolved fluorescence detection obviates need for Abel inversion
- New spectral strategy provides simultaneous determination of electron density and temperature
- First application of diode lasers to high-pressure plasmas

Figure 1. Overview of plasma diagnostic strategy based on spectrally-resolved fluorescence.

which illustrates the features of the data used to infer plasma properties. The measurements are made in an atmospheric pressure, inductively-coupled RF plasma torch assembled previously in this program to provide a controlled, high temperature plasma with convenient optical access. In the experiment, the diode laser is rapidly swept in wavelength across an individual absorption transition of interest, providing a fully resolved record of the absorption lineshape; either line-of-sight absorption or single-point fluorescence recording may be used, but here our goal was to establish LIF, since it provides spatially-resolved data. The lineshape data can be used to infer gas temperature (through Doppler broadening of the line) and electron density (through the Stark-induced shift in the line position). Since the lineshape also is influenced by Stark broadening, the linewidth data can be interpreted to yield a second, independent determination of the electron density. In general, excellent agreement is found between the two measurements of electron density. Inferred temperatures are typically in the range 6000-8000 K, for both absorption and fluorescence measurements, thereby illustrating the power of this diagnostic for probing very high temperature gases. The extension of this diagnostic to fluorescence is significant, because most past plasma diagnostics have been based on line-of-sight emission approaches which require use of Abel inversion methods to establish spatial distributions; inversion methods are applicable only to plasmas with radial symmetry while LIF diagnostics have no symmetry limitation.

Although most experiments are conducted with relatively low laser power, so as to minimize perturbation to the plasma under study, we have recognized that intentional use of high laser power densities, sufficient to cause partial saturation of the absorption transition, may present new diagnostic strategies. The basic concept we have been pursuing is illustrated in Fig. 2. A laser source is used to partially saturate a specific absorption transition, between the lower state l and the upper state u, and the emitted LIF signal is used to infer the primary unknown (in the fluorescence yield equation), namely the collisional transfer rate, Q. This quantity, Q, represents the rate of collisionally-induced transfer of the excited species between the state u and nearly electronic states. The primary process is by electron collisions, and hence a measurement of Q can either be used to infer the electron density (if the relevant cross-section for the transfer process is known) or the cross-section for transfer (if the electron density is known). A measurement of the saturated (or partially saturated) LIF signal thus represents a new plasma diagnostic with potential for measuring either fundamental properties (e.g., cross-sections) or plasma parameters (e.g., electron density). Details of this work are available in paper 1 of Sec. 3.2.

We can also mention briefly our initial work in a low pressure xenon plasma discharge. Our goal is to extend the ideas previously demonstrated in argon and oxygen to xenon plasmas. Xenon is the species most relevant to current work on ion thrusters for

COLLISIONAL TRANSFER RATE MEASUREMENTS IN PLASMAS WITH DIODE LASERS

- Technique yields local determination of collisional transfer rate

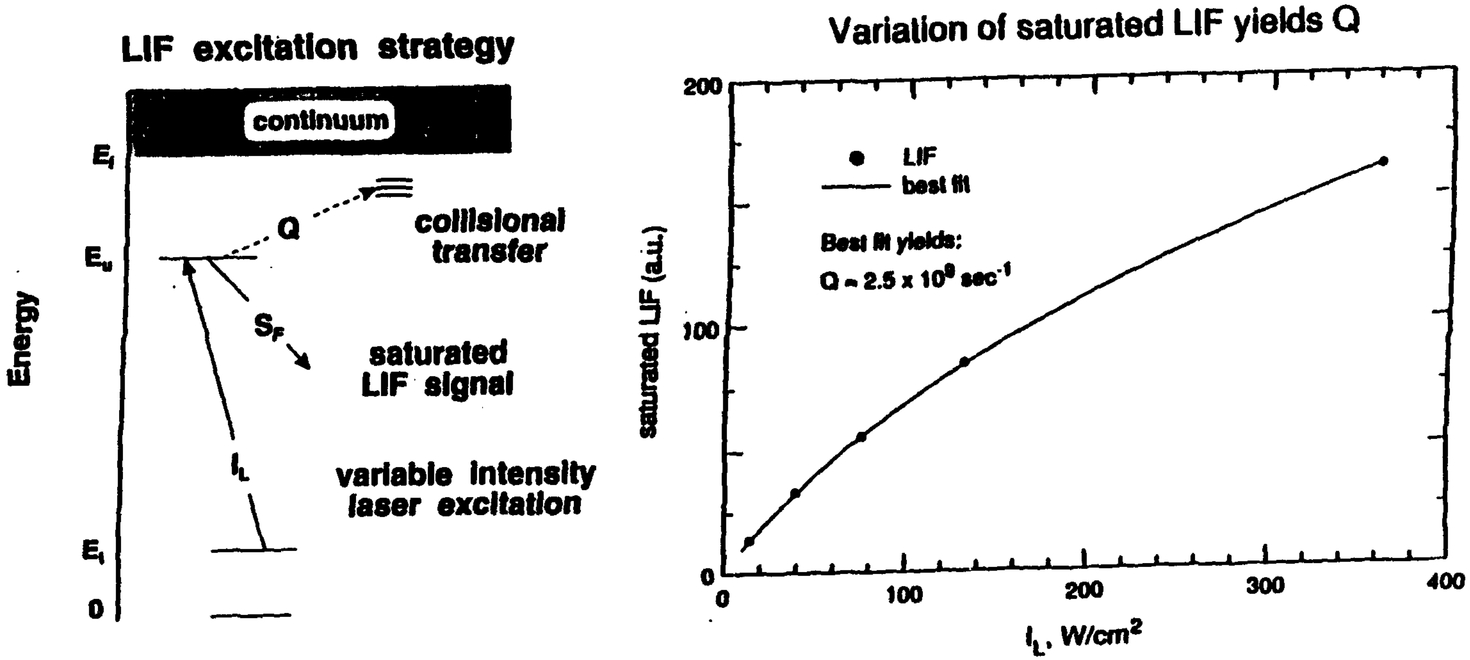

LIF excitation strategy

Variation of saturated LIF yields Q

- First application of diode lasers for LIF saturation spectroscopy
- *Measurements allow quantitative use of LIF signals*
- Measured values validate theoretical collision rates

Figure 2. New diode laser diagnostic strategy for plasmas based on saturated LIF.

electric propulsion, and hence development of nonintrusive diagnostics capable of probing the exhausts of such thrusters is critical to the evolution of improved ion thruster engines. Thus far we have achieved only line-of-sight absorption measurements in a simple DC discharge, but work is now in progress to extend measurements to fluorescence. Although xenon spectroscopy is complex, owing to the existence of several strong isotopes and the role of hyperfine splitting in each atomic transition, we are hopeful to be able to fit fully resolved LIF spectra in a way which will allow extraction of quantities such as velocity (Doppler shift), temperature (Doppler widths) and density (integrated spectral absorption). These critical quantities have not previously been monitored by nonintrusive means in ion thrusters.

2.2 Diode Laser Thermometry in High Enthalpy Flows

For gases at combustion temperatures, i.e. up to about 3000 K, spectroscopic diagnostics for temperature typically probe molecular species, such as OH, O_2, NO and N_2; and a number of experimental methods are now available for such temperature measurements, including LIF, Raman scattering and CARS. At higher temperatures, however, as may be found in various high enthalpy hypersonic flows and plasmas, it will be necessary to establish new techniques which recognize that the major species present are neutral and ionized atoms. To illustrate this point, Fig. 3 shows the neutral and charged particle mole fractions as a function of temperature in equilibrium air at 1 atm. Note that above 3500 K the mole fraction of O-atoms exceeds that of molecular oxygen, and above about 7000 K, the atomic species O and N are the primary components of air; above 14000 K, the primary constituent becomes N^+. It is thus apparent that spectroscopic diagnostics intended for gases at very high temperatures should be based on atomic rather than molecular species.

The approach we have been pursuing (see Fig. 4) for the past two years is based on spectrally resolved absorption (and, in some cases, fluorescence) of excited-state transitions of atomic oxygen. The laser source is a tunable diode laser, and the experimental procedure involves recording at least one fully resolved absorption line. At high temperatures, the width of the line is dominated by Doppler broadening, and thus a measurement of linewidth is easily converted to a value for the translational (i.e., kinetic) temperature of the gas. The integrated area under the measured spectral absorption coefficient curve yields the number density of atoms in the absorbing (i.e., lower) state, from which one can invoke a Boltzmann distribution to infer an "electronic" or population temperature, assuming that the density of the species is known. (The density of a species is known from theory once the translational temperature and pressure are specified for a mixture of known atomic proportions.) It is important to note that the two temperatures inferred with these methods, i.e. the kinetic and

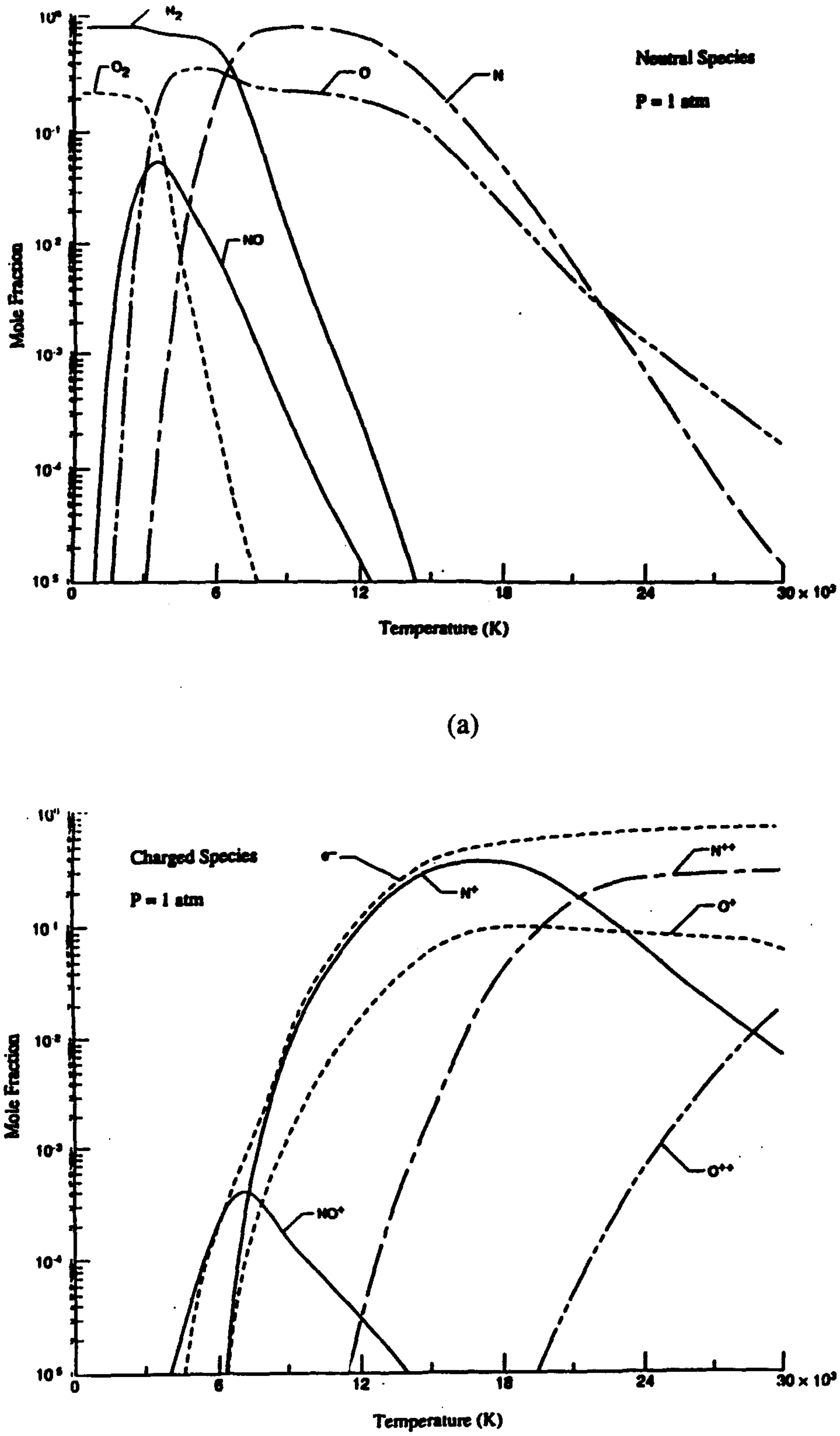

(a)

(b)

Figure 3. Composition of equilibrium air at 1 atm versus temperature.

electronic temperatures, may differ in gases at very high temperatures where radiative and collisional transfer processes are not in balance, and such difficulties motivate the need for diagnostics sensitive to these different temperatures in gases with very high enthalpies. The elements of these ideas are illustrated in Fig. 4 which shows a representative lineshape and the key theoretical relationships.

Measurement Approach

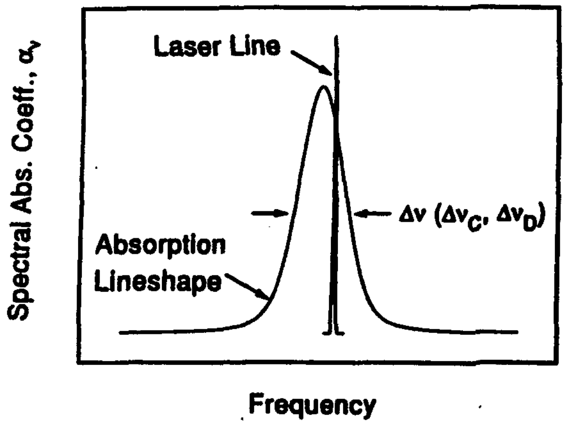

- **Beer's Law**

  $I/I_0 = \exp(-\alpha_\nu L)$

- $\Delta\nu_D \propto \sqrt{T_{kin}}$

- **Boltzmann Equation**

  $\frac{n_i}{n_a} = \frac{g_i}{Z_a} \exp\left(\frac{-E_i}{kT_{pop}}\right)$

Laser Linewidth	**≈ MHz**
Absorption Linewidth	**≈ GHz**

Figure 4. Measurement concept for spectral lineshape thermometry.

Our work to explore high-temperature laser thermometry has been carried out in a conventional pressure-driven shock tube, using reflected shock waves to provide a wide range of known gas temperatures and pressures. A schematic of the experimental arrangement is shown in Fig. 5. Experiments have been conducted primarily in O_2-argon mixtures for simplicity, and the absorption line probed is the 3s→3p transition of O-atoms at 777 nm. The laser utilized is a commercial GaAlAs semiconductor laser with an output power level of 5 mW.

An energy level diagram for the relevant O-atom transitions, and a representative single-sweep data trace (converted from time to laser frequency) are shown in Fig. 6. The laser is repetitively modulated at 6-10 kHz, and so a complete spectrally resolved lineshape is recorded at approximately 100 microsecond intervals. The absorption data are converted through Beer's law to a plot of the spectral absorption coefficient and then best fit with a

Voigt profile. This allows determination of the Gaussian component of the lineshape, which yields directly the kinetic temperature through the known Doppler-broadening relationship. The integrated area under the lineshape curve is used to infer the electronic or population temperature of the absorbing state. Note, in this case, that these temperatures are in close agreement (8400-8500 K). Experiments thus far have been limited to temperatures in the range from 6000 to 13000 K, owing primarily to shock tube design limitations, but we anticipate being able to extend the temperature range in future work.

The concept of using absorption between excited electronic states is versatile, since the specific lower (absorbing) state used may be varied to give appropriately large fractional absorption as the temperature of interest changes. For example, as the temperature increases, one would utilize excited states with a higher electronic energy. In addition, the species selected for thermometry may be varied depending on the temperature and the specific gas mixture under study; and each of the atomic species typically has many possible absorption transitions which may be utilized.

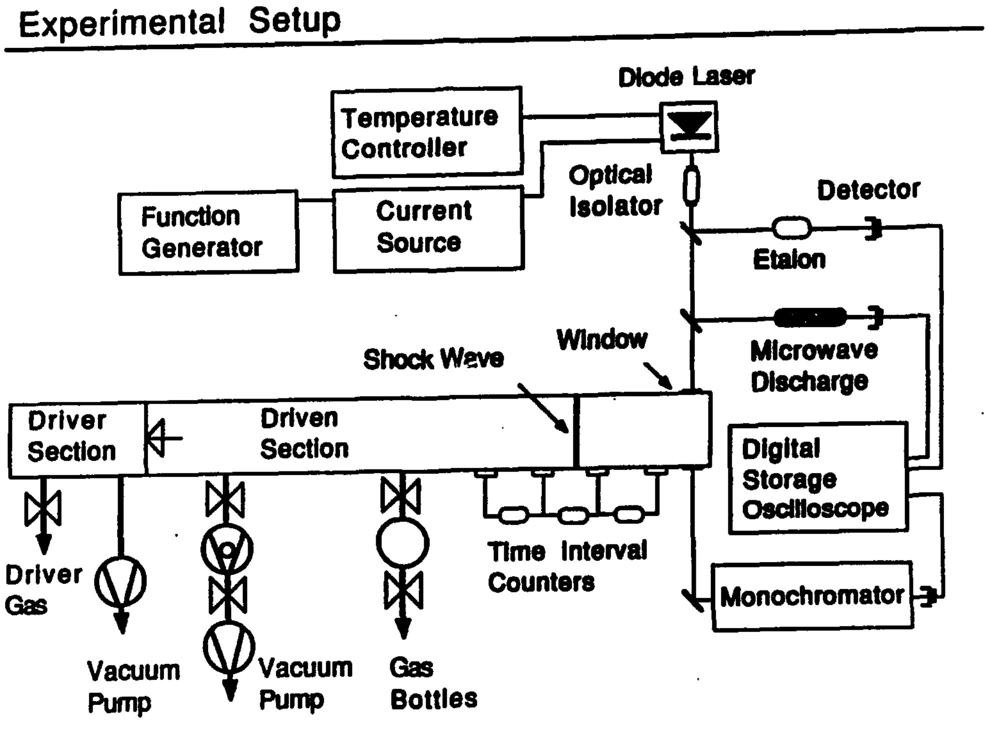

Figure 5. Experimental set-up for diode laser thermometry at high temperatures.

Research is continuing on this diagnostic concept. Following some work to improve the experimental arrangement and reduce system noise, we plan to conduct experiments which will include: other transitions of O-atoms, N-atom transitions, and a wider temperature range.

DIODE-LASER THERMOMETRY FOR HIGH-ENTHALPY AIR FLOWS

- Excited-state absorption enables measurements of high temperatures

O-atom Excitation Strategy

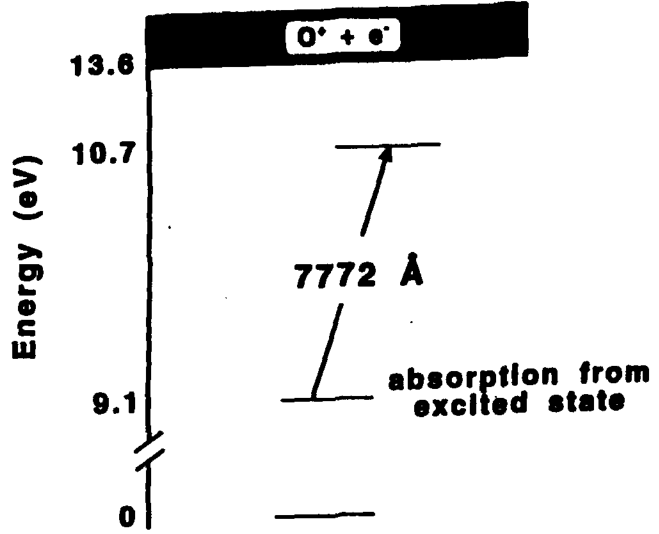

O-atom lineshape in shock-heated flow

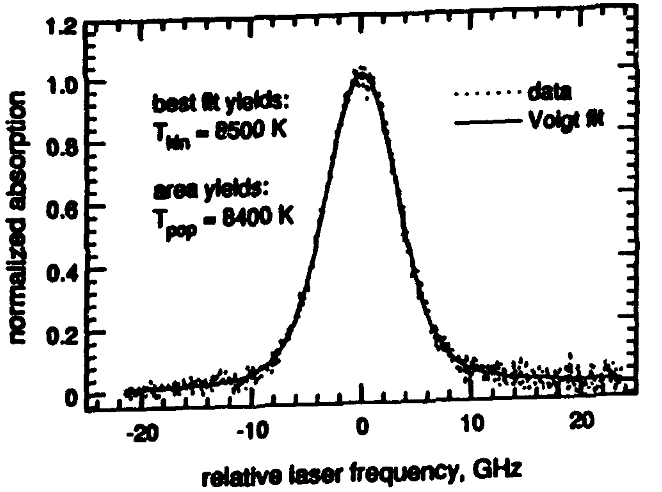

- Simultaneous determination of kinetic and population temperatures
- First measurement of atomic oxygen in high-enthalpy flows
- Measurement technique validated in shock tubes up to 14000 K

Figure 6. Diode laser thermometry in high temperature gases.

2.3 Fiberoptic Multi-Laser Absorption Diagnostic

During the past year we have continued our effort to establish diagnostic methods, based on diode laser line-of-sight absorption, suitable for probing supersonic and hypersonic propulsion flows. The goal has been to identify new, improved techniques which enable accurate, fast and simultaneous measurements of multiple gasdynamic properties; properties of interest include velocity, temperature, pressure, species concentration and derived quantities based on combinations of these primary properties, such as thrust and mass flux. The approach we have been taking is based on the fact that spectral lineshapes are sensitive to precisely the thermodynamic and gasdynamic quantities of interest, and also that semiconductor diode lasers offer good prospects for monitoring these lineshapes in an economical and simple manner. In work thus far, we have used a single rapid-scanning diode laser source which is tuned to coincidence with a pair of absorption lines of the species being monitored (typically O_2 or H_2O). Spectrally resolved absorption lineshapes are then recorded in the flowfield of interest, and these data are interrogated to yield the quantities of interest. For example, the ratio of peak absorption in the two lines yields temperature, the widths of the lines yields pressure, the Doppler shift of the lines gives velocity, the perfect gas law gives the density, and the integrated absorption gives the species concentration. Although this general approach has been extremely successful, and has provided the first laser-based diagnostic method capable of simultaneously monitoring several flowfield properties (included derived quantities such as mass flux and thrust), we have been limited in this work by the relatively narrow continuous tuning range of these lasers.

One attractive feature of diode laser absorption has been that it is a method that is compatible with the use of fiberoptics, which enables remote measurements in hostile environments. During the past year, as we have progressed with a project to demonstrate remote measurements of H_2O in a supersonic combustor exhaust, we realized that the fiberoptic components now available for splitting and combining light as it propagates through optical fibers could also be used to allow simultaneous use of multiple laser beams along a single absorption path. This simple idea has significant implications, since one can now consider measurement strategies based on multiple lasers tuned to entirely different spectral regions. Such capability will eliminate the limitation on tuning range of single diode lasers, and will provide improved capabilities for measuring temperature and also for measuring multiple species.

The essence of this diagnostic strategy is illustrated in Fig. 7. Here, for simplicity, we show only two laser sources, which in this case are tuned with a single function generator. The outputs of the two lasers, which are scanned alternately in time, are combined using a fiberoptic beam combiner and then distributed through a beam splitter to three paths: an

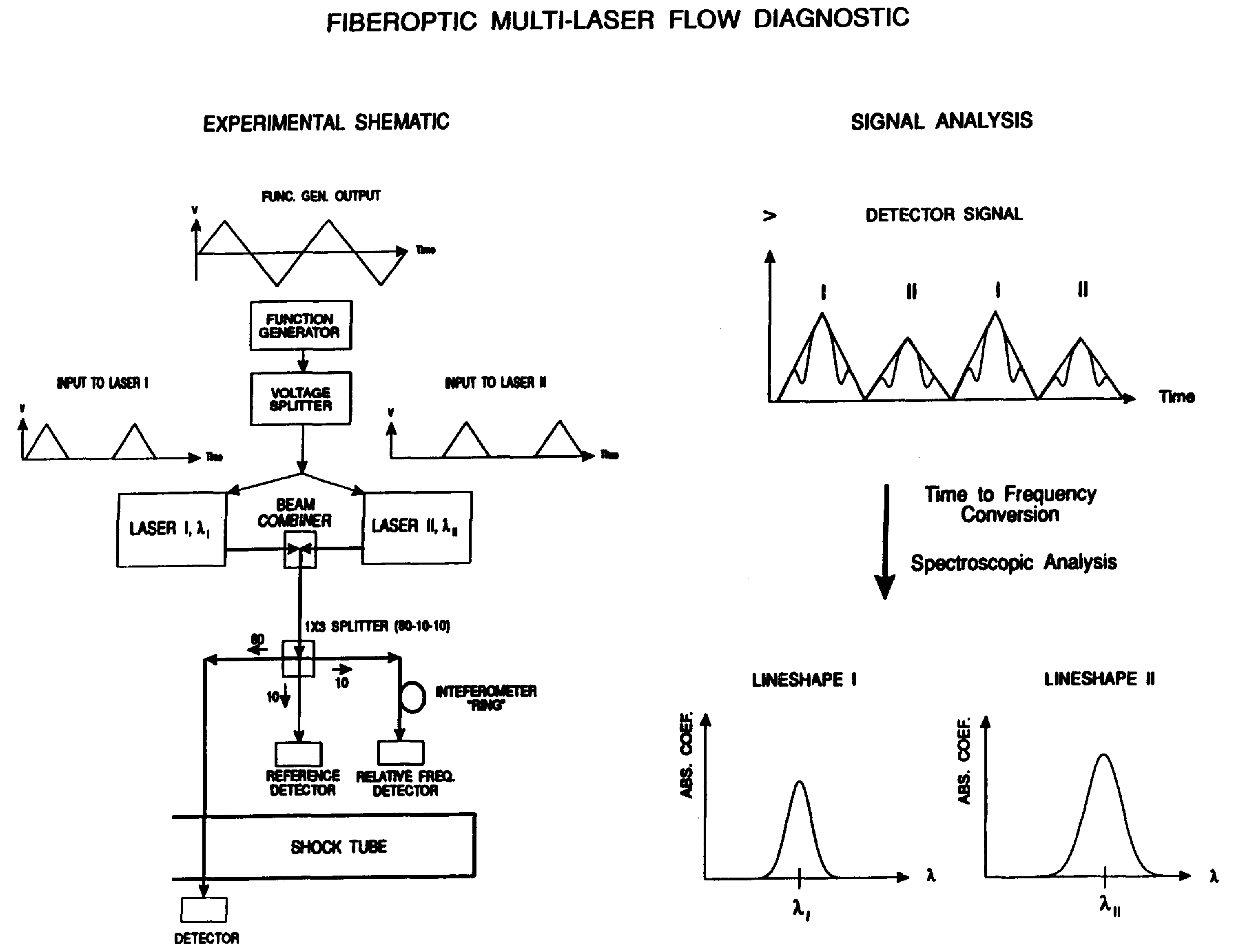

Figure 7. Schematic of fiberoptic, multi-laser scheme for absorption measurements.

interferometer ring (serves as an etalon for measuring frequency change during laser tuning), a reference detector (to monitor the laser intensity during each scan), and the absorption path. The important point to note here is that the light beams are entirely confined to optical fibers, except for the path through the test medium (here a shock tube). There are no lenses or traditional optical elements; all of the beam processing occurs in fiberoptic components. The change in this optical setup, relative to our past work with traditional optical components, is quite striking. When one views the optical table, it now consists of numerous lengths of fiber and fiberoptic components, coupled together with hand-tightened connectors. Obviously, the usual steps of aligning laser beams and detectors is greatly simplified. It is clear that this form of optical system is the way of the future, at least for low power laser systems and for practical applications requiring ruggedness.

The signal seen by the absorption detector is sketched on the right of Fig. 7. The detector alternately sees the modulation of laser I and II, each with a triangular waveform. Conversion from time to frequency is carried out via the detector signal produced by the interferometer ring, leading to the absorption lineshape data plotted in the lower right corner of the figure.

We have only recently attempted to implement this idea in the laboratory. Example data from our first effort are shown in Fig. 8. The experiment involved monitoring water vapor using two diode lasers emitting near 1.40 microns, a combination vibrational band ($\nu_1 + \nu_3$) which is the strongest of the non-fundamental bands. The experiments were conducted in a shock tube to produce a known high temperature, high velocity stream containing water vapor, with the objective of simulating the exhaust stream from a scramjet combustor. The data have been analyzed, with the result shown in the inset table of Fig. 8. Note that the agreement between measured and calculated conditions is good.

This new project has significant potential and will be continued during the forthcoming year. We hope to explore several modifications to our initial strategy, including approaches for increasing the number of laser sources, for measuring multiple species (rather than temperature, and for separating the laser beams by spectral methods rather than by time.

2.4 PLIF Imaging in Nonequilibrium Hypersonic Flows

Nonequilibrium supersonic/hypersonic flows, relevant to current research on scramjets, pose new measurement problems for experimentalists. For example, experiments are often conducted in pulsed flow facilities in which the available measurement time is quite limited, thereby putting a premium on the ability to acquire complete data sets in very short times. In addition, many flows of interest exhibit a high degree of nonequilibrium, requiring

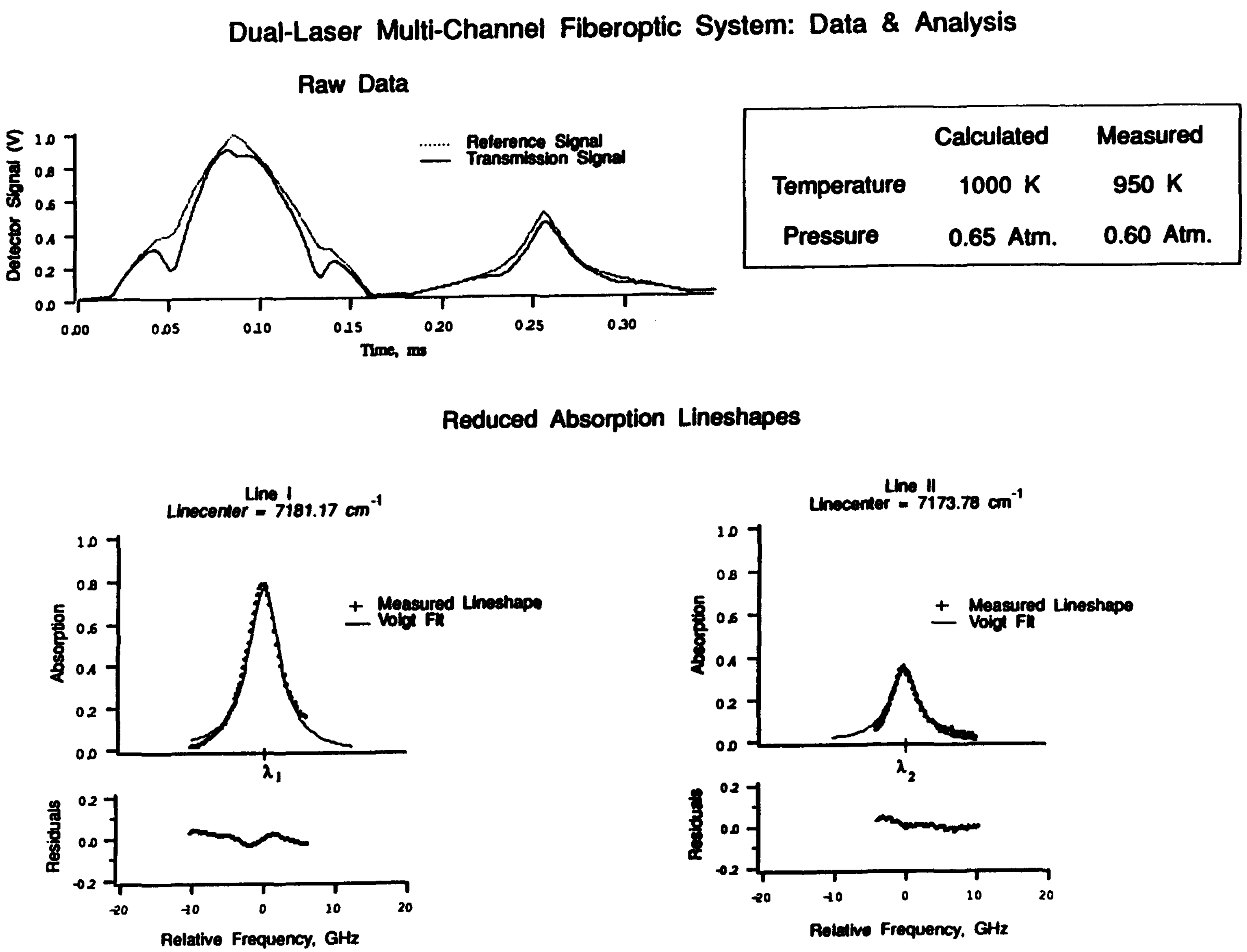

	Calculated	Measured
Temperature	1000 K	950 K
Pressure	0.65 Atm.	0.60 Atm.

Figure. 8. Initial results to measure temperature and pressure in shock-heated water vapor using multi-laser absorption system.

experimental methods sensitive to such nonequilibrium effects. PLIF has high potential for dealing with both of these critical problems, in that the data provide population densities in specific quantum states of the species probed at a very large number of flowfield locations. Our experiments have been carried out in a standard pressure-driven shock tube, built specifically for research on PLIF imaging diagnostics for supersonic flows. Three years ago we added a free-jet shock tunnel to the facility to allow study of PLIF in rapidly expanding, high enthalpy flows. Shock tubes and tunnels provide an economical and convenient means of studying nonequilibrium gasdynamic phenomena and of simulating the extreme conditions relevant to advanced air-breathing propulsion systems. The chief limitation of such facilities, of course, is the short run times which can be produced. A schematic of the current experimental facility is shown in Fig. 9.

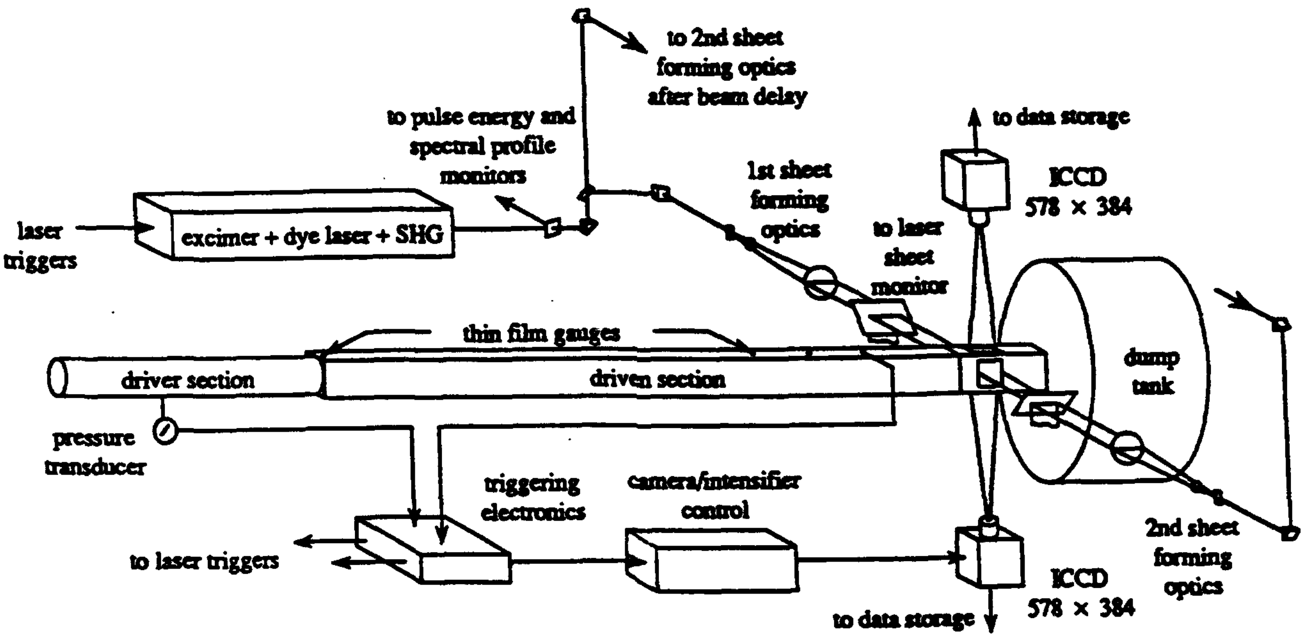

Figure 9. Schematic of experimental facility with associated optical and electronic components for instantaneous one-laser/two-camera PLIF imaging.

The PLIF diagnostics ideas we have been pursuing in the past year are based on the use of two gated CCD cameras (see Fig. 9) and either one or two pulsed dye laser sources. The quantities of primary interest are velocity and temperature. The typical arrangement of the laser sheets used to extract two velocity components in the free jet flowfield is shown in Fig. 10. Here the angle β may be varied to optimize the detection sensitivity of either the radial or axial velocity; a typical value for β in recent experiments has been 57°. In the case of temperature measurements, this angle is usually set to 90°.

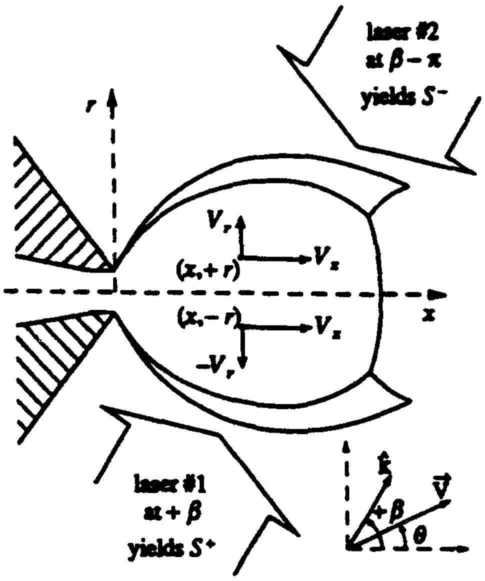

Figure 10. PLIF velocimetry technique utilizing broad-band, counter-propagating laser sheets in a symmetric flowfield.

Our objective in the past year has been to extend velocity measurements to single-shot imaging of two velocity components. This can be accomplished, in a symmetric flow, with two illumination beams, as has been discussed in detail in our publications (e.g., see paper 10 in Sec. 3.3). In the present case, these beams are produced from a single dye laser source, tuned to excite a single transition of NO in the A ← X system near 225 nm. The single output pulse from the laser is formed into two counterpropagating sheets, one of which is optically delayed by 300 nsec, so as to interrogate the flow from opposite directions. This arrangement simplified the analysis, since the Doppler shifts measured along the illumination direction are equal in magnitude (but opposite in sign) for a specific flowfield point. The two values of fluorescence signal measured for each point, together with the information that the flow is symmetric, allows inference of two components of velocity in the illumination plane. In cases which involve nonsymmetric flow, it would be necessary to monitor the Doppler shift at an additional angle; that was not pursued here since only two cameras were available.

As we worked to make the velocity measurements as quantitative as possible, we learned that it was critical to monitor, on a shot-by-shot basis, certain parameters of the laser beam; these include pulse energy, sheet distribution, and the spectral distribution of the laser pulse. In addition, we found it necessary to intentionally broaden the spectral linewidth of the laser to ensure that the maximum Doppler shifts were still contained within a portion of the line containing significant energy. To further improve measurement accuracy and reproducibility, we also developed improved procedures for setting and monitoring the center frequency of the laser relative to the absorption line, and even considered the pressure shift of the absorption line. The apparatus built to enable monitoring of key experimental parameters is shown in Fig. 11.

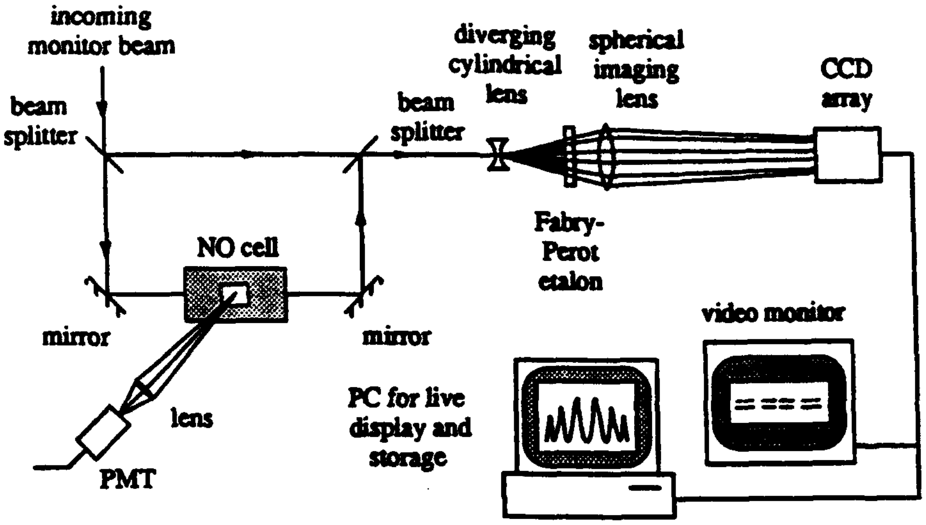

Figure 11. Schematic of equipment used for laser tuning and pulsed spectrum analysis.

Details of the experimental arrangement and procedures as discussed in our publications. Here we will only highlight our findings to indicate the status of the method. Figure 12 provides results for both the radial and axial velocity components along four specific coordinates of the flowfield: the jet centerline and radial cuts at three values of x/D. The critical flow parameters are: stagnation pressure = 4 atm, stagnation temperature = 2000 K, gas mixture 4.6% NO in argon, jet pressure ratio (stagnation/ambient) = 95, jet diameter D = 5 mm, imaged area = 45 mm x 30 mm, laser pulse energy approximately 1 mJ/sheet, transition excited is the $Q_{21} + R_1(3)$; the camera was a time-gated, intensified CCD (576 x 384 pixels).

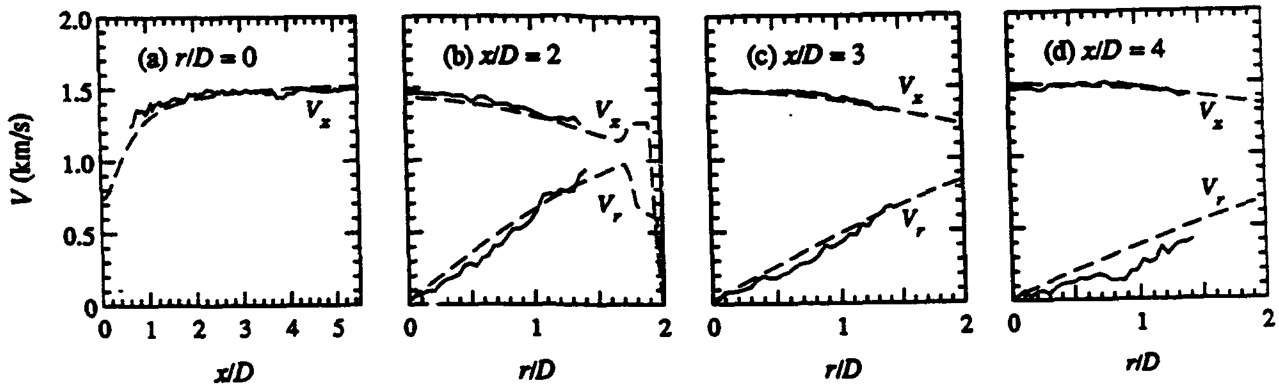

Figure 12. Velocity profiles from MOC prediction (dashed curves) and from analysis of a single-shot PLIF image pair (solid curves): (a) along jet axis, (b) on radial cut at x/D = 2, (c) at x/D = 3, and (d) at x/D = 4.

Note that the results obtained are compared with calculations based on a method-of-characteristics (MOC) code developed earlier in this program. In general, the measurements and calculations may be regarded as in excellent agreement, except for regions close to the barrel shock which bounds the steady, interior flow. Since this flow features a very wide range of temperature, velocity and density, we regard these experiments as a stringent test of the PLIF method. It should be noted that although the maximum velocities measured here are about 1.5 km/sec, extension of this measurement technique to higher velocities should pose no serious problem.

The second diagnostics activity in this flow facility during the past year aimed at PLIF imaging of vibrational and rotational temperatures in a vibrationally relaxing field. The species probed was gain NO, and the flowfield conditions were virtually the same as for the velocity imaging work, except that the gas mixture contained about 8% water vapor to increase the vibrational relaxation rate so that the vibrational temperature would freeze in the portion of the flowfield imaged. The basic strategy of the measurement, illustrated in Fig. 13, is to excite separate vibrational and rotational levels, using a total of three wavelengths. Appropriate ratios of the PLIF signals can then be used to infer both the vibrational temperature and rotational temperature. Although these temperatures are initially equal, as the gas expands to lower temperatures in the free jet, the finite vibrational relaxation rate is eventually insufficient to maintain equilibrium with the rotational and translational temperatures. This phenomenon, known as "vibrational freezing", is of practical importance in rapidly expanding flows such as found in rocket exhausts and possibly the exhaust stream of scramjet combustors. Our research seeks to provide the first diagnostic suitable of providing full-field measurements of these temperatures.

A sample result, shown in a false-color display, is included in Fig. 13. The results, for either of the two temperatures, are obtained in a single firing of the two-laser system. Simultaneous measurement of both temperatures, on a single shot, would require a third laser so as to allow generation of three laser wavelengths. Details of this work are available in paper 7 in Sec. 3.3.

PLIF MEASUREMENTS OF MULTIPLE TEMPERATURES IN A VIBRATIONALLY-RELAXING, SUPERSONIC FLOWFIELD

- Vibrationally-nonequilibrated flows have two temperatures: T_{rot} and T_{vib}

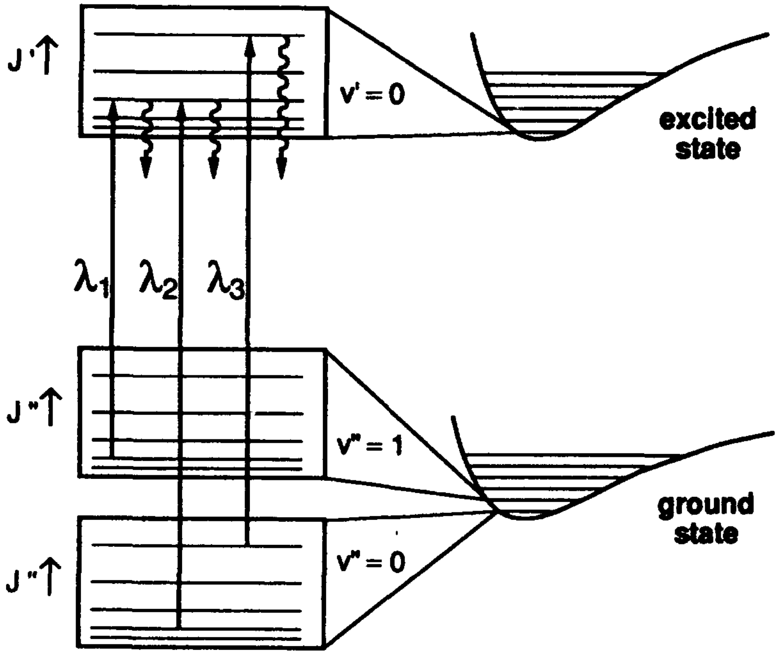

PLIF Image of Free Jet
4.6% NO/8% H_2O/Ar, P_s = 4.0 atm, T_s = 2000 K
43 × 27 mm region

- Use of 3 excitation wavelengths yields T_{rot} and T_{vib}
- PLIF imaging technique extended to multi-temperature flows
- Single-shot capability demonstrated in hypersonic shock tunnel

Figure 13. PLIF strategy and results for thermometry imaging in vibrationally relaxing flowfield.

2.5 PLIF Imaging of Acetone-Seeded Flows

About three years ago, we initiated an effort to survey alternatives to the use of biacetyl as a flowfield tracer in PLIF studies on turbulent mixing in nonreactive flows. Until that time, biacetyl was the preferred choice as an additive owing to its relatively high vapor pressure, convenient excitation wavelength range, high fluorescence yield, and other less critical factors. The development and use of biacetyl seeding in turbulent jet mixing experiments, particularly at Stanford, had previously led to the first high-quality image data for instantaneous scalar fields. These data were well received by the turbulence community owing both to their uniqueness (in providing instantaneous, full-field results for the jet mixture fraction) and to the high quality of the data, especially the high signal-to-noise ratio and high dynamic range achieved. Unfortunately, biacetyl is limited in its applicability to high-speed flows owing to the relatively long radiative decay time (about 1 millisecond) of the phosphorescent emission (long decay times lead to blurring in single-shot images). Thus, as the direction of our research began to emphasize high-speed and supersonic flows, we decided to review alternative molecular tracers.

Although our survey identified several attractive compounds, we eventually selected acetone as best-suited to our needs for a fluorescent tracer. Details of our analysis of acetone photophysics were published this year (see paper 3 in Sec. 34.2). Here we mention only the primary advantages of acetone: (1) acetone has a high vapor pressure, about 180 torr at room temperature, so that it can be easily seeded at high levels; (2) it is economical, easily handled and non-toxic, so that safety is not a problem; (3) the peak absorption is at 275 nm, but reasonably efficient excitation occurs at the convenient laser wavelengths of 248 nm, 266 nm and 308 nm; (4) the fluorescence quantum yield is high, about 0.2%, even in air; (5) the emission has short lifetime (4 nsec) and occurs in a wide band which peaks at 480 nm, in the visible, so that it can be recorded on an unintensified camera; and (6) we estimate that, at room temperature and with existing laser sources, the fluorescence signals achievable with acetone are only about a factor of six less than the high phosphorescence signals obtained with biacetyl. Thus it is possible to obtain both high SNR and high signal resolution (dynamic range), comparable to our past experience with biacetyl, in high speed flows seeded with acetone.

In reviewing options for exciting acetone, we realized that 308 nm light from a xenon chloride (XeCl) excimer laser offered important advantages. For example, by using a tunable excimer, already available in our laboratory, we could simultaneously excite fluorescence of OH, which has a few absorption lines which lie under the output curve of typical (XeCl) laser output. To demonstrate this concept of simultaneous PLIF imaging of multiple species (i.e., acetone and OH), we first performed experiments in a simple diffusion flame. The fuel, nominally H_2, was seeded with acetone (about 10% by mol fraction), and burned in ambient air. Two time-gated intensified CCD cameras were used to capture the resulting PLIF images, as indicated schematically in Fig. 14. The OH images were separated

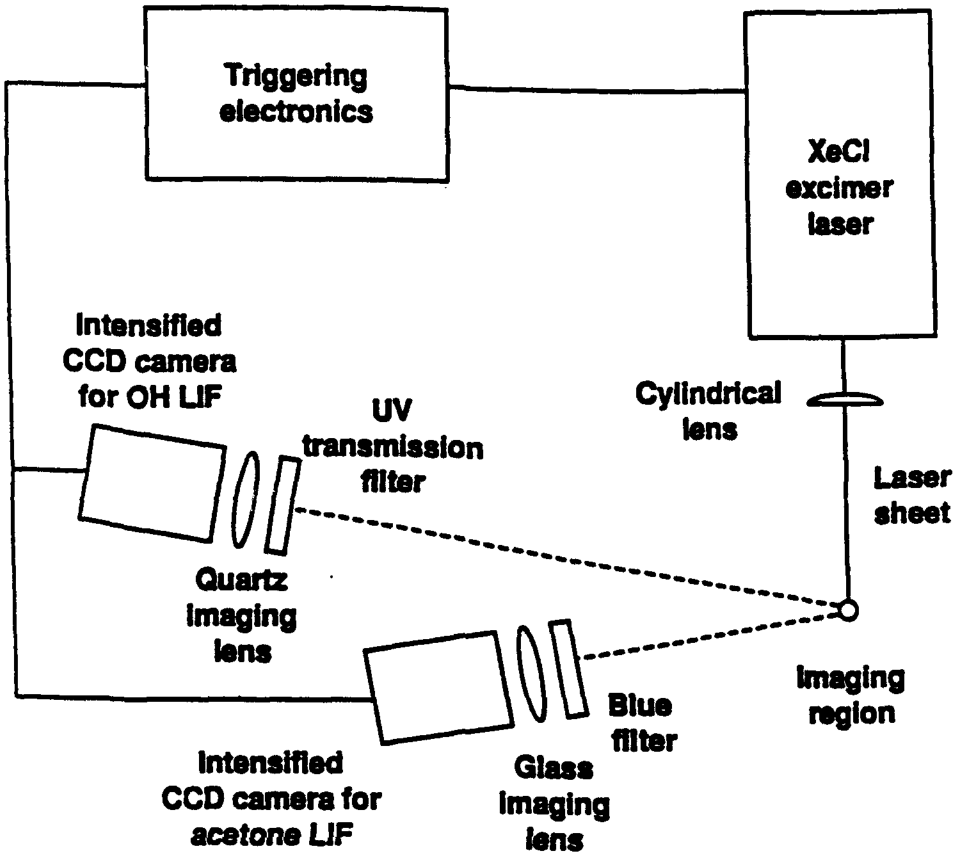

Figure 14. Experimental setup for combined OH/acetone PLIF imaging.

from the acetone images through use of spectral filters; a 10 nm bandpass filter centered at 310 nm was used for the OH channel and a broad bandpass filter selected the 350-470 nm light from the acetone emission. Example results for a flame with jet Re = 24,000 are shown in Fig. 15. The field imaged is 6 cm x 8 cm, the bottom of which is 16 dia above the 2.2 mm nozzle. Note the capability to obtain high quality images for both species with a very simple experimental arrangement. Mie scattering from dust in the ambient air is also evident. The virtue of this diagnostic strategy is the ability to utilize a single laser while obtaining information on multiple species.

During this past year, we also investigated the applicability of the combined OH/acetone imaging concept for supersonic flows. A detailed analysis was carried out to establish the regimes in which acetone could serve as representative tracer of hydrocarbon fuels in reacting (combusting) flows, and this analysis pointed clearly to high-speed flows as optimum. There is good reason to believe that the primary difficulty observed in using acetone as a tracer in a low speed diffusion flame, namely the difference in thermal decomposition of the true fuel and the acetone tracer, would be eliminated in supersonic

SIMULTANEOUS OH AND ACETONE FLUORESCENCE IMAGING USING ONE EXCITATION LASER

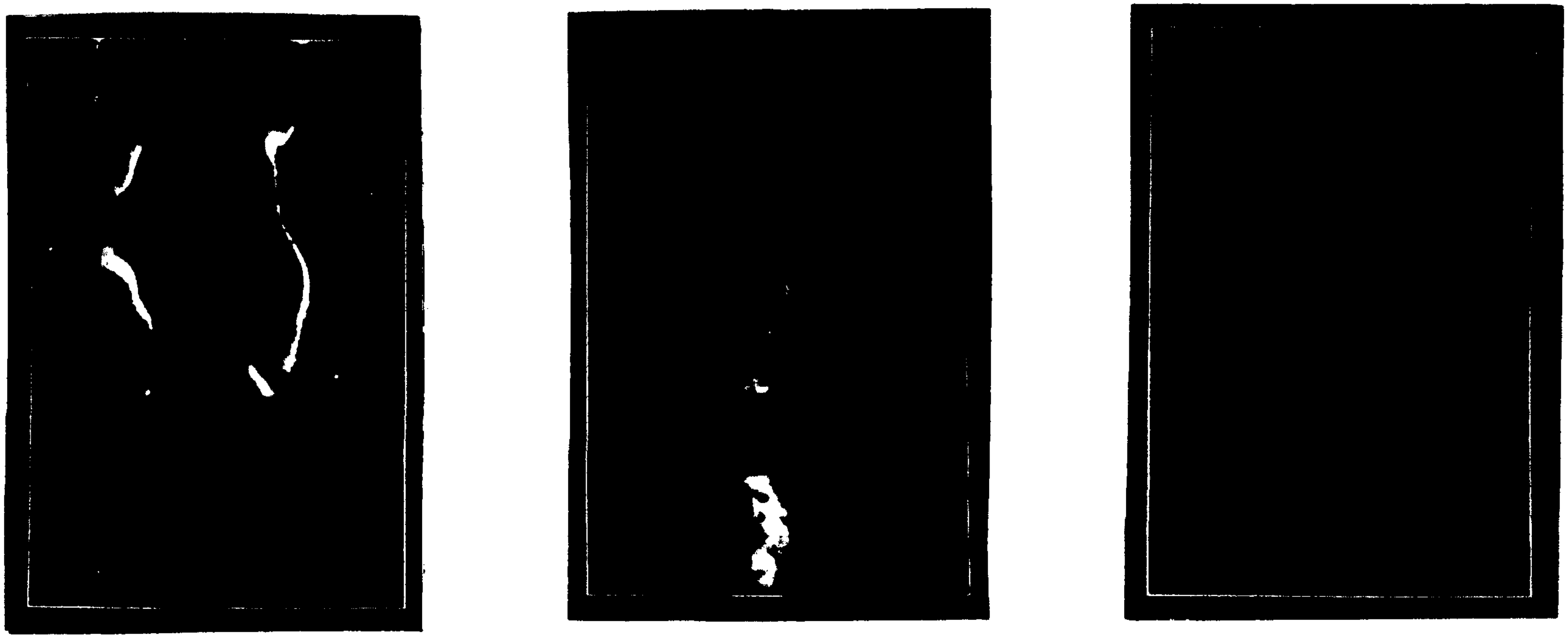

Instantaneous images acquired in an acetone/H_2 diffusion flame (Re = 24,000). Left: OH fluorescence and ambient air dust Mie scattering. Center: acetone fluorescence. Right: superposition of left and center.

Single-laser excitation, two-camera detection strategy enables simultaneous imaging of :

- OH fluorescence (reaction zone information)
- Acetone fluorescence (cold fuel information)
- Air dust Mie scattering (ambient air information)

Figure 15. Simultaneous OH and acetone fluorescence imaging using one excitation laser.

mixing layers where the time scales of interest are very short. The experiments to test this hypothesis, conducted in Stanford's supersonic mixing layer facility, were a collaboration involving Drs. Yip and Seitzman of our diagnostics group with Mike Miller and Toby Island, who are graduate students conducting their Ph.D thesis work in this facility under separate AFOSR support. The flowfield under study is a planar supersonic mixing layer, with high-speed vitiated air on top and lower speed (sonic) fuel (H_2) seeded with acetone on the bottom. The mixing and subsequent combustion of these gases, under supersonic flow conditions, is highly relevant to current research on scramjets. We explored two excitation strategies: (1) 308 nm light from a tunable XeCl laser; and (2) 285 nm light from a tunable dye laser. Both schemes excite both OH and acetone, but the use of 285 nm allows excitation of the 1-0 band of OH and, by use of 1-1 plus 0-0 detection, gives excellent discrimination against elastically scattered light. The result of this measurement strategy is a significant improvement in the signal-to-noise ratio of the OH images.

The experiments in the reacting supersonic mixing layer were highly successful, yielding good signal-to-noise ratios in both measurement channels. The imaging data obtained are the first to provide simultaneous information on the spatial distribution of both the fuel and the combustion product (OH); this information is of critical value to engine designers. In terms of fundamental fluid mechanical insight, these new PLIF data provide useful confirmation of the increasingly three-dimensional character of mixing layers at high convective Mach numbers.

As a last example of PLIF employing acetone, we summarize work during the past two years to develop a scheme for measuring mixing on a molecular scale. The objective is to find a way to eliminate the bias in PLIF measurements of mixing owing to the finite size of the imaged volume. (In short, our usual PLIF images are unable to resolve mixing scales below the size of the imaged volume.) Our strategy, which is a refined version of ideas put forth previously by other groups, can be described with the help of the schematic shown in Fig. 16. We imagine that the problem of interest involves the mixing between two gaseous streams, one seeded with biacetyl and the other with acetone. A pulse of laser light is used to excite the first excited singlet state of acetone, and the absorbed photons nearly all are returned to the ground state by quenching collisions. A small fraction of these absorbed photons are emitted as fluorescence, and this signal, in the blue, is directly proportional to the local concentration of acetone. However, wherever acetone molecules are in intimate contact with biacetyl molecules, a transfer of energy occurs to the first excited triplet state of biacetyl, and some of these molecules then emit fluorescence in the green. Thus, green light is only emitted when mixing has occurred to the molecular level. A typical two-color image acquired in a preliminary study of this concept appears in Fig. 16.

ACETONE-SENSITIZED BIACETYL PHOSPHORESCENCE ALLOWS MEASUREMENT OF MOLECULAR MIXING IN GASEOUS FLOWS

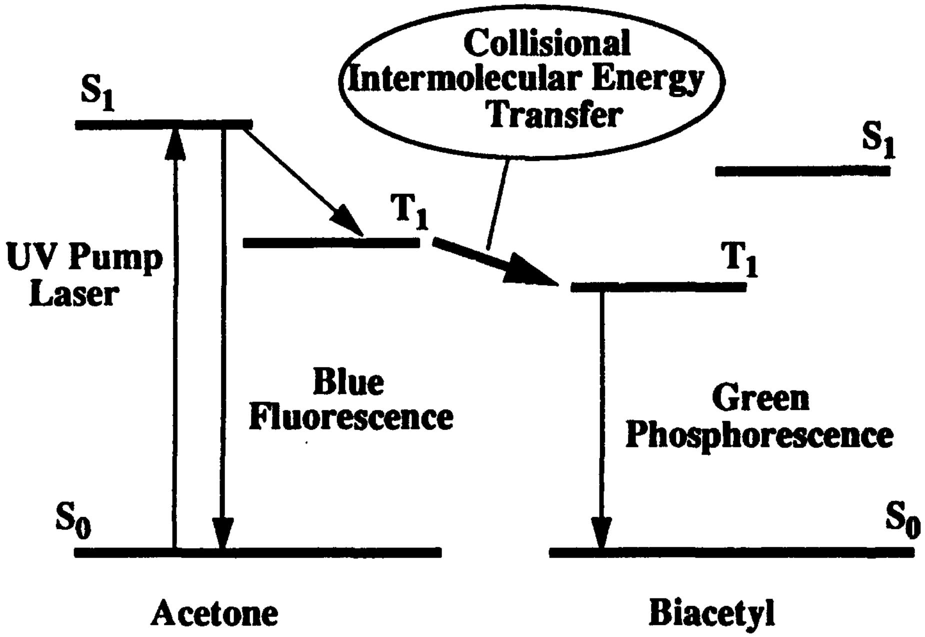

Schematic of energy diagram and photophysical processes.

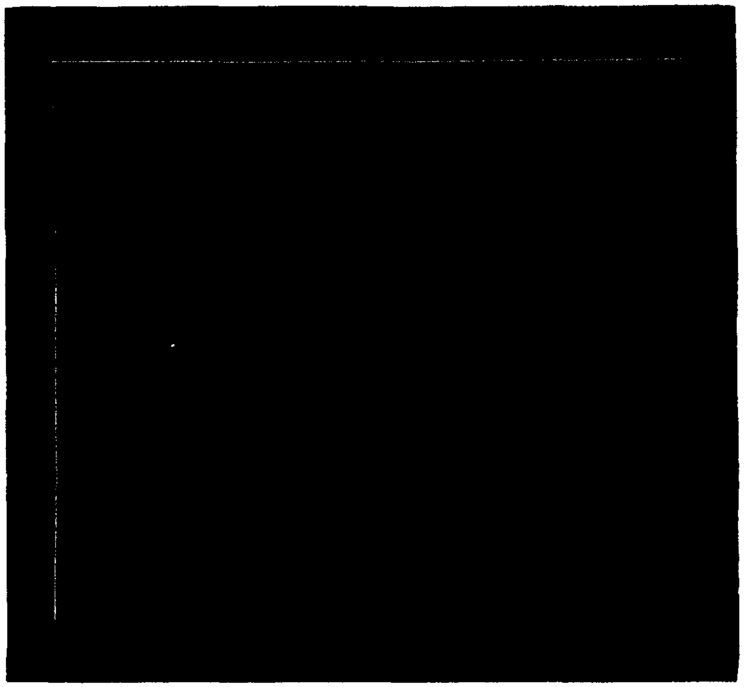

Combined image of acetone fluorescence (blue) and sensitized biacetyl phosphorescence (green).

- Collisionally-induced biacetyl phosphorescence marks flowfield regions where two fluids have mixed molecularly
- Study is in progress to obtain quantitative mixing information from sensitized biacetyl phosphorescence and simultaneous acetone fluorescence

Figure 16. Schematic diagram and example results for PLIF imaging of molecular mixing.

We have developed a detailed model to characterize the behavior of acetone-biacetyl systems as a function of the various parameters: e.g., mixture fraction, pulse energy, collisional cross-sections, radiative rates, etc. This model, presented at the Aerospace Sciences Meeting this past January by Dr. Yip (see paper 8, Sec. 3.3), who is largely responsible for our efforts on this topic, confirms the feasibility of the approach and allows prediction of the signal dependences (uv and green) on the extent of molecular mixing. Although difficulties remain, we believe that this general approach has considerable merit for application in fundamental studies of mixing.

2.6 Degenerate Four-Wave Mixing

Three years ago, we initiated a study of innovative diagnostic methods based on degenerate four-wave mixing (DFWM). A relatively new diagnostic, DFWM is a spatially resolved technique which is complementary to LIF. It offers several advantages in some applications, though it is more complicated and less well understood than LIF. In particular, DFWM generates a coherent signal beam which is useful for both remote sensing and rejection of unwanted background light; and it is a Doppler-free technique allowing very highly resolved (spectrally) spectroscopic measurements. Furthermore, DFWM shows a reduced dependence on quenching compared to LIF. Finally, although this technique requires absorption of light, it does not necessarily require subsequent re-emission of light. Thus, it can be used to probe non-fluorescing transitions as are commonly found in the infrared. In summary, while it is more difficult to perform and understand, DFWM has several attractive qualities when compared to LIF, and hence continued research on this subject is merited.

Since completing and publishing the first study of a single-laser-pulse DFWM temperature measurement over a year ago (see paper 6, Sec. 3.2), we have turned our attention to several different topics related to DFWM. We have continued to invest time in developing an "engineering" understanding of the DFWM process. This has led to simple interpretation of otherwise complicated phenomena observed in the laboratory. Furthermore, this basic understanding has allowed us to consider some new diagnostic methods using DFWM.

Our continued collaboration with researchers at Sandia National Laboratories in Livermore, CA (SNLL), has yielded several results in the last year. (The SNLL component of the effort is sponsored by DOE.) One of the most important experiments was designed to isolate the effects of collisional quenching on both DFWM and LIF. In the limit of strong quenching, LIF signal intensities are expected to scale as l/Q (where Q is the quench rate, which is gas-dependent and is proportional to pressure). If the quench rate is not known, then LIF signal intensities are difficult to interpret On the other hand, the dependence of DFWM on quenching is more complicated, but much less severe than LIF's. In the case of DFWM, quenching is one of several loss mechanisms for the laser-induced grating process. For example, rotational energy transfer (RET) often depopulates the grating faster than quenching. Since RET is much less gas-dependent than quenching, DFWM is expected to be less sensitive to gas composition, and quenching, in most environments.

To investigate this effect directly, we probed a well-isolated line in the A-X band of nitric oxide. Using ~100 Torr mixtures of nitrogen and carbon dioxide as buffer gases with a trace concentration of NO in a cell, the quench rate could be varied by a factor of 10^4 while the pressure broadening was held constant. Figure 17 shows the results of this experiment. On the left of the graph, the buffer gas is pure nitrogen, while on the right the buffer gas is pure carbon dioxide. Intermediate points are mixtures of these two gases. The quench rate is increased by 10^4 from left to right in this graph, while the RET rate increased only 28%. The LIF signal intensity (shown by the triangles) drops by more than a factor of 300 as quenching is increased. For the same conditions, the DFWM intensity (circles) dropped by a factor of 2. Clearly, DFWM is less sensitive to quenching for these conditions. DFWM's reduced sensitivity to quenching is expected when homogeneous broadening is insensitive to quench rate, which is often the case in flames and other practical environments. This study supports early claims that DFWM has a reduced dependence on quenching.

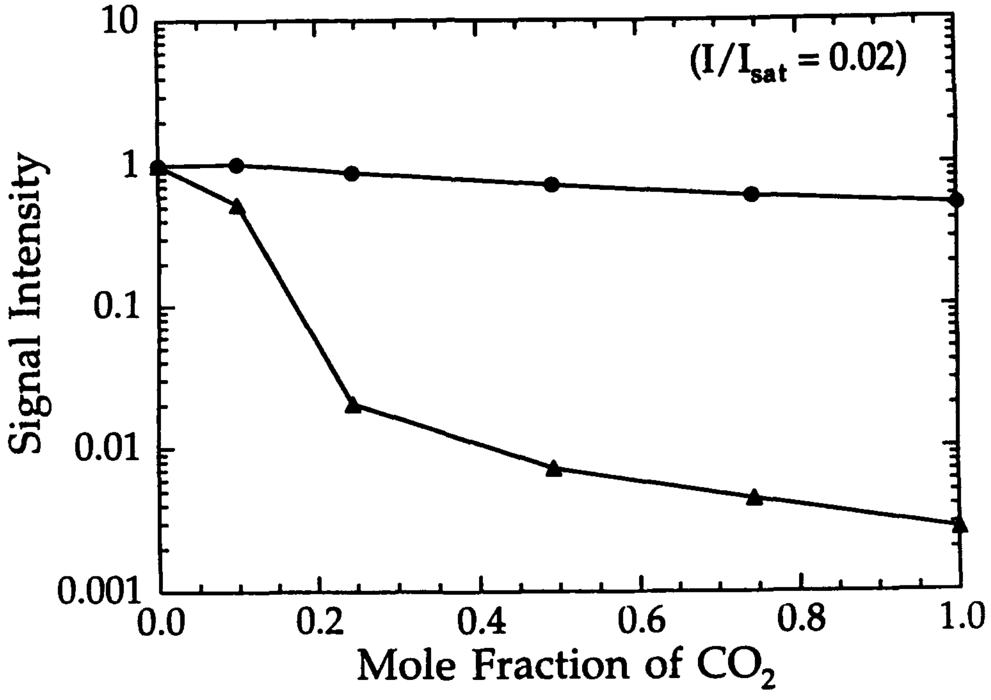

Figure 17. **Nearly unsaturated experimental DFWM (circles) and LIF (triangles) signal intensities versus mole fraction of CO_2 in an N_2/CO_2 mixture. The data are normalized to 1.0 at the left axis and are connected by straight lines to guide the eye.**

Another result of this work was a determination of the laser intensity which minimizes DFWM's sensitivity to quenching. While LIF reaches minimum dependence on quenching at $I >> I_{sat}$, we showed that DFWM reaches minimum dependence on quenching at $I \approx I_{sat}$. This result is very useful to experimentalists attempting to use DFWM in environments such as flames where quenching is unpredictable.

At higher buffer gas pressures, quenching was also found to generate DFWM signal by a mechanism not frequently observed in gases, known as thermal gratings (for a detailed description of this key observation see paper 16 in Sec. 3.2). When light is absorbed in the fringe pattern used in DFWM, it can collisionally relax, resulting in a spatially modulated heat addition. This heat addition perturbs the gas density, which spatially modulates the refractive index of the gas. These index of refraction modulations can contribute to the DFWM signal. Using our physical understanding of DFWM, we are currently developing a simple model for this heat addition process to predict the major temperature and pressure dependences of the thermal gratings. Adding more physics to the model, we are able to predict the time evolution of the thermal grating, which can have a ringing structure. The frequency of the ringing structure is dependent only upon known experimental parameters and the speed of sound in the gas. By measuring this frequency, we are able to measure the speed of sound, and can estimate the temperature. This technique could be used to measure temperature in certain environments where LIF is not applicable.

Finally, in recent work we have successfully demonstrated the use of nearly-degenerate four-wave mixing (NDFWM) to make velocity measurements. These preliminary experiments helped to suggest several improvements to the technique. We are currently planning to investigate this velocity measurement technique in more detail, again in collaboration with researchers at SNLL.

2.7 Diagnostics for High-Pressure Systems

During this past year we have initiated a new research effort aimed at exploring fundamental aspects of laser-based diagnostics for high-pressure combustion systems. This work is motivated by the emerging need for nonintrusive diagnostic methods suitable for probing the variety of advanced combustion and propulsion systems which will operate at increased pressure levels. Systems of special interest include aircraft engines, the ram accelerator, chemical rockets, fuel handling systems of future aircraft (which will involve combinations of high pressure and temperature), and certain solid propellant systems. Until recently, nearly all work with laser-based diagnostics has been done at pressures near atmospheric, with the notable exception of measurements in IC engines which may involve pressure levels of 30-50 atm. Research to establish quantitative laser diagnostic methods for application in systems at higher pressures is clearly needed and timely.

Our plan has been to utilize a shock tube as a device for generating a wide range of accurately known pressures and temperatures. This is an attractive approach owing both to our long experience with shock tubes and to the fact that ONR is currently funding a new high-pressure shock tube in our laboratory which will be used for studies of gas-phase kinetics relevant to combustion of energetic materials. We plan to use this same facility for our AFOSR-sponsored research. At present, the facility design is complete and fabrication is in process. Delivery of the components is scheduled for January, 1994, and we anticipate having the facility operational by March, 1994. This facility will be unique in the United States, and will allow fundamental investigation of spectroscopic and chemical kinetic aspects of gases at pressures up to 1000 atm and at temperatures of several thousand degrees Kelvin.

Although there are several diagnostic methods we wish to study, including spontaneous Raman, laser-induced fluorescence, degenerate four-wave mixing (and related wave-mixing concepts), and line-of-sight absorption, we have focussed our analytical work thus far on the simplest problem, namely the influence of pressure on absorption lineshapes. This is a critical issue, since laser absorption is our most quantitative tool, and it will be essential to use this measurement method as we push the shock tube into an operating regime where ideal gas theories will no longer apply without corrections, e.g. for dense gas effects.

An example of calculations conducted thus far for the influence of pressure on spectral absorption coefficients is shown in Fig. 18. This is a plot of the absorption coefficient across the 0,0 band of the $A \leftarrow X$ system of OH. We have begun with OH owing to its significance as a combustion species in many practical systems and to the fact that we have considerable experience with its spectral properties. Note that the spectrum consists of a relatively large number of discrete features (absorption lines) at 1 atm, but that as pressure is increased to 100 and 500 atm the spectrum becomes a continuous distribution, with significant overlap between the various lines and branches. Our calculations are based on a simple model which simply sums the spectral absorption coefficients at each wavelength and neglects various collision-narrowing interactions which may occur at extreme conditions. Validation of the model used to deal with spectral overlaps and interactions is essential to the future use of absorption as a quantitative tool. Once absorption is fully established, it can be used both for verification of shock tube operating conditions and as a reference method for investigating other diagnostic techniques of interest.

We believe that this new research area will grow in importance during the next few years and that our work will have significant impact on other combustion/propulsion researchers as their needs develop for quantitative measurement tools useful at high pressures.

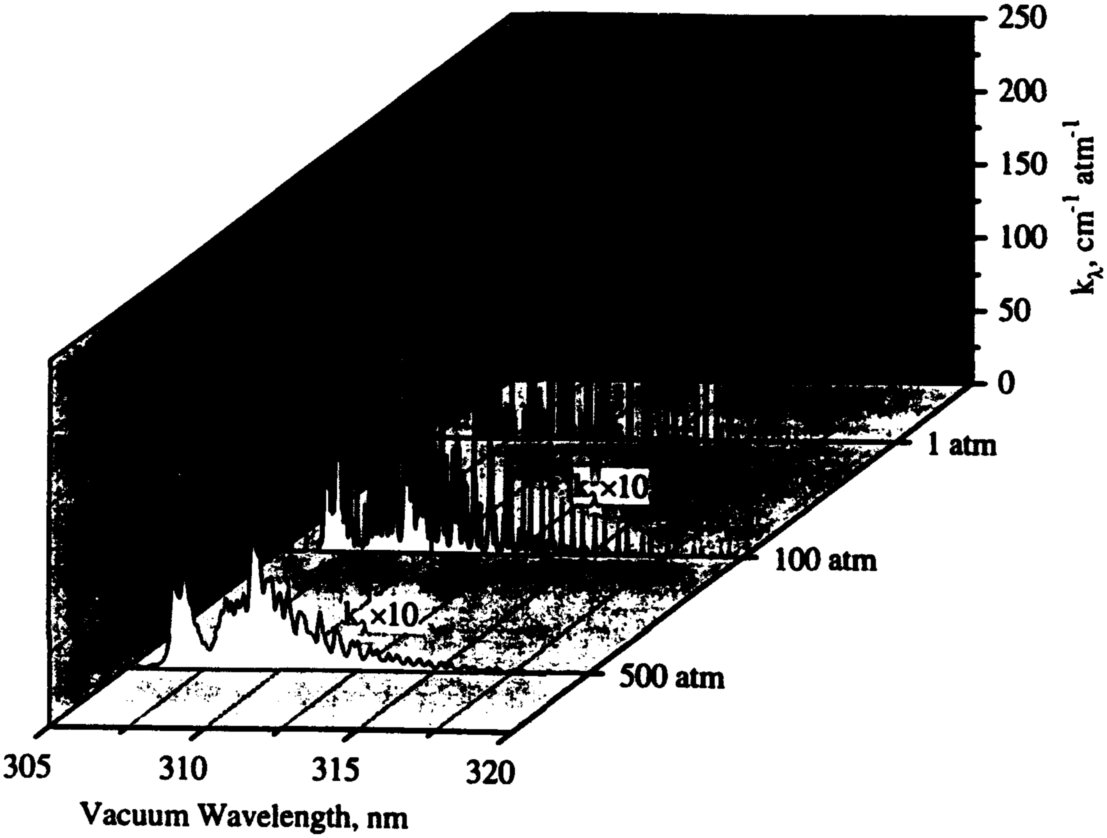

Figure 18. **OH A ← X(0,0) absorption spectrum broadened by argon at 3 pressures; T = 2000 K.**

3.0 PRESENTATIONS AND PUBLICATIONS

3.1 Presentations (11/92 – 10/93)

1. R. K. Hanson, "Laser Diagnostics for Combustion and Propulsion," presented at OE/LASE '93, Jan. 18, 1993.
2. S. H. Smith, A. Lozano, M. G. Mungal and R. K. Hanson, "Scalar Mixing in the Subsonic Jet in Crossflow," paper at AGARD 72nd Fluid Dynamics Meeting, April 19-23, 1993, Winchester, United Kingdom.
3. B. K. McMillin, J. L. Palmer, A. L. Antonio and R. K. Hanson, "Comparison of Two SCRAMJET Model Flowfields Using Instantaneous Two-Line PLIF Temperature Imaging," presented as AIAA Paper 93-0044, 31st Aerospace Sciences Meeting, Reno, NV, January 11-14, 1993
4. R. K. Hanson, "MultiParameter and Multi-Point Measurements," invited presentation at Rank Prize Symposium on Laser Techniques for Combustion Diagnostics, Lake District, Great Britain, April 19-22, 1993
5. R. K. Hanson, "Quantitative LIF and PLIF Diagnostics," invited paper at Third Int. Symp. on Special Topics in Chemical Propulsion: Nonintrusive Diagnostics," Scheveningen, The Netherlands, May 10-13, 1993.
6. D. S. Baer, H. A. Chang and R. K. Hanson, "Semiconductor Laser Diagnostics of Atomic Oxygen in Atmospheric Pressure Plasmas," paper AIAA-93-0822, AIAA 31st Aerospace Sciences Meeting, Reno, Jan. 1993.
7. H. A. Chang, D. S. Baer and R. K. Hanson, "Semiconductor Laser Diagnostics of Atomic Oxygen for Hypersonic Flowfield Measurements," paper AIAA-93-0628, AIAA 31st Aerospace Sciences Meeting, Reno, Jan. 1993.
8. G. W. Butler, D. Q. King, J. G. Liebeskind, R. K. Hanson and M. A. Cappelli, "A Comparison of Arcjet Plume Properties to Model Predictions," paper AIAA-93-0820, AIAA 31st Aerospace Sciences Meeting, Reno, Jan. 1993.
9. B. J. Patrie, J. M. Seitzman and R. K. Hanson, "Planar Imaging at High Framing Rates: System Characterization and Measurements, Part II," paper AIAA-93-0364, AIAA 31st Aerospace Sciences Meeting, Reno, Jan. 1993.
10. J. L. Palmer, B. K. McMillin, and R. K. Hanson, "Planar Laser-Induced Fluorescence Temperature Measurements in Free Jet Flow with Vibrational Nonequilibrium," paper AIAA-93-0046, AIAA 31st Aerospace Sciences Meeting, Reno, Jan. 1993.
11. B. Yip, A. Lozano and R. K. Hanson, "Gas Phase Molecular Mixing Imaging Measurements Using the Acetone-Biacetyl System," paper AIAA-93-0221, AIAA 31st Aerospace Sciences Meeting, Reno, Jan. 1993.

12. B. K. McMillin, J. M. Seitzman and R. K. Hanson, "Comparison of NO and OH PLIF Temperature Measurements in a Scramjet Model Flowfield," paper AIAA-93-2035 at 29th AIAA/SAE/ASME/ASEE Joint Propulsion Conf., Monterey, CA, June 1993.

13. J. L. Palmer, M. Thurber, and R. K. Hanson, "Single-Shot Velocimetry Using Planar Laser-Induced Fluorescence Imaging of Nitric Oxide," paper AIAA-93-2020 at AIAA/SAE/ASME 29th Joint Propulsion Conf., Monterey, CA, June 1993.

14. J. M. Seitzman, J. L. Palmer, A. L. Antonio, R. K. Hanson, P. A. DeBarber and C. F. Hess, "Instantaneous Planar Thermometry of Shock-Heated Flows using PLIF of OH," paper AIAA-93-0802, AIAA 31st Aerospace Sciences Meeting, Reno, Jan. 1993.

15. H. A. Chang, D. S. Baer and R. K. Hanson, "Semiconductor Laser Diagnostics for Simultaneous Determination of Kinetic and Population Temperatures in High-Enthalpy Flows," 19th Int. Symp. on Shock Waves (ISSW 19), Marseille, July 26-30, 1993.

16. R. K. Hanson, "The Role of Lasers in Shock Tube Studies of Chemical Kinetics," invited keynote lecture at 19th Int. Symp. on Shock Waves (ISSW 19), Marseille, July 26-30, 1993.

17. B. K. McMillin, J. M. Seitzman, J. L. Palmer and R. K. Hanson, "Dual-Laser PLIF Imaging Techniques for Shock Tube Studies of Mixing and Combustion," 19th Int. Symp. on Shock Waves (ISSW 19), Marseille, July 26-30, 1993.

18. A. Lozano, B. Yip and R. K. Hanson, "Simultaneous OH and Acetone Fluorescence Imaging in Diffusion Flames," presented at Joint Meeting of Italian and Spanish Sections of the Combustion Instituto, Stresa, Italy, July 1, 1993.

19. R. K. Hanson, D. S. Baer, B. J. McMillin and P. Arroyo, "Multi-Parameter and Multi-Point Measurements," invited paper at Symposium on Laser Diagnostics for Industrial Processes, Heidelberg, June 28, 1993.

3.2 Refereed Publications (11/92 – 10/93)

1. D. S. Baer and R. K. Hanson, "Semiconductor Laser-Based Measurements of Quench Rates in an Atmospheric Pressure Plasma Using Saturated-Fluorescence Spectroscopy," Applied Optics **32**, 948-955 (1993).

2. D. S. Baer, H. J. Chang and R. K. Hanson, "Fluorescence Diagnostics for Atmospheric Pressure Plasmas Using Semiconductor Lasers," J. Opt. Soc. Am. B, Vol. 9, 1968-1978 (1992).

3. A. Lozano, B. Yip and R. K. Hanson, "Acetone: A Tracer for Concentration Measurements in Gaseous Flows by Planar Laser-Induced Fluorescence," Experiments in Fluids **13**, 369-376 (1992).

4. J. M. Seitzman and R. K. Hanson, "Comparison of Excitation Techniques for Quantitative Fluorescence Imaging of Reacting Flows," AIAA J. **31**, 513-519 (1993).

5. M. D. DiRosa, A. Y. Chang and R. K. Hanson, "CW Dye Laser Technique for Simultaneous, Spatially-Resolved Measurements of Temperature, Pressure and Velocity of NO in an Underexpanded Free Jet," Applied Optics **32**, 4074-4087 (1993).

6. B. Yip, P. M. Danehy and R. K. Hanson, "Degenerate Four-Wave Mixing Temperature Measurements in a Flame," Optics Letters **17**, 751-753 (1992).

7. M. P. Lee, B. K. McMillin and R. K. Hanson, "Temperature Measurements in Gases Using Planar Laser-Induced Fluorescence Imaging of NO," App. Optics **32**, 5379-5396 (1993).

8. M. P. Arroyo and R. K. Hanson, "Absorption Measurements of Water Vapor Concentration, Temperature and Lineshape Parameters Using a Tunable InGaAsP Diode Laser," Applied Optics **32**, 6104-6116 (1993).

9. B. K. McMillin, J. L. Palmer and R. K. Hanson, "Instantaneous Temperature Imaging of a H_2/NO Jet in Supersonic Crossflow Using Two-Line PLIF," Applied Optics, in press.

10. B. K. McMillin, J. M. Seitzman and R. K. Hanson, "Comparison of NO and OH PLIF Temperature Measurements in a Scramjet Model Flowfield," submitted to AIAA J., August 1993.

11. J. M. Seitzman and R. K. Hanson, "Planar Fluorescence Imaging in Gases," Chapter 6, (pp. 405-466) in Experimental Methods for Flows with Combustion, ed. A. Taylor, Academic Press, London, 1993.

12. M. P. Arroyo, S. Langlois, and R. K. Hanson, "Diode Laser Absorption Technique for Simultaneous Measurements of Multiple Gasdynamic Parameters in High-Speed Flows Containing Water Vapor," Applied Optics, in press.

13. J. M. Seitzman, R. K. Hanson, P. A. DeBarber, and C. F. Hess, "Application of Quantitative Two-Line OH PLIF for Temporally Resolved Planar Thermometry in Reacting Flows," Applied Optics, in press.

14. D. S. Baer and R. K. Hanson, "Semiconductor Laser Absorption Diagnostics of Atomic Oxygen in an Atmospheric-Pressure Plasma," J. Quant. Spectrosc. and Radiat. Transfer, in press.

15. B. J. Patrie, J. M. Seitzman and R. K. Hanson, "Instantaneous 3-D Flow Visualization by Rapid Acquisition of Multiple Planar Flow Images," Opt. Engineering, in press.

16. P. M. Danehy, E. J. Friedman-Hill, R. P. Lucht and R. L. Farrow, "Effects of Collisional Quenching on Degenerate Four-Wave Mixing," App. Phys 57, 243-248 (1993).

17. J. M. Seitzman and R. K. Hanson, "Two-Line Planar Fluorescence for Temporally Resolved Temperature Imaging in Reacting Supersonic Flow over a Body," App. Phys. B, in press.

18. B. Yip, A. Lozano and R. K. Hanson, "Sensitized Phosphorescence: A Gas-Phase Molecular Mixing Diagnostic," Experiments in Fluids, in press.

19. S. Langlois, T. B. Birbeck and R. K. Hanson, "Diode Laser Measurements of H_2O Line Intensities and Self-Broadening Coefficients in the 1.4 μm Region," J. Molec. Spectroscopy, submitted May 1993.

20. J. M. Seitzman, R. K. Hanson, P. A. DeBarber and C. F. Hess, "Application of Quantitative Two-Line OH PLIF for Temporally Resolved Planar Thermometry in Reacting Flows," Applied Optics, in press.

21. R. K. Hanson, D. S. Baer, B. J. McMillin and P. Arroyo, "Multi-Parameter and Multi-Point Measurements," Int. J. Phys. Chem., in press.

22. J. M. Seitzman and R. K. Hanson, "Planar Fluorescence Imaging: Basic Concepts for Scalar and Velocity Measurements," chapter 14 in *Combusting-Flow Diagnostics*, eds. D. Durao, M. Heitor, J. Whitelaw and P. Witze, Kluwer Academic Publishers, NATO/ASI Series E, 1991.

3.3 Technical Reports (11/92 – 10/93)

1. R. K. Hanson, "Laser Diagnostics for Combustion and Propulsion," OE/LASE '93, Jan. 18, 1993, symposium proceedings, in press.

2. S. H. Smith, A. Lozano, M. G. Mungal and R. K. Hanson, "Scalar Mixing in the Subsonic Jet in Crossflow," Proceedings of AGARD 72nd Fluid Dynamics Meeting, April 19-23, 1993, Winchester, United Kingdom.

3. B. K. McMillin, J. L. Palmer, A. L. Antonio and R. K. Hanson, "Comparison of Two SCRAMJET Model Flowfields Using Instantaneous Two-Line PLIF Temperature Imaging," AIAA Paper 93-0044, 31st Aerospace Sciences Meeting, Reno, NV, January 11-14, 1993

4. D. S. Baer, H. A. Chang and R. K. Hanson, "Semiconductor Laser Diagnostics of Atomic Oxygen in Atmospheric Pressure Plasmas," paper AIAA-93-0822, AIAA 31st Aerospace Sciences Meeting, Reno, Jan. 1993.

5. H. A. Chang, D. S. Baer and R. K. Hanson, "Semiconductor Laser Diagnostics of Atomic Oxygen for Hypersonic Flowfield Measurements," paper AIAA-93-0628, AIAA 31st Aerospace Sciences Meeting, Reno, Jan. 1993.

6. B. J. Patrie, J. M. Seitzman and R. K. Hanson, "Planar Imaging at High Framing Rates: System Characterization and Measurements, Part II," paper AIAA-93-0364, AIAA 31st Aerospace Sciences Meeting, Reno, Jan. 1993.

7. J. L. Palmer, B. K. McMillin, and R. K. Hanson, "Planar Laser-Induced Fluorescence Temperature Measurements in Free Jet Flow with Vibrational Nonequilibrium," paper AIAA-93-0046, AIAA 31st Aerospace Sciences Meeting, Reno, Jan. 1993.

8. B. Yip, A. Lozano and R. K. Hanson, "Gas Phase Molecular Mixing Imaging Measurements Using the Acetone-Biacetyl System," paper AIAA-93-0221, AIAA 31st Aerospace Sciences Meeting, Reno, Jan. 1993.

9. B. K. McMillin, J. M. Seitzman and R. K. Hanson, "Comparison of NO and OH PLIF Temperature Measurements in a Scramjet Model Flowfield," paper AIAA-93-2035 at 29th AIAA/SAE/ASME/ASEE Joint Propulsion Conf., Monterey, CA, June 1993.

10. J. L. Palmer, M. Thurber, and R. K. Hanson, "Single-Shot Velocimetry Using Planar Laser-Induced Fluorescence Imaging of Nitric Oxide," paper AIAA-93-2020 at AIAA/SAE/ASME 29th Joint Propulsion Conf., Monterey, CA, June 1993.

11. J. M. Seitzman, J. L. Palmer, A. L. Antonio, R. K. Hanson, P. A. DeBarber and C. F. Hess, "Instantaneous Planar Thermometry of Shock-Heated Flows using PLIF of OH," paper AIAA-93-0802, AIAA 31st Aerospace Sciences Meeting, Reno, Jan. 1993.

12. H. A. Chang, D. S. Baer and R. K. Hanson, "Semiconductor Laser Diagnostics for Simultaneous Determination of Kinetic and Population Temperatures in High-Enthalpy Flows," Proceedings of 19th Int. Symp. on Shock Waves (ISSW 19), Marseille, July 26-30, 1993, in press.

13. R. K. Hanson, "The Role of Lasers in Shock Tube Studies of Chemical Kinetics," Proceedings of 19th Int. Symp. on Shock Waves (ISSW 19), Marseille, July 26-30, 1993, in press.

14. B. K. McMillin, J. M. Seitzman, J. L. Palmer and R. K. Hanson, "Dual-Laser PLIF Imaging Techniques for Shock Tube Studies of Mixing and Combustion," Proceedings of 19th Int. Symp. on Shock Waves (ISSW 19), Marseille, July 26-30, 1993, in press.

4.0 PERSONNEL

Individual researchers supported by the program are listed below. All the work has been carried out in the High Temperature Gasdynamic Laboratory, in the Department of Mechanical Engineering, under the supervision of Professor R. K. Hanson.

4.1 Postdoctoral Research Associates

Dr. B. Yip (50% time)
Dr. P. Arroyo (25% time)
Dr. J. Seitzman (25% time)
Dr. D. Baer (25% time)

4.2 Graduate Research Assistants

Tim Birbeck
Renato Cedolin (50% time)
Andrew Chang
Paul Danehy
Brian McMillin
Jennifer Palmer
Brian Patrie

4.3 Ph.D. Degrees Awarded (1990-1993)

Dr. David Hofeldt, 11/90, "Instantaneous Imaging Diagnostics for Measuring Particle Sizes and Spatial Distributions over Extended Regions in Two-Phase Flows"

Dr. Larry Cohen, 11/90, "Emission and Laser-Induced Fluorescence Diagnostics of a Supersonic Jet of Plasma-Heated Nitrogen,"

Dr. Jerry Seitzman, 6/91, "Quantitative Applications of Fluorescence Imaging in Combustion,"

Dr. Michael Lee, 11/91, "Temperature Measurements in Gases Using Planar Laser-Induced Fluorescence Imaging of NO and O_2,"

Dr. Antonio Lozano, 8/92, "Laser-Excited Luminescent Tracers for Planar Concentration Measurements in Gaseous Jets," Dr. Douglas Baer, 3/93, "Plasma Diagnostics with Semiconductor Lasers using Fluorescence and Absorption Spectroscopy,"

Dr. Brian McMillin, 5/93, "Instantaneous Two-Line PLIF Temperature Imaging of Nitric Oxide in Supersonic Mixing and Combustion Flowfields."

5.0 SIGNIFICANT INTERACTIONS

In addition to the interactions associated with the presentations and publications listed in Section 3, we have had numerous visitors to our laboratory during this past year. Foreign visitors have come from Germany, France, Great Britain, Canada, Spain, Portugal and Japan; industrial and national laboratory visitors have included representatives from Rocketdyne, Aerometrics, Physical Sciences, Boeing, Metrolaser, AEDC, NASA Ames, NASA Lewis, NIST, Sandia, Lawrence Livermore, General Motors, Nissan, Hitachi, Kao Corporation and Toyota. Professor Hanson has given invited presentations on AFOSR-sponsored diagnostics research to industrial laboratories and government groups in the U.S. and Europe, including key addresses at a special meeting of the Rank Prize Funds organization, in Great Britain; the International Symposium on Special topics in Chemical Propulsion, in the Netherlands; the Nineteenth International Symposium on Shock Waves, in France; a special symposium on Laser Diagnostics for Industrial Processes, in Germany, and at an annual meeting of S.P.I.E., in Los Angeles. Members of our group have provided technical information and advice, by telephone and mail, to several external researchers interested in duplicating or extending our diagnostics concepts.

Interest in the potential application of advanced laser diagnostics to various practical problems, especially associated with hypersonic flow and the NASP program, continues at a high level, and the AFOSR-sponsored program at Stanford has achieved a high level of recognition for its contributions to this field. During the past few years, we have collaborated with researchers at NASA-Ames to implement two of our diagnostics schemes (ring dye laser absorption of OH and diode laser absorption of O_2) in their 16-inch shock tunnel; in the past year, we have initiated a further collaboration to monitor H_2O at the exit of a model scramjet using diode laser absorption. The increased interest we are witnessing is a useful indicator of the extent of technology transfer which is occurring in laser diagnostics between Stanford and industrial and government labs. Further effort is required, however, to ensure the success of this technology transfer.

6.0 COPIES OF KEY PUBLICATIONS

Reprints of key refereed papers at attached. These include papers 1 through 8 listed in Sec. 3.2.

a reprint from Journal of the Optical Society of America B

Fluorescence diagnostics for atmospheric-pressure plasmas using semiconductor lasers

Douglas S. Baer, H. Andrew Chang, and Ronald K. Hanson

High Temperature Gasdynamics Laboratory, Department of Mechanical Engineering, Stanford University, Stanford, California 94305

Received February 3, 1992; revised manuscript received May 26, 1992

Semiconductor laser diagnostics based on laser-induced fluorescence and absorption have been developed to probe the $4s^3P_1 \rightarrow 4p^3D_1$ transition (8104 Å) of argon in an atmospheric-pressure plasma produced by an inductively coupled plasma torch. Spatially resolved measurements of electron number density, atomic kinetic temperature, and electron temperature have been inferred from a line-profile analysis of Stark-affected absorption spectra. State parameters determined from simultaneous fluorescence and absorption line-shape and line-shift measurements are mutually consistent and show good agreement in the analytical region of the plasma. The results represent what are to our knowledge the first spectrally resolved fluorescence measurements of argon in an atmospheric-pressure plasma.

INTRODUCTION

The thermodynamic state of an atmospheric-pressure plasma is determined predominantly by the electron number density (n_e), the electron temperature (T_e), and the atomic kinetic temperature (T). Local values of these state parameters control the transport mechanisms, atomic excitation, and ionization. For example, ambipolar diffusion and the electrical conductivity are determined by n_e and T_e; thermal conductivity by n_e, T_e, and T; and viscosity by T. In quasi-neutral plasmas, the electron-impact excitation, ionization, recombination, and charge-transfer processes are specified by n_e and T_e. In addition, these parameters influence various interactions and processes that lead to the primary spectral line-broadening mechanisms. Consequently, a spectral line shape reflects the physical state of the environment and may be used, in conjunction with reliable theory, to determine the important plasma parameters.

Recently, spectrally resolved measurements of argon absorption line shapes have been recorded by tuning the narrow-band output of a semiconductor (tunable-diode) laser over the argon transitions $4s^3P_1 \rightarrow 4p^3D_1$ (8104 Å) and $4s^3P_2 \rightarrow 4p^3D_3$ (8115 Å).[1] Stark-broadening analyses and integrated line shapes were used to determine n_e, T, and the population temperature (T_{pop}) of the probed states in the analytical region of an inductively coupled plasma flow field. In the research reported in the present paper, a semiconductor (GaAlAs) laser operating single mode was tuned over the $4s^3P_1 \rightarrow 4p^3D_1$ argon transition at 8104 Å (Fig. 1). Fluorescence monitoring of the absorption spectra yielded improved spatial resolution. Simultaneous absorption line-shape measurements in a low-pressure dc discharge provided a wavelength reference that permitted determination of the Stark shift. An analysis of the Stark broadening and the shift was used to infer spatially resolved values of n_e, T_e, and T in the plasma. An experimental evaluation of these diagnostics is the principal subject of this paper.

THEORY

Line Shape

The transmission of a probe beam of light through a linearly absorbing medium may be described by the Beer–Lambert relationship given by

$$T(\nu) \equiv I(\nu)/I_0 = \exp\left[-\int k(\nu)\mathrm{d}x\right], \tag{1}$$

where $T(\nu)$ is defined as the spectral transmittance of the medium, $I(\nu)$ is the intensity at frequency ν after propagation through the absorbing medium, I_0 is the incident intensity of the probe beam, and $k(\nu)$ is the spectral absorption coefficient.

The absorption coefficient near a spectral line for a system in Boltzmann equilibrium can be expressed in terms of the number density in the absorbing state, n_l, a line-shape function, $\phi(\nu)$, the Einstein coefficient for absorption between levels l and u, B_{lu}, and the energy difference between levels l and u, $E_u - E_l \equiv h\nu$,[2]

$$k(\nu) = h\nu n_l(B_{lu}/c)[1 - \exp(-h\nu/kT_{\mathrm{ex}})]\phi(\nu), \tag{2}$$

where the frequency integral of the line shape is normalized to unity, i.e., $\int \phi(\nu)\mathrm{d}\nu \equiv 1$. The second term in the brackets in Eq. (2), which accounts for stimulated emission, becomes nonnegligible when the energy difference between laser-coupled levels l and u becomes comparable with the excitation temperature, i.e., $E_u - E_l \approx kT_{\mathrm{ex}}$. Note that, since terms on the right-hand side of Eq. (2) may vary over the probed region, the spectral absorption coefficient is an implicit function of position along the path length.

The line-shape function, $\phi(\nu)$, reflects the thermodynamic state of the plasma and is a result of the various broadening mechanisms acting on the absorbing particles. In partially ionized, atmospheric-pressure plasmas, a spectral line is broadened primarily by Doppler- and

0740-3224/92/111968-11$05.00

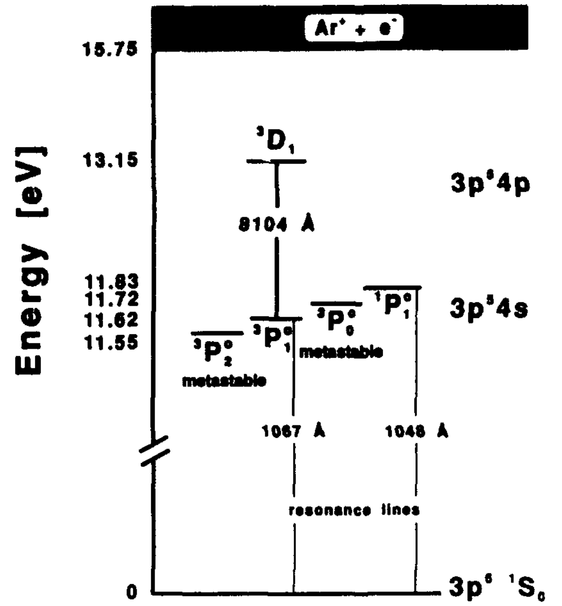

Fig. 1. Energy-level diagram of argon, illustrating the relevant transitions for the present investigation.

collisional-broadening mechanisms. Natural broadening, which is due to the radiative decay of the laser-coupled states, is relatively small (<4%) compared wth the environmental broadening processes. Doppler broadening, which is due to the relative motion of an absorbing (emitting) particle and the light source (observer), is particularly significant at the temperatures typically encountered in atmospheric-pressure plasmas.[3] For a system of particles with a Maxwellian velocity distribution, the relation between the Doppler-broadening line width (FWHM) $\Delta\nu_D$ and the kinetic temperature T(K) is given by[3]

$$\Delta\nu_D/\nu_0 = (8kt \ln 2/Mc^2)^{1/2}, \tag{3}$$

where M is the mass of the absorber (kg), k is the Boltzmann constant (J/K), c is the speed of light (m/s), and ν_0 is the line-center frequency of the transition.

The collisional mechanisms that yield Lorentzian profiles in argon include van der Waals, resonance, and Stark broadening. Van der Waals broadening is due to interactions between argon and all neutral species (R^{-6} dependent, where R is the interatomic separation) not optically coupled to the levels involved in the probed transition. Calculations indicate that these collisional-broadening effects are insignificant for the conditions present in this investigation.[1] Resonance broadening (R^{-3} dependent), however, which is due to collisions with similar atoms, may have effective cross sections orders of magnitude larger than foreign gas kinetic cross sections.[3] The resonance interaction can occur when an atom in an excited state radiatively interacts with a similar atom in the ground state. The effect of the interaction is a reduction in the lifetime of the upper state and a broadening of line shapes that include this level. For example, in the present investigation the $4s\,^3P_1$ state is strongly coupled to the ground state through the resonance transition $4s\,^3P_1 \rightarrow 3p^6\,^1S_0$.[4] As a result, resonance broadening of the $4s\,^3P_1$ state must be included in a line-shape analysis when one is probing transitions that include this level.

The theoretical Lorentzian line width (FWHM) $\Delta\nu_{\text{res}}$ (rad/s), which is due to resonance broadening, may be expressed by the relation[3]

$$\Delta\nu_{\text{res}} \approx 3/2(g_0/g_1)^{1/2} e^2 f_{01} N/(\epsilon_0 m_e \omega_{01}), \tag{4}$$

where g_0 and g_1 are the degeneracies of the ground state and the resonance level, respectively; f_{01} is the oscillator strength of the resonance transition; ω_{01} (rad/s) is the angular frequency of the resonance transition; N (m^{-3}) is the ground-state number density; ϵ is the free-space permittivity; and m_e is the electron mass. Lines corresponding to transitions between the resonance level and other excited levels are unshifted.[3]

Stark broadening, which is due to Coulombic interactions with charged particles, is often the most significant collisional-broadening mechanism in atmospheric-pressure plasmas. The spectral lines of nonhydrogenlike atoms, such as argon, are generally influenced by the square of the local electric field strength through the quadratic Stark effect, resulting in an essentially Lorentzian line shape.[3] The results of detailed calculations that use a generalized quantum-mechanical treatment of Stark broadening and shift of a spectral line yield relations involving transition-specific parameters that relate width and shift to electron number density and temperature. For singly ionized plasmas, the total theoretical width (FWHM) that is due to quadratic Stark broadening, w_{th} (Å), and the total theoretical Stark shift, d_{th} (Å), may be determined by using the formulas[3,5]

$$w_{\text{th}} \approx 2[1 + 1.75 \times 10^{-4} n_e^{1/4} \alpha (1 - 0.068 n_e^{1/6} T_e^{-1/2})] 10^{-16} w n_e, \tag{5}$$

$$d_{\text{th}} \approx [d/w \pm 2.0 \times 10^{-4} n_e^{1/4} \alpha (1 - 0.068 n_e^{1/6} T_e^{-1/2})] 10^{-16} w n_e, \tag{6}$$

where n_e is in units of inverse cubic centimeters; T_e is in kelvins; w, in angstroms, is the electron impact parameter; α is the ion-broadening parameter; and d/w is the relative electron impact shift.[5] The appropriate sign in Eq. (6) is the same as that of d/w. In general, the Stark shift is toward longer wavelengths except for negative values of d/w. Effects that are due to ion broadening and quadrupole interactions may be included, if necessary, by appropriately modifying the electron impact parameter.[1,5] Equations (5) and (6) have been written in a form that explicitly includes the numerical dependence on n_e and T_e so that the tabulated Stark parameters may be used directly.

In addition, a line shape may be wavelength shifted as a result of relative motion between the absorber and the light source (Doppler shift) or of collisional interactions (pressure shift). The laser beam was directed perpendicular to the axial component of the argon bulk flow velocity to minimize Doppler shift. For atmospheric-pressure plasmas with $n_e > 10^{15}$ cm^{-3}, calculations indicate that pressure shifts resulting from collisional interactions (assuming a van der Waals potential) between atomic species are insignificant relative to those induced from charged particle interactions for the $4s\,^3P_1 \rightarrow 4p\,^3D_1$ transition. Thus a net shift in the measured spectral line may be attributed solely to charged particle interactions.

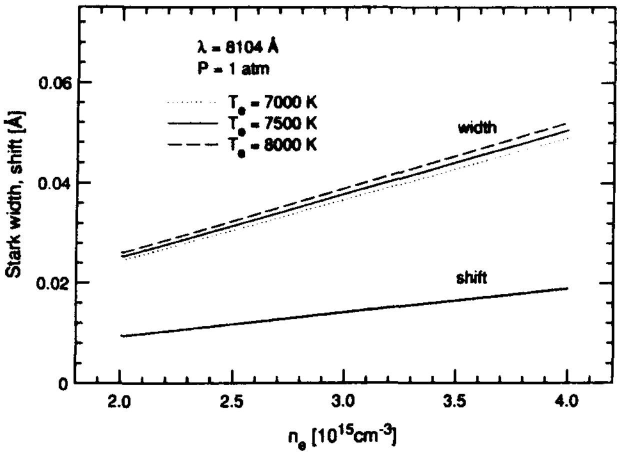

Fig. 2. Calculations, using relation (5) and the transition-specific parameters given in Ref. 4, of Stark width (FWHM) and shift for a range of values of electron number density and temperature encountered in this investigation.

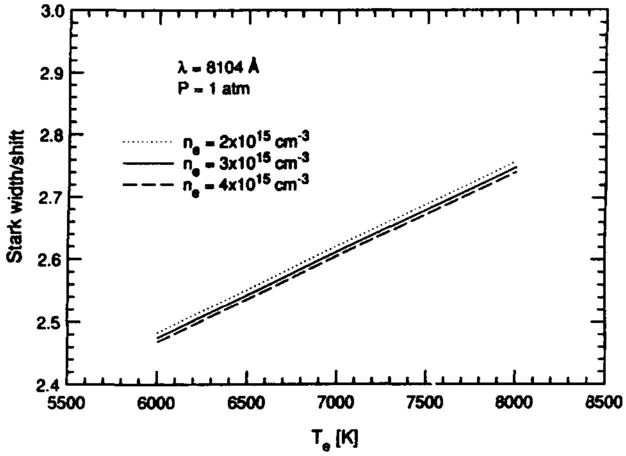

Fig. 3. Calculations, using relation (6) and transition-specific parameters, of the ratio of Stark width to Stark shift for a range of values of electron number density and temperature encountered in this investigation.

Figures 2 and 3 show results of calculations of the Stark width the Stark shift, and the ratio of the Stark width to the Stark shift (Stark width/shift) made by using Eqs. (5) and (6) for a range of electron number density and temperature values typically encountered in inductively coupled plasmas. The net effect of the various terms contributing to the Stark broadening and shift of a line shape yields a relation essentially linearly dependent on n_e and only weakly dependent on T_e. Consequently a measurement of the Stark width or of the wavelength shift of a spectral line relative to its unperturbed value can yield a determination of n_e. The ratio Stark width/shift is dependent sensitively on T_e and weakly on n_e. Therefore an accurate measurement of the ratio Stark width/shift can, in principle, permit a determination of T_e.

If collisions and thermal motion are uncorrelated, the measured line shape is a Voigt profile, given by a convolution of the Doppler and Lorentzian profiles. The line-shape function may be expressed in terms of a Voigt function through the relation

$$\phi(\nu) = (4 \ln 2/\pi)^{1/2}/\Delta\nu_D V(x - s, \mathbf{a}), \tag{7}$$

where $\mathbf{a}$ is the Voigt $\mathbf{a}$ parameter, defined by

$$\mathbf{a} \equiv (\ln 2)^{1/2}\Delta\nu_c/\Delta\nu_D, \tag{8}$$

and $\Delta\nu_c$ is the total Lorentzian component (FWHM) of the line shape. The normalized frequency of detuning, x, is defined as $x \equiv (4 \ln 2)^{1/2}(\nu - \nu_0)/\Delta\nu_D$. Similarly, the collision (Stark) shift, $\Delta\nu_0$, is related to the normalized shift, s, according to the relation $s \equiv (4 \ln 2)^{1/2}\Delta\nu_0/\Delta\nu_D$. Finally, the Voigt function is normalized such that $\int V(x - s, \mathbf{a})\mathrm{d}x = \pi^{1/2}$.

Ionization Equilibrium

For a system in ionization equilibrium, the law of mass action may be expressed by using the Saha equation[3]

$$n_e n_i/n_a = 2(2\pi m_e kT_e)^{3/2}/h^3(Z_i/Z_a)\exp[-(E_i - \Delta E_i)/kT_i], \tag{9}$$

where T_i is the ion temperature, E_i is the ionization energy, ΔE_i is the decrease in the ionization energy caused by electric microfields in the plasma, m_e is the electron mass, and Z_i and Z_a are the partition functions of the ionic and atomic species, respectively. The first term on the right-hand side of Eq. (9) (including the factor of 2 to account for the two possible spin states) is the total partition function for the electrons, and therefore the electron temperature is used explicitly. The second term, the ratio of ion and atom internal partition functions (Z_i/Z_a), is relatively insensitive to temperature changes. The exponential factor serves to give the state sum of the ion the same zero energy reference as the state sum of the atom and describes the relative ion population. Consequently the ion temperature is the appropriate temperature to be used in this term. Since Eq. (9) depends relatively weakly on the electron temperature in the pre-exponential term, however, the ion temperature is the characteristic parameter that effectively describes the concentration of charged particles. Conversely, for a quasi-neutral plasma at a given pressure, a measurement of the electron number density can be used to determine the ion temperature.

Relative Fluorescence Signal

Since the present measurements use laser excitation, which does not significantly perturb the populations in the states coupled in the transition, a sufficient LIF signal analysis need consider only weak excitation by a narrow-bandwidth laser uniformly illuminating a region in the flow field. For collection optics oriented perpendicular to the probe beam and negligible radiative trapping, the LIF signal (S_{LIF}) may be expressed through the relation[6]

$$S_{\mathrm{LIF}} = \eta h\nu(\Omega/4\pi)A_{ul}/(A_{ul} + Q)\int I_L k(\nu)\mathrm{d}V_{\mathrm{LIF}}, \tag{10}$$

where I_L is the incident laser intensity at the probe volume, η is the overall detection system efficiency, Ω is the solid angle subtended by the collection optics, A_{ul} is the spontaneous transition probability from the upper state of the fluorescence transition, and Q is the nonradiative quench rate and accounts for processes that depopulate the upper level without yielding fluorescence radiation in the detection bandwidth. The integration is taken over the observation volume defined by the collection optics and the probe beam. The spectral distribution of the monitored fluorescence is determined by the bandpass of the monochromator, which, for the present analysis, is assumed to be large enough effectively to integrate the entire fluorescence line shape. For uniform conditions inside the observed fluorescence volume, integration of Eq. (10) yields

$$S_{\mathrm{LIF}} = \beta I_L k(\nu) A_{ul}/(A_{ul} + Q), \tag{11}$$

where β is a term that combines all wavelength-dependent quantities and the fractional term is the fluorescence yield, or Stern–Volmer factor, representing the fraction of absorbed laser energy radiated as observed fluorescence. The results of previous absorption measurements have shown that the plasma is not optically thick for the particular transition and conditions investigated.[1] Consequently Eqs. (10) and (11) may be used to describe the spectral characteristics of the fluorescence line shape. Hence, for weak (nonsaturating) laser intensities, absorption line shapes are preserved by using narrow-band excitation with fluorescence monitoring.

For the general case, including excitation by sufficiently high intensities that significantly perturb the populations in the laser-coupled levels, the fluorescence equation may be expressed as[7]

$$S_{\mathrm{LIF}} = \eta(\Omega/4\pi) k_s(\mathbf{a}_s, \nu) I_L A_{ul}/(A_{ul} + Q) V_{\mathrm{LIF}}, \tag{12}$$

where $k_s(\mathbf{a}_s, \nu)$ is the saturated spectral absorption coefficient; $\mathbf{a}_s$ is the saturated Voigt $\mathbf{a}$ parameter, defined as $\mathbf{a}_s \equiv \mathbf{a}(1 + I_L/I_{\mathrm{sat}})^{1/2}$; and I_{sat} is the saturation intensity. The saturated spectral absorption coefficient, which accounts for nonlinear effects such as a significant reduction in the lower state population and additional line broadening resulting from the strong laser intensity coupling the probed energy levels, may be expressed as[7]

$$\begin{aligned} k_s(\mathbf{a}_s, \nu) &\equiv h\nu (B_{lu}/c) n_l [1 - \exp(-h\nu/kT_{\mathrm{ex}})] \\ &\quad \times (1 + I_L/I_{\mathrm{sat}})^{-1/2} \phi(\mathbf{a}_s, \nu), \end{aligned} \tag{13}$$

where the saturation intensity, for a two-level system, is defined as[7,8]

$$I_{\mathrm{sat}} \equiv 2/(\pi \Delta\nu_c)(A_{ul} + Q)/[(B_{lu}/c)(1 + g_l/g_u)]. \tag{14}$$

The line-shape function used in Eq. (13) is defined by Eq. (7), except that the term $\mathbf{a}_s$ should be used in place of the (unsaturated) Voigt $\mathbf{a}$ parameter to account for saturation-broadening effects.

The relatively high temperatures generated in the plasma necessarily lead to significantly populated upper states, a requirement for effective absorption measurements from excited levels. In addition, for conditions in which the difference in energy between laser-coupled states becomes comparable with the excitation temperature, $\Delta E_{ul} \approx kT_{\mathrm{ex}}$, emission from the upper state becomes nonnegligible. Consequently the optical detection system can collect substantial thermal emission in addition to fluorescence induced by the laser. The total photomultiplier-tube anode current is proportional to the sum of the thermal emission and LIF intensities in the observed spectral region.

The total emissive power (S_{em}) of an optically thin spectral line at frequency ν collected by the optical detection system is given by

$$S_{\mathrm{em}} = \eta(\Omega/4\pi) A_{ul} h\nu \int n_u \mathrm{d}V_{\mathrm{em}}, \tag{15}$$

where the n_u is the upper-state number density and the integral is over the entire volume observed by the detection optics.

For conditions encountered in the present investigation, the ratio of thermal emission relative to LIF collected by the detection optics can be of the order of 10^3. As a result, amplitude fluctuations in emission of the order of 0.1% can significantly perturb the fluorescence signal. Consequently, the ability to resolve a given fluorescence signal accurately may be limited by the ability of the detection electronics to suppress a steady-state background signal. Thus the ratio of the LIF signal-to-background thermal emission (S/B) is an important quantity describing the relative magnitude of the observed LIF that may be used to determine the signal processing requirements for a reliable fluorescence line-shape measurement.

For predominantly Lorentzian line shapes or sufficiently large laser intensities, S/B may be obtained by dividing Eq. (12) by Eq. (15), yielding the relation

$$\begin{aligned} \mathrm{S/B} &\approx (I_L/I_{\mathrm{sat}})/(1 + I_L/I_{\mathrm{sat}})^{1/2}[g_l/(g_l + g_u)] \\ &\quad \times (V_{\mathrm{LIF}}/V_{\mathrm{em}}) \exp(h\nu/kT_{\mathrm{ex}}), \end{aligned} \tag{16}$$

where $n_l/n_u = g_l/g_u \exp[-(E_l - E_u)/kT_{\mathrm{ex}}]$.

Relation (16) highlights experimental parameters that affect S/B for arbitrary values of laser intensity. If the detection optics subtend a small solid angle and the image of the entrance slit width is not wider than the beam width in the plasma, the volumetric collection ratio $V_{\mathrm{LIF}}/V_{\mathrm{em}}$ may be approximated by the ratio of the beam depth to the plasma depth (d_L/d_p) at the observed radial position. For these conditions, S/B may be expressed as

$$\begin{aligned} \mathrm{S/B} &\approx (I_L/I_{\mathrm{sat}})/(1 + I_L/I_{\mathrm{sat}})^{1/2}[g_l/(g_l + g_u)] \\ &\quad \times (d_L/d_p) \exp(h\nu/kT_{\mathrm{ex}}). \end{aligned} \tag{17}$$

Thus, for a given transition and radial position within a flow field, the local laser intensity-beam depth product controls S/B. In addition, S/B is related to the energy separation between the laser-coupled levels in the exponential term. Consequently, for given values of I_L/I_{sat} and d_L/d_p, S/B can be increased by probing a lower-wavelength transition with a relatively smaller upper-level population.

S/B for the argon $4s\,^3P_1 \rightarrow 4p\,^3D_1$ transition may be estimated by using the appropriate spectroscopic and experimental parameters and relation (16). Calculations based on argon–argon and argon–electron collisional interactions suggest that the nonradiative collisional quench rate, Q, out of a $4p$ state is approximately $2\text{–}3 \times 10^9\ \mathrm{sec}^{-1}$, yielding $I_{\mathrm{sat}} \approx 1400\text{–}2200\ \mathrm{W/cm}^2$ and $I_L/I_{\mathrm{sat}} \approx 0.03$ at the probed volume under the following conditions: a laser power of 8 mW, a beam cross-sectional area of approximately $1.7 \times 10^{-3}\ \mathrm{cm}^2$, and a value of the line-center line-shape function $\phi(\nu_0) = 4.1$ cm, for $\mathbf{a} = 0.7$ and $T = 8000$ K. Hence, for the transition $4s\,^3P_1 \rightarrow 4p\,^3D_1$, an excitation temperature $T_{\mathrm{ex}} \approx 8000$ K and a depth ratio $d_L/d_p \approx 0.04$ yield an estimated S/B of 2×10^{-3}, a factor of 2 greater than the maximum S/B achieved in the pre-

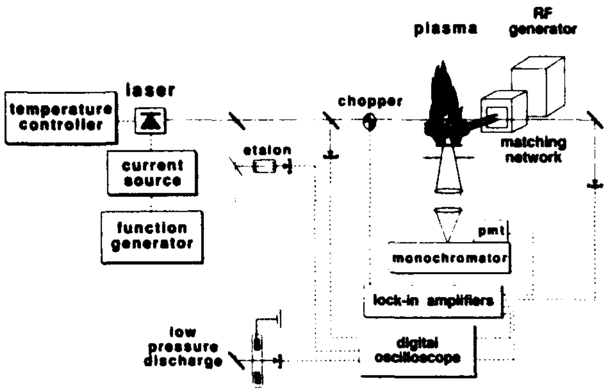

Fig. 4. Schematic diagram of the experimental setup used for LIF and absorption line shape measurements.

sent investigation. Possible sources of discrepancy between the calculated and the measured S/B's include errors in the estimates of total collisional quench rate, absolute laser power, and beam/plasma depth ratio. The S/B may also decrease as a result of misalignment of the laser beam and the image of the monochromator entrance slit or as a result of scattered thermal emission entering the collection optics.

Although S/B is ideally independent of the collection solid angle and monochromator bandpass, careful control of these parameters by appropriately positioned adjustable apertures can provide a useful means to regulate the total collected light intensity and minimize detection of unwanted scattered light.

EXPERIMENTAL DESCRIPTION

A schematic of the experimental setup is shown in Fig. 4. The semiconductor laser system used in the present investigation was described previously.[1] The laser diode (Sharp LT016MD0) was tuned by coupling a triangular-waveform signal for a frequency generator into the external input of a dc current source while maintaining a constant laser case temperature. The operating parameters that enabled the output of the laser to scan over the 8104-Å absorption line included an injection current of 75 mA, a case temperature of 18.6°C, and a triangular-waveform current amplitude of 4 mA. Each waveform cycle from the frequency generator provided a pair of symmetric scans over a 60-GHz interval about the absorption center line. An upper bound of the laser line width at the selected operating conditions (40 MHz) was determined with a spectrum analyzer (Burleigh SA-200; free spectral range 2.00 GHz) with a finesse of 200.

The wavelength-modulated laser output was split to measure transmission simultaneously through the plasma and through a low-pressure argon dc discharge. A fraction of the beam was directed through a fixed-length étalon (free spectral range 2.00 GHz) to provide a relative measurement of the laser wavelength during tuning. The absolute laser wavelength was monitored with a wavemeter (Burleigh WA-10).

The loosely focused laser beam was directed through an optical chopper and into the plasma by a 7.5-mm focal-length lens located inside the laser mount. The elliptical beam cross section at the fluorescence volume had major and minor axes with dimensions of 0.59 and 0.29 mm, respectively, corresponding to the depth and the height of the fluorescence volume, respectively. The major axis of the beam cross section was oriented parallel to the axis of the collection optics to maximize the d_L/d_p ratio for the given laser intensity.

Transmission intensities through the plasma, the low-pressure discharge, and the étalon were converted into voltage signals by silicon photodiodes mounted in amplifier/filter packages. Neutral-density filters were placed in front of the transmission detectors, when necessary, to avoid saturating the photodiodes and were oriented at Brewster's angle to minimize étalon effects and retroreflections.

The LIF and thermal emission was collected at a right angle by a simple lens located one focal length (f_{lens} = 15 cm; diameter 5 cm) from the fluorescence volume. Apertures placed around the collection lens helped to minimize the thermal emission signal entering the optical train directly and reflections off the quartz torch body. The collimated light was focused by a simple lens (f_{lens} = 25 cm; diameter 5 cm) onto the entrance slit of a monochromator (Spex 500M; slit height 2 mm, entrance slit width 0.480 mm, exit slit width 0.180 mm) with a 2.16-Å spectral bandpass centered at 8104 Å. Since the nearest argon emission line (8115.31 Å) is located 11.62 Å to the red, the monochromator effectively excluded undesirable broadband and nonresonant line emission.

A pair of mirrors rotated the collected light 90° so that the slit height was oriented parallel to the direction of beam propagation. The entrance slit width was adjusted so that the image of the laser beam filled the slit. The LIF signal was recorded from a volume (length 1.2 mm, height 0.29 mm, d_L = 0.59 mm) with dimensions determined by the image of the entrance slit and the depth of the laser beam in the flow field. An infrared-sensitive photomultiplier tube (Hamamatsu R928) coupled to the monochromator exit slit converted the intensity within the monochromator bandpass to a current. The anode current was converted to a voltage by a 20-kΩ load resistor and input into a lock-in amplifier (Stanford Research Systems 510), which provided the necessary phase-sensitive detection and relatively high dynamic reserve (60 dB) to discriminate the LIF signal from the thermal emission. All voltage signals were simultaneously recorded with a multichannel digital storage oscilloscope (Nicolet 4094B) and subsequently transferred to a laboratory computer for analysis.

The laser was tuned over the absorption line (f_{laser} = 500 s/scan) at the maximum rate that permitted a reliable fluorescence line-shape measurement for the given detection system time constant. The measurements recorded as the laser was repetitively tuned across the transition yielded symmetric fluorescence line shapes and shifts with respect to the reference absorption line. The absence of asymmetries between successive line shapes suggested that the detection system response time was adequate and that instrumental broadening effects may be neglected.

The plasma was sustained with 1 kW of electrical power from a 27.12-MHz generator (Henry 3000D). The plasma torch and impedance-matching network were fabricated in the laboratory and configured to permit unrestricted

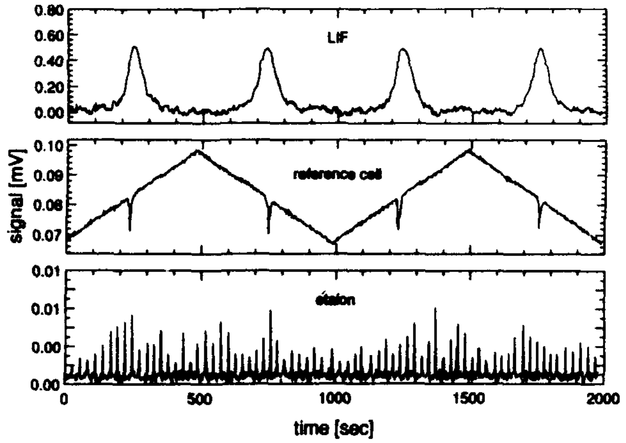

Fig. 5. Typical raw-data set. The top trace corresponds to the argon LIF signal recorded in the inductively coupled plasma at the center line 11 mm above the load coil. The middle trace corresponds to the argon transmission signal recorded through the positive column of a low-pressure dc discharge. The bottom trace is the transmission signal through a (free spectral range 2.00 GHz) fixed-length étalon.

optical access to the flow field. The torch and the matching network were mounted upon a three-axis translation stage, which allowed the plasma to move relative to the incident laser beam, permitting measurements from all regions in the flow without altering the optical alignment.

The plasma torch consisted of three concentric glass tubes. The two outer tubes, with inside diameters of 18 and 13 mm, were made of silica and were used to contain the plasma. The inner tube, made of borosilicate glass (1-mm i.d.) may be used to inject aerosols into the plasma, although this option was not pursued in the present investigation. The argon flow was injected tangentially into the outer tube and monitored (8 L/min) by a calibrated rotameter.

A dc discharge served as a wavelength reference source of essentially unshifted argon lines.[1] The discharge, sustained with a 2-mA current, consisted of a glass spectrum tube (diameter 1.3 cm) with nickel electrodes filled with argon at a nominal pressure of 4 Torr.

Figure 5 shows a sequence of single-sweep data traces of spectrally resolved LIF and transmission profiles simultaneously observed through the plasma, the low-pressure discharge, and a fixed-length étalon over a measurement time of four scan cycles. In each scan the laser was tuned over a 60-GHz spectral interval about the transition center-line wavelength. The top trace was recorded with the laser beam directed across the diameter of the plasma flow field 11 mm above the load coil. The center trace was recorded with the laser focused through the positive column of the dc discharge reference cell. The bottom trace shows a transmission trace recorded through the étalon.

All measurements were made by using laser intensities that did not significantly perturb the populations in the energy levels coupled in the transition. The possibility of laser saturation was checked with a set of calibrated neutral-density filters to regulate the laser intensity entering the plasma. The absorption and LIF line shapes were determined to be independent of laser intensity despite more than an order-of-magnitude reduction in laser intensity. The nominal incident laser power at the probe volume (8 mW) was measured with a (Lexel) powermeter.

DATA ANALYSIS

Line Shape

In the line-shape fitting procedure, the measured intensities were normalized by the incident laser intensity. For the absorption measurements, the optical depth (i.e., the absorption coefficient–path-length product) was computed by taking the negative logarithm of the normalized transmission signal. The time-dependent signals were converted to a relative frequency by using the étalon transmission trace. For the LIF measurements, the determination of the actual line shape was complicated by the nonnegligible absorption in the probe intensity with position within the flow field. For example, the line-center absorption through the diameter of the plasma 11 mm above the induction coil was approximately 23%. When the LIF probe volume was in the center of the symmetric flow field, the optical depth was assumed to be half of the total path-length value. The variation in laser intensity at arbitrary positions in the flow field was slightly more complicated. The effective optical depth up to the observed region in the flow field was determined by plotting the relative fluorescence intensity as a function of position and multiplying the computed area under the curve up to the observed region normalized by the total enclosed area by the spectral absorption coefficient–path-length product. The laser intensity at the probed region was then calculated. Each calculation of the local laser intensity influenced the relative fluorescence signal, which, in turn, required a readjustment of the local laser intensity. The entire iterative procedure usually converged within two iterations.

In order to infer the parameters n_e and T from the relative contributions of the dominant broadening mechanisms, we least-squares fitted each measured line shape to a Voigt profile, using the Voigt **a** parameter and the kinetic temperature T. The Stark-broadening contribution to the total Lorentzian linewidth, $\Delta\nu_c$, was determined after we subtracted the resonance broadening effects, using relation (4). We subsequently calculated the electron number density, using Eqs. (5) and (6), and appropriately modified the tabulated Stark parameters to include effects from quadrupole interactions.[3,5] Although the atomic kinetic temperature, determined from the Gaussian component of the measured line shape, describes the translational motion of the atoms, the proper temperature for the calculation of the theoretical Stark widths and shifts is the electron temperature. Owing to the rapid electron–atom collision rates in atmospheric-pressure plasmas and to the relatively small external electric fields outside the load-coil region, where the present measurements were recorded, nonequilibrium calculations suggest that the gas and electron kinetic temperatures should be nearly identical.[1] In addition, since the theoretical Stark width is relatively insensitive to the electron temperature, errors resulting from differences between electron and atomic kinetic temperatures should be small. For example, for a given electron number density, an error in electron temperature of 1000 K corresponds to a 5% change in the calculated Stark width.

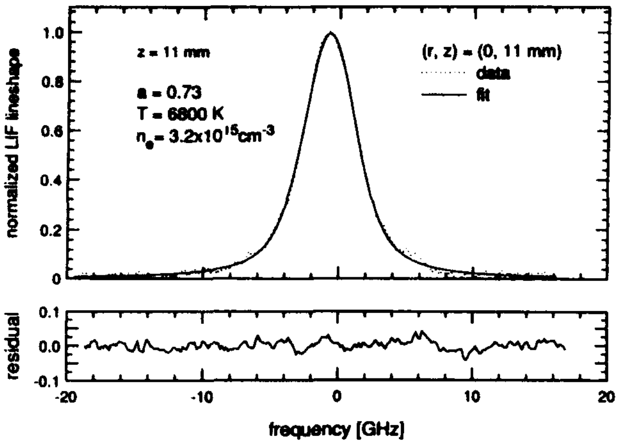

Fig. 6. Example plot of a reduced LIF line shape and best-fit Voigt profile of the argon $4s^3P_1 \rightarrow 4p^3D_1$ transition (8104 Å) recorded at the center line 11 mm above the load coil. The residual shows the difference between the data and the best-fit Voigt profile.

Hence n_e calculations were performed by assuming translational equilibrium among all species at the measured atomic kinetic temperature.

Each measured spectral line shape was fitted to a computed profile with a particular set of Voigt-fit parameters $\mathbf{a}$ and T. The integrated area under the computed profile was normalized to the same area under the measured line shape. The best-fit values of $\mathbf{a}$ and T for a particular measured line shape were determined by independently varying the Voigt parameters until the area between the fit and data, Δ, was minimized.[1]

Minor corrections to the baseline were necessary for traces for which precise identification of the zero signal level was difficult so that the residual approached zero in the wings of the line shape, as expected theoretically.

Figure 6 illustrates the results of the formal line-shape fitting procedure applied to a fluorescence line shape, normalized by the value at line center, measured at the center line 11 mm above the load coil. The best-fit values, $\mathbf{a} = 0.73$ and $T = 6800$ K, yielded a total collisional (Lorentzian) line width of $\Delta\nu_c = 3.05$ GHz. The resonance-broadening component of the line shape, $\Delta\nu_{\text{res}} = 1.31$ GHz, was calculated by using relation (4), the measured kinetic temperature, and appropriate spectroscopic constants ($f_{01} = 0.049$, $\omega_{01} = 1.8 \times 10^{16}$ rad/s, $g_0 = 1$, $g_1 = 3$).[9,10] Finally, the Stark-broadening component of the line shape ($\Delta\nu_{\text{Stark}} = 1.76$ GHz) and the appropriate Stark parameters ($w = 0.059$ and $d = 0.044$; Refs. 1 and 5) permitted the determination of the electron number density ($n_e = 3.2 \times 10^{15}$ cm^{-3}).

The results of previous argon absorption line-shape measurements originating from metastable (i.e., not radiatively coupled to the ground state) and resonance levels yielded mutually consistent values of n_e after resonance-broadening effects were accounted for by using relation (4) when appropriate.[1] Hence the agreement between n_e measurements determined from Stark-broadened absorption profiles originating on metastable and resonance levels (to within ±10% experimental uncertainty) suggests that relation (4) provides a reliable estimate of the resonance-broadening contribution to the line shape for transitions including the argon $4s^3P_1$ state.

The determination of accurate values of n_e hinges on the ability to fit the data properly in the wings of the line where collisional broadening effects predominate. Similarly, an accurate determination of the kinetic temperature requires an accurate fit over the central portion of the line shape, where Doppler broadening effects are most influential. In addition, meaningful measurements of the plasma parameters require a unique determination of the best-fit Voigt parameters. The accuracy and reliability of the fit procedure may be assessed by measuring the relative sensitivity to independent changes in the Voigt-fit parameters. To illustrate the relative accuracy of the fitting procedure and verify the existence and uniqueness of a pair of best-fit Voigt parameters for a particular measured line shape, we determined values of Δ for all reasonable values of $\mathbf{a}$ and T by optimizing $\mathbf{a}$ for each value of T. The procedure was repeated over a range of temperatures until the minimum Δ, $\Delta_{\min}$, corresponding to the best-fit Voigt parameters were determined. A Voigt-fit sensitivity analysis may be displayed on a three-parameter graph with the variation from $\Delta_{\min}$ (% variation) plotted as a function of $\mathbf{a}$ and T, where % variation = $(\Delta - \Delta_{\min})/\Delta_{\min} \times 100\%$. The slope of the trajectory illustrates the relative sensitivity to changes in the fit parameters and provides a quantitative uncertainty estimate of the best-fit parameters for a given measured line shape. The sets of $\mathbf{a}$ and T values that cause Δ to vary from $\Delta_{\min}$ by 5% were arbitrarily chosen as criteria to estimate the relative accuracy of the best-fit parameters for a single line shape. The total measurement uncertainty was based on a combination of the uncertainty in Voigt-fit parameters for a single line shape and the mean variation of plasma parameters over several measurements in the flow field.

The results of the Voigt-fit parameter sensitivity analysis applied to a typical measurement of the 8104-Å LIF line shape are presented in Fig. 7. The best-fit Voigt parameters, $\mathbf{a} = 0.73$ and $T = 6800$ K, yielded $\Delta_{\min} = 3.4 \times 10^{-3}$ for a measurement at the center line of the discharge. The quadratic trajectory of $\Delta(\mathbf{a}, T)$ yielded two

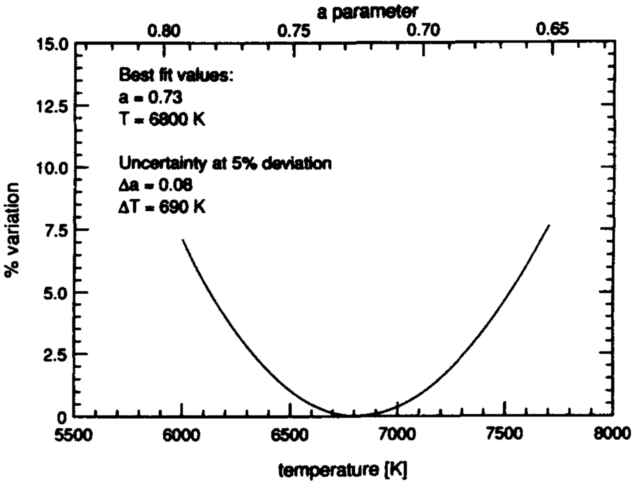

Fig. 7. Voigt-fit sensitivity analysis applied to the line shape in Fig. 6. The ordinate, % variation, corresponds to the normalized frequency-integrated squared difference, $(\Delta - \Delta_{\min})/\Delta_{\min} \times 100\%$, where Δ is the squared point-by-point difference between a particular Voigt-fit and the data, integrated over the measured line shape, and $\Delta_{\min}$ is the value of Δ from the best-fit parameters.

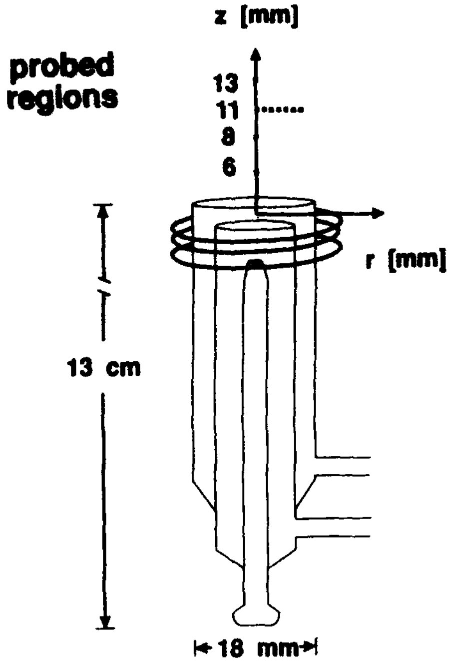

Fig. 8. Schematic diagram of the plasma torch and relative positions of the regions probed with LIF. The position along the axis of the torch at the top of the load coil, 2 mm below the top of the torch, defines the origin of the coordinates.

sets of fit parameters corresponding to values of Δ 5% above Δ_{min}: (a = 0.82, T = 6130 K) and (a = 0.65, T = 7510 K). Hence the estimated uncertainties in the fit parameter determination for this particular line shape were $\Delta a \approx \pm 0.085$ and $\Delta T \approx \pm 690$ K. Variations in values of n_e and T from scan to scan, combined with the uncertainty associated with a particular line shape, yielded a total measurement uncertainty of $\Delta n_e \approx \pm 0.6 \times 10^{15}$ cm^{-3}, $\Delta n_e/n_e \approx 0.19$, and $\Delta T \approx \pm 800$ K for LIF measurements for fluoresence volumes within 3 mm from center line. For radial distances greater than 5 mm from the center line, the signal-to-noise ratio decreased as a result of the entrainment of cooler room air, which induced flow field fluctuations and decreased the absorbing state ($4s^3P_1$) population. Despite the net shift of the measured transition line center, no significant line-shape asymmetries in the Stark-affected profiles or in the calculated residuals were evident.

Since the measured flow field was axially symmetric, LIF line shapes were analyzed in regions up to and including the center line of the flow field so that minimum compensation for beam attenuation was required. Figure 8 is a schematic diagram that shows the locations of the probed regions relative to the plasma torch. The position along the axis of the torch at the top of the load coil, 2 mm below the top of the torch, defines the origin of the coordinates.

Spatially resolved distributions of n_e and T were determined by repeating the measurements at various radial positions along the beam path 11 mm above the load coil. Vertical error bars were determined from the range of n_e and T that could be calculated given the range of a and T values resulting from a combination of noise within individual scans and the variation in the mean value of best-fit parameters observed during a sequence of several scans recorded at each location.

Figure 9 shows a comparison of T and n_e determined from simultaneous absorption and LIF measurements in the inductively coupled plasma at a height 11 mm from the load coil. The dashed lines indicate the path-length-averaged values determined from the absorption line shape. The solid lines join spatially resolved values of T or n_e determined from analyses of fluorescence line shapes at various radial distances from the center line. The mean value of kinetic temperature determined from LIF measurements was slightly above the value determined by using absorption, at the center of the flow field for this axial position but dropped below the path-length averaged value toward the edges of the flow field. The kinetic temperatures determined from LIF measurements confirm the essentially top-hat-shaped temperature distribution measured by laser absorption at this axial position.[1] Similarly, n_e values determined from LIF measurements bracket the value determined by using ab-

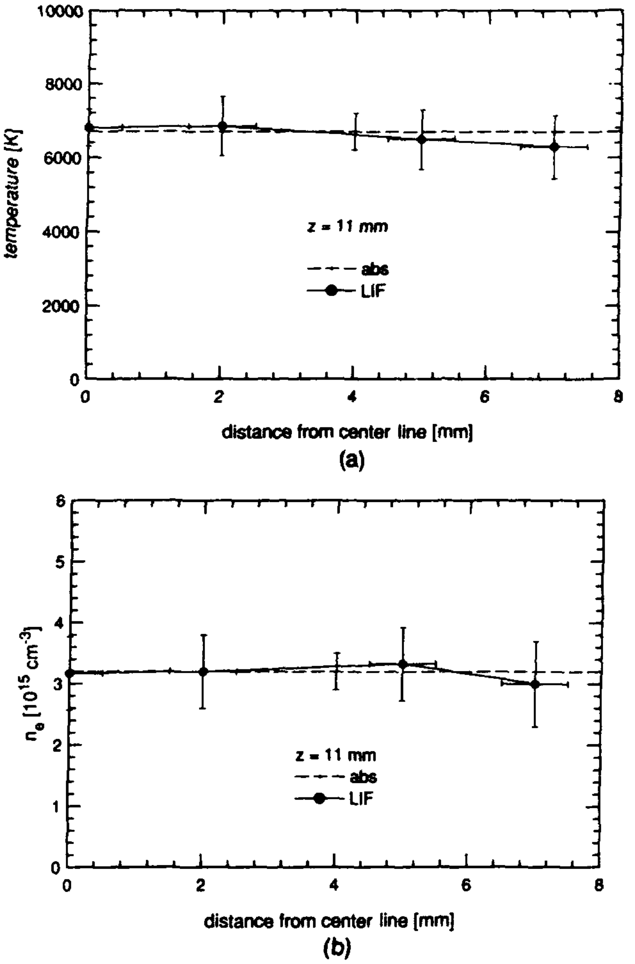

(a)

(b)

Fig. 9. (a) Comparison of atomic kinetic temperatures determined from the Gaussian component of the absorption and LIF line shapes at an axial distance 11 mm above the load coil. The dashed line indicates the temperature determined from the absorption line shape. The solid line joins temperature values determined from LIF line shapes at various radial positions. (b) Comparison of electron number density values determined from LIF and absorption line shapes at an axial distance 11 mm above the load coil. The dashed line indicates n_e values determined from the absorption line shape. The solid line joins n_e values determined from LIF line shapes at various radial positions.

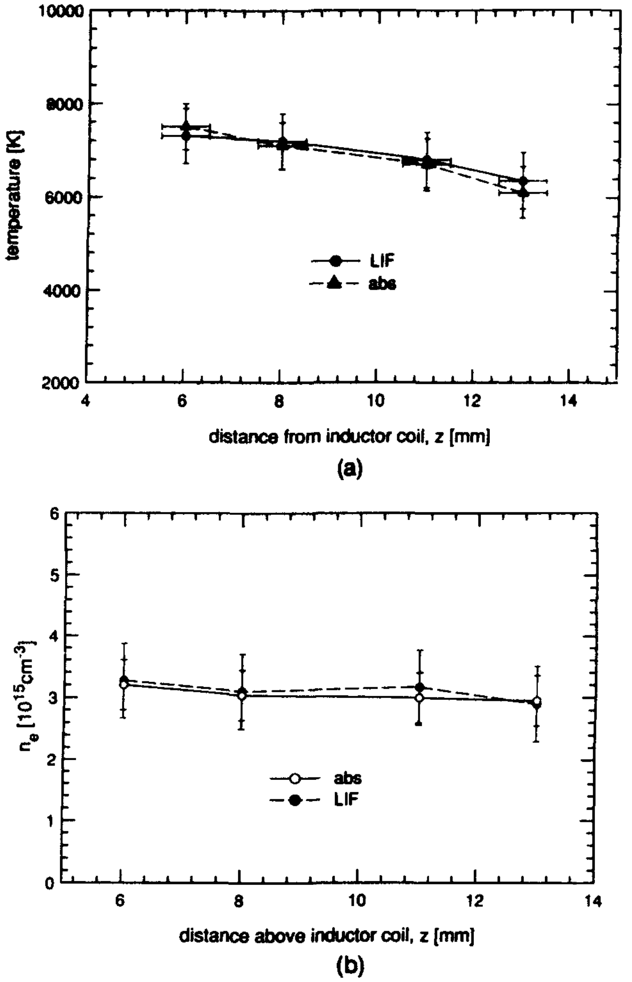

(a)

(b)

Fig. 10. (a) Comparison of atomic kinetic temperature values as a function of axial distance from the load coil at the center line determined from the Gaussian component of LIF and absorption line shapes. (b) Comparison of electron number density values as a function of axial distance from the load coil at the center line determined from LIF and absorption line shapes.

sorption and suggest a relatively uniform electron number density distribution at this distance above the load coil.

Fluorescence line shapes recorded along the center line for axial positions from 6 to 13 mm above the load coil indicate a slight decrease in T and n_e with increasing distance from the load coil (Fig. 10). The lack of a significant decrease of n_e at distances far from the ionizing region between the windings of the load coil may be due to a relatively slow electron–ion recombination rate. Fluorescence measurements at distances outside the probed region yielded line shapes with inadequate signal-to-noise ratios for accurate state parameter determinations. For instance, for axial distances greater than 13 mm above the load coil, flow-field fluctuations and a decreasing fluorescence signal prevented a meaningful determination of the Stark parameters from a line-shape analysis. The LIF signal at line center, however, could be detected at distances 15–16 mm above the load coil. Accurate measurements at axial positions slightly above the torch (3 mm $\leq z \leq$ 6 mm) were problematic as a result of an increase in background line and continuum emission and possibly because of scattering from the inner walls of the torch entering the collection optics. At these positions, S/B was below the minimum level necessary for determining reliable line shapes by using the given detection system electronics. Since all measurements were recorded with laser intensities significantly below I_{sat}, an increase in laser power would yield higher relative fluorescence signals for the given beam-collection geometry and permit accurate line-shape measurements to be made over a larger region in the flow field.

Figure 11 compares ion temperatures calculated by values of n_e inferred from a Stark-broadening analysis with kinetic temperatures determined from the Doppler-broadening component of the fluorescence line shape at an axial distance 11 mm above the load coil. At this axial distance, the kinetic temperature is consistently below the ion temperature. The spatially resolved measurements of n_e and corresponding calculations of T_i agree with previous measurements and calculations made with absorption line shapes measured over various chords at this axial position as a result of the nearly uniform n_e radial distribution.[1]

Stark broadening theory requires that the electrons and ions maintain a Maxwellian velocity distribution and is independent of local thermodynamic equilibrium considerations.[3,5] Consequently the measurements strongly suggest the presence of an overpopulation of electrons in the plasma flow field. These results are consistent with previous measurements of n_e and T made by using a Stark-broadening analysis of the H_β emission line and Boltzmann plots of various analyte emission line intensities[11] and from Thomson-scattering experiments.[12]

The elevated electron population, a result of an incomplete equilibration between atoms and electrons, may be due to the relatively slow and inefficient energy transfer process. In effect, electrons that absorb energy from the electromagnetic fields in the ionizing region within the load coil may not transfer their energy through collisions to the relatively heavy neighboring atoms before reaching the observation zone. Penning ionization, because of nonelastic collisions between the ground state and atoms

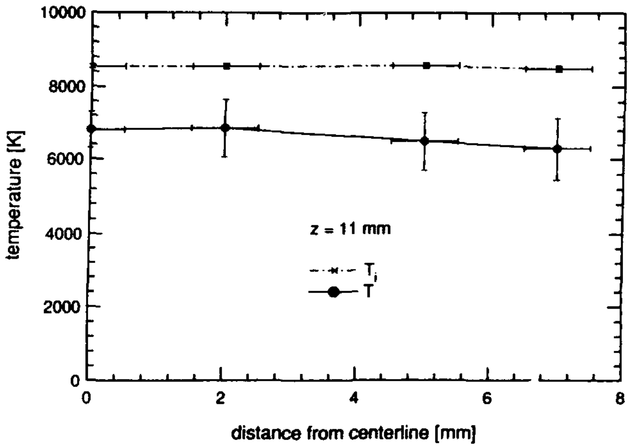

Fig. 11. Comparison of temperature values as a function of radial distance from the center line at an axial distance 11 mm above the load coil. The ion temperatures (T_i) were determined from electron number density values from the Saha equation. The atomic kinetic temperatures were determined from the Gaussian component of the line shape.

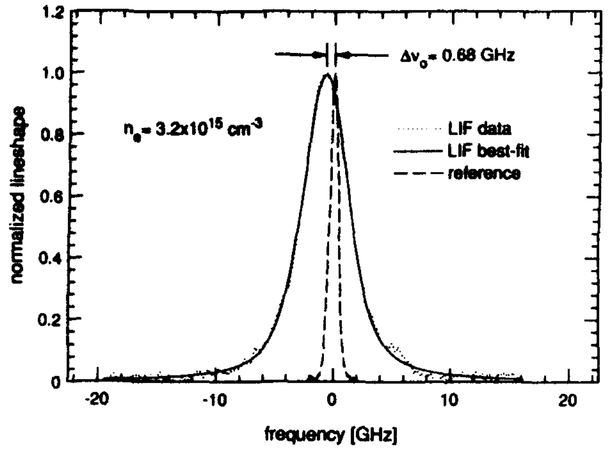

Fig. 12. Reduced Stark-affected LIF line shape and unshifted absorption profile recorded simultaneously in the inductively coupled plasma at the center line 11 mm above the load coil and through the positive column of a low pressure dc discharge, respectively.

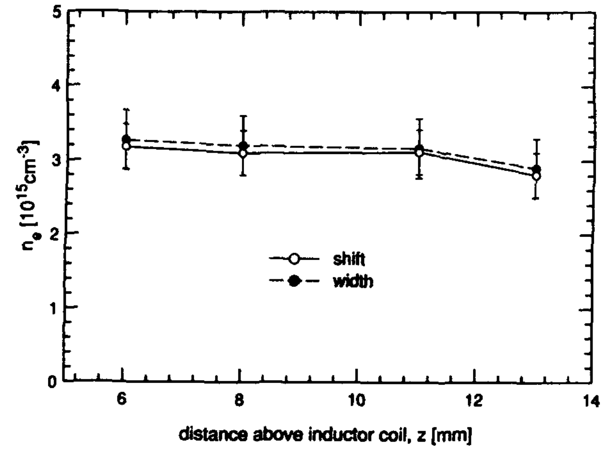

Fig. 13. Comparison of electron number density values as a function of axial distance above the load coil determined from Stark-broadening and shift measurements.

in the metastable state[4] or of a relatively slow electron–ion recombination process,[13,14] may also contribute to the overabundance of electrons.

Stark Shift

Figure 12 shows a pair of reduced line shapes of the $4s^3P_1 \rightarrow 4p^3D_1$ transition recorded simultaneously at the center of the inductively coupled plasma by fluorescence detection and through the positive column of the dc discharge by absorption. The net shift was determined from the difference in the relative positions of best-fit profiles of each line shape. Subsequently, relation (6), measured shift, and atomic kinetic temperature were used to calculate a value of n_e. Figure 13 compares values of n_e determined from measurements of the Stark broadening and shift for axial distances from 6 to 13 mm above the coil. The width and shift measurements yield n_e values that show good agreement and indicate a slight decrease in n_e with increasing distance above the load coil, as expected.

The accuracy of the Stark shift measurements was determined from the combined uncertainty of the shifted and reference line-center wavelengths resulting from noise present within a single scan and from variations in the mean value of the shift over several successive scans. The relatively large total line (collision + Doppler) width/shift ratio limited the accuracy but did not preclude the determination of the Stark shift. For example, although measurements along the axis 11 mm above the load coil yielded a total width/shift ratio of 7.2, the narrow laser linewidth provided the necessary spectral resolution for an accurate determination of the magnitude of the Stark shift. By contrast, measurements of Stark shift that use conventional emission diagnostics are typically recommended for conditions in which the width/shift ratio is of the order of unity,[3] and they require relatively expensive spectrometers or specially designed Fabry–Perot étalons.[15]

In addition, accurate measurements of the Stark shift permitted a determination of the electron temperature from the Stark width/shift ratio. Figure 14 compares values of T_e, T, and T_i for various radial positions at an axial distance 11 mm above the load coil and for various axial

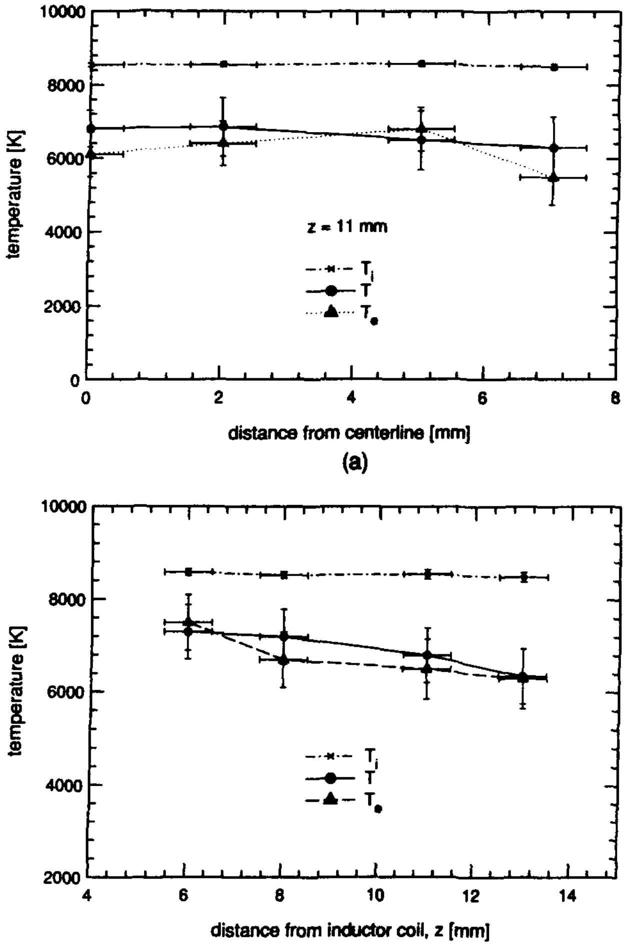

(a)

(b)

Fig. 14. (a) Comparison of radial temperature distributions determined from LIF profiles recorded at an axial distance 11 mm above the load coil. The ion temperature (T_i) was calculated from measured electron number density values with the Saha equation. The atomic kinetic temperature (T) was determined from the Gaussian component of the line shape. The electron temperature (T_e) was determined from the ratio of the Stark width to the Stark shift. (b) Comparison of axial temperature distributions determined from LIF profiles recorded at the center line.

positions along the center line. The mutual agreement between the atomic kinetic temperature and the electron temperature suggests that the atoms and the electrons are in translational equilibrium at a temperature significantly below the ion temperature. Apparently the influence of external electromagnetic fields generated by the rf current in the load coil does not lead to a measurable difference between the kinetic temperatures of charged and neutral species in the probed region of the plasma.

CONCLUSIONS

An important new class of plasma diagnostics, based on fluorescence and absorption spectroscopy with a semiconductor laser, has been demonstrated for the study of atmospheric-pressure plasmas. Spatially resolved measurements of electron number density, atomic kinetic temperature, and electron kinetic temperature have been inferred from Stark-affected fluorescence line shapes recorded by tuning a semiconductor laser over the argon transition $4s^3P_1 \rightarrow 4p^3D_1$ (8104 Å) in an inductively coupled atomospheric-pressure plasma. A low-pressure dc discharge filled with argon served as a wavelength-reference source. The simultaneous determination of multiple state parameters from a Stark-affected fluorescence line shape is a powerful diagnostic that requires only that all species maintain a Maxwellian velocity distribution.

Values of kinetic temperature and electron number density determined from fluorescence measurements of Stark width and shift at the center line were consistent with values determined from absorption line-shape measurements and indicate a slight decrease in electron number density and kinetic temperature with increasing axial distance from 6 to 13 mm above the load coil. Calculations of the ion temperature from electron number density measurements with the Saha equation suggest that the inductively coupled plasma is not in local thermodynamic equilibrium and that an elevated electron population exists throughout the measured flow field. Values of atomic kinetic temperature and electron temperature determined by using the Gaussian component of the fluorescence line shape and the Stark width/shift ratio, respectively, were in mutual agreement and suggest that the electrons and atoms are in translational equilibrium.

ACKNOWLEDGMENT

This research was supported by the U.S. Air Force Office of Scientific Research, Aerospace Sciences Directorate, with J. Tishkoff as the technical monitor.

REFERENCES

1. D. S. Baer and R. K. Hanson, "Tunable diode laser absorption diagnostics for atmospheric pressure plasmas," J. Quant. Spectrosc. Rad. Transfer **47**, 455–475 (1992).
2. A. Corney, *Atomic and Laser Spectroscopy* (Oxford U. Press, Oxford, 1977).
3. H. Griem, *Plasma Spectroscopy* (McGraw-Hill, New York, 1964).
4. J. M. Mermet, "Excitation mechanisms of elements inducted into a HF (high frequency) argon plasma," C. R. Acad. Sci. Ser. B **281**, 273–275 (1975).
5. H. Griem, *Spectral Line Broadening by Plasmas* (Academic, New York, 1974).
6. G. F. Kirkbright, *Atomic Absorption and Fluorescence Spectroscopy* (Academic, New York, 1974).
7. W. Demtroder, *Laser Spectroscopy* (Springer-Verlag, Berlin, 1982).
8. E. H. Piepmeier, "Theory of laser saturated atomic resonance fluorescence," Spectrochim. Acta **27B**, 431–443 (1972).
9. W. L. Wiese, M. W. Smith, and B. M. Glenon, *Atomic Transition Probabilities*, Natl. Bur. Stand. (U.S.) Ref. Ser. **4** (1966).
10. K. Tachibana, H. Harima, and Y. Urano, "Measurements of collisional broadening and the shift of argon spectral lines using a tunable diode laser," J. Phys. B **15**, 3169–3178 (1982).
11. M. W. Blades, "Some considerations regarding temperature, electron density and ionization in the argon inductively coupled plasma," Spectrochim. Acta **37B**, 869–879 (1982).
12. M. Huang, P. Yang, D. S. Hanselman, C. A. Monnig, and G. M. Hieftje, "Verification of a Maxwellian electron-energy distribution in the ICP," Spectrochim. Acta **45B**, 511–520 (1990).
13. T. Fujimoto, "Kinetics of ionization-recombination of a plasma and population density of excited ions. III. Recombining plasma—high temperature case," J. Phys. Soc. Jpn. **49**, 1561–1568 (1980).
14. T. Fujimoto, "Kinetics of ionization-recombination of a plasma and population density of excited ions. III. Recombining plasma—low temperature case," J. Phys. Soc. Jpn. **49**, 1569–1576 (1980).
15. J. M. Vaughan, "Self-broadening and the resonance oscillator strengths in krypton," Phys. Rev. **166**, 13–17 (1968).

a reprint from Applied Optics

Semiconductor laser-based measurements of quench rates in an atmospheric pressure plasma by using saturated-fluorescence spectroscopy

D. S. Baer and R. K. Hanson

Plasma diagnostics based on saturated fluorescence and absorption spectroscopy with a semiconductor (diode) laser are developed to probe the $4s\,^3P_1 \rightarrow 4p\,^3D_2$ transition (8425 Å) of argon in an atmospheric pressure plasma produced by an inductively coupled plasma torch. Spatially resolved measurements of saturation intensity, nonradiative collisional transfer (quench) rate, and fluorescence yield (Stern–Volmer factor) are inferred from variations of spectral profile characteristics (line shape, line-center value, and frequency-integrated signal) with laser intensity. The results obtained by using fluorescence and absorption spectroscopy are mutually consistent in the analytical region 10 mm above the induction coil. The measured quench rates compare favorably with computed rates from a multilevel collisional radiative model that assumes a suprathermal electron population relative to the local thermodynamic equilibrium value at the kinetic temperature.

Introduction

Laser-induced fluorescence (LIF) and absorption spectroscopy techniques that use narrow-bandwidth semiconductor lasers offer a significantly improved class of plasma diagnostics compared with conventional emission-based techniques. These spectrally sensitive methods have been used recently to determine the electron number density n_e, electron temperature T_e, atomic kinetic temperature T, and population temperature T_{pop} in an atmospheric pressure plasma from analyses of Stark-affected line shapes.[1,2] In these previous investigations, a nonintrusive probe beam enabled the determination of the plasma parameters directly from line-broadening analyses.

For the case in which the intensity is sufficiently high, the lower-state population in a given probed transition may decrease significantly, and the measured signal (LIF or transmitted intensity) is no longer linearly related to the incident laser intensity. Consequently a proper line-shape analysis of the measured spectra must include effects such as saturation (power) broadening and bleaching.[3,4] Conversely a careful examination of the nonlinear behavior can permit a quantitative determination of nonradiative collisional transfer rates that influence the excited-state population distribution.

In the current investigation, a semiconductor (GaAlAs) laser operating single mode was tuned over the $4s^3P_1 \rightarrow 4p\,^3D_2$ Ar transition (8425 Å) to record partially saturated absorption line shapes in an atmospheric pressure Ar plasma produced by an inductively coupled plasma (ICP) torch. Spatial resolution was improved by monitoring the nonresonance fluorescence from the $4p\,^3D_2 \rightarrow 4s\,^3P_2$ transition (8015 Å) (Fig. 1). The sensitivity of the measured spectral profiles to local laser intensity was determined by regulating the incident laser power while maintaining a constant beam cross section. The saturation intensity I_{sat} was inferred from the observed variations of the line shape, the line-center (peak) signal, and the frequency-integrated signal with laser intensity. The quench rate and fluorescence yield were determined from I_{sat} measurements. The measured quench rates were compared with computed values of the total collisional transfer rate out of the laser-coupled upper $(4s\,^3D_2)$ state. An experimental evaluation of these diagnostics is the principal subject of this paper.

Theory

The detailed theory of saturated atomic fluorescence using a rate equation analysis has been well documented.[3-5] Consequently this paper presents only a brief

---

The authors are with the High Temperature Gasdynamics Laboratory, Department of Mechanical Engineering, Stanford University, Stanford, California 94305.

Received 1 July 1992.
0003-6935/93/060948-08$05.00/0.

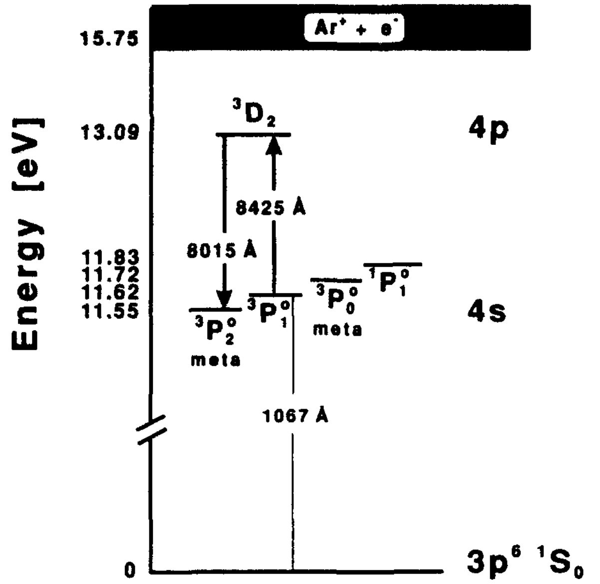

Fig. 1. Ar energy-level diagram illustrating the LIF excitation–detection scheme used in the current investigation.

summary of the important relations describing absorption and fluorescence spectroscopy with a narrow-bandwidth source.

When a narrow-bandwidth laser with arbitrary intensity is tuned near an absorption line, the resultant LIF signal $S_F(\nu)$, assuming negligible radiative trapping, may be expressed by using the general fluorescence equation[2–4]:

$$S_F(\nu) = \eta \frac{\Omega}{4\pi} V_F I_L k_s(\nu) Y, \tag{1}$$

where η is the overall detection system efficiency, Ω is the solid angle subtended by the collection optics, V_F is the fluorescence volume that is defined by the overlap region of the laser beam and the collection solid angle, I_L is the incident laser intensity at the probe volume, $k_s(\nu)$ is the spectral absorption coefficient for arbitrary laser intensities, and Y is the fluorescence yield, the fraction of absorbed laser energy radiated into the detection bandwidth. In this paper, the subscript s and the term saturated are used to denote spectroscopic parameters that do not vary linearly with the probe laser intensity. Similarly the subscript 0 and the term unsaturated refer to those parameters in the low-intensity limit. For simplicity all quantities within the probe volume, including the laser intensity, are assumed to be spatially uniform.

In general, for arbitrary values of laser intensity, the absorption coefficient near an isolated spectral line may be expressed as the product of a frequency-independent term and a ling-shape function[4]:

$$k_s = K_s \phi(a_s, \nu), \tag{2}$$

where K_s is the frequency-integrated (total) absorption coefficient, $\phi(a_s, \nu)$ is the observed line-shape function, and a_s is the observed (saturated) Voigt a parameter. The unsaturated Voigt a parameter a_0, a nondimensional term that describes the relative contributions of collisional and Doppler broadening, may be defined as $a_0 \equiv (\ln 2)^{1/2} \Delta\nu_c/\Delta\nu_D$, where $\Delta\nu_c$ and $\Delta\nu_D$ are the homogeneous (Lorentzian profile) and inhomogeneous (Gaussian profile) line widths (FWHM), respectively. The frequency integral of the line-shape function is normalized to unity (i.e., $\int \phi(\nu)d\nu \equiv 1$).

The total absorption coefficient is a function of transition-specific constants and the difference in population densities between the laser-coupled levels. For sufficiently high laser intensities near the transition wavelength, the population difference significantly decreases and, consequently, the fraction of laser energy that is absorbed declines. For arbitrary values of I_L, the effective total absorption coefficient may be described by the relation[4]

$$K_s = K_0 \left(1 + \frac{I_L}{I_{\text{sat}}}\right)^{-1/2}, \tag{3}$$

where K_0 is the unsaturated total absorption coefficient and I_{sat} is the saturation intensity, which is defined as the intensity at which the absorption coefficient is reduced to $\sqrt{1/2}$ of the unsaturated value. For a two-level model and narrow-bandwidth excitation, I_{sat} may be expressed as[5]

$$I_{\text{sat}} \equiv \frac{g_2}{g_1 + g_2} \frac{\pi c \Delta\nu_c}{2} \frac{A_{\text{ul}} + Q}{B_{12}}, \tag{4}$$

where A_{ul} is the spontaneous emission coefficient of the observed line, B_{12} is the Einstein coefficient for absorption, g_i is the degeneracy of level i, and Q is the nonradiative collisional transfer (quench) rate.

For sufficiently high values of laser intensity, the homogeneous width and, consequently, the effective Voigt a parameter a_s increase because of saturation (power) broadening.[3] The variation of a_s with I_L may be expressed as the product of the unsaturated value a_0 and an intensity-dependent term through the relation[4]

$$a_s = a_0 \left(1 + \frac{I_L}{I_{\text{sat}}}\right)^{1/2}. \tag{5}$$

The fluorescence yield Y is defined according to the relation[6]

$$Y \equiv \frac{A_{\text{ul}}}{A_{\text{ul}} + Q}. \tag{6}$$

In order to highlight the spectral characteristics of the measured fluorescence signal, the LIF equation may be expressed in the simplified form

$$S_F(\nu) = \beta I_L k_s(\nu), \tag{7}$$

where β includes factors that are independent of the laser frequency. Thus the effective absorption line

shape is preserved by using fluorescence detection, although it is scaled in magnitude by the laser intensity, fluorescence yield, and system responsivity factors.

The (saturated) spectral absorption coefficient, which is defined by Eq. (2), may be expressed in terms of the unsaturated absorption coefficient and an intensity-dependent factor by the relation[4]

$$k_s(\nu_0) = k_0(\nu_0)\left(1 + \frac{I_L}{I_{\text{sat}}}\right)^{-\alpha}. \tag{8}$$

In the theoretical limits of pure homogeneous ($a_0 = \infty$) and inhomogeneous ($a_0 = 0$) broadening, the value of the exponent α equals 1 and 1/2, respectively. For the intermediate case, in which the broadening mechanisms act independently, a_0 and α assume corresponding values between the two limits, i.e., $0 < a_0 < \infty$ and $1/2 < \alpha < 1$. The appropriate α for a particular a_0 may be determined by performing a least-squares fit of calculated line-center spectral absorption coefficient values $k_s(\nu_0)$ for a given a_0 over a range of values of I_L/I_{sat} to the functional form given by Eq. (8) by using α as the free parameter. The results of calculations of α for various a_0 values are plotted in Fig. 2. Thus the variation of the spectral absorption coefficient that is relative to the unsaturated value may be determined by using Eq. (8) for arbitrary values of the ratio I_L/I_{sat}.

Figure 3(a) shows the results of calculations of the saturated spectral absorption coefficient at line center, normalized by the unsaturated value k_s/k_0 as a function of the ratio I_L/I_{sat} for various values of a_0. (The frequency dependence of the ratio k_s/k_0 has been suppressed for conciseness). The solid curves illustrate the overall decrease in line-center absorption with increasing laser intensity that is due to saturation effects. The dashed curve indicates the theoretical limit of linear (intensity-independent) absorption. Fig. 3 illustrates that the onset of nonlinear (saturated) behavior begins at lower intensities for predominately Lorentzian profiles than for essentially Gaussian line shapes. For example, for the case in which the probe laser intensity equals the saturation intensity ($I_L/I_{\text{sat}} = 1$) with $a_0 = 0.2$ and 1.0, the effective saturated absorption coefficient is 35% ($k_s/k_0 = 0.65$) and 44% ($k_s/k_0 = 0.56$) below the unsaturated value, respectively. In addition, Eq. (5) suggests that saturation broadening increases the Lorentzian character of the observed profile.

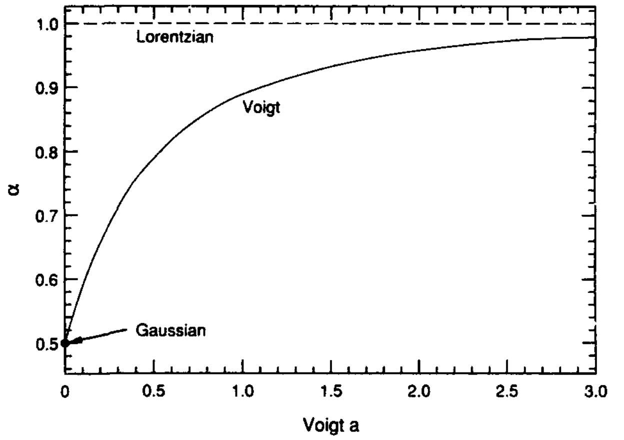

Fig. 2. Calculations of α for various values of Voigt a parameter [e.g. for $a = 0$ (Gaussian), $\alpha = 0.5$; for $a = \infty$ (Lorentzian), $\alpha = 1$].

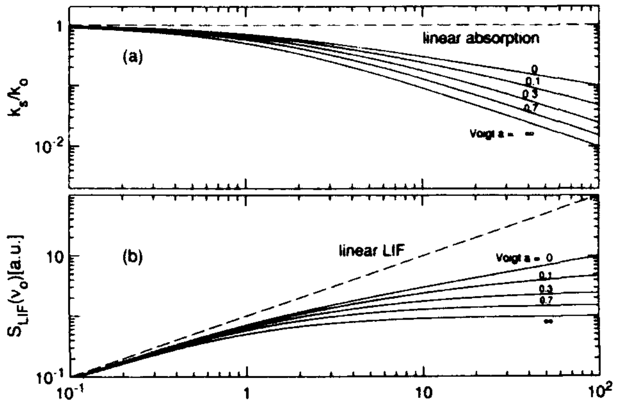

Fig. 3. Theoretical calculations that illustrate the influence of narrow-bandwidth laser intensity on line center values of (a) the absorption coefficient and (b) the LIF signal, normalized by the respective unsaturated values, as a function of the ratio I_L/I_{sat}. The solid curves show the effects of saturation on measured spectra. The dashed curves show the theoretical intensity-independent limits.

As Eq. (7) suggests, the measured line-center LIF signal $S_F(\nu_0)$ is proportional to the product of the spectral absorption coefficient and the local laser intensity. Figure 3(b) shows the results of calculations of $S_F(\nu_0)$ as a function of the ratio I_L/I_{sat} for various values of a_0 along with the theoretical intensity-independent linear fluorescence case. Saturation effects are apparent from the significant departure from linearity and decreasing first derivative as the ratio I_L/I_{sat} increases.

The frequency integral over the absorption line shape in Eq. (7) yields an expression for the total fluorescence signal S_F, where $S_F \equiv \int S_F(\nu)\mathrm{d}\nu$. The variation of S_F with I_L may be expressed in terms of the unsaturated value S_{F_0} and a laser intensity-dependent factor through the relation

$$S_F = S_{F_0}\left(1 + \frac{I_L}{I_{\text{sat}}}\right)^{-1/2}. \tag{9}$$

Equations (3), (5), and (7)–(9) have been written in a general form that relates the variation of a particular line-shape characteristic to the ratio I_L/I_{sat} in terms of the product of an unsaturated term and an intensity-dependent parameter. Thus the saturation intensity may be determined from measurements of an intensity-dependent profile parameter, relative to the unsaturated value, as a function of the probe laser intensity. In turn, the quench rate Q and fluorescence yield Y out of the laser-coupled upper state may be determined by using Eqs. (5) and (6), respectively.

Experimental Procedure

Figure 4 shows the experimental schematic used in the current investigation. Since a detailed description of the basic setup has been described previously,[1,2] only the relevant details are presented here. The semiconductor laser (Spectra Diode Labs 5410) was tuned in wavelength across the desired transition by modulating the injection current while maintaining a constant case temperature. The output beam was directed through an optical isolator that prevented unwanted back reflections from disturbing the single-mode operation of the laser. The laser operating conditions (case temperature 10.5°C, bias current 85 mA, current modulation amplitude 7.5 mA) provided a 52-GHz-wide spectral scan centered about the absorption line. A fraction of the beam was split off into two channels and directed through a fixed-length étalon (free spectral range 2.00 GHz) to measure the relative wavelength changes while tuning and into a photodetector to monitor the incident laser power to the flow field. The absolute laser wavelength was determined with a wavemeter.

Before entering the flow field, the beam was directed through a rectangular aperture to yield an essentially rectangular beam cross section with an approximately uniform transverse intensity distribution, through an optical chopper, and focused into the flow field by using a fused silica lens (f_{lens} 17 cm, diameter 2.5 cm). The dimensions of the beam cross section, which correspond to the depth (direction parallel to the axis of the collection optics) and the height (direction parallel to the bulk gas flow) of the LIF volume, were 130 and 75 μm, respectively. The beam path was maintained at a constant axial distance of 10 mm from the induction coil for this investigation. The unattenuated laser power entering the plasma, which was measured by a power meter, was 44 mW. Calibrated neutral density (ND) filters were inserted in the beam path to regulate the incident laser intensity while maintaining constant probe volume dimensions.

Fluorescence was collected at a right angle by using a simple lens located 1 focal length (f_{lens} 15 cm, diameter 5 cm) from the probe volume. An adjustable aperture placed between the lens and the probe volume reduced the amount of thermal emission entering the collection optics. The collimated light was rotated 90° by a pair of mirrors and focused by a simple lens (f_{lens} 25 cm, diameter 5 cm) onto the entrance slit of a 0.5-m monochromator (1800 lines/mm grating) with a spectral bandpass of 1.5 Å centered at 8015 Å. The slit height was oriented parallel to the direction of beam propagation in the flow field. The LIF signal was collected from a volume with dimensions determined by the image of the entrance slit and the depth of the laser beam in the flow field [1.2 mm (length) × 75 μm (height) × 130 μm (depth)]. Nonresonance fluorescence detection was used to avoid resonance Rayleigh scattering. An infrared-sensitive photomultiplier tube coupled to the exit slit (width 125 μm) was used to detect the transmitted LIF and emission signals through the monochromator. An analog lock-in amplifier provided the necessary phase-sensitive detection to discriminate effectively against background thermal emission.

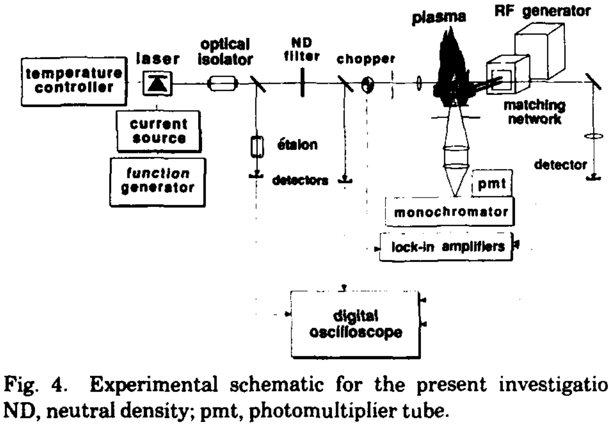

Fig. 4. Experimental schematic for the present investigation. ND, neutral density; pmt, photomultiplier tube.

The laser was tuned over the absorption line at the maximum rate (f_{scan} 500 s/scan), which permitted a reliable fluorescence line-shape measurement for the given detection system time constant. The transmitted intensities through the plasma and the étalon were monitored with Si photodetectors. All voltage signals were simultaneously recorded using a digital oscilloscope and subsequently transferred to a laboratory computer for analysis.

The atmospheric pressure plasma was sustained by inductively coupling 1 kW of electrical power from a rf (27.12 MHz) generator into Ar flowing (at 8 L/min) inside a quartz torch positioned coaxially with a three-turn induction coil. The coil functioned as a fixed inductor in the circuit of an impedance-matching network that effectively minimized reflected power into the generator. The entire plasma system (torch, induction coil, and matching network) was mounted on a three-axis translation stage to facilitate measurements from all regions of the flow field.

Figure 5 shows a schematic diagram of the torch and the relative locations of the probed regions. The origin of the coordinates is along the torch axis at the top of the induction coil, 1.5 mm below the nozzle exit.

Data Analysis

Values of I_{sat} were determined from spectral profile parameters that were recorded using absorption and LIF measurements for various values of probe laser intensity. Each measured line shape was analyzed using the detailed line-shape-fitting procedure described previously.[1,2] Briefly, each recorded fluorescence or transmission signal was normalized by the incident laser intensity. For the LIF measurements, probe beam absorption was determined by using the measured transmission through the flow field and the effective path length preceding the probe volume.[2] For the absorption measurements, the optical depth

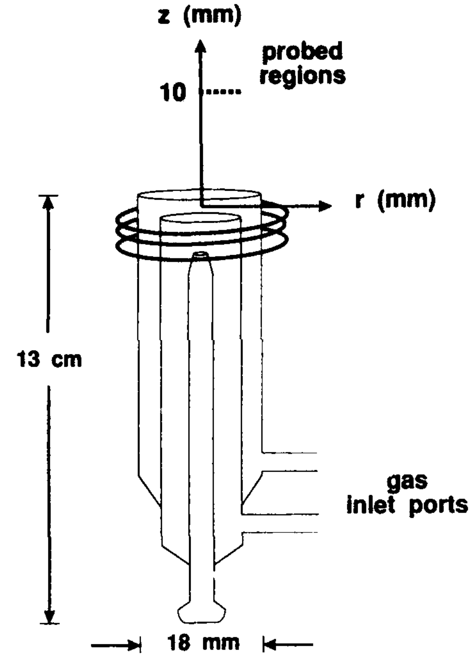

Fig. 5. Schematic diagram of the quartz torch and relative positions of the regions probed by LIF. The origin of the coordinates is along the torch axis, at the top of the load coil, 2 mm below the nozzle exit.

was computed by taking the negative logarithm of the transmission signal normalized by the incident laser intensity. The étalon transmission signal was used to convert the time-dependent trace to a relative frequency. The measured line shape was then least-squares fit to a Voigt profile by using a_s and T as free parameters. The best-fit parameters were used to calculate a synthetic Voigt profile to include properly the line wings and provide an accurate determination of the integrated profile parameters.

The saturation intensity was determined from a least-squares fit of measured values of an intensity-dependent parameter by using the appropriate relation [Eq. (3), (5), (8), or (9)] with I_{sat} as the free parameter. The line-shape parameter recorded using the lowest laser intensity served as a first-order estimate of the unsaturated value. A value of I_{sat}, which was determined from the initial least-squares fit, was used to correct the first-order estimate for saturation effects and the procedure was repeated. Analysis of the frequency-sensitive (line-center) values $k_s(\nu_0)$ and $S_F(\nu_0)$ by using Eqs. (7) and (8), respectively, required the additional step of calculating the parameter α from the value of a_0, which was determined from the line-shape analysis. The entire process usually converged to within 1% of the unsaturated limit in less than four iterations.

Figure 6 shows a typical sequence of single-sweep raw data traces of LIF profiles recorded from a region 10 mm above the induction coil and the transmitted signal through a fixed-length étalon over a measurement time of two scan cycles. In each scan, the laser was nominally tuned 52 GHz about the absorption line-center wavelength. The laser intensity at the probe volume was 360 W/cm^2. A set of measurements from a given probe volume was recorded using decreasing values of laser intensity by inserting calibrated ND filters with decreasing transmissivity in the beam path (ND = 0.3, 0.5, 0.7, 1.0, 1.3). The minimum value of I_L in a measurement set yielded a line shape with a signal-to-noise ratio greater than 12 and a ratio of LIF to thermal emission on the order of 10^{-3}.

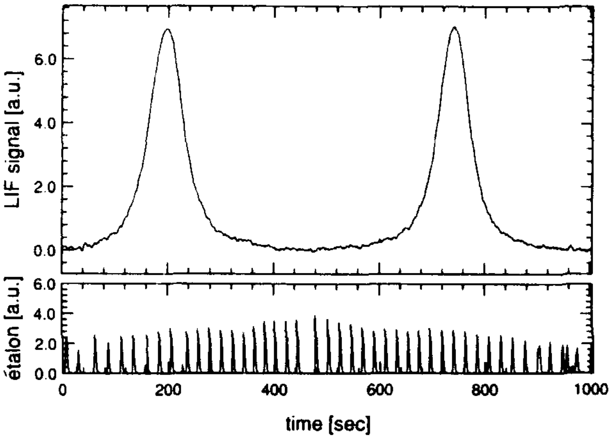

Fig. 6. Example of a raw data set. The top frame shows a pair of saturated fluorescence profiles recorded at the axis 10 mm above the induction coil with a laser intensity of 360 W/cm^2. The bottom frame shows the transmission through a fixed-length (2.00-GHz) étalon.

Figure 7 shows results from line-shape analyses of a single set of LIF profile measurements recorded at the center line by effective probe laser intensities ranging from 14.3–360 W/cm^2. Figure 7(a) shows a best-fit curve, which is given in Eq. (5), to measured a_s values as a function of I_L bracketed by a pair of fits in

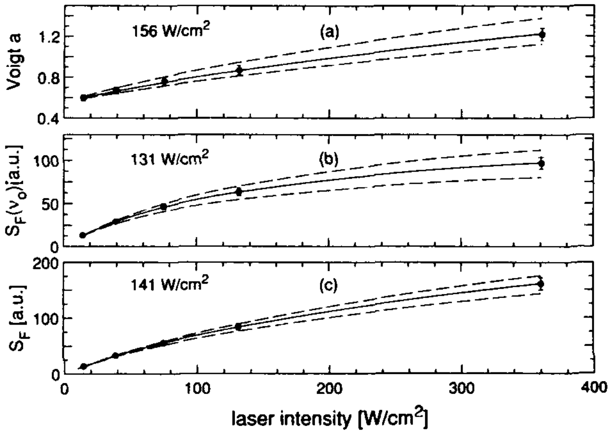

Fig. 7. Variation of measured values of the profile parameters (a) a_s, (b) $S_F(\nu_0)$, and (c) S_F, as functions of probe laser intensity. The solid curve is the best-fit curve to the appropriate relation [Eq. (5), (8), or (9)] with I_{sat} as the fit parameter. The dashed curves represent fits that use $I_{sat} \pm \sigma$ in the appropriate relation, where σ represents the total measurement uncertainty.

which I_{sat} was varied by $\pm\sigma$ from the best-fit value of 156 W/cm^2, where σ represents the total measurement uncertainty. The best-fit Voigt profile yielded $T = 6700$ K and a low intensity value of $a_s = 0.59$, which corresponded to $a_0 = 0.54$ and $\alpha = 0.81$. The electron number density, which was determined from the Stark-broadening component of the total collision width ($\Delta\nu_{\mathrm{Stark}} = 1.0$ GHz), by using the proper transition-specific Stark parameters and relations,[7] was 2.9×10^{15} cm^{-3}. The values of T and n_e that were determined from the appropriate line-shape parameters were consistent with previous measurements of Ar profiles that used relatively nonintrusive absorption and LIF spectroscopy techniques.[1,2]

Figure 7(b) plots measured $S_F(\nu_0)$ (line-center LIF signal) values as a function of I_L, the best-fit curve from Eqs. (7) and (8) with $\alpha = 0.81$, and a pair of similar curves in which I_{sat} was varied $\pm\sigma$ from the best-fit value of 131 W/cm^2. The determination of I_{sat} was relatively insensitive to variations in the parameter α. For example, a 20% change in a_0 corresponded to a 4% change in α and resulted in a 5% variation in the determination of I_{sat}. Thus a precise determination of α was not necessary for an accurate calculation of I_{sat} from $S_F(\nu_0)$ measurements.

Similarly, Fig. 7(c) shows a plot of measured S_F (spectrally integrated LIF) values as a function of I_L, the best-fit curve from Eq. (9), and a pair of curves in which I_{sat} was varied $\pm\sigma$ from the best-fit value of 141 W/cm^2. A comparison of the results illustrated in Fig. 7 indicates that the values of I_{sat} determined from analyses of the measured quantities a_s, $S_F(\nu_0)$, and S_F for a single set of LIF profiles agree to within ±8%.

The relative uncertainty in the determination of I_{sat} ($\Delta I_{sat}/I_{sat}$) was due to a combination of measurement noise and the sensitivity of the appropriate intensity-dependent relation [Eq. (5), (8), or (9)] to variations in I_{sat}. For example, at the center line the ±7% uncertainty in the S_F measurements corresponded to $\Delta I_{sat}/I_{sat} = \pm 18\%$, whereas the ±10% uncertainty in the a_s measured values yielded $\Delta I_{sat}/I_{sat} = \pm 22\%$, and the ±12% measurement uncertainty in $S_F(\nu_0)$ yielded $\Delta I_{sat}/I_{sat} = \pm 23\%$. Therefore, for minimum uncertainty and analytical simplicity, saturated S_F measurements and Eq. (9) were used to determine I_{sat} at various locations in the plasma flow field.

Figure 8 shows I_{sat} values determined from S_F measurements recorded along the beam path from the torch axis to a distance 6 mm from the center line. The dashed line indicates the I_{sat} value determined from absorption measurements. The solid curve connects spatially resolved I_{sat} values determined from LIF measurements and straddles the path-averaged value determined from absorption measurements, as expected. Reliable measurements were limited to regions less than 6 mm from the torch axis because of a strong decrease in the absorbing species number density and an increase in flow-field fluctuations near the boundary of the plasma and the cooler room air.

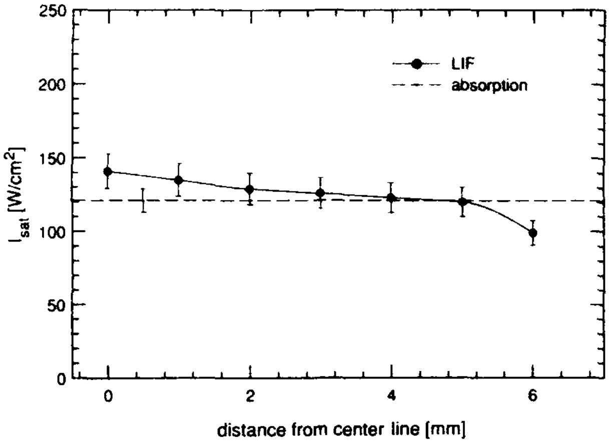

Fig. 8. Lateral distribution of I_{sat} values that were determined from measurements of total fluorescence intensity S_F and recorded along the beam path from the torch axis to a distance 5 mm from the center line, 10 mm above the induction coil. The dashed line indicates the I_{sat} value determined from path-averaged absorption measurements. The solid curve connects I_{sat} values determined from measured LIF line shapes at various radial positions relative to the center line.

In weakly ionized atmospheric pressure plasmas, the atomic population distribution is determined primarily by two-body electron–atom and atom–atom collisions.[7,8] As a result, the total quench rate may be estimated from the sum of two-body collisional deexcitation and mixing rates out of the laser-coupled upper state. These reaction rates are proportional to the number density and relative velocity (kinetic temperature) of the collision partners and cross section of the particular inelastic process. Figure 9 compares the lateral distribution of Q values determined from I_{sat} measurements by using absorption and LIF line shapes given in Fig. 8 with calculations of the total collisional transfer rates for the same region. The calculations employ analytical expressions of state-specific reaction-rate coefficients that describe two-body collisions between Ar in the probed upper state ($4p\,^3D_2$) and collisional partners, including ground and excited atomic Ar, in states up to and including the $4f$(14.965-eV) level, free electrons, and ground-state Ar ions.[8] The plasma state parameters used to calculate the total collisional transfer rate Q_{ex} included experimentally measured values of electron and atomic number densities and kinetic temperature that were determined from analyses of Stark-affected LIF and absorption line shapes.[1,2,8] The state parameters used to calculate the total collisional transfer rate Q_{LTE} were based on values that assumed local thermodynamic equilibrium (LTE) at the measured kinetic temperature. The Ar excited-state population distribution was calculated by using the measured population temperature T_{pop}.[1] For example, at the center line, the values $I_{sat} = 141$ W/cm^2, $\Delta\nu_c = 2.4$ GHz, and $A_{ul} = 9.38 \times 10^6$ s^{-1}, (see Ref. 9) yielded a measured value of $Q = 2.5 \times 10^9$ s^{-1}. Calculation of Q_{ex} for the same region by using tabulated col-

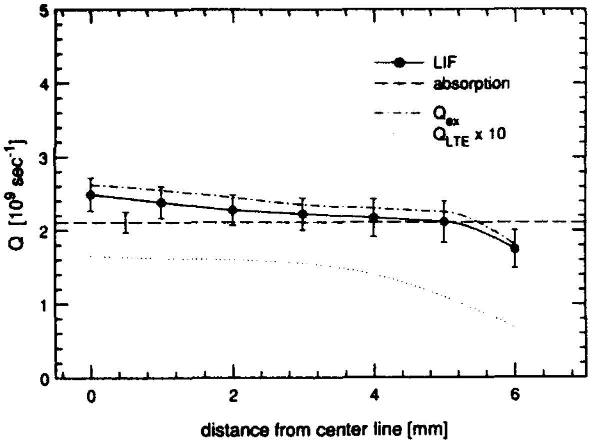

Fig. 9. Variation of quench rate Q out of the Ar $4p\,^3D_2$ state determined from measured I_{sat} values given in Fig. 8. The dashed line indicates the path-averaged Q values determined from absorption measurements. The solid curve connects Q values determined from measured LIF line shapes at various radial positions relative to the centerline. Q_{ex} (dot-dashed curve) and Q_{LTE} (dotted curve) represent computed values of the total nonradiative collisional rate out of the $4s\,^3D_2$ level for plasma states described by experimentally measured (see Refs. 1 and 2) parameters (n_2, n_a, and T) and local thermodynamic equilibrium distributions at the measured kinetic temperature, respectively.

lision rates[8] and measured state parameters[1,2] [$n_e = 3.2 \times 10^{15}$ cm^{-3}, $T_{pop} = 7700$ K (where T_{pop} describes the population among the excited states),[1] $T = 6700$ K] yielded $Q_{ex} = 2.6 \times 10^9$ s^{-1}. Similarly, for a system in LTE at $T = 6700$ K, calculation of the collisional transfer rate yields $Q_{LTE} = 1.6 \times 10^8$ s^{-1}. The kinetic temperature of a system in LTE that yields the value of the measured quench rate 10 mm from the induction coil at the center line is approximately 8250 K, over 1500 K greater than the measured temperature, where the measurement uncertainty is $\Delta T \approx 690$ K.[2]

The theoretical quench rate calculations suggest that two-body (deexcitation and mixing) collisions involving free electrons contribute over 99% of the total quench rate out of the $4p\,^3D_2$ state. Thus quenching collisions with atomic Ar are insignificant relative to those with electrons in the probed regions of the plasma flow field (presumably because of the large electron mobility relative to that of heavy particles for the conditions in the present investigation), and the neglect of collisions involving Ar atoms in excited states above the $4f$ configuration is justified. The effective quenching cross section for collisional transfer to all other states, assuming a hard-sphere interaction between electrons and Ar atoms in the $4p\,^3D_2$ state, is approximately 175 Å^2 for the conditions in the center of the flow field ($T = 6700$ K, $n_e = 3 \times 10^{15}$ cm^{-3}, $Q = 2.5 \times 10^9$ s^{-1}).

The random uncertainty in the determination of Q may be estimated by considering the relative uncertainties of the individual terms that enter Eq. (8). Since the quench rate is significantly larger than the radiative decay rate ($Q \gg A_{ul}$) in all regions in the flow field and the uncertainty of the Einstein absorption coefficient for the probed transition is relatively small ($\approx 5\%$),[9] the accuracy of the measured Q values is predominantly determined by the uncertainties of the measured $\Delta\nu_c$ and I_{sat} values. For example, in the central region of the discharge ($r < 4$ mm), relative measurement uncertainties of 10% and 12% in the values $\Delta\nu_c$ and I_{sat}, respectively, correspond to a total relative uncertainty of $\Delta Q/Q = 16\%$. Near the boundary of the plasma flow field ($r \geq 4$ mm), measurement uncertainties increase to an estimated 18% for both $\Delta\nu_c$ and I_{sat}, and correspond to a total quench rate uncertainty of $\Delta Q/Q = 25\%$.

The agreement between the measured Q and the calculated Q_{ex} values and the relative insignificance of quenching collisions that involve atomic species suggest the presence of an elevated electron population in the flow field relative to the calculated value, assuming LTE at the measured kinetic temperature. This interpretation is consistent with previous n_e measurements from Stark-affected Ar profiles,[1,2] Stark-broadening measurements of the H_β emission line, Boltmann plots of various analyte emission line intensities,[10] and Thomson-scattering experiments.[11] Although, to the best of our knowledge, independent measurements of Ar quench rates have not been reported for atmospheric pressure Ar plasmas, the consistency between measured and calculated values suggests that the demonstrated diagnostic techniques may offer a reliable determination of quench rates and effective lifetimes.

An overpopulation of n_e in the ICP may result from a combination of an inefficient energy transfer between energetic electrons and the cooler Ar atoms and the slow recombination rate of Ar ions and electrons relative to the transit time through the observation zone.[12] Thus, since electrons significantly influence the quench rates in plasmas, the temperature that most accurately describes the electron number density, the ionization temperature, may be an appropriate temperature to characterize the relevant collisional processes.

Values of fluorescence yield Y may be determined directly from calculated Q values by using Eq. (6). For example, at the center line, fluorescence monitoring of the 8015-Å transition and a value of $Q = 2.48 \times 10^9$ s^{-1} yields $Y = 3.77 \times 10^{-3}$. In addition, measurements of I_{sat} and subsequent calculations of Q and Y can enable a local determination of the absorbing species number density (population temperature) from absolute measurements of LIF intensity and permit quantitative LIF measurements by using excitation schemes that do not share a common upper level. If addition, a comparison of measured quench rates from multiple levels may permit the determination of specific reaction rates between particular excited states.

Conclusions

Measurements of saturation intensity, nonradiative collisional transfer (quench) rate, and fluorescence yield have been inferred from saturated line shapes recorded by tuning a semiconductor laser over the Ar transition $4s\,^3P_1 \rightarrow 4p\,^3D_2$ (8425 Å) in an atmospheric pressure ICP. Spatial resolution was improved by monitoring nonresonance fluorescence from the $4p\,^3D_2 \rightarrow 4s\,^3P_2$ (8015 Å) transition. The variation of the measured line shape, line center, and frequency-integrated (absorption and fluorescence) line shape as a function of probe laser intensity relative to the respective unsaturated values yielded mutually consistent determinations of saturation intensity.

The quench rates determined from measured saturation intensity values were consistent with calculations of the total collisional transfer rate out of the probed $4s\,^3D_2$ state that were made by using measured values of kinetic temperature, (non-LTE) electron number density and theoretical two-body Ar collisional rate coefficients. The agreement between measured and calculated values suggests the presence of an elevated electron population in the ICP flow field relative to the value, assuming LTE at the kinetic temperature. This result is consistent with previous measurements of electron number density determined from Stark-broadening analyses of Ar absorption and fluorescence line shapes, (H_β) emission profiles, Thomson-scattering measurements, and emission-based Boltzmann plots.

The techniques presented here are not inherent to the particular environment or species investigated and were made possible by the tuning capability, power output, and spectral bandwidth of the laser. Hence other flow fields may be investigated by using different probe species that are naturally present or introduced as tracers.

This research was supported by the U.S. Air Force Office of Scientific Research, Aerospace Sciences Directorate, with J. Tishkoff as technical monitor.

References

1. D. S. Baer and R. K. Hanson, "Tunable diode laser absorption diagnostics for atmospheric pressure plasmas," J. Quant. Spectrosc. Radiat. Transfer **47,** 455–75 (1992); in *Proceedings of the Twenty-Second Plasma Dynamics and Lasers Conference,* publ. AIAA-91-1945 (American Institute of Aeronautics and Astronautics, New York, 1991).
2. D. S. Baer, H. A. Chang, and R. K. Hanson, "Fluorescence diagnostics for atmospheric pressure plasmas using semiconductor lasers," J. Opt. Soc. Am. B **9,** 1968–1978 (1992); "Fluorescence diagnostics for atmospheric pressure plasmas using tunable diode lasers," in *Proceedings of the Thirtieth Aerospace Sciences Meeting,* publ. AIAA-92-0679 (American Institute of Aeronautics and Astronautics, New York, 1992).
3. E. H. Piepmeier, "Theory of laser saturated atomic resonance fluorescence," Spectrochim. Acta. **27B,** 431–443 (1972).
4. W. Demtroder, *Laser Spectroscopy* (Springer-Verlag, Berlin, 1982), Chap. 2, pp. 42–46.
5. A. Yariv, *Quantum Electronics* (Wiley, New York, 1975), Chap. 8, pp. 165–173.
6. G. F. Kirkbright, *Atomic Absorption and Fluorescence Spectroscopy* (Academic, London, 1974), Chap. 4, pp. 65–95.
7. H. Griem, *Spectral Line Broadening by Plasmas* (Academic, New York, 1974), App. IV, p. 350.
8. J. Vlcek, "A collisional-radiative model applicable to argon discharges over a wide range of conditions. IV. Application to inductively coupled plasmas," J. Phys. D **24,** 309–317 (1989).
9. W. L. Wiese, J. W. Brault, K. Danzmann, V. Helbig, and M. Kock, "Unified set of atomic transition probabilities for neutral argon," Phys. Rev. A **39,** 2461–2471 (1989).
10. M. W. Blades, "Some considerations regarding temperature, electron density and ionization in the argon inductively coupled plasma," Spectrochim. Acta **37B,** 869–879 (1982).
11. M. Huang, P. Yang, D. S. Hanselman, C. A. Monnig, and G. M. Hieftje, "Verification of a Maxwellian electron-energy distribution in the ICP," Spectrochim. Acta **45B,** 511–520 (1990).
12. D. C. Schram, I. J. M. M. Raaymakers, B. van der Sijde, H. J. W. Schenkelaars, and P. W. J. M. Boumans, "Approaches for clarifying excitation mechanisms in spectrochemical sources," Spectrochim. Acta. **38B,** 1545–1557 (1983).

Experiments in Fluids 13, 369–376 (1992)

Experiments in Fluids

Acetone: a tracer for concentration measurements in gaseous flows by planar laser-induced fluorescence

A. Lozano, B. Yip and **R. K. Hanson**

High Temperature Gasdynamics Laboratory, Department of Mechanical Engineering, Stanford University, Stanford, CA, 94305, USA

Abstract. This paper explores the use of acetone as a suitable tracer in planar laser-induced fluorescence concentration measurements in gaseous flows. The photophysics and physical properties of acetone relevant to its use as a fluorescent marker are discussed and compared to those of alternative molecular tracers, particularly the biacetyl molecule. Finally, as a direct example, concentration images obtained in a turbulent air jet seeded alternatively with acetone and biacetyl are compared.

1 Introduction

Planar laser-induced fluorescence (PLIF) is an attractive technique for fluid diagnostics. It is non-intrusive, instantaneous and can be used to determine different flowfield properties in a plane without integration along the line of sight. Its use of molecular markers greatly reduces the possibility of particle tracers lagging the fluid, and allows high spatial resolution measurements with minimal alteration of the flow conditions. PLIF has been successfully applied to non-reacting (Epstein 1974), and reacting gaseous flows (Kychakoff et al. 1982) to measure species concentration (Dyer and Crosley 1982), temperature (Seitzman et al. 1985; Lee et al. 1987), pressure and velocity (Hiller and Hanson 1988). A recent review of PLIF theory, hardware and applications is given by Hanson et al. (1990). The method is especially attractive for tracer concentration measurements which provide a direct way to study fluid mixing in flowing systems.

In a typical PLIF experiment, the flow is illuminated by a laser sheet whose wavelength is tuned to excite a particular transition of a molecular tracer, which can be a species naturally occurring in the flow (e.g. CH, OH, NO in flames), or added for this purpose (e.g. acetone, biacetyl, I_2, NO, or fluorescein for liquid flows). A fraction of the molecules in the appropriate lower energy level absorbs the incident light and is promoted to a higher energy state. Some of the excited molecules may dissociate. The rest return to the equilibrium state either by emitting photons or by transferring the excess of energy through nonradiative decay processes (collisional quenching, intersystem crossing or internal conversion). The photons can be spontaneously emitted on short time scales (this is the laser-induced fluorescence), or on much longer time scales when metastable electronic states are involved (phosphorescence).

Assuming a low intensity laser sheet at wavelength λ propagating in the x direction and a single absorbing and emitting species, the total photon emission per unit longitudinal sheet area, per unit time, N_e, is

$$N_e(x,y,t,\lambda) = \int N_i(y,z,t)\, e^{-\sigma(\lambda)\int C(x,y,z)\,dx}\, \sigma(\lambda)\, C(x,y,z)\, \phi(\lambda)\, dz \qquad (1)$$

where

z is the coordinate transverse to the laser sheet;
$N_i(y,z,t)$ is the incident photon flux, the number of photons per unit time per unit transverse area incident on the flow;
$\sigma(\lambda)$ is the molecular absorption cross-section of the tracer in cm^2;
$C(x,y,z)$ is the absorbing species concentration in the lower energy level in cm^{-3}; and
$\phi(\lambda)$ is the species ‘quantum efficiency’ for emission (or Stern-Volmer factor) for this transition.

Rayleigh scattering has been ignored since its cross-section is usually much less than $\sigma(\lambda)$. Saturation effects in the absorption have also been neglected (low excitation intensity limit). The integral in the z direction extends to the width of the laser sheet. If the laser is pulsed, the total number of emitted photons is obtained by integrating the equation with respect to time.

The first term inside the integral comes directly from Beer's law and relates the incident intensity at a certain point in the flow with the initial laser beam intensity, following absorption by previous fluid elements. If concentration values at different points in the flow $C(x,y)$ are approximated by a mean value C_{avg} then

$$\sigma(\lambda)\int C(x,y)\,dx \approx \sigma(\lambda)\, C_{avg}\, x = x/l \qquad (2)$$

where $l = 1/(C_{avg}\sigma)$ is the optical depth of the medium. When $x \ll l$, the medium is said to be optically thin, light absorption is negligible and the exponential term can be approximated by 1.

The emission quantum efficiency $\phi(\lambda)$, can, in the most general case, depend on wavelength, flow temperature, pressure, bulk velocity, and gas composition. In this case, a relation between measured emitted intensity and tracer concentration would be extremely difficult to infer. For some substances, however, the quantum efficiency is independent of many of the cited parameters, and in other instances some of the parameters are flowfield constants (e.g. isothermal, isobaric flows). In particular, for the polyatomic tracers to be discussed later, the fluorescence efficiency ϕ_f is largely independent of temperature and pressure, and for a large variety of gases, independent of the mixture composition. In this case, if the absorbing medium is optically thin, the image intensity obtained from a point in the flow is directly proportional to the desired concentration $C(x, y)$. By imaging the fluorescence from the illuminated slice of the flow onto a camera, a 2-D map of the concentration of the marked fluid is obtained.

As will be shown in detail, acetone ($CH_3-CO-CH_3$) satisfies most of the requirements of a PLIF tracer for gaseous flows. It has a fairly high vapor pressure, 180 torr at room temperature (20 °C), which allows a maximum seeding density of $\sim 30\%$ mole fraction. It absorbs over a broad band of wavelengths (225–320 nm) with a maximum between 270 and 280 nm ($\sigma = 4.7 \times 10^{-20}\,\mathrm{cm}^2$). The fluorescence emission is broadband in the blue (350–550 nm) with peaks at 445 and 480 nm, an efficiency $\phi = 0.2\%$, and a short lifetime of less than 4 ns. The fluorescence is independent of temperature and local gas composition. Acetone is not toxic, and its cost is economical.

2 Acetone physical characteristics

Acetone (Dimethyl ketone, or 2-Propanone) $CH_3-CO-CH_3$ is a ketone of molecular weight 58.08. Under normal conditions it is a transparent liquid with specific gravity 0.79. It is highly flammable with melting point −95 °C, boiling point 56 °C, and autoignition temperature 465 °C; the flammable limits in air (by volume) are 2.6% and 12.8%. The vapor pressure of acetone determines its maximum possible seeding density when used as a fluorescent molecular marker. Figure 1 shows experimental measurements of the acetone vapor pressure as a function of temperature taken by Ambrose et al. (1974), compared to the fitted Antoine equation:

$$\log_{10} P(\mathrm{Torr}) = 7.125267 - \frac{1214.208}{230.002 + T(^\circ\mathrm{C})}. \tag{3}$$

The vapor pressure at 20 °C is $\sim$180 Torr, with a vapor density of 2 (where the reference, air, has a vapor density of 1).

Acetone toxicity is very mild although prolonged exposure to its vapor or mist can irritate the eyes, mucous membranes and upper respiratory tract, and cause nausea, headaches, vomiting and dizziness. It can also be harmful if swallowed. Acetone is not considered to ba a carcinogen. The odor threshold is 2 ppm.

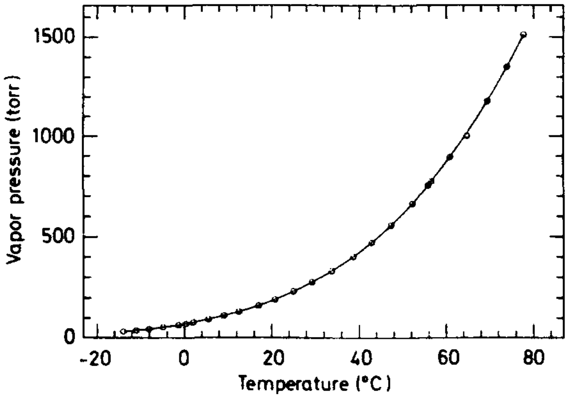

Fig. 1. Acetone saturation vapor pressure as a function of temperature

Dilution in a laboratory exhaust system quickly reduces acetone concentrations below the limits of toxicity and flammability, making it a safe working fluid.

3 Acetone photophysics

3.1 Historical background

Studies of acetone vapor luminescence were published as early as 1933 by Damon and Daniels. They observed a strong green emission, which became a dimmer blue with the addition of oxygen. Matheson and Zabor (1939) later assigned the green emission to the presence of biacetyl ($CH_3-(CO)_2-CH_3$), which forms from acetone photolysis. Because of the higher intensity of the green biacetyl phosphorescence, part of the acetone research was diverted to biacetyl, with a view to its use as a gas phase emission standard and as an energy acceptor in the study of collisional energy transfer. Biacetyl photophysics were fairly well understood when Epstein proposed its use as a tracer in fluid mechanics experiments (Epstein 1974). Although in part he selected biacetyl for its high phosphorescence efficiency, most of his experiments were based only on its much weaker blue fluorescence emission. Since then, biacetyl has become a common tracer in gaseous flows, with both the phosphorescence and fluorescence having been exploited (see, for example, van Cruyningen et al. 1990, or Yip et al. 1988). As will be demonstrated, the use of acetone will generally be advantageous for fluorescence imaging.

3.2 Relevant reactions

There are three electronic states involved in the photoemission processes: the ground state singlet A_g (often referred to as S_0), the first excited singlet $I^1 A_u$ (or S_1), and the first excited triplet, $I^3 A_u$ (or T_3). Each electronic state has a

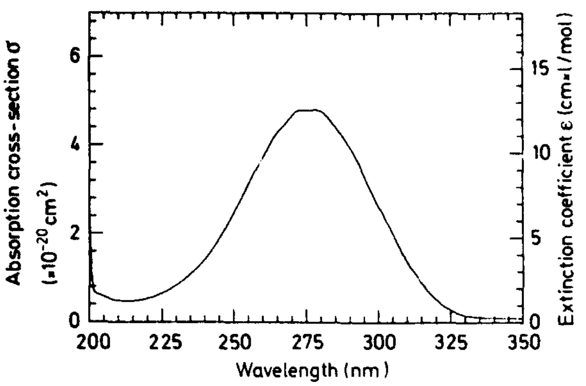

Fig. 2. Acetone absorption spectrum corresponding to excitation from the ground state to the first excited singlet

Table 1. Acetone excitation schemes; the figure of merit in the last column is the laser energy per pulse multiplied by the absorption cross-section at the laser wavelength

Laser	λ (nm)	Energy/ pulse	$E\sigma$ ($\times 10^{-20}$ J cm^2)
XeCl excimer	308	300 mJ	0.48
KrF excimer	248	300 mJ	0.7
Quadrupled Nd: YAG	266	120 mJ	0.52
Doubled flashlamp-pumped dye Rhodamine 590	280	400 mJ	1.9
Raman-shifted ArF excimer	254	2 mJ	0.006
	284	1 mJ	0.0045

manifold of vibrational levels, but for simplicity only the lowest vibrational level of each state will be considered. Under atmospheric pressure, singlet thermalization will, in any case, be faster than fluorescence.

Excitation. Acetone absorption corresponding to excitation from S_0 to S_1 was measured using a Perkin-Elmer Lambda 9 Spectrophotometer. The results, shown in Fig. 2, are in good agreement with previous measurements (see for example Hansen and Lee 1975a). The spectrum was scanned with a resolution of 0.05 nm and digitized with a resolution of 1 nm and shows little vibrational structure. The absorption band extends from 225 to 320 nm with a flat region between 270 and 280 nm ($\sigma = 4.7 \times 10^{-20}$ cm^2).

The absorption spectrum suggests several possible excitation sources for pumping acetone in a LIF experiment. These include a XeCl excimer laser ($\lambda = 308$ nm, $\sigma = 1.6 \times 10^{-20}$ cm^2), a KrF excimer laser ($\lambda = 248$ nm, $\sigma = 2.3 \times 10^{-20}$ cm^2), a frequency-quadrupled Nd: YAG ($\lambda = 266$ nm, $\sigma = 4.4 \times 10^{-20}$ cm^2), or the frequency-doubled output of a dye laser (Rhodamine emission includes the 550–620 nm region). Since dye efficiencies will not exceed 30%, if the dye laser is YAG or excimer pumped, it will be more efficient to use the pump laser, rather than the dye laser, to excite the acetone. Dye lasers should be considered only if they are flashlamp-pumped. In this case, they can probably provide the highest energy output. Note, however, that although the absorption cross-section may increase, the fluorescence efficiency decreases slightly for shorter wavelengths because dissociation increases. Still other possibilities include using a Raman cell to downshift an ArF excimer laser (3rd Stokes, $\lambda = 254$ nm, $\sigma = 3 \times 10^{-20}$ cm^2, with a conversion efficiency of ~2%, or 4th Stokes, $\lambda = 284$ nm, $\sigma = 4.5 \times 10^{-20}$ cm^2, with a conversion efficiency of ~1%). Downshifting a KrF emission to 278 nm (1st Stokes), or upshifting XeCl to 273 nm (1st anti-Stokes) is inefficient and does not compensate for the increase in acetone absorption. Different excitation schemes are summarized in Table 1. To compare the different options, a figure of merit has been included (the laser energy per pulse, using values representative of current commercially available lasers, multiplied by the absorption cross-section at the laser wavelength). From this table, the most efficient practical pumping system appears to be a flashlamp-pumped dye laser. However, the maximum pulse repetition rate for this type of laser is usually low when delivering such high pulse energies. A XeCl excimer laser was chosen for the experiments described later because of its availability and ease of operation, and because, as well as pumping acetone directly, it could be used to pump a dye laser for exciting biacetyl.

Dissociation. Some of the acetone molecules that absorb the excitation laser radiation can photolyze or predissociate. The principal dissociation process is

$$CH_3COCH_3 + h\nu \rightarrow CH_3CO + CH_3 .$$

The free acetyl radical can recombine with another one to form a biacetyl molecule. This is responsible for the green biacetyl phosphorescence emission observed in some static cell acetone experiments. Biacetyl formation occurs only for temperatures below 100°C (see Hunt and Noyes 1948, and references therein), and originates from acetone triplets. Dissociation of acetone singlets (for excitation wavelengths shorter than 312 nm) follows the alternative path

$$CH_3COCH_3 + h\nu \rightarrow 2\,CH_3 + CO$$

and when the excitation wavelength is shorter than 250 nm, another reaction can occur (to a lesser extent)

$$CH_3COCH_3 + h\nu \rightarrow CH_2COCH_3 + H$$

(Calvert and Pitts 1966). Biacetyl formation will therefore decrease with decreasing excitation wavelengths. Biacetyl is not formed in an excited state. It is collisionally excited by acetone triplets that promote the biacetyl molecules to their triplet state (Almy and Anderson 1940; Heicklen and Noyes 1969). Biacetyl triplets phosphoresce with high efficiency (15%) unless there is oxygen present in the flow. Biacetyl singlets fluoresce in the blue, but the fluorescence efficiency is very low when the excitation wavelength is shorter than 320 nm. In these experiments, acetone was mixed with air, and was excited at 308 nm. Accordingly, biacetyl fluorescence will be negligible, and its phosphorescence will be almost entirely quenched by the oxygen. In summary, any interference in the measurements of acetone fluorescence due to biacetyl emission should be negligible.

Fluorescence. Most of the excited acetone molecules in the singlet state are transferred to the triplet state (intersystem crossing) with nearly 100% efficiency. Almost all of the remaining excited singlet molecules fluoresce. The fluorescence spectrum, which was measured using a prism spectrograph (whose responsivity was determined using a calibrated quartz halogen-tungsten lamp), is broadband, extending from 350 to 550 nm with peaks at 445 and 480 nm (Fig. 3). There is general agreement about the spectral shape's independence of pressure, incident intensity or wavelength. Different quantum efficiency values have been reported in the literature. Heicklen (1959) measured a value of 0.21% when exciting at 313 nm. Halpern and Ware (1971), however, calculated a lower value, 0.12% for the same excitation wavelength. Heicklen's measurements show a decrease in the fluorescence quantum efficiency with decreasing wavelength, probably due to increased dissociation. The values are independent of pressure.

The lifetime value of the fluorescence, τ, can be used to estimate the transition saturation limit. Breuer and Lee (1971) measured a fluorescence lifetime of 2.7 ± 0.3 ns for 313 nm excitation, decreasing to 1.7 ± 0.3 ns when exciting at 280 nm. To operate in the linear fluorescence regime the requirement is that $N_i \ll (\sigma \tau)^{-1}$. Using the maximum σ value gives $N_i \ll 7.7 \times 10^{27}$ photons/cm^2/sec. For a pulsed laser emitting at 308 nm, with a pulse duration of 20 ns, this limit translates into $I_i \ll 100$ J/cm^2. For a laser sheet of thickness 250 µm and height 10 cm, saturation will not occur until pulse energies approach ~ 25 J.

To verify that measurements were performed in the linear fluorescence regime, the emission was recorded for different incident intensities (Fig. 4). Linearity of the laser-induced fluorescence with respect to acetone pressure was also verified (Fig. 5). These tests were made by measuring the fluorescence emission from the potential core of a flowing jet of air seeded with acetone, in order to avoid spurious effects caused by the biacetyl buildup (and the consequent acetone concentration reduction) which would occur in a static cell. To vary the initial acetone seeding density, the acetone-air mixture was further diluted with air.

Phosphorescence. Phosphorescence is the radiative decay from an excited state (in this case a triplet) to another of different multiplicity (in this case, the singlet ground state) by the emission of photons over a long time scale. According to some authors (see, for example, Heicklen 1959), acetone phosphoresces in the blue, with a similar emission to the fluorescence spectrum, but slightly shifted towards the red. The phosphorescence efficiency is $\sim 1.8\%$ for 313 nm excitation, and the decay lifetime is 200 µs (Kaskan and Duncan 1950). Although phosphorescence (in particular from biacetyl) has been used to perform concentration measurements, its

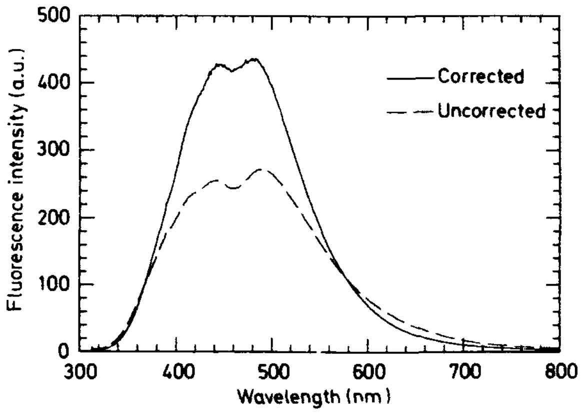

Fig. 3. Acetone fluorescence spectrum when excited at 308 nm; the *dashed line* corresponds to the detected signal; the *solid line* is the same curve corrected for the detection system responsivity

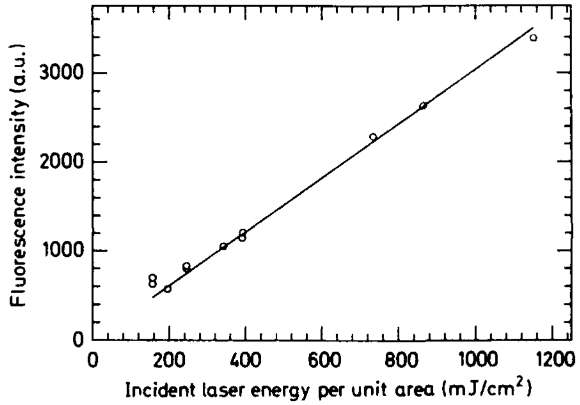

Fig. 4. Linearity of the acetone fluorescence signal with respect to the incident laser energy per unit area

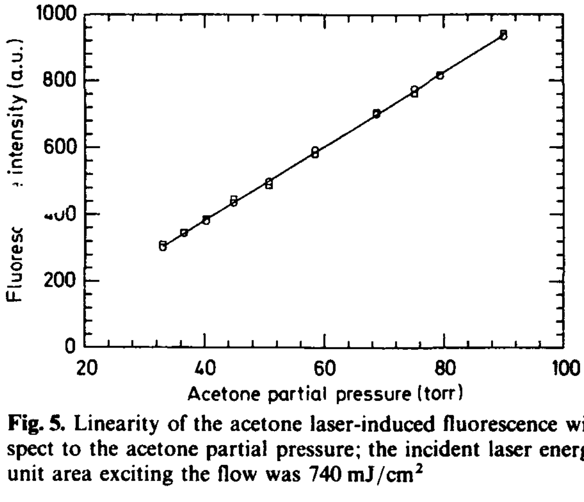

Fig. 5. Linearity of the acetone laser-induced fluorescence with respect to the acetone partial pressure; the incident laser energy per unit area exciting the flow was 740 mJ/cm^2

use is restricted to slow flows, because the long lifetime of the emission can cause motion blur when imaging without gating is performed in a flowing system.

Quenching. Excited molecular levels can be depopulated through non-radiative relaxation processes which include predissociation, internal conversion, intersystem crossing and collisional quenching. Collisional quenching rates vary with temperature and local gas composition, thus complicating the interpretation of PLIF signals when such quenching is significant. The dominant deexcitation path for acetone singlets is the intramolecular intersystem crossing to triplet levels: collisional quenching is negligible, and therefore the quantum yield is independent of molecular collisions, hence independent of temperature and local gas composition. For concentration measurements, acetone fluorescence signals are particularly easy to interpret.

Acetone phosphorescence, on the other hand, is greatly quenched by trace amounts of oxygen, and is also temperature dependent. Since all concentration measurements were performed in acetone-seeded air flows, no long-lived acetone phosphorescence interfered with the fluorescence experiments described here.

Confirming the theoretical predictions no temperature dependence of the fluorescence emission in the temperature range of these experiments was detected. Neither were appreciable self-quenching, or quenching of the acetone fluorescence by oxygen or nitrogen observed.

4 Comparison with other tracers

Relatively few molecular tracers have been used thus far in fluid mechanics PLIF experiments in gaseous flows. This comparison will concentrate on tracers for non-reacting flows, and not consider combustion radicals such as OH, CH or C_2.

Several simple fluorescent tracer molecules have been used for concentration measurements in gas flows, including I_2, NO, and NO_2 (see the review on I_2 characteristics by Hiller and Hanson 1990). These molecules have well-characterized spectral properties. Specific rotational-vibrational states can be excited, and temperature, concentration and/or velocity information can be obtained from the fluorescence signal. However, all these substances are highly toxic, and I_2 in particular is highly corrosive. Furthermore, their fluorescence is strongly quenched by collisions with oxygen molecules. For these reasons, these tracers are better suited to low pressure, low flow rate applications.

For concentration measurements, the tracer molecule need not have a simple discrete absorption spectrum. The fluorescence need simply be related to concentration with a known dependence (preferably linear). A number of organic polyatomic molecules have been used, including biacetyl, acetaldehyde (Arnold et al. 1990) and here, acetone. These have the advantages of lower toxicity and lower reactivity, and suffer less fluorescence quenching than the species cited above. These products have fairly low fluorescence efficiencies, however. Unfortunately most chemicals with high emission efficiencies are solids with extremely low vapor pressures (anthracene, naphthalene, fluorene, laser dyes). Though acetone, acetaldehyde, and biacetyl are liquids, their vapor pressures are high, and seeding is relatively easy, either by bubbling or injecting the carrier gas into the liquid container, or by spraying the liquid to a mixing tank. The more volative a fluorescent marker, the higher the concentration that can be seeded in the flow, consequently increasing the emission signal.

Acetaldehyde (CH_3-CHO) absorption (250–340 nm) peaks at 290 nm (Hansen and Lee 1975b), with an absorption cross-section $\sigma = 4.67 \times 10^{-20}\,cm^2$. Acetaldehyde has a high vapor pressure (boiling point 21 °C), which enables extremely high concentrations, although at some point the fluid will become an optically thick medium. At a partial pressure of 760 Torr of acetaldehyde, 90% of incident radiation at 290 nm is absorbed after a pathlength of only 2 cm. The same reduction for 180 Torr of acetone requires 10 cm. Acetaldehyde fluoresces broadband in the blue with a ~ 4 ns lifetime and a wavelength-dependent quantum efficiency ranging from 0.08% at 280 nm to 0.18% for 325 nm excitation (0.14% for 308 nm). The fluorescence spectrum was measured in this laboratory as being identical to that of acetone, suggesting some acetone forming reaction. Other authors however, have recorded a spectrum somewhat different from acetone with a single broad peak at 420 nm (Parmenter and Noyes 1962). Reportedly, acetaldehyde also phosphoresces with a quantum efficiency two to four times lower than its fluorescence and with exactly the same emission spectrum. In short, acetaldehyde has properties rather similar to those of acetone, but with the significant drawback that it is toxic and carcinogenic.

Biacetyl ($CH_3-(CO)_2-CH_3$) has been widely used as a PLIF tracer, and its photophysical behavior has been studied extensively (see, for example, Okabe and Noyes 1957; Sidebottom et al. 1972; Liu et al. 1988). Biacetyl toxicity is very mild and its boiling point is 88 °C (vapor pressure ~ 40 Torr at 20 °C). The absorption is broadband (340–470 nm) with a peak at 417 nm ($\sigma = 8 \times 10^{-20}\,cm^2$). In emits both by fluorescence ($\phi_f = 0.2\%$), and by phosphorescence ($\phi_p = 15\%$). The fluorescence emission is broadband in the blue with a lifetime of ~ 15 ns and a peak at 485 nm. The phosphorescence is long-lived (lifetime of 1.5 ms), and presents a strong peak at 512 nm, a secondary peak at 560 nm, and a much fainter peak at 610 nm. Phosphorescence is 60 times stronger, but its long lifetime prevents its use in fast flow experiments, unless a gated camera system is used. Phosphorescence is also temperature dependent and strongly quenched by oxygen.

Another complex molecule, hexafluoroacetone ($CF_3-CO-CF_3$), should be mentioned. It is a gas at room temperature (b.p. −26 °C). The absorption cross-section is $3.1 \times 10^{-20}\,cm^2$ at 303 nm, with the absorption band extending

Table 2. Photophysical characteristics of some organic molecules relevant to their use as fluorescent tracers. Table columns are: boiling point (B.P.), absorption band, maximum value of the molecular absorption cross-section (σ_{max}) with the corresponding wavelength value in parentheses, fluorescence quantum efficiency (ϕ_f), fluorescence emission spectrum (with the wavelength of peak emission), fluorescence lifetime (τ_f), and a figure of merit ($N \sigma \phi C$); the values used to calculate this figure are explained in the text

	B.P.	Absorption	σ_{max} ($\times 10^{-20}$ cm^2)	ϕ_f	Emission (nm)	τ_f	$N \sigma \phi C$
Acetone	56 °C	225–320 nm	4.7 (275 nm)	0.2%	350–550 (435)	4 ns	7.2×10^{13}
Biacetyl	88 °C	340–470 nm	8 (417 nm)	0.25%	420–520 (485)	15 ns	7.0×10^{12}
Acetaldehyde	21 °C	250–340 nm	4.6 (290 nm)	0.15%	350–480 (420)	4 ns	1.0×10^{14}
Hexafluoroacetone	−26 °C	245–355 nm	3.1 (302 nm)	1.85%	410–580 (430)	84 ns	1.2×10^{15}

Table 3. Photophysical characteristics of some organic molecules relevant to their use as phosphorescent tracers. Table columns are: phosphorescence quantum efficiency (ϕ_p), phosphorescence emission spectrum (with the wavelength of peak emission in parentheses), phosphorescence lifetime (τ_p), and a figure of merit ($N \sigma \phi C$); the values used to calculate this figure are explained in the text

	ϕ_p	Emission (nm)	τ_p	$N \sigma \phi C$
Acetone	1.8%	350–600	200 µs	6.5×10^{14}
Biacetyl	15%	475–675 (512)	1.5 ms	4.2×10^{14}
Acetaldehyde	0.04%	350–480 (420)	2.5 µs	2.7×10^{13}
Hexafluoroacetone	11%	380–650 (495)	3.4 ms	7.3×10^{15}

from 245 to 355 nm. Its fluorescence emission extends from 347 nm to 600 nm with a maximum at about 430 nm (Okabe and Steacie 1958), a quantum yield of 1.85% (Gandini and Kutschke 1968), and a lifetime $\tau_f = 84$ ns (Halpern and Ware 1971). A stronger, long-lived phosphorescence ($\phi_f = 11\%$, $\tau_p = 3.4$ ms), peaking at 495 nm is quenched by trace amounts of oxygen (Bowers and Porter 1964; Gandini and Kutschke 1968). Hexafluoroacetone would seem to be an ideal tracer for gaseous PLIF imaging. Unfortunately it is extremely toxic, and potentially lethal if inhaled.

Relevant characteristics of all these chemicals pertaining to their use as markers in PLIF concentration measurements are summarized in Table 2. The last column is a figure of merit which is essentially the number of photons emitted by a unit volume (1 cm^3) of fluid when excited by a total number of photons N. The emission depends on the type of tracer, seeding density, and wavelength and number of incident photons (Eq. 1). For this calculation, the same seeding density has been assigned to acetone, acetaldehyde and hexafluoroacetone (150 Torr). It is lower than the saturation vapor pressure at 20 °C, but should assure optically thin behavior for most practical cases. Biacetyl has been considered at a seeding concentration of 30 Torr. The value for the excitation energy in the biacetyl case has been taken as 20 mJ at 440 nm. For the rest of the tracers an energy of 300 mJ at 308 nm has been selected. These values are close to those obtained in the experimental part of this work. For completeness, Table 3 summarizes the phosphorescence characteristics of these substances. From Table 2, acetone is clearly a better practical fluorescent marker than biacetyl, and its fluorescence signal is only six times weaker than that of biacetyl phosphorescence, with a lifetime almost 4×10^5 times shorter. Acetone and acetaldehyde fluorescence signals are quite similar, so that acetone's lower toxicity makes it a preferable choice as a tracer molecule. Only hexafluoroacetone clearly performs better than acetone, but its extreme toxicity makes it impractical. Note, finally, that the figure of merit serves only as a rough guide. Energies as high as 700 mJ can be obtained at 440 nm with a flashlamp-pumped dye laser, and similar energies may be obtainable with this type of laser at 280 nm, by doubling the output of a Rhodamine dye.

5 Experiments

To demonstrate the use of acetone as a tracer in PLIF concentration measurements, images were acquired of a turbulent axisymmetric air jet. The jet exited vertically upward from a 2.2 mm nozzle at a velocity of 45 m/s (Reynolds number Re = 8,000). The air was seeded alternatively with acetone, and then with biacetyl as tracer molecules. In both cases the seeding procedure was to bubble the air into the bottles containing the liquids. The tracer concentrations at the nozzle were measured by comparing the Rayleigh scattering signals of the seeded and unseeded jets. The exit acetone seeding density was 90 Torr. In the biacetyl case, the exit partial pressure was 30 Torr. In both cases the tracer concentration was below the saturation vapor pressure at the room temperature, due to the decrease in the liqud temperature caused by evaporation (especially in the acetone case). Stable seeding was achieved once thermal equilibrium was reached, after approximately 10 minutes. The seeding concentration can be readily increased (to increase signal levels), by placing the seeding bottles in a heated constant temperature bath.

Acetone was excited with a Lambda Physik 203 EMG (Göttingen, Germany) XeCl pulsed excimer laser ($\lambda = 308$ nm, 300 mJ/pulse, 20 ns pulse duration). To excite the biacetyl, the excimer laser was used to pump a Lambda Physik FL 2002 (Göttingen, Germany) dye laser, operated with Coumarin 440 dye ($\lambda = 440$ nm, 16 mJ/pulse). The laser beam was formed into a sheet, 9 cm high and 500 µm thick for the acetone case, and 8.6 cm high for the biacetyl case, and passed through the axis of the flow.

The imaging system was a Photometrics Star 1 CCD camera (Tucson, Arizona), with a 50 mm F 1.2 photographic

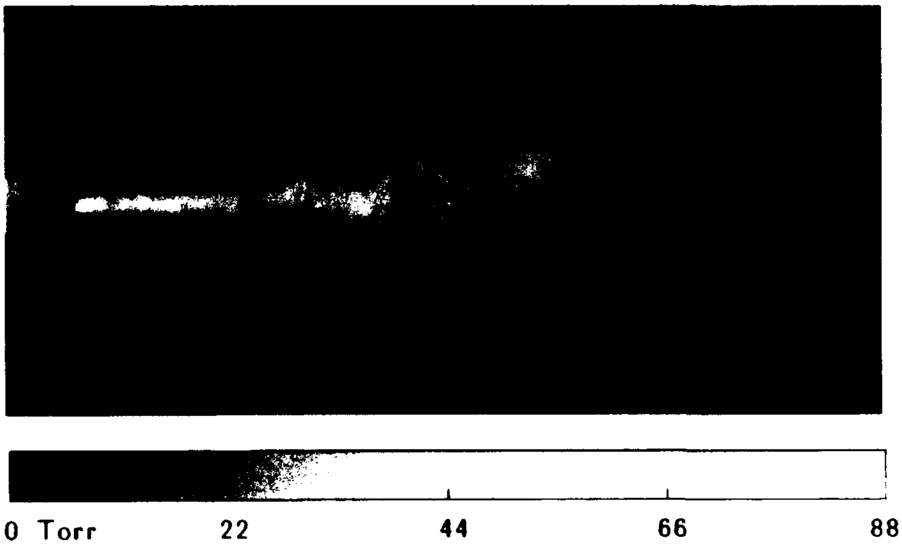

Fig. 6. Instantaneous PLIF concentration image of the first 40 diameters of a free axisymmetric acetone-seeded air jet, corrected for intensity variations in the laser sheet; the inner diameter of the vertically-oriented nozzle is 2.2 mm; measured acetone partial pressures are marked in Torr

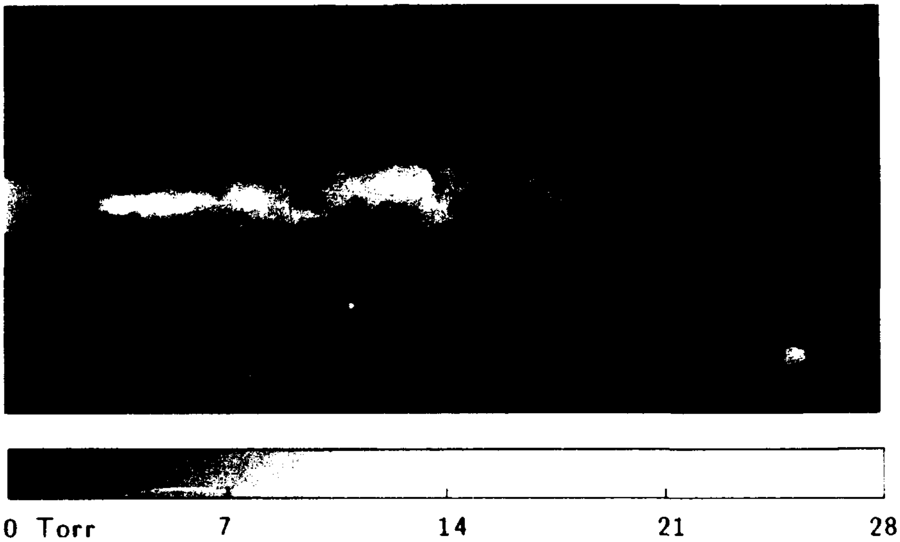

Fig. 7. Instantaneous PLIF concentration image of the first 40 diameters a biacetyl-seeded jet, corrected for intensity variations in the laser sheet; pixel intensities have been multiplied by a factor of 4 with respect to those in Fig. 6 in order to make the weaker signals more visible; measured biacetyl partial pressures are indicated in Torr

lens. With the camera located at 40 cm from the nozzle, the imaged field of view was 11.4 × 7.6 cm (slightly larger than the laser sheet height). Under identical conditions, single-hot and frame-averaged images were aquired for acetone-air and biacetyl-air mixtures.

The minimum detectable acetone and biacetyl concentrations can be estimated for the excitation/detection system employed. Considering the detectability limit to be that for which the signal to noise ratio is one, the minimum measurable concentrations can be estimated as 93 ppm for biacetyl, and 65 ppm for acetone (where 0.12% has been used as the value for acetone quantum efficiency). As the exit partial pressures were 30 Torr for biacetyl (39,000 ppm), and 90 Torr for acetone (118,000 ppm), this yields potential signal dynamic ranges of 420 and 1,815 respectively. The maximum value of the product $\sigma \phi_f CN/h$, where N is the total number of photons in a laser pulse and h is the laser sheet height (the sheet profile is approximated by a top hat function), is $6.4 \times 10^{11}\ \mathrm{cm}^{-2}$ for biacetyl and $2.9 \times 10^{12}\ \mathrm{cm}^{-2}$ for acetone in the present experimental conditions. For this experimental configuration, acetone imaging thus is capable of providing higher signal levels, and a larger signal dynamic range.

Figure 6 shows a single shot image of the acetone-seeded jet corrected for intensity variations in the laser sheet. Figure 7 corresponds to a corrected image of the same jet seeded with biacetyl. Due to the weaker biacetyl signal, intensities in the biacetyl image have been multiplied by a factor of 4, to produce maximum values comparable to those in Fig. 6. Higher noise levels in the image of the biacetyl-seeded jet are particularly noticeable in the downstream end of the flow, where dilution of the jet fluid by ambient air produces lower concentration of the marker gas. Mie scattering of the 440 nm laser beam from dust particles in the air surrounding the jet is visible in the image of the biacetyl-seeded jet. This scattering can be rejected by placing an appropriate optical filter in the detection optics, at the expense of reducing the collected biacetyl fluorescence signal. This discrimination has been achieved in the acetone-seeded jet images because the glass imaging lens transmits the blue fluorescence while blocking the Mie scattering from dust particles at 308 nm. Intensity levels in these images are directly proportional to tracer concentration. If the absolute concentration is known for an imaged point in the flow (in this case, near the nozzle), intensities can be readily converted into seeding concentrations, or to the mole fraction of jet fluid in the mixture of jet and ambient air.

An emission intensity comparison can be best obtained from averaged images. Averages of 30 acetone frames, and 160 biacetyl frames were acquired. The total collected signals integrated along the jet centerline were compared and acetone was found to yield a signal strength 4.5 times superior to that of biacetyl, in good agreement with the previous estimate. Acetone signals were readily increased by a further factor of 2 by placing the acetone seeding bottle in a bath of warm water.

6 Conclusions

The properties of acetone relevant to its use as a tracer in PLIF concentration measurements in gaseous flows have been summarized. Its luminescent characteristics, together with low toxicity make it an attractive choice as a fluorescent marker. Concentration images obtained from acetone fluorescence emission give signal levels consistent with estimates based on its photophysical parameters. In a practical situation, acetone fluorescence produces signal levels over four times greater than those obtained using biacetyl as the fluorescent tracer.

Acknowledgements

This research was sponsored by the Air Force Office of Scientific Research, Aerospace Sciences Directorate, with Dr. Julian Tishkoff as the technical monitor.

References

Almy, G. M.; Anderson, S. 1940: Lifetime of fluorescence in diacetyl and acetone. J. Chem. Phys. 8, 805-814

Ambrose, D.; Sprake, C. H. S.; Townsend, R. 1974: Thermodynamic properties of organic oxygen compounds XXXIII. The vapour pressure of acetone. J. Chem. Thermodyn. 6, 693-700

Arnold, A.; Becker, H.; Suntz, R.; Monkhouse, P.; Wolfrum, J.; Maly, R; Pfister, W. 1990: Flame front imaging in an internal-combustion engine simulator by laser-induced fluorescence of acetaldehyde. Opt. Lett. 15 (15), 831-833

Bowers, P. G.; Porter, G. B. 1964: Fluorescence and phosphorescence of hexafluoroacetone vapor. J. Phys. Chem. 68 (10), 2982 2985

Breuer, G. M.; Lee, E. K. C. 1971: Fluorescence decay times of cyclic ketones, acetone, and butanal in the gas phase. J. Phys. Chem. 75 (7), 989 990

Calvert, J. G.; Pitts, J. N. 1966: Photochemistry. New York: Wiley

Cruyningen, I. van; Lozano, A.; Hanson, R. K. 1990: Quantitative imaging of concentration by planar laser-induced fluorescence. Exp. Fluids 10 (1), 41 49

Damon, G. H.; Daniels, F. 1933: The photolysis of gaseous acetone and the influence of water. J. Am. Chem. Soc. 55, 2363 2375

Dyer, M. J.; Crosley, D. R. 1982: Two-dimensional imaging of OH laser-induced fluorescence in a flame. Opt. Lett. 7 (8), 382 384

Epstein, A. H. 1974: Fluorescent gaseous tracers for three-dimensional flow visualization. MIT Gas Turbine Lab. Rep. 117

Gandini, A. A.; Kutschke, K. O. 1968: The primary process in the photolysis of hexafluoroacetone vapour II. The fluorescence and phosphorescence. Proc. R. Soc. London, Ser. A, 306, 511 528

Halpern, A. M.; Ware, W. R. 1971: Excited singlet state radiative and nonradiative transition probabilities for acetone, acetone-d_6, and hexafluoroacetone in the gas phase, in solution, and in the neat liquid. J. Chem. Phys. 54 (3), 1271 1276

Hansen, D. A.; Lee, E. K. C. 1975a: Radiative and nonradiative transitions in the first excited singlet state of symmetrical methyl-substituted acetones. J. Chem. Phys. 62 (1), 183 189

Hansen, D. A., Lee, E. K. C. 1975b: Radiative and nonradiative transitions in the first excited singlet state of simple linear aldehydes. J. Chem. Phys. 62 (1), 3272 3277

Hanson, R. K.; Seitzman, J. M.; Paul, P. H. 1990: Planar laser-fluorescence imaging of combustion gases. Appl. Phys. B, 50, 441 454

Heicklen, J. 1959: The fluorescence and phosphorescence of biacetyl vapor and acetone vapor. J. Am. Chem. Soc. 81, 3863 3866

Heicklen, J.; Noyes, W. A. 1959: The photolysis and fluorescence of acetone and acetone-biacetyl mixtures. J. Am. Chem. Soc. 81, 3858-3863

Hiller, B.; Hanson R. K. 1988: Simultaneous planar measurements of velocity and pressure fields in gas flows using laser-induced fluorescence. Appl. Opt. 27, 33 48

Hiller, B.; Hanson, R. K. 1990: Properties of the iodine molecule relevant to laser-induced fluorescence experiments in gas flows. Exp. Fluids 10, 1 11

Hunt, R. E.; Noyes, W. A. 1948: Photochemical studies XXXIX. A further study of the fluorescence of acetone. J. Am. Chem. Soc. 70, 467 476

Kaskan, W. E.; Duncan, B. F. 1950: Mean lifetime of the fluorescence of acetone and biacetyl vapors. J. Chem. Phys. 18 (4), 427 431

Kychakoff, G.; Howe, R. D.; Hanson, R. K.; McDaniel, J. C. 1982: Quantitative visualization of combustion species in a plane. Appl. Opt. 21, 3225 3227

Lee, M. P.; Paul, P. H.; Hanson, R. K. 1987: Quantitative imaging of temperature fields in air using planar laser-induced fluorescence. Opt. Lett. 12, 75-77

Liu, J. B.; Pan, Q.; Liu, C. S.; Shi, J. R. 1988: Principles of flow field diagnostics by laser-induced biacetyl phosphorescence. Exp. Fluids 6, 505 513

Matheson, M. S.; Zabor, J. W. 1939: Fluorescence of carbonyl compounds in the gas phase. J. Chem. Phys. 7, 536-538

Okabe, H.; Noyes, W. A. 1957: The relative intensities of fluorescence and phosphorescence in biacetyl vapor. J. Am. Chem. Soc. 79, 801 806

Okabe, H.; Steacie, W. R. 1958: The fluorescence and its relationship to photolysis in hexafluoroacetone vapor. Can. J. Chem. 36, 137 146

Parmenter, C. S.; Noyes, W. A. 1962: Energy dissipation from excited acetaldehyde molecules. J. Am. Chem. Soc. 85, 416 421

Seitzman, J. M.; Kychakoff, G.; Hanson, R. K. 1985: Temperature field measurements in combustion gases using planar-laser induced fluorescence. Opt. Lett. 10, 439-441

Sidebottom, H. W.; Badcock, C. C.; Calvert, J. G.; Rabe, B. R.; Damon, E. K. 1972: Lifetime studies of the biacetyl excited singlet and triplet states in the gas phase at 25°. J. Am. Chem. Soc. 94, 13 19

Yip, B.; Schmitt, R. L.; Long, M. B. 1988: Instantaneous three-dimensional concentration measurements in turbulent jets and flames. Opt. Lett. 13, 96 98

Received March 11, 1992

Comparison of Excitation Techniques for Quantitative Fluorescence Imaging of Reacting Flows

J. M. Seitzman and R. K. Hanson

Reprinted from

AIAA Journal

Volume 31, Number 3, March 1993, Pages 513-519

AIAA

A publication of the
American Institute of Aeronautics and Astronautics, Inc.
The Aerospace Center, 370 L Enfant Promenade, SW
Washington, DC 20024-2518

AIAA JOURNAL
Vol. 31, No. 3, March 1993

Comparison of Excitation Techniques for Quantitative Fluorescence Imaging of Reacting Flows

Jerry M. Seitzman* and Ronald K. Hanson†
Stanford University, Stanford, California 94305

To determine the quantitative limitations of fluorescence imaging of OH, various systematic and random errors associated with three excitation approaches are analyzed. The three laser pumping schemes, 1) dye laser excitation of the $A^2\Sigma^+ - X^2\Pi$ (1,0) band, 2) KrF laser excitation of the predissociative (3,0) band, and 3) saturated pumping of the (0,0) band with a XeCl laser, are compared to find which method minimizes the overall error. The approaches are compared by calculating shot-noise limited random errors and systematic deviations between the standard scaling equations and solutions to a time-dependent five-level rate equation model of the population densities. The model is used to address saturation and depletion (bleaching) effects. Dye laser excitation has the lowest overall error for single-shot imaging in turbulent hydrocarbon-air and hydrogen-air flames. XeCl pumping produces the strongest signals, with evidence of strong saturation and ground state depletion effects. KrF pumping of the weakly absorbing and predissociative (3,0) band shows potential for quantitative imaging, when frame averaging is used.

Introduction

PLANAR imaging is a powerful tool for obtaining spatially correlated flowfield information at an instant in time. Thus planar imaging has proven an effective tool for locating flames, regions of burned or unburned gases, recirculation zones, shock waves, large-scale structures, and other features.[1] In addition, planar imaging provides the capability of delivering quantitative information at multiple flowfield points. Planar laser-induced fluorescence (PLIF) is particularly attractive owing to the strength of the process, relative to its primary competitors, Rayleigh and Raman scattering, and to its potential for monitoring several flowfield parameters: species concentration, temperature, velocity and pressure.[2] Thus, advances in PLIF which provide more quantitative data have high potential to generate a better understanding of both reacting and nonreacting flows.

In a typical PLIF measurement, an excited electronic state of a molecule is populated by a laser source with an emission frequency tuned to an optically allowed resonance between the excited state and a lower energy state. Excited molecules can then emit light, fluoresce, producing the PLIF signal. To date, collisional quenching of the excited state has been considered the major limitation to quantitative PLIF measurements, as collision rates depend on local chemical and thermodynamic parameters. Various laser pumping schemes have been suggested to reduce the importance of collisional quenching and produce more quantitative images. It should be noted, however, that in many cases the variation in quench rate across a region is small or can be modeled to some accuracy. To be considered an improvement, therefore, the errors associated with the alternate pumping schemes should be less than the systematic errors associated with quenching variations.

Here, we examine various error sources, both systematic and random, for three different laser pumping methods: the standard linear pumping technique; predissociated PLIF, in which the upper state decay rate is partially controlled by molecular dissociation; and saturated pumping, with laser stimulated emission limiting the decay rate. The systematic errors arise from unmeasured variations in parameters which affect the fluorescence or from failings in the predictive nature of the standard steady-state fluorescence models. In low light level PLIF imaging, the primary source of random error is signal shot noise, which is signal level dependent. By comparing the combined errors for the three pumping schemes, the technique with the smallest overall error in a given flowfield can be determined.

In the present comparison, we consider hydroxyl (OH) imaging in turbulent hydrocarbon-air and hydrogen-air flames. Turbulent combustion, which dominates many practical propulsion and energy conversion devices, presents a particularly challenging application for diagnostic methods. In addition, the crucial role played by large organized structures, for example, in controlling mixing and dissipation rates, has recently been recognized. The measurement of instantaneous spatial structures is therefore essential for verifying various combustion models. The OH radical was chosen for this comparison because of its importance in flame chemistry, because of its ability to mark specific regions of the flow, and because it has relatively well-established spectroscopic and collisional data bases. In premixed hydrocarbon flames, quenching of OH varies by less than 10% across regions of significant OH concentration.[3,4] In methane diffusion flames, proper choice of transitions allow uncorrected LIF measurements of OH to be within ±10% of the actual value of the OH concentration near the reaction zone.[5] In other cases, measurement of some parameters, such as temperature and velocity, can be made by taking ratios of fluorescence images in a way that cancels or significantly reduces the collisional quenching dependence.[6,7] It is against this backdrop that other error sources are compared.

Systematic Errors: Scaling Models

As previously detailed, the laser in a typical PLIF measurement causes molecules to be transferred from a specific rotation-vibration energy level in the ground electronic state to another discrete level in a higher energy electronic state. After excitation, various decay processes affect the laser-populated upper state. For example, the molecule can be returned to its original state by (laser-induced) stimulated emission. In addition, inelastic collisions with other molecules produce rotational and vibrational energy transfer, and also electronic energy transfer or quenching. In some cases, dissociation of the molecule can be produced by a "collisionless" transition from a stable to a repulsive electronic arrangement in the molecule,

---

Received March 20, 1992; revision received May 13, 1992; accepted for publication June 5, 1992.

*Research Associate, High Temperature Gasdynamics Laboratory, Department of Mechanical Engineering. Member AIAA.

†Professor, High Temperature Gasdynamics Laboratory, Department of Mechanical Engineering. Senior Member AIAA.

which is known as predissociation. Finally, the originally populated state, and nearby states indirectly populated through collisions, can fluoresce, producing the PLIF signal.

The fluorescence signal is usually modeled by solving a set of rate equations for the populations of the various energy levels of the molecule. The simplest model uses only the two laser-coupled energy levels and is a steady-state solution. The fluorescence equations derived from this model are generally used to interpret PLIF images and to apply corrections owing to systematic effects such as a laser sheet's spatially nonuniform energy profile.

According to this model for a weak (nonperturbing) laser pulse, the total number of photons N_p striking a photodetector from a collection volume V_c imaged onto the detector is[2]

$$N_p = \eta \frac{\Omega}{4\pi} f_1(T)\, n_a V_c B_{12} E_\nu \frac{A_{21}}{A_{21} + Q_{21}} \tag{1}$$

where η is the transmission efficiency of the collection optics, Ω the collection solid angle, $f_1(T)$ the fractional (Boltzmann) population of the lower laser coupled state in the absence of the laser field, n_a the number density of the absorbing species, and E_ν (J cm^{-2} Hz^{-1}) the spectral fluence of the laser. Additionally, it is assumed the fluorescence is emitted equally into 4π sr and the laser spectral width is broad compared to the bandwidth of the molecular transition.

For fully saturated fluorescence, the number of signal photons would instead be given by[2]

$$N_p = \eta \frac{\Omega}{4\pi} f_1(T)\, n_a V_c \Delta t \frac{A_{21}}{1 + g_1/g_2} \tag{2}$$

where g_1 and g_2 are the degeneracies of the two laser coupled levels and Δt is the effective fluorescence integration time. When coupling to the other populated energy levels is considered, the population fraction term in Eq. (2) can approach unity.[8]

Since these equations or similar ones are used to guide conversion of PLIF images to field measurements of flow variables such as concentration or temperature, deviations of the actual signal from these models will typically represent a source of systematic error. The inaccuracies of the standard equations can be estimated by comparing their predictions to the results from a time-dependent numerical solution of the rate equations. We consider the five-level system depicted in Fig. 1. Similar models have been examined to study the difference in saturation effects between molecular systems and atomic systems, for which two-level models are more pertinent.[8,9]

Levels 1 and 2 represent rovibronic states directly coupled by the laser. Level 4 represents a bath of other rotational energy levels in the same vibrational state, which can exchange population with the absorbing level, 1. Likewise, level 3 is the bath for the excited state. Level 5 accounts for predissociated molecules and for molecules which are electronically quenched to vibrational levels other than the bath level 4. It is assumed that vibrational transfer in the ground electronic state is slow, such that none of these molecules return to the absorbing bath during the laser pulse.

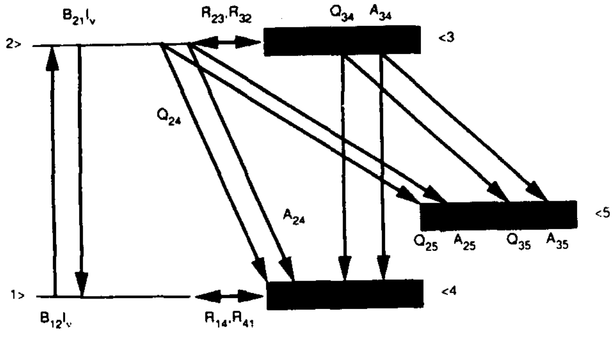

Fig. 1 Energy level schematic for five-level PLIF model, levels 1 and 2 are coupled by the laser, 4 and 3 are their respective bath levels, and level 5 acts as a sink: various processes represented include $B_{ij}I_\nu$, laser *stimulated rates*; Q_{ij}, *collisional quench rates*; A_{ij}, spontaneous emission rates; and R_{ij}, rotational transfer rates.

It must also be noted that the rates R_{41} and R_{32} are not elementary rate coefficients, but depend on the population distribution of the bath, i.e., $n_4 R_{41} = \Sigma n_b r_{b1}$ or $R_{41} = \Sigma f_b r_{b1}$, where r_{b1} is the rate coefficient for collisional transfer from rotational energy level b in the bath and f_b is its relative population. For weak laser pumping and fast rotational transfer, R_{41} and R_{32} closely approach the rates associated with Boltzmann rotational distributions.

Also included in the model is the actual spectral overlap between the laser profile (ϕ_L) and the Doppler-, collision-,[10] and lifetime-broadened absorption profile (ϕ_a) of the molecule, i.e.,

$$g(\nu_L) = \int_{-\infty}^{\infty} \phi_L(\nu, \nu_L)\phi_a(\nu, \nu_a)\, \mathrm{d}\nu \tag{3}$$

where ν_L is the center frequency of the laser and ν_a the center frequency of the molecular absorption transition. For the present comparisons, the laser is modeled with a Gaussian line shape and the molecular absorption transition is given by a Voigt profile. The effect of the overlap integral is to replace the laser stimulated rates, $B_{ij}I_\nu$ (see Fig. 1) by $B_{ij}Ig(\nu_L)$, where I is the total laser intensity. As written, the overlap integral (3) is valid except for inhomogeneous saturation effects.[11]

Random Errors: Noise

The signal-to-noise ratio (SNR) of PLIF images acquired with a typical intensified, solid-state camera system is given by[12]

$$\mathrm{SNR} = \frac{N_p \eta_{pc} G_e}{[N_p \eta_{pc} G_e (G_e K + 1) + N_x^2]^{1/2}} \tag{4}$$

where η_{pc} is the quantum efficiency of the photocathode, G_e the overall electron gain (array detector electrons/photocathode electrons), K a noise factor associated primarily with the electron gain of the intensifier (typically, the lowest value of K for an intensifier is between 1 and 3), and N_x the combined readout, dark and digitization noise of the camera system. The first term in the denominator of Eq. (3) represents the signal shot noise. When the shot-noise term dominates the camera noise term, the signal is shot-noise limited and the SNR is given by

$$\mathrm{SNR} = (N_p \eta_{pc}/K)^{1/2} \tag{5}$$

assuming, as is usually the case, $G_e K \gg 1$.

Laser Pumping Options for OH PLIF

Laser-induced fluorescence of OH is most often performed using the $A^2\Sigma^+ - X^2\Pi(v'' = 0)$ system, with transition wavelengths below approximately 320 nm. For excitation from the $X^2\Pi(v'' = 0)$ state, the (0,0) band has the highest transition probabilities[13] and was used in many of the original PLIF measurements.[14,15] In the absence of collision-induced vibrational excitation in the upper state, practically all of the fluorescence is re-emitted in the (0,0) band. Thus, fluorescence trapping, absorption of the emitted OH fluorescence by other OH molecules, and elastic laser scattering can be problems in some imaging measurements.

Excitation of the (1,0) band near 282 nm combined with detection of the strong (1,1) band near 315 nm has been used to avoid these problems.[15,16] The stimulated absorption coefficient for the (1,0) band (B_{10}) is only slightly lower than that for the (0,0) band, $B_{10}/B_{00} \cong 0.3$. For these approaches, frequency doubled dye lasers are the typical illumination sources. Because of the limited pulse energies (~ 1-30 mJ) available from these sources, the resulting fluorescence measurements are usually considered to fall in the linear fluorescence regime.

The recent introduction of tunable excimer lasers has resulted in new pumping options for OH PLIF. Specifically, commercially available XeCl lasers, which emit near 308 nm, and KrF excimers, operating around 248 nm, provide pulse energies in excess of 100 mJ. With tuning ranges of roughly 1 nm, these two lasers can excite a limited number of OH lines.[17,18] The high pulse energies of the XeCl at 308 nm allow for high signal levels and suggest the potential for saturated fluorescence imaging of the (0,0) band in atmospheric pressure flames.

The more powerful KrF laser permits imaging of OH using the (3,0) band, which has a relatively weak transition probability, $B_{30}/B_{00} \cong 0.006$ (Ref. 13). As with the (1,0) pumping, a significant proportion of the fluorescence occurs in red-shifted vibrational bands, e.g. (3,1), (3,2), and (3,3). Additionally, some of the transitions within the tuning range of the KrF laser have predissociation rates[19] near 10^{10} s^{-1} and may allow quenching-independent PLIF measurements.[20,21] As a potential drawback to predissociated fluorescence measurements, the dissociated O and H atoms will most likely fail to recombine during the short laser pulse (~20 ns), and thus depletion of the ground OH energy levels can occur in the absence of quenching repopulation. Furthermore, interferences from O_2 and H_2O transitions, which can be excited by the KrF laser, as well as photodissociation of water and formation of OH, must be considered.[17,22]

A simple comparison of the expected signal level for these pumping options is illuminating. For the comparison, we consider the following five cases: 1) pumping the $Q_1(5)$ (1,0) line with a pulsed dye laser assuming linear fluorescence; 2) exciting the $Q_1(3)$ (0,0) line with a XeCl laser, assuming linear fluorescence; 3) again exciting the $Q_1(3)$ (0,0) line with a XeCl laser, now assuming saturated fluorescence; 4) pumping the predissociative $P_1(8)$ (3,0) line with a KrF excimer, assuming the steady-state linear fluorescence equation; and 5) also pumping the $P_1(8)$ (3,0) line with a KrF excimer, now assuming enough energy to totally depopulate the ground rotational level with no rotational repopulation. For the (1,0) band, the $Q_1(5)$ line was chosen to obtain good signals without a significant temperature dependence of the Boltzmann population. For the XeCl and KrF options, which can access only a small number of OH lines, the specific rotational lines were chosen based on similar constraints.

Table 1 compares the relative fluorescence, N_p/C, that would be expected for the five pumping options, assuming identical collection optics and detectors. In each case, the temporally integrated fluorescence N_p is proportional to a factor $C = \eta(\Omega/4\pi)\, V_c n_{OH}$, [see Eq. (1)]. Also shown is the shot-noise limited SNR for each approach assuming $\eta = 60\%$, $\Omega/4\pi = 0.0001$ ($f/4$ collection optics for good spatial resolution; imaging an 80-mm high sheet onto an 18-mm intensifier), $V_c = 0.049$ mm^3 (500-μm sheet width and 256×256 pixel array), $n_{OH} = 2.4 \times 10^{16}$ cm^{-3} (0.5% of OH at 1 atm, 1500 K) and $\eta_{pc} = 10\%$. For excitation to $v' = 1$, it is assumed that one-third of the fluorescence comes from the $v' = 0$ state, because of vibrational transfer. For KrF excitation, fluorescence from lower lying vibrational states produced by vibrational transfer from the excited $v' = 3$ (Ref. 17) is omitted, since it would increase the quenching dependence of the fluorescence.

XeCl pumping provides the most intense signals, while the low B coefficient and small fluorescence yield (A/Q) for KrF pumping result in much lower signal levels, even compared to traditional dye laser pumping. The expected KrF signal levels in otherwise identical atmospheric pressure measurements is at least 50 times less than for dye or XeCl pumping.

The fourth column in Table 1, BE_v, is especially noteworthy. In the linear fluorescence limit, BE_v represents the ratio $(\int n_1\, dt)/n_1^0$, the number of times the original population must cycle through level 1 (by quenching or rotational redistribution). In case 1, for example, quenching combined with rotational transfer from nearby rotational levels must effectively resupply the $N = 5$ ($J = 5.5$) state with its original population 16 times. On the other hand, BE_v for XeCl pumping is so large that saturation and possibly bleaching of the ground electronic state are likely.

For predissociative KrF pumping, there is effectively no quenching repopulation. Therefore, signals greater than that possible from the original number of molecules in level 1 can only be achieved by rotational redistribution in the ground levels. Thus, although predissociation has the potential to reduce the dependence of N_p on collisional electronic quenching, the signal can still depend on collisions through rotational transfer in the ground state (and in the upper state, since the predissociation rate in the upper state is also a function of rotational quantum number[19]).

Model Results

The set of rate equations illustrated in Fig. 1 was solved for each of the pumping schemes with a standard ordinary differential equation solver on a personal computer. The flowfield calibration condition is the same one used for the steady-state comparison of Table 1, e.g., 1500 K, 1 atm, 0.5% of OH, total collisional quenching rate Q_e of 0.7×10^9 s^{-1}, with a 80×0.5 mm laser sheet. The laser energies and bandwidths, stimulated rate coefficients, and predissociation rates are also identical to those listed in Table 1. At the calibration conditions, the overlap integrals, Eq. (3), are $g_{dye} = 1.50$ cm, $g_{KrF} = 1.33$ cm and $g_{XeCl} = 1.1$ cm.

Additionally, the rotational transfer rate R_{14} is assumed to be the same as R_{23}, which is 10^{10} s^{-1} for the calibration condi-

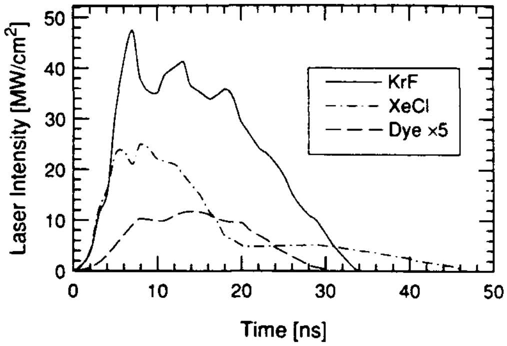

Fig. 2 Temporal profiles for the three pump lasers.

Table 1 Comparison of relative OH fluorescence signals for various pump lasers

Case	Equation for N_p	B, 10^{12} cm^2/Js	BE_v^b	A, $10^6 s^{-1}$	Q $10^9 s^{-1}$	f_b^h, %	N_p/C 10^{-4}/pixel	Shot, SNR[j]
1, Dye	$Cf_1 BE_v\,(A/Q)$	9.7	16[c]	1.0	0.7[f]	3.2	7.4	51
2, XeCl	$Cf_1 BE_v\,(A/Q)$	33	370[d]	1.5	0.7[f]	2.9	230	280
3, XeCl	$C(f_1 \rightarrow 1) A\,\Delta t/2^i$	——[a]	——[a]	1.5	——[a]	2.9	4.4→150	39→230
4, KrF	$Cf_1 BE_v\,(A/Q)$	0.12	4[e]	1.1	11.7[fg]	2.3	0.084	5.4
5, KrF	$Cf_1 A/Q$	——[a]	——[a]	1.1	11.7[fg]	2.3	0.021	2.7

[a] Not applicable. [b] 80-mm × 500-μm sheet. [c] 10 mJ, 15-GHz bandwidth. [d] 100 mJ, 23-GHz bandwidth. [e] 200 mJ, 15-GHz bandwidth. [f] Collisional quench rate in 1 atm H_2-air flame. [g] Predissociation rate[20] of 11×10^9 s^{-1}. [h] 1500 K. [i] Integration time, $\Delta t = 20$ ns laser pulse. [j] $K = 2$.

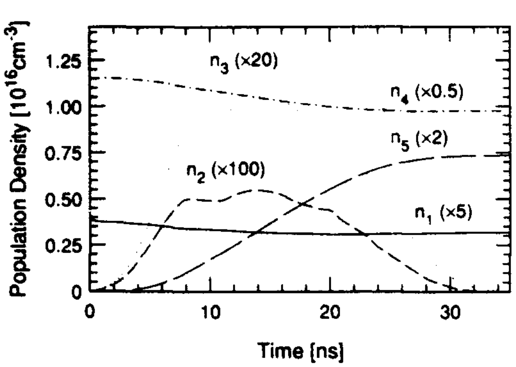

Fig. 3 Temporal development of the population densities for five-level OH model, with 10 mJ of dye laser energy pumping of the $Q_1(5)$ (1,0) line.

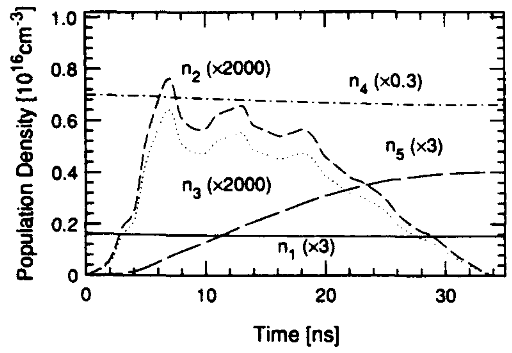

Fig. 4 Temporal development of the five-level model population densities, with a 200 mJ KrF laser pumping the $P_1(8)$ (3,0) line.

tions.[23,24] Finally, the electronic quenching is assumed to be equally divided between transfer to the $v = 0$ bath vibrational level (level 4) and to the other vibrational states, that is $Q_{e4} \equiv Q_{24} = Q_{34}$ and $Q_{e5} \equiv Q_{25} = Q_{35}$ are both $0.35 \times 10^9\ s^{-1}$.

Figure 2 shows the laser temporal profiles used in the calculations. They are measured profiles for Lambda-Physik excimer and excimer-pumped dye lasers. Calculations were also made using the shorter [8 ns full-width at half-maximum (FWHM)] temporal pulse of a Nd:YAG-pumped dye laser and do not significantly vary from the excimer-pumped results presented subsequently. The OH population histories are shown in Figs. 3-5. In all cases, there is some depletion of the laser-pumped level and its bath. For the dye and XeCl pumping, it is produced by quenching to excited vibrational levels, while predissociation plays a key role for KrF pumping. The high laser intensity, large absorption coefficient and assumed quenching ratio ($Q_{e5}/Q_e = ½$) combine to make depletion effects greatest in the XeCl case. In addition, XeCl pumping is unique in that the laser-coupled levels have almost the same population during the peak of the laser pulse, the traditional definition of saturation.

The population histories of the excited levels (2 and 3) illustrate two differences between predissociative pumping and the other approaches. Because of the high-predissociation rate associated with KrF pumping, the population of the laser-excited rotational level exceeds the bath population and produces over 50% of the fluorescence. On the other hand, significant rotational transfer within the upper levels occurs in both of the other cases, with less than 10% of the fluorescence coming from the initially excited rotational level. In terms of the total population of the two levels, or equivalently the total fluorescence, KrF pumping is at least 100 times less effective than the other two approaches, as expected from the steady-state analysis (Table 1).

To test the predictive accuracy of the steady-state models, Eqs. (1) and (2), the time-dependent analysis was carried out for other laser energies, Boltzmann fractions, and pressures. In each case, the rotational transfer rates and quenching ratio (Q_{e5}/Q_e) were also changed to examine their effect on the model results. Both the fluorescence signal $N_p/[\eta(\Omega/4\pi)V_c]$ and the systematic error resulting from the difference between the simple model's scaling predictions and the time-dependent results were calculated. The error in measuring OH concentration associated with a change in a single variable x, e.g., laser energy, is defined by

$$\begin{aligned} \text{error} &= (n_{\text{OH}}^S - n_{\text{OH}})/n_{\text{OH}} \\ &= \left[N_p(x)/N_p(x_{\text{cal}}) \cdot S(x_{\text{cal}})/S(x)\right] - 1 \end{aligned} \tag{6}$$

where n_{OH} is the OH concentration in the volume imaged onto a pixel, n_{OH}^S is the concentration that would be deduced using the simple model to scale the fluorescence from the calibration point, $N_p(x)$ is the fluorescence according to the five-level model, and $S(x)$ is the fluorescence prediction for the simple scaling model. The variable x_{cal} is the calibration value for the variable x at, for example, a point in the flowfield or in another OH source, where conditions are well characterized.

Laser Energy

Figures 6-8 show the effect of laser energy on the fluorescence signal. Some nonlinearities associated with perturbations of the ground state population are seen for all three excitation methods. For the (1,0) dye laser case (Fig. 6), errors as large as 20% are predicted, based on a linear energy dependence. For the calibration conditions, a laser fluence of less than ~10 mJ/cm² (4 mJ for the 80×0.5 mm sheet) would be required to ensure linearity within ±5% down to zero energy. As might be expected, increases in the rotational transfer rate (R) and decreases in the ratio Q_{e5}/Q_e tend to reduce the ground state depletion and extend the linear response regime.

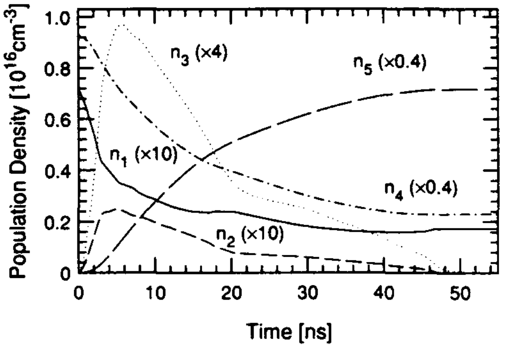

Fig. 5 Temporal development of the five-level model population densities, with 100 mJ of XeCl laser energy pumping the $Q_1(3)$ (0,0) line.

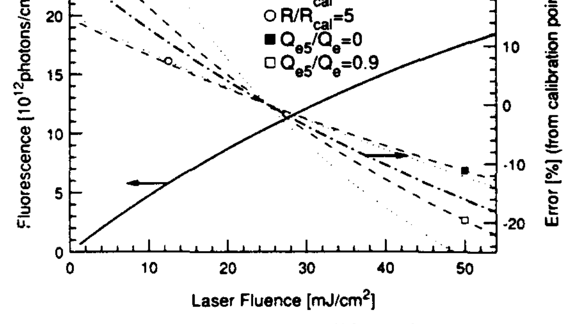

Fig. 6 Variation in the PLIF signal (solid curve) and systematic error (dot-dash curve) with laser energy for dye laser excitation of the $Q_1(5)$ (1,0) line: dotted lines represent error plots for values of R different from the calibration point $10^{10} s^{-1}$; the dashed curves show effects of other electronic quench ratios, $(Q_{e5}/Q_e)_{\text{cal}} = 0.5$.

As evidenced in Fig. 7, the small B coefficients for (3,0) KrF pumping help limit the ground state depletion, such that a linear energy response is maintained within ±5% up to 400 mJ of pump energy. In this case, variations in the quench ratio have a negligible consequence because of the large predissociative rate. Changes in R still affect ground state depletion, however, and thus the linearity of the fluorescence.

Nonlinear behavior is most severe for XeCl pumping of the (0,0) band (Fig. 8). The flatness of the response at high energies is a product of saturation and depletion of the lower bath level. So in Fig. 8, the errors associated with both the linear [Eq. (1)] and saturated [Eq. (2)] fluorescence models are shown. Now, changes in rotational rates have little consequence (and thus are not shown), while the quench ratio has the larger effect. Because saturation is most pronounced at the peak of the laser pulse, temporal gating of the detector from 3 to 15 ns (see Fig. 2) was studied. Whereas the signal is reduced, the shape of the saturation curve and the error values are almost identical to those of Fig. 8. However for the gated case, the error results are more sensitive to variations in R and are comparable to the quench ratio variations shown in Fig. 8.

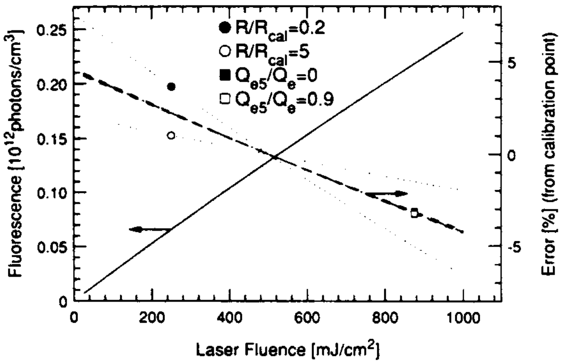

Fig. 7 Variation in PLIF signal with laser energy for KrF laser pumping of the $P_1(8)$ (3,0) line (see Fig. 6 for details).

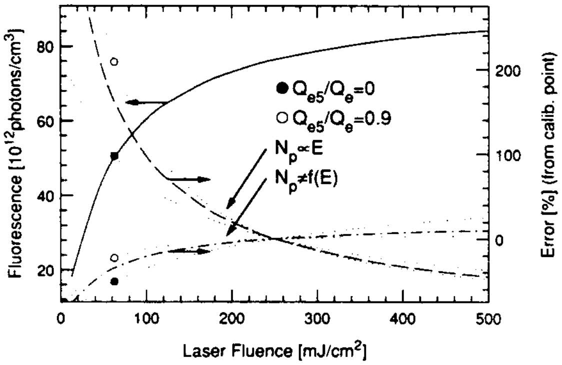

Fig. 8 Variation in PLIF signal with laser energy for XeCl laser excitation of the $Q_1(3)$ (0,0) line: dashed line represents systematic errors associated with the linear model; dot-dashed line is for the saturation model.

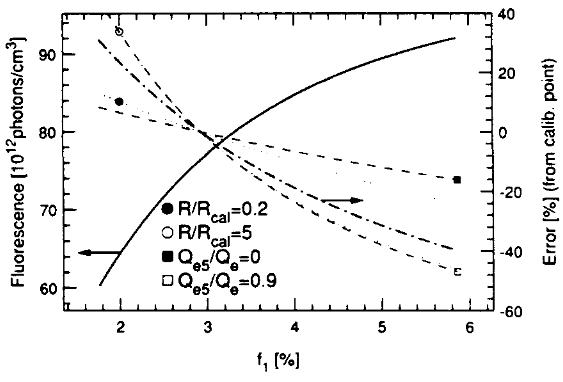

Fig. 9 Variation in the PLIF signal with population fraction of the absorbing state for XeCl laser excitation of the $Q_1(3)$ transition (see Fig. 6 for explanation of the various curves).

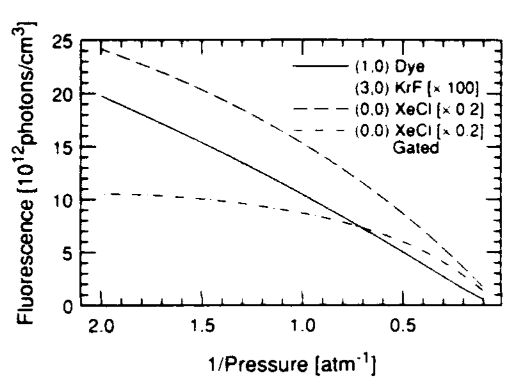

Fig. 10 Variation in OH PLIF signal with pressure for the three pump options; also the result of gating (12 ns) the detector during the peak of the XeCl laser pulse.

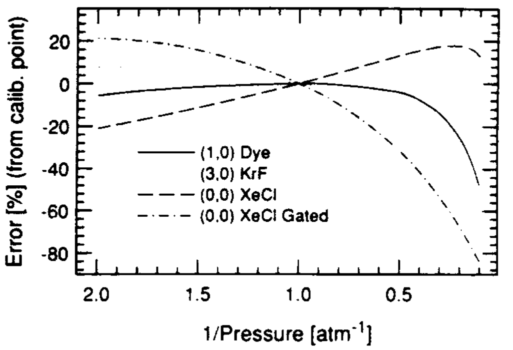

Fig. 11 Systematic errors associated with pressure scaling: $1/P$ scaling for the dye and standard XeCl approaches, pressure-independent scaling for KrF and gated XeCl pumping.

Population Fraction

As evidenced in the population time histories (Figs. 3-5), some ground state depletion occurs with all three pump lasers and is one source of the nonlinear dependence of the fluorescence signal on laser energy. In addition, this depletion produces a nonlinear response to local changes in the absorbing state's population fraction. Within the scope of the present model and its assumption of negligible ground state vibrational transfer, the depletion is truly a function of population fraction, not ground state number density.

Figure 9 illustrates the effect for the XeCl pump laser. The limits on the initial population fraction (f_1) correspond to Boltzmann distributions ranging from 700 to 2500 K. For XeCl pumping, large errors are associated with linearly scaling the fluorescence with respect to initial population fraction. As shown, decreasing the quench ratio or rotational transfer rate reduces the systematic error. Similar calculations for the dye and KrF cases predict errors not larger than ±5%, again for Boltzmann fractions corresponding to a 700-2500 K range.

Pressure

The pressure dependence of the fluorescence can be important for nonisobaric flows. Pressure changes primarily affect the various collision rates and, therefore, quenching, rotational transfer, and collisional broadening. Figure 10 shows the pressure dependence of the PLIF signal for all three pump options, including XeCl pumping combined with the 12-ns time gating. For the dye and standard XeCl pumping, the fluorescence is primarily inversely proportional to pressure. On the other hand, the signal is nearly independent of pressure, below 1-2 atm, for KrF (predissociation) and gated XeCl (saturation) excitation.

The systematic errors associated with these two scaling laws are displayed in Fig. 11. In general, the dye and KrF methods exhibit the smallest scaling errors. For KrF pumping below ~1.6 atm and below ~2.7 atm for dye pumping, the error is less than 10%. Additionally, KrF and (gated) XeCl pumping have the obvious advantage of not requiring a pressure calibration measurement.

Overlap Integral

The isolated effects of the overlap integral are shown in Figs. 12 and 13, based on the Doppler width associated with dye laser excitation of the (1,0) band. Since the Doppler widths (proportional to ν_a) for the XeCl and KrF pumped transitions differ from the (1,0) band by only ~10%, the results shown in the figures also apply in general to these other excitation options. As evidenced in Fig. 12, the overlap integral is sensitive to pressure, especially above 2 atm, but less sensitive for spectrally broader lasers.

Unlike the strong pressure dependence, Fig. 13 shows that the overlap integral varies little over a broad temperature range, for a 0.5-cm^{-1} laser. With more narrow bandwidths, the variations grow. The small change at 1 atm is a result of the counterbalancing effects of Doppler and collision broadening.

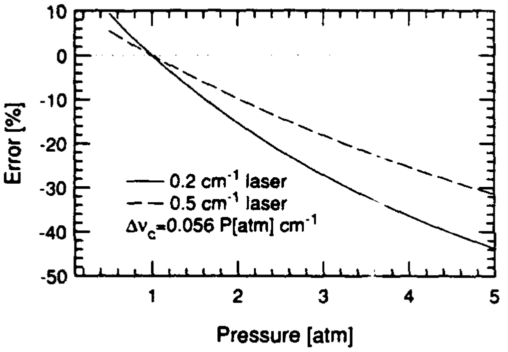

Fig. 12 Pressure-related systematic errors associated with the overlap integral for dye (1,0) excitation at 1800 K, shown for two laser (FWHM) bandwidths ($\Delta\nu_c$ is the collision-broadening width for products of a stoichiometric H_2-air flame[10]).

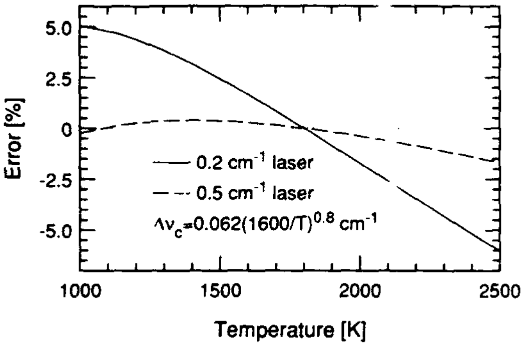

Fig. 13 Temperature-related systematic errors associated with the overlap integral for dye (1,0) excitation at 1 atm (the temperature scaling[10] for $\Delta\nu_c$ is also shown).

At 5 atm, the effect increases to ±10%, for the 0.5-cm^{-1} laser. As an additional error source, consider the pulse-to-pulse variations in laser bandwidth. For ±10% variations in the nominal 0.5-cm^{-1} laser width, the error in OH concentration is ±7% if no corrections are attempted, and the error is ±3% for a $1/\Delta\nu_{las}$ scaling [Eq. (1)].

Summary

A collection of the results is listed in Table 2. Dye laser pumping of the (1,0) band and KrF pumping of the (3,0) band exhibit relatively low systematic errors. XeCl pumping of the (0,0) band involves relatively large errors. The table also includes the random error (1/SNR) for two conditions: the calibration concentration of OH (2.4×10^{16} cm^{-3}, or 5000 ppm at 1500 K and 1 atm) and 10% of this value (500 ppm) to indicate dynamic range limits. As suggested by the earlier analysis (Table 1), XeCl excitation can produce very high signal levels, while single-shot images produced with KrF pumping will contain excessive random errors. Dye pumping provides a reasonable compromise between these two extremes. The errors listed in the table are based on values of $R = 10^{10}$ s^{-1} and $Q_{e5}/Q_e = 0.5$, but variations of R from 0.2 to 5×10^{10} s^{-1} and Q_{e5}/Q_e from 0 to 0.9 do not significantly alter the comparison.

Conclusions

For quantitative OH imaging and the study of large organized structures in turbulent combustion, single-shot imaging with good spatial resolution is required. Under these constraints, dye laser excitation of the (1,0) band of OH appears to be the best approach, compared to XeCl excimer pumping of the (0,0) band and KrF pumping of the (3,0) band. In many of these flames, quench rates appear to vary by less than 10% in regions of significant OH concentration. Nonlinear responses to changes in laser energy, population fraction, and pressure effects related to saturation and depletion are within this range for dye laser excitation of the (1,0) band. To stay within these limits, however, the output of some dye laser systems may have to be reduced below the maximum available energy. Use of a dye laser also allows the greatest flexibility in choosing excitation transitions optimized for a specific flow condition. For example, a line with a lower absorption coefficient can be chosen when laser absorption is a problem. Combined with the excess available laser energy, this can result in no loss of signal.

Because of the extremely low B coefficients for excitation of the (3,0) band, the KrF laser does not significantly perturb the absorbing state population. Even low rotational transfer rates can maintain the population of the laser excited rotational level. Unfortunately, the low fluorescence signals preclude meaningful single-shot images. For situations where only average flowfield data is required, frame averaging many images will significantly reduce the random error.

XeCl excitation produces bright, low-noise images, which permits measurements of large flowfields and application of a number of image processing methods.[18] The increased laser energy available in the XeCl laser, compared to typical dye lasers, is capable of approaching saturation conditions, thus reducing the laser energy and quenching dependences of the fluorescence. The quenching dependence can be further reduced with very fast detector gates. Unfortunately, saturation

Table 2 Systematic and random (noise) errors associated with OH PLIF

Laser	N_p, model	Systematic error, % E^a	f_1^b	P^c	N_p^d ($E_{cal}/2$) photons	SNR^{-1}, % $n_{OH,cal}$ $K=2$	SNR^{-1}, % $n_{OH,cal}/10$ $K=2$
Dye	$\propto Ef_1/P$	±8	±5	±15	17,000	±3.4	±11
KrF	$\propto Ef_1$	±2	±2	±29	190	±32	±100
XeCl	$\propto f_1/P$	±34	±36	±20	190,000	±1.0	±3.2
Gated XeCl	$\propto f_1$	±38	±26	±44	110,000	±1.3	±4.2

[a] $E/E_{cal} = 0.25$-1. [b] $f_1/f_{1,cal}$ for 700-2500 K. [c] $P/P_{cal} = 0.5$-5. [d] Detection constants from Table 1.

combined with depletion makes the fluorescence a nonlinear function of population fraction (f_1). While this obstacle could be reduced by choosing an absorbing rotational level with nearly temperature-independent population fraction, no such transition exists within the limited tuning range of the XeCl laser for temperatures within the range 700–2500 K (or even for more limited ranges such as 1000–2000 K).

For quantitative OH imaging with relatively broadband lasers, uncorrected variations in the spectral overlap integral are a significant source of error at high pressures or when there are large variations in the laser spectral width. In the latter case, corrections can be performed by monitoring the laser linewidth.

There are a number of other aspects of quantitative PLIF imaging which require further examination. These include the effects of rotation-level and vibration-level dependent collision and predissociation rates, laser absorption, fluorescence trapping, and laser-created interferences. For example, the high intensities of ultraviolet excimer lasers can cause damage to "dirty" combustor windows or produce fluorescence of photodissociated hydrocarbon species.

Acknowledgments

This work was supported by the U.S. Air Force Office of Scientific Research, Aerospace Sciences Directorate, with J. Tishkoff as technical monitor. The authors acknowledge the assistance of M. P. Lee.

References

[1] Hanson, R. K., "Combustion Diagnostics: Planar Flowfield Imaging," *Twenty-First Symposium (International) on Combustion*, Combustion Inst., Pittsburgh, PA, 1987, pp. 1677–1691.

[2] Hanson, R. K., Seitzman, J. M., and Paul, P. H., "Planar Laser-Fluorescence Imaging of Combustion Gases," *Applied Physics B*, Vol. 50, No. 6, 1990, pp. 441–454.

[3] Stepowski, D., and Cottereau, M. J., "Study of the Collisional Lifetime of Hydroxyl ($^2\Sigma^+$, $v'=0$) Radicals in Flames by Time-Resolved Laser-Induced Fluorescence," *Combustion and Flame*, Vol. 40, No. 1, 1981, pp. 65–70.

[4] Allen, M. G., "Digital Imaging Techniques for Single- and Multi-Phase Reacting Flowfields," Ph.D. Dissertation, Dept. of Mechanical Engineering, Stanford Univ., Stanford, CA, April 1987.

[5] Barlow, R. S., and Collignon, A., "Linear LIF Measurements of OH in Nonpremixed Methane-Air Flames: When are Quenching Corrections Unnecessary," AIAA Paper 91-0179, Jan. 1991.

[6] Cattolica, R. J., "OH Rotational Temperature From Two-Line Laser-Excited Fluorescence," *Applied Optics*, Vol. 20, No. 7, 1981, pp. 1156–1166.

[7] Hiller, B., and Hanson, R. K., "Simultaneous Planar Measurements of Velocity and Pressure Fields in Gas Flows Using Laser-Induced Fluorescence," *Applied Optics*, Vol. 27, No. 1, 1988, pp. 33–48.

[8] Berg, J. O., and Shackleford, W. L., "Rotational Redistribution Effect on Saturated Laser-Induced Fluorescence," *Applied Optics*, Vol. 18, No. 13, 1979, pp. 2093–2094.

[9] Lucht, R. P., Sweeney, D. W., and Laurendeau, N. M., "Balanced Cross-Rate Model for Saturated Molecular Fluorescence in Flames Using a Nanosecond Pulse Length Laser," *Applied Optics*, Vol. 19, No. 19, 1980, pp. 3295–3300.

[10] Rea, E. C., Jr., "Rapid-Tuning Laser Wavelength Modulation Spectroscopy with Applications in Combustion Diagnostics and OH Line Shape Studies," Ph.D. Dissertation, Dept. of Mechanical Engineering, Stanford Univ., Stanford, CA, Dec. 1990.

[11] Greenstein, H., and Bates, C. W., Jr., "Line-Width and Tuning Effects in Resonant Excitation," *Journal of the Optical Society of America*, Vol. 65, No. 1, 1975, pp. 33–40.

[12] Hanson, R. K., and Seitzman, J. M., "Planar Fluorescence Imaging in Gases," *Experimental Methods for Flows with Combustion*, edited by A. Taylor, Academic Press, London, 1993, Chap. 6.

[13] Chidsley, I. L., and Crosley, D. R., "Calculated Rotational Transition Probabilities for the A-X System of OH," *Journal of Quantitative Spectroscopy and Radiative Transfer*, Vol. 23, No. 2, 1980, pp. 187–189.

[14] Kychakoff, G., Howe, R. D., Hanson, R. K., and McDaniel, J. C., "Quantitative Visualization of Combustion Species in a Plane," *Applied Optics*, Vol. 21, No. 18, 1982, pp. 3225–3227.

[15] Dyer, M. J., and Crosley, D. R., "Two-Dimensional Imaging of OH Laser-Induced Fluorescence in a Flame," *Optics Letters*, Vol. 7, No. 8, 1982, pp. 382–384.

[16] Allen, M. G., and Hanson, R. K., "Digital Imaging of Species Concentration Fields in Spray Flames," *Twenty-First Symposium (International) on Combustion*, Combustion Inst., Pittsburgh, PA, 1987, pp. 1755–1761.

[17] Andresen, P., Bat, A., Gröger, W., Lülf, H. W., Meijer, G., and ter Meulen, J. J., "Laser-Induced Fluorescence with Tunable Excimer Lasers as a Possible Method for Instantaneous Temperature Field Measurements at High Pressures: Checks with an Atmospheric Pressure Flame," *Applied Optics*, Vol. 27, No. 2, 1988, pp. 365–378.

[18] Seitzman, J. M., Üngüt, A., Paul, P. H., and Hanson, R. K., "PLIF Imaging Analysis of OH Structures in a Turbulent Nonpremixed H_2-Air Flame," AIAA Paper 90-0160, Jan. 1990.

[19] Gray, J. A., and Farrow, R. L., "Predissociation Lifetimes of OH $A^2\Sigma^+(v'=3)$ Obtained From Optical-Optical Double-Resonance Linewidth Measurements," *Journal of Chemical Physics*, Vol. 95, No. 10, 1991, pp. 7054–7060.

[20] Massey, G. A., and Lemon, C. J., "Feasibility of Measuring Temperature and Density Fluctuations in Air Using Laser-Induced O_2 Fluorescence," *Journal of Quantum Electronics*, Vol. 20, No. 5, 1984, pp. 454–457.

[21] Lee, M. P., and Hanson, R. K., "Calculations of O_2 Absorption and Fluorescence at Elevated Temperatures for a Broadband Argon Fluoride Laser Source at 193 nm," *Journal of Quantitative Spectroscopy and Radiative Transfer*, Vol. 36, No. 5, 1986, pp. 425–440.

[22] Meijer, G., ter Meulen, J. J., Andresen, P., and Bath, A., "Sensitive Quantum State Selective Detection of H_2O and D_2O by $(2+1)$ Resonance Enhanced Multiphoton Ionization," *Journal of Chemical Physics*, Vol. 85, No. 12, 1986, pp. 6914–6922.

[23] Lucht, R. P., Sweeney, D. W., and Laurendeau, N. M., "Time-Resolved Fluorescence Investigation of Rotational Transfer in $A^2\Sigma^+(v=0)$ OH," *Applied Optics*, Vol. 25, No. 22, 1986, pp. 4086–4095.

[24] Carter, C. D., Salmon, J. T., King, G. B., and Laurendeau, N. M., "Feasibility of Hydroxyl Concentration Measurements by Laser-Saturated Fluorescence in High-Pressure Flames," *Applied Optics*, Vol. 26, No. 21, 1987, pp. 4551–4562.

a reprint from Applied Optics

Continuous wave dye-laser technique for simultaneous, spatially resolved measurements of temperature, pressure, and velocity of NO in an underexpanded free jet

Michael D. Di Rosa, Albert Y. Chang, and Ronald K. Hanson

Gas dynamic quantities within an underexpanded nitrogen free jet, seeded with 0.5% NO, were measured nonintrusively by using an intracavity-doubled, rapid-tuning, cw ring dye laser. The UV beam passed obliquely through the jet axis, and its frequency repetitively scanned across adjacent rotational lines in the NO gamma band near 225 nm at a rate of 4 kHz. Spatially resolved excitation scans were obtained by monitoring the induced broadband fluoresence. Modeling the Doppler-shifted excitation scans with Voigt profiles permitted simultaneous determinations of NO velocity, rotational temperature, and pressure. Zero Doppler shift was referenced to an absorption trace obtained across a static cell and recorded concurrently with the excitation scan. Typically, the measured and predicted axial distributions agreed within 10%. At high Mach numbers there was evidence of rotational freezing of NO.

Key words: NO, velocity, rotational temperature, free jet.

Introduction

In earlier endeavors at our laboratory, the fast-tuning attributes of lead-salt diode lasers were successfully emulated in a cw ring dye laser. These efforts culminated in the refinement of a dual rhomb tuner, which when inserted within a commercially available ring dye laser, enabled seamless, repetitive scans of the $D2$ sodium line (589 nm) at kilohertz rates.[1] The frequency-doubled output of such a modified ring dye laser can attain sweep ranges of 3 wave numbers at sweep repetition rates of several kilohertz.

The qualities of a rapid-tuning dye laser, its narrow linewidth, fast scanning rate, and tunability within the UV, were initially applied to spectroscopic studies of single $A \leftarrow X$ (0, 0) transitions of OH, produced at high temperatures behind reflected shocks within a shock tube.[2,3] Although these studies were necessarily confined to isolated lines, the scan width of ~ 3 cm^{-1} was sufficiently wide to encompass two rotational lines fully, the intensity ratio of which would yield the rotational temperature. To demonstrate this capability, the rapid-tuning technique was later exercised as a fast-sampling temperature diagnostic, probing adjacent OH $A \leftarrow X$ (0, 0) absorption transitions near 306 nm within shock-heated flows[4] and flames.[5]

In principle, spectrally resolving a pair of rotational lines of a constituent species of a flow field admits measurements of velocity and pressure as well as temperature. Gas velocities are quantified by exploiting the Doppler effect, which for nonorthogonal arrangements of the wave and velocity vectors is manifest as a shift in the center line absorption frequency. Modeling the line pair yields values for both the collision width and the intensity ratio from which the pressure and temperature are inferred, respectively. By the use of rapid-tuning, these simultaneous measurements can be repetitively effected on submillisecond time scales, as demonstrated in investigations of first a combustion-driven free jet[6] and then the transient, uniform flow fields generated by a shock tube.[7] In the former investigation, OH transitions near 306 nm were resolved through fluorescence detection, whereas in the latter study these same transitions were monitored in absorption.

Recently, the tunable outputs of cw ring dye lasers were extended further into the UV, to 215 nm, with

---

When this work was performed, all authors were with the Department of Mechanical Engineering, High Temperature Gasdynamics Laboratory, Stanford University, Stanford, California 94305-3032. A. Y. Chang is now with Exxon Research and Engineering Company, Annandale, New Jersey 08801-0998.

Received 20 March 1992.
0003-6935/93/214074-14$06.00/0.

the introduction of barium borate (BBO) crystals to angle-tuned, intracavity doubling.[8] This development was significant, for it broadened the range of species and transitions accessible by the direct outputs of ring dye lasers. Although doubling the laser fundamental extracavity would provide the same wavelengths, substantially lower UV powers would result. Within our laboratory, a cw ring dye laser equipped for intracavity doubling with BBO provides tunable, single-frequency radiation from 210 to 230 nm at milliwatt power levels. A dual rhomb tuner was constructed for this laser,[9] and the rapid-tuning strategy for measurements of high-speed flows was applied to UV transitions of NO (gamma band)[10,11] and O_2 (Schumann–Runge bands).[11] The high-speed, uniform flow fields were produced by incident shocks propagating through a shock tube, and an analysis of the NO data yielded the simultaneous measurements of velocity, rotational temperature, and pressure. These measurements, obtained through the established technique of path-integrated absorption, provided a strong foundation for the current advancement of rapid tuning to laser-induced fluorescence of NO.

Extracting quantitative information by nonintrusively monitoring NO could be useful in a variety of experimental investigations. For example, in hypersonic testing, such capabilities could be applied to studies of wings, inlets, combustors, or other flow fields in which NO is a known constituent. NO (in dilute amounts) is also an appealing seed species because of its chemical and phase stability over a wide range of conditions. Its toxicity and also its oxidation to NO_2 in the presence of O_2 may, however, restrict this particular usage.

Several flow-measurement schemes based on laser-induced fluorescence (LIF) of NO have been demonstrated,[12-15] with all techniques employing high-power pulsed lasers to produce detectable fluorescence yields from either point volumes or two-dimensional sheets. As required of all pulsed LIF methods, the measured quantities were correlated with changes in fluorescence magnitudes. Because fluorescence magnitudes are generally affected by all flow properties, pulsed LIF experiments are often tailored to measure a single flow property such as temperature[12,13,15] or velocity.[14] Multiple flow properties could be measured simultaneously, but not without incurring the complexities of managing multiple pulsed lasers and cameras. Yet, by applying an intracavity-doubled, rapid-tuning ring dye laser, one can obtain spatially resolved measurements of multiple properties through LIF of NO. Because the UV output power of this cw laser is low, probing a planar field, which is common to pulsed LIF techniques, is not practical. However, the application of a rapid-tuning dye laser can return flow measurements at repetition rates of several kilohertz, far exceeding the repetition rates of pulsed lasers.

Reported here is the first demonstration of a strategy in which NO was nonintrusively probed to yield spatially resolved, simultaneous measurements of velocity, temperature, and pressure. In addition, the measurement repetition rate was in excess of 4000 samples/s. The flow field investigated was an underexpanded free jet that flowed a mixture of 0.5% NO in N_2. The UV beam from a frequency-doubled cw ring dye laser, modified for rapid tuning, was directed obliquely through the jet axis; the laser frequency, nominally at 227 nm, swept repetitively over adjacent NO rotational lines chosen for their sensitivity to temperatures present within the jet. Using a single lens and field stop, we collected LIF from a small probe volume along the jet axis to produce excitation scans that were replicas of the absorption profile at the point of fluorescence collection. Modeling single-sweep fluorescence traces with Voigt profiles yielded values for the collision broadening and intensity ratio from which the pressure and temperature were inferred, respectively. Velocity was obtained as well by comparing the Doppler-shifted fluorescence trace to a reference absorption trace obtained across a static cell.

Theory

Linewidths of cw ring dye lasers are typically several megahertz, much narrower than the gigahertz Doppler widths exhibited by UV spectral lines. Under such conditions, attenuation of the laser beam follows the Beer–Lambert relation given by

$$T_\nu = I/I_0 = \exp\left[-\int k_\nu(x)P_{\text{abs}}(x)\mathrm{d}x\right], \tag{1}$$

where the limits of integration are from $x = x_0$ to $x = L > x_0$. In Eq. (1), T_ν is the transmission fraction at frequency ν, I_0 is the laser intensity at location x_0, I is the intensity at location L, P_{abs} is the partial pressure of the absorbing species, and k_ν [cm^{-1} atm^{-1}] is the spectral absorption coefficient evaluated at frequency ν. Assuming a uniform medium reduces Eq. (1) to

$$T_\nu = \exp(-k_\nu P_{\text{abs}} L), \tag{2}$$

where, in this instance, L is the total length of the absorbing medium.

The spectral absorption coefficient is directly proportional to the number density of absorbers and to the value of a frequency-dependent line-shape function, ϕ, through

$$k_\nu = (273\, N_L/T)(\pi e^2/mc^2)F_B(T)f[S/(2J'' + 1)]\phi, \tag{3}$$

where N_L is Loschmidt's number, e and m are the electron charge and mass, c is the speed of light, $F_B(T)$ is the Boltzmann fraction of the absorbing state, f is the oscillator strength for a given rovibronic band, $S/(2J'' + 1)$ is the normalized Hönl–London factor, and ϕ is the line-shape function normalized such that $\int \phi \mathrm{d}\nu = 1$.

In the limit of a small absorbing path, Eqs. (1) and (2) become

$$1 - T_\nu = \Delta I/I_x = k_\nu(x)P_{\mathrm{abs}}(x)\Delta x, \tag{4}$$

where $\Delta I/I_x$ is the fractional absorption, ΔI is the intensity absorbed, I_x is the intensity incident at x, and Δx is the minute path over which the absorption occurs. According to Eq. (4), the power absorbed over Δx is proportional to the incident power and the absorption coefficient. Consequently, the induced fluorescence collected from a small segment of the beam path is also proportional to I_x and $k_\nu(x)$. In total, the signal (S_f) of LIF is expressed by

$$S_f = Ck_\nu(x)P_{\mathrm{abs}}(x)I_x[A/(A + Q)], \tag{5}$$

where the constant C incorporates factors of size of measurement volume, collection efficiency, and spectral sensitivity. The terms A and Q denote, respectively, the total emission and quenching rates unique to the upper-state distribution resulting from a specific excitation. The quantity in brackets is termed the fluorescence yield, which for detection of NO $A \rightarrow X$ in a relatively low-pressure environment of N_2 is nearly unity.

Spectral profiles bear signatures of the environment through their relative magnitudes, shapes, and shifts of center-line frequency. Profiles acquired from a flow can then be analyzed to extract properties such as temperature, pressure, and velocity. As indicated by Eqs. (2) and (5), spectral profiles can be measured by monitoring either the absorption of the laser beam or the fluorescence that it excites. Of the two methods, monitoring fractional absorption is simplest but is limited, being a line-of-sight technique, to measurements of uniform flows. Fluorescence methods, although complicated by considerations of optical access and adequate signal level, do offer improved spatial resolution, realized by collecting and detecting the fluorescence emanating from a small segment of the beam. The size of the probe volume is ideally small compared with the thickness of local gradients within the flow. Though these two methods are configured differently, the analysis of the spectral profile resolved by either proceeds similarly.

Integrating k_ν [Eq. (3)] over frequency leads to an expression for the line intensity of an individual transition. The ratio R of two line intensities from the same vibronic band yields the expression

$$R = (S_a/S_b)\exp[(E_b'' - E_a'')/(\mathbf{k}T)], \tag{6}$$

from which the rotational temperature may be calculated. Subscripts a and b denote the different lines, E_j'' is the ground-state energy from which transition j originates, S_a and S_b are known constants, and $\mathbf{k}$ is the Boltzmann constant. The measured ratio of fluorescence signals induced by two independent absorption transitions likewise yields the intensity ratio through

$$R = \left\{\left[\int (S_f/I_x)\mathrm{d}\nu\right]_a \Big/ \left[\int (S_f/I_x)\mathrm{d}\nu\right]_b\right\} \Big/ \{[A/(A + Q)]_a/[A/(A + Q)]_b\}. \tag{7}$$

The rotational temperature is then determined by connecting Eq. (7) to Eq. (6).

One complication of extracting rotational temperatures from excitation scans is that the ratio of fluorescence yields, i.e., $[A/(A + Q)]_a/[A/(A + Q)]_b$, generally depends on the excitation transitions as well as the gas composition.[5] Possibly compounding this complication are biases, not accounted for in Eq. (7), attributable to radiative trapping or the spectral bandwidth of detection. However, for the case of NO in N_2, neither complication arises. First, the ratio of fluorescence yields reduces to unity either if A and Q are individually identical for all states of the excited vibronic level or if the identical upper-state rotational distribution results following either excitation. For NO in N_2, the latter condition appears likely because rates of rotational energy transfer[16,17] are far greater than those for quenching[18] or spontaneous emission.[19] Then, with fluorescence originating from identical upper-state distributions, the equality of Eqs. (6) and (7) is ensured irrespective of bands of radiative trapping or the spectral bandwidth of detection.

Determining rotational temperature through Eq. (7) requires monitoring the fluorescence induced by two absorption transitions (independent in ground-state energy and separated in frequency) as a function of the narrow-linewidth excitation frequency. Should the two transitions be even slightly overlapped in frequency, establishing the intensity ratio would require proper modeling of ϕ, the line-shape function. Under most circumstances, Voigt profiles adequately represent measured line shapes. This model profile arises from the convolution of Gaussian and Lorentzian profiles that represent line shapes in the limits of pure Doppler broadening and pure collision broadening, respectively. Imposing the normalization condition of $\int \phi \mathrm{d}\nu = 1$ leads to

$$\phi = [2(\ln 2/\pi)^{0.5}/\nu_D]V(y, \mathbf{a}), \tag{8a}$$

where $V(y, \mathbf{a})$ is the Voigt function and y is the normalized frequency of

$$y = 2(\ln 2)^{0.5}(\nu - \nu_0)/\nu_D. \tag{8b}$$

In Eq. (8b), ν_0 is the center-line frequency and ν_D is the FWHM Doppler width defined by

$$\nu_D = 7.16 \times 10^{-7}\nu_0(T\,[\mathrm{K}]/M\,[\mathrm{amu}])^{0.5}. \tag{8c}$$

Also appearing in Eq. (8a) is the Voigt $\mathbf{a}$ parameter,

$$\mathbf{a} = (\ln 2)^{0.5}(\nu_c/\nu_D), \tag{8d}$$

through which the contributions of collision and Doppler broadening are compared in a ratio of FWHM collision width, ν_c, with FWHM Doppler width.

As expressed by Eqs. (8), the Voigt function is controlled by temperature (through ν_D) and **a**. The explicit influence of pressure on the line shape arises when the Voigt **a** is cast in the form of[20]

$$\mathbf{a} = \beta(P/T^n), \qquad (9)$$

where both the constant of proportionality β and n depend on the gas composition. For dilute concentrations of NO in nitrogen, experiments in this laboratory have shown that the Voigt **a** of NO $A \leftarrow X\,(0, 0)$ transitions at 227 nm varies as[21]

$$\mathbf{a} = 6020(P[\text{atm}])/(T[\text{K}])^{1.25} \qquad (10)$$

over the temperature range 295–2700 K.

Using Eqs. (8) and (9), one can infer both the pressure and the temperature from a single Voigt profile.[22] This technique for extracting temperature, however, lacks the sensitivity potentially offered by ratios of temperature-dependent line intensities. In two-line thermometry, a temperature-sensitive line pair is resolved and modeled with Voigt profiles. Their intensity or area ratio then yields the temperature through Eq. (6), and pressure is separately inferred from a relation in the form of Eq. (9). An important advantage of two-line thermometry is that the measured temperature is highly insensitive to appreciable changes (up to 50%) of the Voigt **a** parameter away from its best-fit value.[5] In fact, if the lines constituting the pair do not overlap, the measured rotational temperature is completely independent of the function chosen to represent the observed profiles. This insensitivity of the measured temperature to broadening leads to more accurate estimations of the collision width, and hence to improved measurements of pressure.

Underlying this development, beginning with Eq. (1), is the assumption that the laser intensity does not saturate or even perturb the states defining the absorption transition. In this weak-intensity limit, both the absorption coefficient and the measured linewidth are, to a very good approximation, unaffected by the incident intensity. When resolving line shapes for purposes of determining flow properties, operating in this limit is then necessary for reliable measurements, particularly of pressure that is based on the collision or homogeneous width extracted from a fit to the data. For these experiments, $A \rightarrow X$ fluorescence of NO within the jet was induced by a ~1-mW probe beam loosely focused at the point of fluorescence collection. This focused beam yielded sufficient fluorescence signals yet, as we will explain next, was very moderate in intensity compared with that at which saturation is initiated.

A simplified physical picture and analysis will suffice for qualifying the moderate intensity of the probe beam. In this model the jet fluid, 0.5% NO in N_2, has a bulk velocity of 650 m/s and traverses across a circular region, 200 μm in diameter, defining a slice through the focused 1-mW laser beam. On average, the flow dwells Δt = 200 ns within this region where the intensity I_x is assumed to be uniform at 3.2 W/cm^2. The chosen representative jet velocity of 650 m/s coincides with static properties of 70 K and 0.007 atm.

The laser radiation, nominally at 225 nm, stimulates absorption transitions from level J'' to level J' at a rate constant of $B_{J''J'} I_x$,[23] where $B_{J''J'}$ is the stimulated absorption coefficient and is directly related to the Einstein coefficient $A_{J'J''}$.[24] For NO $A \rightarrow X\,(0, 0)$, the *band* Einstein coefficient A_{00} is approximately 10^6 s^{-1} (Refs. 19 and 25). $A_{J'J''}$ is then assumed equal to A_{00} multiplied by 0.5, a reasonable normalized Hönl–London factor. Relating $A_{J'J''}$ to the line center value of $B_{J''J'}$ yields[24] $B_{J''J'}$ = 7200 s^{-1} W^{-1} cm^2. The rate constant $B_{J''J'} I_x$ for stimulated absorption at line center is then 23,000 s^{-1}. With $B_{J''J'} I_x \times \Delta t \approx 0.005$ the lower level is, at the very most, depopulated 0.5% over the flow's dwell within the laser beam. Given this maximum percentage of depopulation, saturation is of no practical concern. This conclusion was verified through detailed analyses of a more realistic radiative system, patterned after the four-level system of Berg and Shackleford,[26] which also incorporated rates of rotational energy transfer[16,17] and electronic quenching[18] at conditions representative of the current experiment. For frequencies off resonance, the minimal perturbation of the absorbing state diminishes further because $B_{J''J'}$ is a maximum at line center.

Finally, gas velocities are measured by exploiting the Doppler effect that describes a relative shift in the laser frequency between laboratory and particle frames of reference. From the laboratory frame, this effect is perceived as an apparent shift, $\Delta\nu_D$, of the center-line absorption frequency, ν_0, in accordance with

$$\Delta\nu_D = \nu_0(\mathbf{V} \cdot \mathbf{i})/c, \qquad (11)$$

where **V** is the velocity vector and **i** is a unit vector in the direction of the laser beam. Determining the gas velocity thus requires knowledge of both $\Delta\nu_D$ and the beam direction with respect to the velocity. In the plane formed by the beam and velocity vectors, Eq. (11) reduces to

$$V[\text{m/s}] = (\Delta\nu_D\,[\text{GHz}])(\lambda\,[\text{nm}])/(\cos\theta), \qquad (12)$$

where θ is the angle between the two vectors.

In general, both a Doppler and a collision shift, $\Delta\nu_s$, contribute to the total shift of a spectral feature probed within a moving gas. The total shift $\Delta\nu_T$ of the center-line frequency is then

$$\Delta\nu_T = \Delta\nu_D + \Delta\nu_s. \qquad (13)$$

The temperature dependence of collision shifts of NO $A \leftarrow X\,(0, 0)$ transitions was measured previously in this laboratory[21] by using a rapid-tuning ring dye laser. For dilute amounts of NO in N_2, the collision shift exhibited the following dependence,

$$\Delta\nu_s\,[\mathrm{GHz}] = (-130)(P\,[\mathrm{atm}])/(T\,[K])^{0.56}, \quad (14)$$

over the temperature range 295–2700 K. As signified by the minus sign, collisions negatively shift the center-line frequency. For the experiments reported here, the collision shift was a significant fraction, nearly 40% for measurements close to the nozzle exit, of the total shift. In such instances, accounting for the collision shift is imperative for accurate velocity measurements.

Application to Flow Measurements

Rapid tuning provides the capability of yielding spatially resolved, simultaneous measurements of velocity, pressure, and temperature. Data, which result from LIF, are acquired continuously as the laser frequency is repetitively swept over a spectral feature of the probe species at a rate of 4 kHz. The temporal variation of the laser frequency is simultaneously tracked in order to map single-sweep records to a relative frequency scale for analysis. Velocities are measured by comparing center-line frequencies of concurrently scanned Doppler-shifted and reference (i.e., non-Doppler-shifted) features. If these features are recorded from environments dissimilar in static conditions, their separation in frequency could comprise a relative collision shift. Negating the effects of collision shifts can be accomplished by acquiring a reference trace from the flow itself.[7,10,11] However, static gas samples at room temperature provide convenient reference sources, and their use does not compromise the accurate determination of the Doppler shift if the functional dependence of the collision shift is known.

Diagrammed in Fig. 1 is the strategy for determining velocities. The output of the rapid-tuning ring dye laser is set to scan repetitively over a pair of rotational lines suitable for thermometry at conditions present within the flow field. One portion of this output beam is directed through a reference cell, and another, the probe beam, is passed through the flow at an oblique angle with respect to the flow direction. Fluorescence induced by the cw probe beam is collected from a small segment of the beam path, defining the limit of spatial resolution, while the reference feature is simultaneously traced by monitoring the fractional transmission of the reference beam. The acquired fluorescence and reference profiles, jointly resolved by a single sweep in laser frequency, are then fit to Voigt functions through which their respective pressures and temperatures are inferred from Eqs. (10) and (6). Typically, though, the conditions within the reference cell are measured independently. Comparing center-line frequencies of the profiles yields the total shift $\Delta\nu_T$ [Eq. (13)] from which the relative collision-shift contribution is removed by employing Eq. (14). This process exposes the Doppler shift which, through Eq. (12), permits determination of the velocity. In this method, extracting the pressure requires only that the feature be at least partially collision broadened. Effectively measuring the temperature, however, requires a judiciously chosen intensity pair.

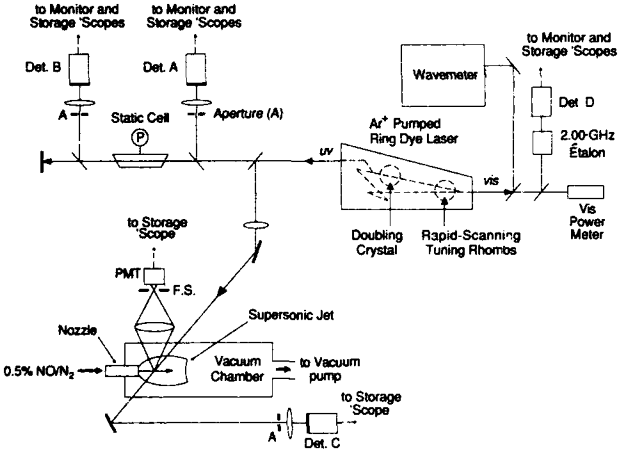

Fig. 1. Experimental schematic for spatially resolved measurements of jet properties. A Doppler-shifted fluorescence trace is recorded simultaneously with the reference-absorption trace. The undoubled laser output is passed through a fixed-length étalon to provide a frequency marker. Det., detector; 'Scopes, oscilloscopes; F.S., field stop; vis, visible.

Selection of Intensity Pairs for Thermometry

Modeling the shape of a single absorption line can yield both pressure and temperature.[22] However, resolving a pair of absorption lines, whose intensity ratio is temperature dependent, potentially offers greater sensitivity to temperature. Criteria for selecting intensity pairs are detailed elsewhere.[5,10] Briefly, the two lines must originate from different ground-state rotational levels but be close enough in frequency for complete coverage by the laser scan. The region scanned should contain only those lines of interest, being free from interfering adjacent lines. Also, the candidate lines should have similar absorption coefficients so that each can be recorded with comparable accuracy and signal-to-noise ratio. Given the rapid-tuning scan width of approximately 80 GHz in the UV and the desirability of resolving individual lines completely but distinctly, the optimal frequency separation of a candidate line pair lies between 15 and 25 GHz. At greater separations, the trailing wings of both lines will be clipped at the scan's limits. With too little separation, the individual lines become obscured in a blended feature.

As we will illustrate in the ensuing discussion, all intensity pairs have finite applicability for purposes of temperature measurements. Candidate NO intensity pairs for use at high temperatures (extending to 4000 K) were previously rated.[10] Because the relevant temperature region for the experiments reported here is 160–60 K, examples will be specific to two-line thermometry at low temperatures.

The applicable temperature range of a candidate line pair is addressed through an analysis of the intensity ratio, facilitated by first recasting Eq. (6) so that R never exceeds unity. The intensity ratio then takes the form

$$R = A\exp(-B/T), \qquad T \le T_{R=1},$$
$$R = A^{-1}\exp(B/T), \qquad T > T_{R=1}, \qquad (15)$$

where B is a positive quantity and $T_{R=1}$ is the temperature (if any) for which R is unity. Expressed in this fashion, R is simply the ratio of the smaller to the larger line intensity. One convenience of this definition is that some quantities, such as the signal-to-noise ratio, need only be quoted for the larger feature because R or $\sqrt{R}$ can scale the quantity to the smaller feature. The sensitivity of this ratio to temperature can be evaluated by differentiating Eq. (15) with respect to temperature, resulting in

$$\mathrm{d}R/\mathrm{d}T = \pm(B/T^2)R, \qquad (16)$$

where the positive sign corresponds to $T \le T_{R=1}$ and the negative sign to $T > T_{R=1}$. A second derivative of Eq. (15) shows that peak sensitivity to temperature occurs at either $T = B/2$ or $T = T_{R=1}$ with the latter resulting if $T_{R=1} < B/2$. Through Eq. (16), candidate line pairs are compared with regard to their range of maximal temperature sensitivity, as possibly bracketed by minimum acceptable values of R.

Finding candidate line pairs for NO thermometry is difficult because the small rotational constant of NO leads to spectra composed of numerous lines closely spaced in both frequency and ground-state energy. Adjacent lines are therefore abundant, but those displaying good temperature sensitivity are few and rarely isolated from interferences. Selecting candidate pairs within the NO spectrum is further complicated by the virtual coincidence of primary Q_1, Q_2, P_2, and R_1 branches with the respective satellite branches P_{21}, R_{12}, Q_{12}, and Q_{21}. (Transition labels are based on ΔJ followed by N'' in parentheses. Subscript 1 refers to an electron spin of +½ and subscript 2 denotes a spin of −½. The appearance of two subscripts signifies a spin flip.) From the standpoint of thermometry, these highly overlapped transitions are of no value by themselves because each paired primary and satellite transition stems from the same lower state. Their spacing is determined from the small upper-state spin-rotation splitting

$$\Delta E = \gamma'(N' + 0.5), \qquad (17)$$

where γ' is the spin-rotation constant, accurately measured to be 80.35 MHz.[27] For an N' of 8 the lines are separated by 0.64 GHz, which is nearly one fifth the Doppler width at room temperature. Also, the magnitude of the satellite branch is comparable with (but always smaller than) the primary transition. Even at high J'', the Hönl–London factors of the satellite branches remain nonnegligible. Therefore, for estimates of broadening parameters, the seemingly single profile should at least be modeled as an additive superimposition of the primary and satellite lines. However, for the current discussion on thermometry, these overlapped lines, which do originate from the same ground state, are considered to constitute a single transition. Equation (15) is then generalized as the ratio of line intensities of two primary features, of which one may be a highly overlapped pair.

An NO $A \leftarrow X$ (0, 0) spectrum was synthesized by the use of procedures described previously[10] and was searched for intensity pairs that met the criteria of adequate separation, relative isolation, and sensitivity to low temperatures. Five candidate low-temperature thermometry pairs, listed in order of increasing wavelength, were located: $R_1 + Q_{21}(4)$, $R_{21}(1)$; $Q_2 + R_{12}(9)$, $R_2(5)$; $Q_2 + R_{12}(8)$, $R_2(4)$; $P_2 + Q_{12}(14)$, $R_2(3)$; and $Q_2 + R_{12}(5)$, $R_2(2)$.

Inclusion of the first pair is conditional because 2 GHz from $R_{21}(1)$ lies an interfering line, $P_1(20)$. Yet at 160 K, the absorption coefficient of $R_{21}(1)$ is greater than that of $P_1(20)$ by a factor of 50. Disregarding this interference at low temperatures would then incur little error.

A portion of the synthesized NO absorption spectrum is shown in Fig. 2 that includes all but one of the five listed thermometry pairs. At the wavelengths of Fig. 2, the scanning range of the rapid-tuning laser is ~0.014 nm. The conditions of 300 K and 0.1 atm are representative of a reference static cell, and all individual lines are modeled by Voigt functions incorporating a collision-broadening parameter estimated from Eqs. (8d) and (10). The variation of R with temperature for candidate intensity pairs $Q_2 + R_{12}(5)$, $R_2(2)$; $Q_2 + R_{12}(8)$, $R_2(4)$; and $P_2 + Q_{12}(14)$, $R_2(3)$ is shown in Fig. 3. Curves of temperature sensitivities for these same candidate pairs are shown in Fig. 4. The omitted candidate pairs of $R_1 + Q_{21}(4)$, $R_{21}(1)$ and $Q_2 + R_{12}(9)$, $R_2(5)$ would, in both figures, exhibit trends closely resembling those of $Q_2 + R_{12}(5)$, $R_2(2)$ and $Q_2 + R_{12}(8)$, $R_2(4)$, respectively. As we see in Fig. 4, the candidate intensity pairs collectively provide a finite sensitivity to temperature ranging 10–250 K. Over the temperature range 50–160 K antic-

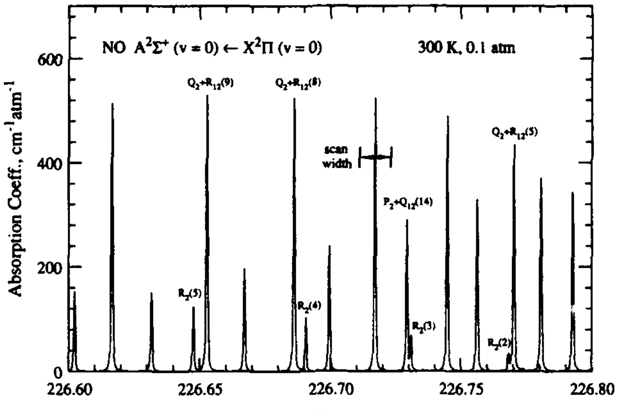

Fig. 2. Calculated NO spectrum at 300 K and 0.1 atm showing four candidate intensity pairs suitable for measurements of low temperatures. The abscissa is the vacuum wavelength.

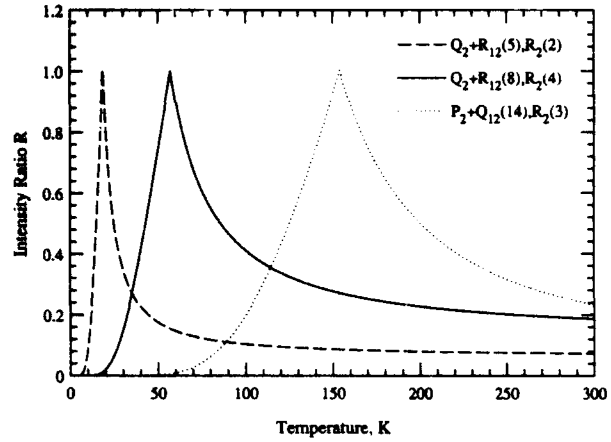

Fig. 3. Intensity ratio versus temperature for three of the candidate low-temperature intensity pairs. The intensity ratio is defined so as not to exceed unity.

ipated for the experiments, line pairs $Q_2 + R_{12}(8)$, $R_2(4)$ and $Q_2 + R_{12}(9)$, $R_2(5)$ possess good temperature sensitivity and remain resolvable with $R > 0.2$.

Laser Modifications

A Coherent 699 ring dye laser was run with stilbene 420 dye and pumped with 5.5 W (all lines UV) from a Coherent Innova 25/5 Ar^+ laser. A custom-built BBO angle-tuned intracavity doubling system was used to obtain approximately 1.2 mW of UV radiation at 227 nm. To permit rapid-tuning operation, the standard étalon assembly was removed and the vertex-mounted Brewster plate located in front of the visible output coupler was replaced by a dual rhomb tuner assembly. The tuner was similar to that used in the modification of a Spectra-Physics 380 laser[1] and consisted of a pair of Brewster-cut fused-silica rhombs mounted on a magnesium platform, which was secured to the shaft of a General Scanning G102 galvanometer. The galvanometer assembly was driven sinusoidally at its resonant frequency of 2.2 kHz, and the resulting changes in the cavity length smoothly and repetitively tuned the laser wavelength 2–3 cm^{-1} in the UV. Tunability and stability of the laser frequency were improved by inserting a 900-GHz uncoated thin étalon in a collimated leg of the cavity. Because line shapes were resolved during both forward and reverse scans in laser frequency, the measurement repetition rate was twice the galvanometer resonant frequency, or 4.4 kHz.

Underexpanded-Jet Flow Facility

The strategy for acquiring spatially resolved, simultaneous measurements of temperature, pressure, and velocity was applied to the flow field of an axisymmetric, underexpanded free jet issuing steadily from a sonic exit into an evacuated chamber. Conditions were controlled such that a barrel shock formed and adjoined a Mach disk several exit diameters downstream of the jet exit. Such jets have been studied extensively[28,29] and are characterized by a supersonic expansion region, which begins at the sonic exit and is interior to the barrel shock and Mach disk. Along the jet axis within this region the flow properties change substantially. For example, within the first two exit diameters, the flow expands to a Mach number of ~4 and a density that is 5% of the density at the exit. Thus, this single flow field provided the opportunity to demonstrate the rapid-tuning technique over a wide range of conditions.

Within the expansion region, the variation of Mach number along the axis of this class of jet can be predicted from the fitting formula of Ashkenas and Sherman[29] and its extrapolation to axial locations less than one nozzle diameter from the exit. As consistent with the development of the fitting formula, the flow within the barrel shock and Mach disk (the location of which may be predicted[29]) is assumed to expand isentropically. Flow properties along the axis can then be estimated through isentropic relations,[30] referencing pertinent stagnation conditions and the predicted Mach number.

The facility, designed similarly to those previously employed by Hiller[31] and by Lee *et al.*,[15] is diagrammed in Fig. 5. The underexpanded jet of dilute NO in N_2 flowed continuously within a test section

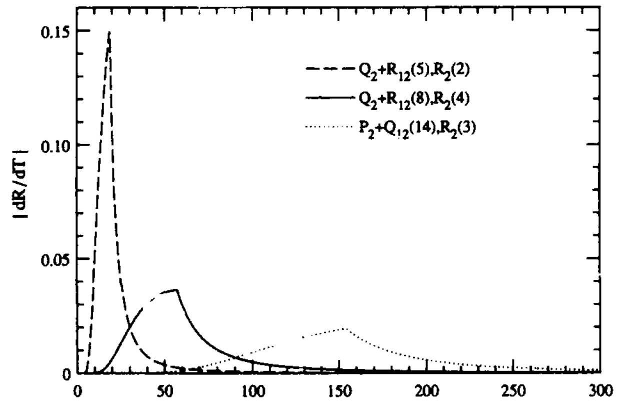

Fig. 4. Temperature sensitivity of the candidate low-temperature intensity pairs of Fig. 3.

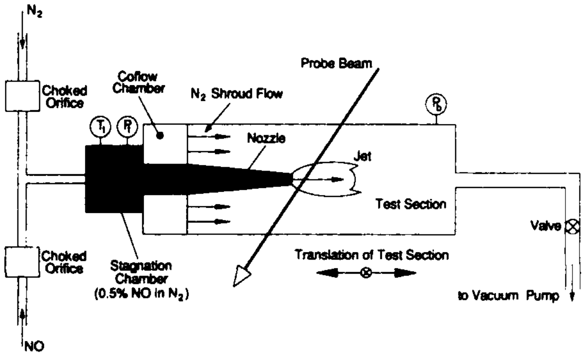

Fig. 5. Schematic of the continuous-flow jet facility. N_2 and NO are metered to yield a 0.5% NO/N_2 mixture. Stagnation and test-section pressures are independently variable and monitored continually. The test section is traversable in both the streamwise and cross-stream directions.

that was maintained at constant vacuum. The overall dimensions of the test section were 10 cm × 10 cm × 27 cm. Recessed in the top and bottom faces were quartz windows (6 mm thick) through which the 227-nm probe beam entered and emerged. Fluorescence was collected through a 7.6-cm^2 fused-silica window mounted on the side of the test section. The test section itself was supported by crossed translation stages lying parallel and perpendicular to the jet axis. These translation stages were beneficial in alignment procedures and provided the means of traversing the free jet in relation to the stationary measurement volume.

N_2 and NO, stored in separate cylinders, were individually metered through choked orifices and then mixed upstream of the stagnation chamber where conditions were monitored with a Heise mechanical pressure gauge and a type-K thermocouple. The individual flow rates were regulated to yield an NO concentration of 0.5%, and the total flow rate was adjusted to maintain a stagnation pressure (P_t) of 1.0 atm. The stagnation temperature (T_t), though not controlled, stabilized near 290 K after 2 minutes of continuous operation. From the 36-mm-i.d. stagnation chamber, the mixture accelerated through a 100.3-mm-long nozzle that was tapered in inside diameter with a half-angle of ~5° from 19.1 mm to the final diameter of 3.13 mm at a point 17 mm before the exit. A straight bore, 3.13 mm i.d., continued out to the nozzle exit. After the nozzle exit, the flow expanded into the test section that was evacuated continuously by a 300-CFM vacuum pump. The test-section pressure, termed the back pressure (P_b), was measured with a 0- to 200-Torr Wallace and Tiernan mechanical pressure gauge. Throttling a valve aft of the test section set the back pressure at 0.046 atm, causing the Mach disk to settle ~9 mm downstream of the nozzle exit. For the stated stagnation conditions, the predicted flow properties along the jet axis varied from 521 m/s, 159 K, and 0.123 atm at $x/D = 0.75$ to 650 m/s, 40 K and, 0.002 atm just before the Mach disk.

An important feature of this facility was the shroud flow of N_2 that displaced NO from regions outside the jet periphery. By employing the shroud we considerably diminished unwanted attenuation of the probe beam, thus improving estimates of the spectral laser intensity incident at the measurement volume. Functionally, the shroud flow of N_2 created an ambient environment that was transparent to 227 nm. As seen in Fig. 5, the shroud flow issued from a separate chamber within the test section. N_2 was ported into the coflow chamber and flowed outward through a sintered copper plate that met the inner walls of the test section and surrounded the base of the nozzle. The sintered plate served to disperse the total flow rate of the shroud uniformly. With a shroud flow rate close to but below the jet flow rate of 1.8 g/s the ambient NO was effectively displaced, as observed by a marked decrease in the overall absorption of the probe beam. Also, as evidenced through schlieren visualization techniques, the shroud did not noticeably perturb the outer structure of the jet.

Experimental Method

The experimental schematic appears in Fig. 1. Spectral features were probed with the frequency-doubled (UV) output of the rapid-tuning ring dye laser, which was set to scan across a particular pair of adjacent rovibronic features within NO $A \leftarrow X$ (0, 0). As shown in Fig. 1, the UV output was divided into two beams. One passed through the reference cell, and the other, the probe beam, was directed through the jet. The cell contained 3 Torr (0.004 atm) of 0.5% NO in N_2 diluent, and the reference absorption feature was monitored by using only 10% of the 1.2-mW UV beam, thus preserving ~1 mW for the probe beam. The signal from detector A indicated the initial laser intensity, while detector B monitored the intensity of the reference beam after it passed through the 19-cm-long cell. The probe beam was angled through the test section at −120° with respect to the jet axis and was focused to ~200 μm at the jet center line by an $f = 30$ cm calcium fluoride lens. Broadband fluorescence induced by the beam was collected by an $f/1$, 5-cm-diameter fused-silica lens positioned 10 cm from the jet axis for 1:1 imaging onto a housing that enclosed a photomultiplier tube (PMT). The axis of fluorescence collection jointly intersected the probe beam and jet axis at right angles to both. An 0.8-mm-diameter field stop secured to the entrance window of the PMT housing limited the length along the beam over which fluorescence was collected. The signal from detector C, which intercepted the probe beam after it transmitted through the test section, was used to account for the small amount the probe beam was absorbed before reaching the measurement volume. Once aligned, the optics were secured in place, and the effective position of the measurement volume was moved along the jet axis by translating the test section.

As diagrammed in Fig. 1, residual outputs of the laser fundamental (visible light) were directed toward instruments, a wavemeter (Burleigh Model WA 20) and a Fabry–Perot 2.00 GHz free spectral range confocal étalon (Spectra-Physics Model 470-2), which gauged the laser's performance. Light passing through the 2.00-GHz étalon was intercepted by detector D, whose signal was a record of the laser tuning rate and longitudinal mode quality. The wavemeter assisted in setting the nominal laser frequency near the desired feature. Ultimately, the correct spectral feature was positively identified by comparing the absorption landscape of the reference trace with synthesized spectra. By slight adjustments of intracavity elements, namely the 900-GHz thin étalon and the angle-tuned doubling crystal, the desired feature and envelope of UV power were centered within the frequency scan.

Detectors A–D were identically constructed, each employing an EG&G Model UV100BQ photodiode in a circuit combining an amplifier and current driver.

Their system response times (0–63% rise times) were matched at 0.35 μs. The PMT was a Hamamatsu R166 solar-blind unit. Its anode was terminated in 3 kΩ through a 1.2-m coaxial cable, yielding a time constant of 0.36 μs that nearly equaled the detector's response time. As dictated by the amount of fluorescence, the voltage applied to the photocathode ranged from −700 V to −1000 V. Signals for the incident intensity and reference absorption were recorded by a four-channel Nicolet Model 4094 oscilloscope employing Model 4570 plug-in amplifiers that sampled at 0.2-μs intervals. The fluorescence and étalon signals, from the PMT and detector D, respectively, were also recorded on the four-channel oscilloscope. A two-channel Nicolet Model 206 oscilloscope, sampling at 0.5 μs/point, recorded signals from detector C that monitored the transmitted intensity of the probe beam. The étalon signal was recorded on the two-channel oscilloscope as well. Both oscilloscopes were triggered by the same pulse, generated manually by switching an external source. Any relative trigger delay between the two oscilloscopes was corrected by referencing the étalon signal recorded on each.

On both oscilloscopes, the data were recorded with 12-bit vertical resolution. The four-channel Nicolet Model 4094, when recording all four channels at a sampling interval of 0.2 μs/point, provided a maximum temporal window of almost 800 μs. Given the laser scanning rate of 4.4 kHz or scan period of 230 μs, this window was sufficiently wide to capture two to three complete sweeps of the spectral feature. All data recorded by the oscilloscopes were transferred to a computer for storage and analysis.

Sample Data and Analysis

Sample raw data, acquired for flow measurements at $x/D = 0.75$, are shown in Fig. 6. These data were obtained with a probe beam angle of −120° with respect to the axial flow direction, and the thermometry pair chosen for this and all other measurements was NO $Q_2 + R_{12}(8)$, $R_2(4)$, centered at 226.69 nm. The top panel of Fig. 6 shows temporal variations in the initial laser intensity (I_0) and also the intensity (I_{cell}) transmitted through the reference cell. For clarity, the I_0 and I_{cell} traces are purposely displaced vertically. Clearly seen in the I_{cell} trace are the reflective scans of $Q_2 + R_{12}(8)$, $R_2(4)$. [The $Q_2 + R_{12}(8)$ feature lies at +26 GHz from $R_2(4)$ and possesses a greater absorption coefficient for all temperatures above 57 K.] The periodicity of I_0 reflects variations in doubling efficiency caused by the laser frequency tuning toward and away from the phase-matched frequency of the stationary doubling crystal.

Shown in the middle panel of Fig. 6 are both the PMT signal (I_{fl}) and the intensity (I_{probe}) of the probe beam after its transmission through the test section. The static pressure at this jet measurement station was ~30 times higher than the cell pressure, and this higher pressure accounts for the larger broadening of the profiles recorded in fluorescence. The bottom panel of Fig. 6 shows the transmission ($I_{\text{étalon}}$) of the visible beam through the 2.00-GHz étalon. The concavity of $I_{\text{étalon}}$ results from the faster tuning rate of the laser in the center of the scan coupled with the finite detector rise time. Each scan comprises 14 peaks over 230 μs, denoting a scan width of 56 GHz in the frequency-doubled UV and a scan rate of 4.4 kHz.

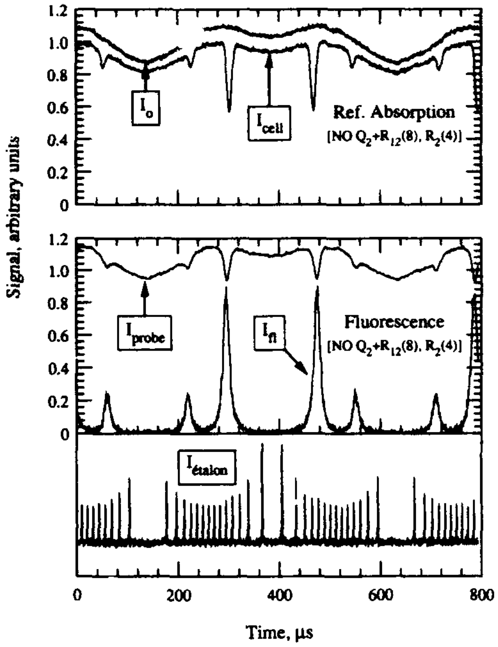

Fig. 6. Raw data trace showing the reference absorption and induced fluorescence traces of $Q_2 + R_{12}(8)$, $R_2(4)$ (near 226.7 nm) obtained for measurements at $x/D = 0.75$ along the jet axis. Predicted, isentropic values at this axial location were $T = 159$ K, $P = 0.123$ atm, $V = 521$ m/s, and $M = 2.03$. The reference cell contained 0.5% NO/N_2 at 0.004 atm and 298 K.

Through Eqs. (2) and (5), the raw data of the second full scan of Fig. 6 were converted to normalized absorption coefficients, producing the reference-absorption and fluorescence profiles of Fig. 7. For both profiles, $Q_2 + R_{12}(8)$ is the larger feature. The

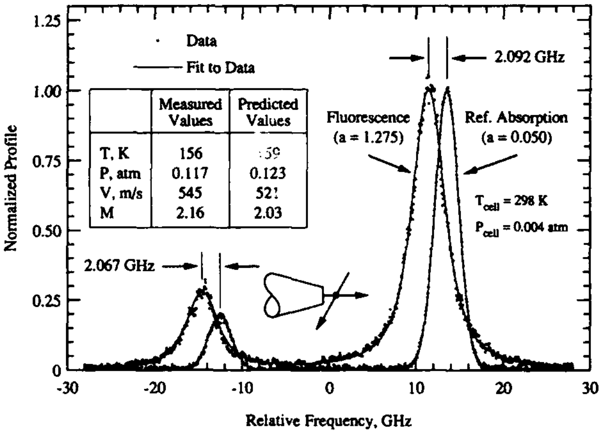

Fig. 7. Reduced single-sweep profile from the data of Fig. 6. Absorption and fluorescence line shapes were fit to Voigt profiles. The flow conditions inferred from these fits are listed. The measured total shift comprised nearly equal Doppler and collision shifts.

abscissa of Fig. 7 is the time base of Fig. 6 converted to a linear frequency scale by using information in the étalon trace. Both profiles were identically offset in relative frequency to establish the arbitrary zero frequency near the center of the scan. On this scale, the greater broadening and expected negative frequency shift of the fluorescence profile, relative to the reference trace, are clearly evident. Because the probe beam in traversing the test section was attenuated by a small amount, the incident intensity used in Eq. (5) was determined from I_0 multiplied by a correction factor that took the form of

$$I_{\text{inc}}/I_0 = (I_{\text{probe}}/I_0)^m, \qquad (m = l/L = 1/2),$$

where L is the total distance traversed by the probe beam through the test section chamber and $l = L/2$ is the distance between the measurement volume and the entry point of the beam into the test section.

The reduced fluorescence profile of Fig. 7 was fit to Voigt functions through an interactive procedure previously described.[10] In short, the procedure sequentially optimized the parameters of center-line frequency, temperature (primarily through the intensity ratio), and Voigt **a**. Optimum values were those that minimized the squared area resulting from the difference between the data and fit. Pressure was inferred by using the best-fit temperature and Voigt **a** in conjunction with Eq. (10). In the fitting process the center-line frequencies of $Q_2(8)$ and $R_2(4)$ were varied independently, but the center-line frequency of the satellite $R_{12}(8)$ was fixed, in accordance with Eq. (17), at −0.683 GHz from $Q_2(8)$. The broadening parameters of $Q_2 + R_{12}(8)$ and $R_2(4)$ were also fit independently. The absorption profile was fit analogously, principally to establish reference (i.e., non-Doppler-shifted) center-line frequencies. Analyses of all single-sweep data followed this same approach.

In total, analyzing the single-scan data of Fig. 7 yielded the (NO rotational) temperature, two measurements of the velocity, and two measurements of the pressure at $x/D = 0.75$. Predicted and measured values, averaged if two, are compared in a table inset to the plot. As seen, the measurements of 156 K and 0.117 atm are both within 5% of their predicted values. The measured total frequency shifts of −2.067 and −2.092 GHz, which would be identical under ideal circumstances, are sums of collision and Doppler shifts. As computed by using Eq. (14), the measured temperature and pressure, and the known cell conditions, the total shifts constitute a significant collision shift (which is known to be J'' independent[21]) of −0.878 GHz. Subtracting this value from each total shift yields an averaged Doppler shift of −1.20 GHz. Through Eq. (12) along with known quantities $\lambda = 226.7$ nm and $\theta = -120°$, this averaged Doppler shift translates to a velocity of 545 m/s, which is within 5% of the predicted velocity. The predicted and measured Mach number, as derived from the measured velocity and temperature, are also in close agreement.

Results and Discussion

Figures 8–11 present the cumulative results of three independent trials (over 3 separate days); for each trial, the optics were realigned and data were recorded for various axial locations downstream of the 3.13-mm-diameter nozzle exit. The measurement range extended from close to the nozzle exit, up to the point where the angled beam was clipped by the nozzle, to beyond the Mach disk. For all three trials, the stagnation and back pressures were maintained at 1.0 and 0.046 atm, respectively, and the stagnation temperature steadied near 290 K. During each trial, the laser frequency scanned continually over the $Q_2+R_{12}(8)$, $R_2(4)$ feature at rates exceeding 4000 scans/s. Single-sweep data were analyzed by using the methods outlined in the previous section.

Each measurement displayed in Figs. 8–11 is an average determined from all single-sweep records, independent of trial number, that were coincident in axial location. Typically, these averaged values comprised the analyses of four to six scans. Vertical error bars represent ±1 standard deviation of the quantity measured at the particular axial location. The positional uncertainty, denoted by the horizontal error bar, for all trials was estimated at ±0.1 exit diameters. The signal-to-noise (S/N) ratio of single-sweep fluorescence signals was limited largely by photon statistics. Because of this dominant noise source, the fluorescence S/N ratio scaled approximately with $n^{0.5}$ where n is the local gas density at the measurement location. At an axial location of 2.6 diameters, where $n \sim 4(10^{17})/\text{cm}^3$, the S/N ratio of single-sweep fluorescence traces was approximately 12. For measurements upstream at 0.75 diameters, where $n \sim 5(10^{18})/\text{cm}^3$, fluorescence traces attained a S/N ratio of ≥ 30.

In Fig. 11, the solid curve represents the algebraic formula of Ashkenas and Sherman,[29] which for $x/D > 1$ accurately fits the variation of center line Mach number as generated by a method-of-characteristics solution. The dotted curve is an extrapolation of this formula back to the nozzle exit ($x/D = 0$) where the sonic condition ($M = 1$) is met. In total,

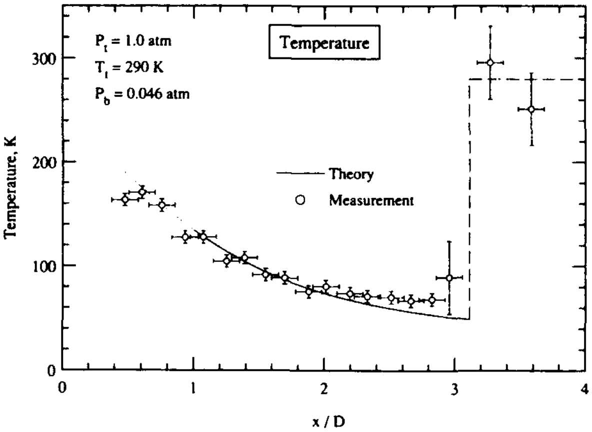

Fig. 8. Comparison of the predicted and measured temperature distributions along the jet axis.

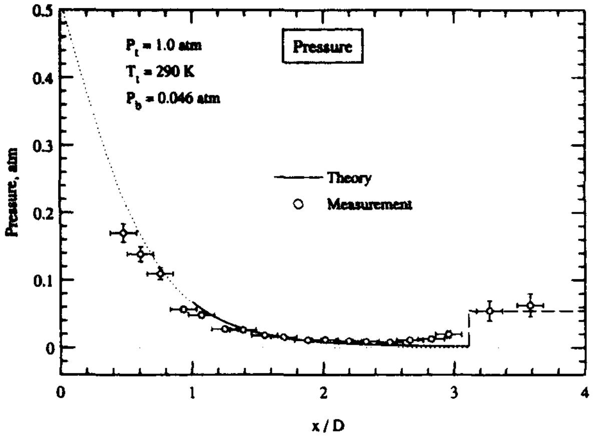

Fig. 9. Comparison of the predicted and measured pressure distributions along the jet axis.

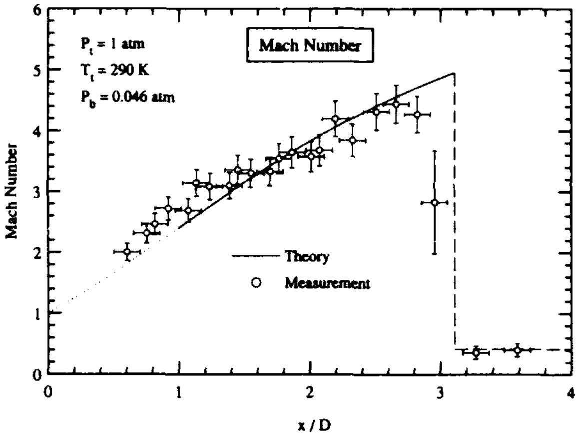

Fig. 11. Comparison of the predicted and measured Mach number distribution along the jet axis. Values of the measured Mach number were derived from the measured temperatures and velocities along with physical constants of the major constituent, N_2. The red- and blue-Doppler-shift velocities of Fig. 10 were averaged if coincident.

the smoothly joined dotted and solid curves of Fig. 11 constitute a prediction of the Mach number distribution along the axis of the expansion region. Concomitant distributions of temperature, pressure, and velocity within this region were generated through the appropriate isentropic relations.[30]

By fitting experimentally obtained data, Ashkenas and Sherman[29] also developed a simple correlation that predicts the axial location of the Mach disk from the stagnation and back pressures alone. The dashed vertical lines seen in Figs. 8–11 are all located at this predicted position. Flow properties after the Mach disk were estimated through relevant normal-shock relations,[30] and these estimated properties define the intersections of the vertical and horizontal dashed lines.

Temperature

Measured and predicted temperatures are compared with each other in Fig. 8. Except for the region near the Mach disk, the standard deviation of the measured temperatures is approximately constant at ±6 K. In the vicinity and downstream of the Mach disk, the greatly increased standard deviations (±35 K) in the measured temperatures can be partly attributed to small, positional oscillations of the Mach disk. Augmenting the standard deviations downstream of the Mach disk is also the relative insensitivity, as seen in Figs. 3 and 4, of Q_2 + $R_{12}(8)$, $R_2(4)$ to elevated temperatures.

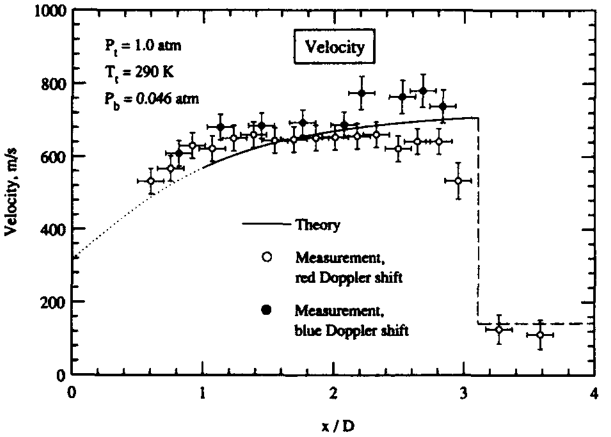

Fig. 10. Comparison of the predicted and measured axial velocity distributions along the jet center line. Red-Doppler-shift data refer to trials for which the component beam direction opposed the center-line velocity. Blue-Doppler-shift data were obtained with the component beam direction aligned with the center-line velocity.

From the furthest upstream measurement station to an x/D of 2, where the predicted temperature is 74 K, the measured and predicted values agree quite closely. On average, however, the measured temperatures in this region are slightly below the predicted curve. Also, the occurrence of the Mach disk, identified experimentally by the sudden onset of increased temperatures and standard deviations, is slightly upstream of its predicted position. These small deviations are known to arise from influences of the nozzle's internal geometry on the transonic region and are often corrected by assigning an effective origin location and exit diameter.[29,32]

Within the expansion beyond $x/D = 2$, the measured rotational temperatures of NO systematically depart from the isentropic temperature curve by values greater than the measurement standard deviation. Apparently, the measured rotational temperatures level off or freeze near 70 K while the isentropic temperature approaches 55 K at $x/D = 2.8$, the last measurement station before the Mach disk.

A similar underexpanded jet was investigated by Lee *et al.*,[15] who applied planar LIF of NO to measurements of rotational temperature along the axis of an NO–air jet. The rotational lines employed for thermometry were NO $A \leftarrow X$ $P_1(3)$ and $R_{21}(0)$ near 226 nm. The analysis of the data by Lee *et al.* yielded a variation of averaged rotational temperature that paired well with the isentropic temperature from 100 to 30 K, which was the temperature just upstream of the Mach disk. Rotational freezing was, therefore, not observed.

Apart from the diagnostic techniques, an important difference between the experiments of Lee *et al.*[15] and those reported here lies with the particular J'' states chosen for thermometry. The observations of Marrone[33] suggest that depopulation of higher J'', states, such as those used for this experiment, may gradually diminish and eventually cease over the course of a rapid expansion. In other words, the higher J'' states may become overpopulated while the lower-lying J'' states, such as those utilized by Lee *et al.*,[15] maintain populations commensurate with the kinetic temperature. The development of such a non-Boltzmann rotational energy distribution could then explain the absence of rotational freezing in the results presented by Lee *et al.*[15] and its occurrence in Fig. 8.

Pressure

In Fig. 9 the measured and predicted pressures are compared with each other. For most of the data, the standard deviation is practically a constant percentage, 8%, of the measured value. Near the Mach disk, however, this percentage deviation increases to 27%. In total, the measured pressures agree reasonably well with predicted values both upstream and downstream of the Mach disk. Like the measured temperatures, the measured pressures locate the Mach disk slightly upstream of the predicted position. Also, for $x/D \leq 1.2$, the measured pressures are displaced from predicted values in the same direction as seen for the measured temperatures. Understandably, this departure of measured from predicted values is more pronounced in Fig. 9 as a result of the steeper initial decline of the pressure. This trend in the measurements for $x/D \leq 1.2$ along with the measured location of the Mach disk are consistent with an effective origin located 0.1 diameter upstream of the nozzle exit.

Between an x/D of 2.2 and the Mach disk location (x_M/D), the absolute discrepancy between the measured and predicted distributions was quite small, although the measured pressures were systematically high by often a factor of 3 or more. This departure from measured values occurred because the fluorescence profiles acquired within this region were collision broadened significantly more than Eq. (10) would suggest. Also in this region, the collision broadening of $Q_2 + R_{12}(8)$ was systematically greater than the collision broadening of $R_2(4)$, and both profiles became noticeably asymmetric with slightly extended tails on the low-frequency side.

Issues of laser saturation, transit-time broadening, and polymerization were considered for explaining the coincident departures of collision broadening and rotational temperatures from predicted values. None of these explanations, however, was found plausible. As we discussed in the theory section, the laser intensity exciting fluorescence was very moderate, and transit-time broadening contributed at most an insignificant 1 MHz to the linewidth. Polymerization, as initiated by a phase change, of either NO or N_2 in this region was unlikely because the static pressure was far below their respective triple-point pressures of 0.216 atm (Ref. 34) and 0.124 atm.[35] Although NO dimers may form at temperatures below 120 K,[36] their presence probably did not measurably affect the collision broadening because NO itself constituted only 0.5% of the flow. However, the process of forming dimers, or possibly the chance interference of a dimer transition, could have influenced the measured broadening or imparted the observed slight asymmetry. Still, the broadening may not have been anomalously large, in which case the overestimations of pressure within $2.2 \leq x/D < x_M/D$ stemmed simply from extrapolating Eq. (10) to temperatures well below 295 K.

Aside from their puzzling origin, these small, systematic offsets in pressure should bias the measured velocities in a predictable manner. For example, at $x/D = 2.7$ the isentropic conditions are 0.003 atm and 56 K, whereas the measured conditions are 0.011 atm and 67 K. Assuming Eq. (14) is applicable at low temperatures, these paired values yield relative collision shifts (with reference to the collision shift imparted by the cell conditions) of −0.044 and −0.140 GHz, respectively. Using the measured pressure then yields an overestimation of the actual collision-shift magnitude by ~0.1 GHz. In turn, the measured velocity magnitude, calculated from the Doppler shift relation, would incur an absolute error of 45 m/s.

Velocity

For one of the three separate trials, flow measurements were obtained with the beam directed at −60° instead of −120° with respect to the jet axis. Distinguishing these trials, which yielded equivalent results for temperatures and pressures, was unnecessary prior to this section. With the beam directed at −120°, as depicted in Figs. 1 and 5, a component direction of the probe beam opposes the axial velocity. In this arrangement, the Doppler shift is toward lower frequencies or toward the red. Conversely, for a beam direction of −60°, the Doppler shift (viewed from the laboratory frame of reference) is toward higher frequencies or toward the blue. Velocity measurements resulting from these symmetrically opposed beam directions are compared with predicted values in Fig. 10. Excluding regions near the Mach disk, the standard deviation of the measured velocities is nearly constant at ±35 m/s. Near and after the Mach disk, the standard deviation increases to ±45 m/s. In concordance with Figs. 8 and 9, an effective origin located upstream of the exit by 0.1 diameters would account for the small but systematic discrepancy between the measured and predicted velocity distributions in the region $x/D \leq 1.2$.

From $0.6 < x/D \leq 2$, the velocities extracted from the blue- and red-Doppler-shift data practically overlap and agree fairly well with the predicted distribution. Yet at $x/D = 2.2$, the measured velocities bifurcate almost symmetrically about the theoretical curve with the red-Doppler-shift data diverging toward lower values. On average, the two velocity sets are separated by 100 m/s over the region of $2.2 \leq x/D < x_M/D$. As noted from the previous section, this same region is coincident with slight overestimations of the relative collision shift, originating from overestimations of the measured pressure, that could impart absolute velocity errors of ~ 45 m/s. Because the relative collision shift is toward the red and overestimated, velocities computed from red-Doppler-shift data would be in error by −45 m/s. Conversely, velocities obtained from blue-Doppler-shift data would err by +45 m/s. The region of velocity bifurcation in Fig. 10 thus supports the estimates of the previous section. Fundamentally, this accord justifies extrapolating the model for collision shifts [Eq. (14)] of NO by N_2 to low temperatures.

Mach Number

The independent measurements of velocity and temperature were combined to yield the measured Mach number through $M = V/(\gamma RT)^{0.5}$, where V and T are the velocity and temperature, γ is the ratio of specific heats ($\gamma = 1.4$ for N_2 at room temperature and below), and R is the gas constant specific to N_2. For $x/D > 2$, blue- and red-Doppler-shift velocities of Fig. 10 were averaged when coincident in axial location. As seen in Fig. 11, the measured variation of Mach number closely matches the predicted values over the entire expansion as well as after the Mach disk. Again, the results are consistent with an effective source located upstream of the nozzle exit. The slight departure, seen between an x/D of 2 and the Mach disk, of the measured Mach number to values below the theoretical curve is ascribed to the elevated rotational temperatures measured within this same range.

Conclusions

An intracavity-doubled cw dye laser can provide milliwatt levels of laser output at 225 nm. Modifying the laser for rapid tuning permits scanning the UV frequency several wave numbers at a repetition rate of 4 kHz. With these combined capabilities, the laser can fully resolve absorption features in the NO gamma band. Simultaneous measurements of flow properties are effected by modeling the acquired absorption features with Voigt profiles. Spatially resolved, simultaneous measurements are achievable by monitoring the induced fluorescence. Rotational temperature is measured by recording adjacent features that differ appropriately in ground-state energy. For NO, candidate features suitable for two-line thermometry over the low-temperature region of 10–250 K have been identified. Pressure is inferred from the measured collision width in conjunction with relations, developed from measurements performed in this laboratory, for the broadening of NO by various species. Measuring the frequency displacement between two simultaneously recorded profiles, of which one exhibits a Doppler shift, yields the flow velocity. If the recorded profiles are obtained from regions disparate in static properties, then accounting for a collision shift in the total frequency displacement is essential for accurate velocity measurements.

This rapid-tuning technique was applied to spatially resolved measurements of temperature, pressure, and velocity along the axis of an underexpanded free jet. Over the region probed within the expansion, the predicted temperature, pressure, velocity, and Mach number varied from 170 K, 0.2 atm, 480 m/s, and $M = 2$ to 55 K, 0.003 atm, 650 m/s, and $M = 4.4$. Overall, the agreement between single-sweep measurements and predicted values, as computed from isentropic relations, was typically within 10%. Comparisons between the measured and predicted distributions consistently signified an effective jet origin, a manifestation of nonidealities of the nozzle, that was slightly upstream of the nozzle exit by 0.1 exit diameters. With theoretical distributions originating from this effective jet exit location, the overall agreement would be further improved.

Between an x/D of 2 and the Mach disk location at $x/D = 2.8$, the measured rotational temperatures systematicallly departed from the predicted isentropic temperature. This departure could be attributed to freezing of the ground rotational states that were probed. Possibly, a non-Boltzmann distribution developed wherein rotational states lying lower in energy than those probed maintained populations commensurate with the kinetic temperature. Also within this region, the measured pressures were slightly greater than the isentropic values, primarily because the fluorescence line shapes were broader than predicted. The consequent overestimations in the collision shift biased the measured velocities, emphasizing the importance of accounting for collision shifts when basing velocity measurements on Doppler shifts of spectral features. Further research is needed to determine whether the coincident departures of broadening and rotational temperatures from predicted values were interrelated.

In all, the results presented here underscore the versatility and effectiveness of diagnostic techniques based on spectrally resolving line shapes with rapid-tuning, narrow-linewidth lasers. Applications of these lasers can yield simultaneous, spatially resolved measurements of flow parameters as well as the spectroscopic database required for the measurements' success. Future progressions of the NO fluorescence technique will include measurements, at kilohertz repetition rates, of two velocity components at a point within the jet.

This research was supported by the U.S. Air Force Office of Scientific Research and the NASA Ames Research Center. The authors thank D. F. Davidson for his guidance and assistance.

References and Notes

1. E. C. Rea, Jr., and R. K. Hanson, "Rapid extended range tuning of single-mode ring dye lasers," Appl. Opt. **22,** 518–520 (1983).
2. E. C. Rea, Jr., S. Salimian, and R. K. Hanson, "Rapid-tuning frequency-doubled ring dye laser for high resolution absorption spectroscopy in shock-heated gases," Appl. Opt. **23,** 1691–1694 (1984).
3. E. C. Rea, Jr., A. Y. Chang, and R. K. Hanson, "Shock-tube study of pressure broadening of the $A\,^2\Sigma^+ - X\,^2\Pi(0, 0)$ band of OH by Ar and N_2," J. Quant. Spectrosc. Radiat. Transfer **37,** 117–127 (1986).
4. A. Y. Chang, E. C. Rea, Jr., and R. K. Hanson, "Temperature measurements in shock tubes using a laser-based absorption technique," Appl. Opt. **26,** 885–891 (1987).
5. E. C. Rea, Jr., and R. K. Hanson, "Rapid laser-wavelength modulation spectroscopy used as a fast temperature measurement technique in hydrocarbon combustion," Appl. Opt. **27,** 4454–4464 (1988).
6. A. Y. Chang, B. E. Battles, and R. K. Hanson, "Simultaneous measurements of velocity, temperature and pressure using rapid cw wavelength-modulation laser-induced fluorescence of OH," Opt. Lett. **15,** 706–708 (1990).
7. D. F. Davidson, A. Y. Chang, M. D. Di Rosa, and R. K. Hanson, "CW laser absorption techniques for gasdynamic measurements in supersonic flows," Appl. Opt. **30,** 2598–2608 (1991).
8. T. F. Johnston, Jr., and T. J. Johnston, "Tunable single frequency 215–235 nm radiation by barium borate intracavity doubling in the stilbene-3 ring dye laser," in *Conference on Lasers and Electro-Optics,* Vol. 11 of 1989 OSA Technical Digest Series (Optical Society of America, Washington, D.C., 1989), paper FE5.
9. A. Y. Chang, "Rapid-tuning continuous-wave laser technique applied to nitric oxide spectroscopy and flow measurements," Ph.D. dissertation (Stanford University, Stanford, Calif., 1991).
10. A. Y. Chang, M. D. Di Rosa, D. F. Davidson, and R. K. Hanson, "Rapid-tuning cw laser technique for measurements of gas velocity, temperature, pressure, density and mass flux using NO," Appl. Opt. **30,** 3011–3022 (1991).
11. M. D. Di Rosa, A. Y. Chang, D. F. Davidson, and R. K. Hanson, "CW laser strategies for multi-parameter measurements of high speed flows containing either NO or O_2," presented at the AIAA Twenty-Ninth Aerospace Sciences Meeting, Reno, Nevada, 1991.
12. J. M. Seitzman, G. Kychakoff, and R. K. Hanson, "Instantaneous temperature field measurements using planar laser-induced fluorescence," Opt. Lett. **10,** 439–441 (1985).
13. K. P. Gross and R. L. McKenzie, "Measurements of fluctuating temperatures in a supersonic turbulent flow using laser-induced fluorescence," AIAA J. **23,** 1932–1936 (1985).
14. P. H. Paul, M. P. Lee, and R. K. Hanson, "Molecular velocity imaging of supersonic flows using pulsed planar laser-induced fluorescence of NO," Opt. Lett. **14,** 417–419 (1989).
15. M. P. Lee, B. K. McMillin, and R. K. Hanson, "Temperature measurements in gases using planar laser-induced fluorescence imaging of NO," Appl. Opt. (to be published). The jet flow-facility used in these experiments is detailed further in M. P. Lee, "Temperature measurements in gases using planar laser-induced fluorescence imaging of NO and O_2," Ph.D. dissertation (Stanford University, Stanford, Calif., 1991).
16. T. Ebata, Y. Anezaki, M. Fuji, N. Mikami, and M. Ito, "Rotational energy transfer in NO ($A\,^2\Sigma^+$, $v = 0$ and 1) studied by two-color double-resonance spectroscopy," Chem. Phys. **84,** 151–157 (1984).
17. W. G. Mallard, J. H. Miller, and K. C. Smyth, "Resonantly enhanced two-photon photoionization of NO in an atmospheric flame," J. Chem. Phys. **76,** 3483–3492 (1982).
18. G. A. Raiche and D. R. Crosley, "Temperature dependent quenching of the $A\,^2\Sigma^+$ and $B\,^2\Pi$ states of NO," J. Chem. Phys. **92,** 5211–5217 (1990).
19. C. O. Laux and C. H. Kruger, "Arrays of radiative transition probabilities for the N_2 first and second positive, NO beta and gamma, N_2^+ first negative, and O_2 Schumann–Runge band systems," J. Quant. Spectrosc. Radiat. Transfer **48,** 9–24 (1992).
20. I. I. Sobel'man, L. A. Vainshtein, and E. A. Yukov, *Excitation of Atoms and Broadening of Spectral Lines* (Springer-Verlag, Berlin, 1981), Chap. 7, pp. 241–253.
21. A. Y. Chang, M. D. Di Rosa, and R. K. Hanson, "Temperature dependence of collision broadening and shift in the NO $A \leftarrow X$ (0, 0) band in the presence of argon and nitrogen," J. Quant. Spectrosc. Radiat. Transfer **47,** 375–390 (1992).
22. S. Cheng, M. Zimmermann, and R. B. Miles, "Supersonic-nitrogen flow-field measurements with the resonant Doppler velocimeter," Appl. Phys. Lett. **43,** 143–145 (1983).
23. W. Demtröder, *Laser Spectroscopy* (Springer-Verlag, Berlin, 1982), Chap. 2, p. 43.
24. R. C. Hilborn, "Einstein coefficients, cross sections, *f* values, dipole moments, and all that," Am. J. Phys. **50,** 982–986 (1982).
25. L. G. Piper and L. M. Cowles, "Einstein coefficients and transition moment variation for the NO ($A\,^2\Sigma^+ - X\,^2\Pi$) transition," J. Chem. Phys. **85,** 2419–2422 (1986).
26. J. O. Berg and W. L. Shackleford, "Rotational redistribution effect on saturated laser-induced fluorescence," Appl. Opt. **18,** 2093–2094 (1979).
27. A. Timmermann and R. Wallenstein, "Doppler-free two-photon excitation of nitric oxide with frequency-stabilized cw dye laser radiation," Opt. Commun. **39,** 239–242 (1981).
28. R. Ladenburg, C. C. Van Voorhis, and J. Winckler, "Interferometric studies of faster than sound phenomena. Part II. analysis of supersonic air jets," Phys. Rev. **76,** 662–677 (1949).
29. H. Ashkenas and F. S. Sherman, "The structure and utilization of supersonic free jets in low density wind tunnels," in *Rarefied Gasdynamics,* J. H. de Leeuw, ed. (Academic, New York 1966), Vol. 2, Suppl. 3, pp. 84–105.
30. R. D. Zucker, *Fundamentals of Gas Dynamics* (Matrix, Beaverton, Ore., 1977), Chap. 4, p. 100; Chap. 6, pp. 151–155.
31. B. Hiller, "Combined planar measurements of velocity and pressure fields in compressible gas flows using laser-induced fluorescence," Ph.D. dissertation (Stanford University, Stanford, Calif., 1986).
32. H. R. Murphy and D. R. Miller, "Effects of nozzle geometry on kinetics in free-jet expansions," J. Phys. Chem. **88,** 4474–4478 (1984).
33. P. V. Marrone, "Temperature and density measurements in free jets and shock waves," Phys. Fluids **10,** 521–538 (1967).
34. H. L. Johnston and W. F. Giauque, "The heat capacity of nitric oxide from 14 °K. to the boiling point and the heat of vaporization. Vapor pressures of solid and liquid phases. The entropy from spectroscopic data," J. Am. Chem. Soc. **51,** 3194–3214 (1929).
35. G. J. Van Wylen and R. E. Sontag, *Fundamentals of Classical Thermodynamics,* 3rd ed. (Wiley, New York, 1985), Chap. 3, p. 37.
36. C. E. Dinerman and G. E. Ewing, "Infrared spectrum, structure, and heat of formation of gaseous $(NO)_2{}^*$," J. Chem. Phys. **53,** 626–631 (1970).

Degenerate four-wave mixing temperature measurements in a flame

B. Yip, P. M. Danehy, and R. K. Hanson

High Temperature Gasdynamics Laboratory, Stanford University, Stanford, California 94305

Received December 2, 1991

Multiplex degenerate four-wave mixing is performed by using OH radicals in an atmospheric-pressure hydrogen–oxygen flame. The ratio of the signal intensities from two OH transitions simultaneously pumped by a single laser pulse is used to determine the local instantaneous flame temperature.

Resonant degenerate four-wave mixing[1,2] (DFWM) in gases has recently generated interest as a laser-based optical diagnostic technique that offers the advantages of remote signal detection and species specificity. Because DFWM is a resonant nonlinear-optical process, strong signals can be generated by minor species. Furthermore, for a collimated pump-and-probe beam geometry, the third-order nonlinear interaction generates a collimated signal beam that can be collected far from the measurement volume, which permits high noise rejection in luminous environments. Relative concentration measurements of Na and OH have been obtained through the use of DFWM in atmospheric-pressure flames.[3-6] Time-averaged rotational temperature measurements have also been performed by scanning the laser wavelength and determining the ground electronic state Boltzmann population distributions of OH and NH molecules in laminar flat flames.[7]

Multiplex DFWM has been proposed as a technique for obtaining time-resolved temperature measurements.[8] The technique is demonstrated here by performing multiplex DFWM measurements of OH in an atmospheric-pressure hydrogen–oxygen flame.

The basic theory of DFWM in a two-level atomic system was developed over a decade ago.[2] In the phase-conjugation geometry, two strong, counterpropagating, collimated pump beams are overlapped in the interaction region by a weak probe beam. The resonant nonlinear interaction of the three beams with the molecules in the probe volume generates a fourth conjugate signal beam of the same frequency, which is also collimated and propagates backward along the path of the probe beam. If we make the approximations of strong, undepleted, monochromatic pump beams, a weak probe beam, low absorption, and a steady state, the generated conjugate signal beam has an intensity given (in mks units) by[9]

$$I_c(\delta) \approx \left[\frac{\omega \Delta N_0 \mu^2 T_2}{2\epsilon_0 c(h/2\pi)}\right]^2 \frac{L^2}{1+\delta^2}\,\frac{4(I/I_{\mathrm{sat}})^2}{(1+4I/I_{\mathrm{sat}})^3}\, I_p, \qquad (1)$$

where I_c, I_p, and I are the intensities of the conjugate, probe, and strong pump beams, respectively, L is the length of the interaction volume, and δ is the detuning of the applied fields from the molecular resonance, normalized by the transition's coherence decay rate. The squared term in brackets is the weak-field line center absorption coefficient α_0, where ω is the angular frequency of the laser radiation, ΔN_0 is the population difference between the two atomic levels, μ is the transition's electric dipole moment, T_2 is the transition's coherence lifetime, and ϵ_0 is the permittivity of vacuum. I_{sat} is the frequency-dependent saturation intensity of the transition, given by[9]

$$I_{\mathrm{sat}}(\delta) = (1+\delta^2)\epsilon_0 c(h/2\pi)^2/2\mu^2 T_1 T_2, \qquad (2)$$

where T_1 is the population decay time for the transition.

For multiplex DFWM, a spectrally broad laser source is used to pump more than one transition in a molecular system simultaneously. A theory for broadband pumping has been developed,[10] and the case of multiple resonances has been considered.[11] If the separation between transitions exceeds their linewidth and there is no coupling between levels, the resonant response will ensure that a conjugate wave is generated independently by each transition. The DFWM signal will then contain spectrally narrow frequency components corresponding to the molecular transitions overlapped by the laser spectral distribution. For temperature measurements, it is necessary to pump molecules in thermal equilibrium, so that the ground-state rotational-energy-level population distribution is a known (Boltzmann) function of temperature. The relative intensities of the spectral components of the generated signal beam, when corrected for the spectral illumination and the different dipole moments of the transitions involved, will provide the relative ground-state populations and hence the rotational temperature of the molecules.

Practically, however, multiplex DFWM thermometry poses some experimental challenges. First, signal-to-noise levels will be low, since much of the broadband laser energy will not be resonant with molecular transitions and so will not contrib-

0146-9592/92/100751-03$5.00/0

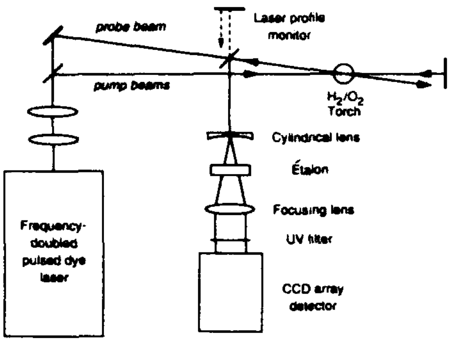

Fig. 1. Experimental arrangement used for multiplex DFWM thermometry.

ute to signal generation. Inefficient spectral dispersion of the multiplexed DFWM signal will further reduce detected light levels. A compromise must be reached with regard to the spectral width of the laser source—greater width allows simultaneous pumping of more transitions and a more accurate temperature determination but will significantly reduce pump and signal spectral intensities. Since the multiplexed signal beam will have contributions from multiple rotational levels with small energy separation, extremely high spectral dispersion will be required to obtain the required single-shot spectral information.

The experimental arrangement used in performing these experiments is shown in Fig. 1. The output of a pulsed Nd:YAG-pumped dye laser system operating on Sulforhodamine 540 (Spectra-Physics DCR2, PDL1, and WEX) was doubled to obtain 1 mJ of energy at 311.78 nm, with a pulse duration of ~10 ns and a bandwidth of ~1 cm^{-1}. The laser energy was collimated to form a 1.5-mm-diameter beam that was split to form a strong (83%) forward pump and weak (17%) probe beam, which crossed at 1°. An interaction length L greatly exceeding the depth of the flame was produced by this geometry. Although this degraded the spatial resolution in this measurement, optical alignment was facilitated and signal generation [by relation (1)] was maximized. A retroreflection of the forward pump was used to obtain the backward pump beam in the common phase-conjugation geometry. The flame tip of a laminar premixed hydrogen–oxygen torch (d = 2.2 mm, ϕ = 0.86) was placed in the overlap region of the pump and probe beams, and a 20% beam splitter was used to recover the conjugate beam (generated by the resonant interaction in OH) propagating backward along the probe-beam path.

The DFWM signal was spectrally dispersed by using a diverging cylindrical lens and a 1-mm-thick étalon (free spectral range 3.3 cm^{-1}, finesse < 20). A spherical lens focused the straight fringe pattern generated by the étalon onto a UV-enhanced cooled CCD detector (Photometrics Star 1) while at the same time focusing in the nondispersed direction to enhance the signal-to-noise ratio in the detected signal. A small fraction of the probe beam was monitored simultaneously with the DFWM signal on an offset portion of the CCD chip, in order to record shot-to-shot fluctuations of the laser spectral distribution. (While the original intent of the monitor beam was to allow corrections for the intensity dependence of the DFWM signal to be made, the spectral resolution proved to be insufficient for this purpose, limiting use of the beam to monitoring the tuning of the dye laser.)

The laser spectral distribution overlaps the $P_1(8)$ and $Q_2(14)$ transitions in the (0, 0) vibrational band of the A–X system of the OH radical. The relatively narrow (~1 cm^{-1}) laser linewidth makes the selection of the transitions to be pumped a critical part of the experiment. Since the OH spectrum is not dense, no more than two transitions will be able to be pumped simultaneously. A transition pair that produces strong DFWM signals of comparable strength and whose ratio is a sensitive function of temperatures in the flame is the most suitable. This ratio may be estimated from relation (1) by applying the Boltzmann distribution for the ground-state populations of the two transitions and using the appropriate spectral constants.[12,13] (The use of this relation, derived for pumping by a monochromatic source, is discussed below.) If we assume identical coherence and population decay rates for the two transitions[14] and $I \gg I_{\text{sat}}$ so that coupling between the levels can be neglected, the ratio of DFWM signal peaks is then

$$R_{12}(T) = \frac{B_1 \Delta N_1^2}{B_2 \Delta N_2^2} = \frac{B_1}{B_2}\left(\frac{2J_1 + 1}{2J_2 + 1}\right)^2 \times \exp\left\{\frac{-2hcB_0[J_1(J_1 + 1) - J_2(J_2 + 1)]}{kT}\right\}, \quad (3)$$

where B_1 and B_2 are the Einstein absorption coefficients for the two transitions (proportional to the square of the dipole moment), J_1 and J_2 are the angular momentum quantum numbers of the ground-state levels of the transitions, and B_0 is the rotational constant for the lower vibrational state. Figure 2 shows the calculated temperature variation of the DFWM peak ratio for the three most promising candidate line pairs. The $Q_2(14)/P_1(8)$ transition line pair of the (0, 0) band, which has the smallest line separation (1.3 cm^{-1}), provides good temperature sensitivity and the strongest signal levels.

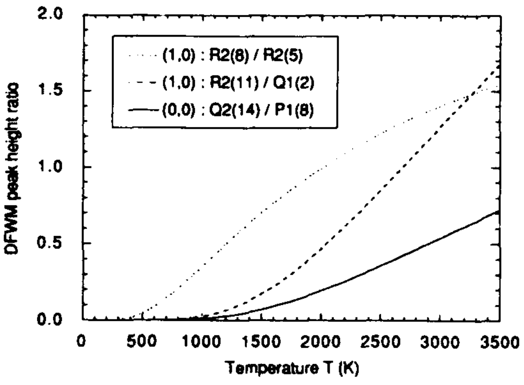

Fig. 2. Calculated temperature sensitivity of the multiplex technique for the three most promising candidate line pairs of the OH system.

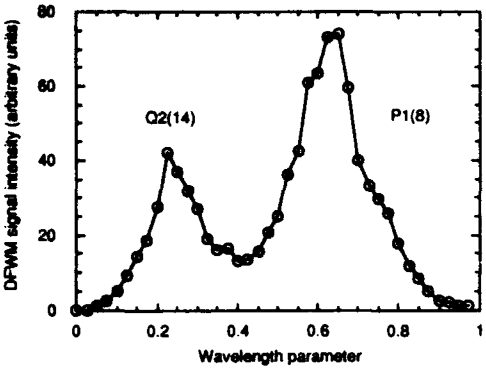

Fig. 3. Multiplex DFWM spectrum obtained by using a single laser shot. Two peaks corresponding to DFWM resonant with the $P_1(8)$ and $Q_2(14)$ transitions of the (0, 0) band of the A–X system of OH are clearly visible. The wavelength normalization corresponds to the free spectral range of the étalon, 3.3 cm^{-1} or 0.032 nm.

Figure 3 shows a representative multiplex DFWM spectrum obtained by using a single laser shot. The étalon fringe pattern was first linearized in wavelength, and then the repeated spectra in four orders of the fringe pattern were summed to obtain the result. The x axis is linear in wavelength with a normalization corresponding to the free spectral range of the étalon, 3.3 cm^{-1} or 0.032 nm. Two peaks corresponding to DFWM resonant with the $P_1(8)$ and $Q_2(14)$ transitions are clearly visible.

As mentioned above, relation (1) applies for the case of pumping by monochromatic radiation and should in principle be generalized for broadband laser excitation. However, the broadband laser distribution used in these experiments is in fact composed of a finite number of discrete longitudinal modes. Although the detailed mode structure was not directly resolvable with the UV étalon system, higher-resolution measurements of the visible dye laser output before doubling indicate that approximately 25 possible modes separated by ~0.04 cm^{-1} lie within the 1-cm^{-1} gain envelope. Adjacent mode intensities appear to be anticorrelated,[15] however, so that the laser pulse energy is distributed among a lower number of modes, with a frequency separation of 0.08 cm^{-1} or more. The mode intensities vary randomly with each laser pulse. Since the homogeneous linewidth of OH transitions in the (0, 0) band at 1 atm and ~2400 K has been measured[14] as 0.10 cm^{-1} (FWHM), each transition may be approximated as being excited by essentially monochromatic light. Using Eq. (2) and the values $T_1 = T_2 = 1.1 \times 10^{-10}$ s for the relaxation times and $A[Q_2(14)] = 6.2 \times 10^5\ \text{s}^{-1}$ and $A[P_1(8)] = 3.8 \times 10^5\ \text{s}^{-1}$ for the Einstein coefficients for spontaneous emission,[16] we obtained line center saturation intensities of 0.59 and 0.95 MW/cm^2. The mean pump intensity applied in the experiment (4.7 MW/cm^2), when divided by the number of modes excited in each laser pulse, approaches these saturation intensities. Based on these estimates, when pumped by energetic modes near their line centers, both transitions will be saturated. As a first approximation, correction for the laser spectral intensity at the transition wavelengths will not be required.

Owing to the random shot-to-shot fluctuation of mode intensities, simultaneous signal from both transitions was generated by only 15% of the laser pulses. All pulses producing two DFWM peaks distinguishable for the background were retained. With the calculated temperature dependence of Fig. 2, the ratio of line peak intensities obtained from the ensemble of single-shot measurements yields an OH rotational temperature of 2880 ± 320 K. This compares favorably with the adiabatic flame temperature of 3070 K, an upper bound on the actual flame temperature.

The accuracy of the temperature determination can be improved by simultaneous monitoring of the nonuniform conjugate beam profile and the use of higher-quality optical elements to improve spectral resolution. Corrections for incomplete or unequal saturation of the two transitions should then be possible. While it may be inefficient for frequency doubling, a modeless laser[17] might also provide better shot-to-shot repeatability in the signal generation.

In conclusion, multiplex degenerate four-wave mixing in OH has been used to perform single-laser-shot thermometry in an atmospheric-pressure hydrogen–oxygen flame. Good signal levels were obtained and feasibility of the technique is indicated.

Research support was provided by the U.S. Air Force Office of Scientific Research, Aerospace Sciences Directorate, and is gratefully acknowledged.

References

1. R. A. Fisher, ed., *Optical Phase Conjugation* (Academic, New York, 1983).
2. R. L. Abrams and R. C. Lind, Opt. Lett. **2,** 94 (1978).
3. J. Pender and L. Hesselink, Opt. Lett. **10,** 264 (1985).
4. P. Ewart, P. Snowdon, and I. Magnusson, Opt. Lett. **14,** 563 (1989).
5. P. Ewart and S. V. O'Leary, Opt. Lett. **11,** 279 (1986).
6. D. J. Rakestraw, R. L. Farrow, and T. Dreier, Opt. Lett. **15,** 709 (1990).
7. T. Dreier and D. J. Rakestraw, Appl. Phys. B **50,** 479 (1990).
8. P. Ewart and P. Snowdon, Opt. Lett. **15,** 1403 (1990).
9. R. L. Farrow, D. J. Rakestraw, and T. Dreier, "Investigation of the dependence of degenerate four-wave mixing intensities on the transition dipole moment," J. Opt. Soc. Am. B (to be published).
10. D. R. Meacher, A. Charlton, P. Ewart, J. Cooper, and G. Alber, Phys. Rev. A **42,** 3018 (1990).
11. D. G. Steel and J. F. Lam, Opt. Lett. **5,** 297 (1980).
12. I. L. Chidsey and D. R. Crosley, J. Quant. Spectrosc. Radiat. Transfer **23,** 187 (1980).
13. G. H. Dieke and H. M. Crosswhite, J. Quant. Spectrosc. Radiat. Transfer **2,** 97 (1963).
14. E. C. Rea, Jr., A. Y. Chang, and R. K. Hanson, J. Quant. Spectrosc. Radiat. Transfer **41,** 29 (1989).
15. L. A. Westling, M. G. Raymer, and J. J. Snyder, J. Opt. Soc. Am. B **1,** 150 (1984).
16. W. L. Dimpfl and J. L. Kinsey, J. Quant. Spectrosc. Radiat. Transfer **21,** 233 (1979).
17. P. Ewart, Opt. Commun. **55,** 124 (1985).

a reprint from Applied Optics

Temperature measurements in gases by use of planar laser-induced fluorescence imaging of NO

Michael P. Lee, Brian K. McMillin, and Ronald K. Hanson

Two techniques based on planar laser-induced fluorescence of NO are applied to the measurement of two-dimensional temperature fields in gaseous flows. In the single-line technique, the NO fluorescence signal, which is in general a function of temperature, pressure, and mole fraction, can be reduced to a function of temperature alone. In this limit, a single measurement of fluorescence can be directly related to temperature. In contrast, in the two-line thermometry technique the ratio of fluorescence signals resulting from excitation of two different rovibronic states is related to the fractional populations in the initial states, which are solely a function of temperature. The one-line method is applied to the study of a laminar heated jet, and the two-line technique is used to measure temperature in a supersonic underexpanded jet. In addition, energy transfer in NO laser-induced fluorescence is analyzed with multilevel rate equation models. Finally, an accurate model is developed for prediction of the temperature dependence of the NO fluorescence signal.

Introduction

Temperature is one of the key variables required for the description of gaseous flows. The need for accurate temperature data has motivated the development of a wide range of temperature measurement (or thermometry) techniques, and the most widely applied methods use physical probes such as thermocouples or gas-sampling probes. Probe-based thermometry has important advantages, including simple implementation, well-developed technology, and relatively low cost, but these techniques also have disadvantages that limit their application. For example the intrusive nature of probes can lead to flow perturbations and measurement errors, particularly in studies of supersonic flows. In addition, probes are subject to degradation in harsh flow environments, and the poor temporal resolution and single-point nature of these techniques limit their utility, particularly for studies of rapidly varying two-dimensional (2-D) and three-dimensional (3-D) flows.

The need for improved temperature measurement methods has prompted the development of diagnostics based on the propagation and detection of light interacting with an atomic or molecular species in the flow. A number of optically based techniques have been developed for single-point thermometry,[1-4] and the extension of these methods to multidimensional imaging will permit acquisition of spatially correlated multipoint measurements. Unfortunately most optical diagnostics for temperature cannot be easily applied to planar measurements, either because of their inherent single-point or line-of-sight nature (e.g., absorption spectroscopy and coherent anti-Stokes Raman spectroscopy), or because the reduced intensity of laser sheet illumination leads to insufficient signal levels (e.g., spontaneous Raman scattering). Rayleigh scattering has been demonstrated for planar thermometry,[5,6] but the applicability of this technique is limited. Thus our emphasis in the development of imaging thermometry has focused on the planar laser-induced fluorescence (PLIF) technique.

Two methods based on PLIF have been developed for planar (i.e., 2-D) temperature measurements. In the one-line technique, the fluorescence signal, which is typically a function of temperature, pressure, and species mole fraction, can be reduced to a function of temperature alone. In this limit a single measurement of the fluorescence signal can be directly related to temperature. In contrast the two-line technique uses the excitation of two transitions originating from different rovibronic states within a molecule. The ratio of the resulting fluorescence

---

The authors are with the High Temperature Gasdynamics Laboratory, Department of Mechanical Engineering, Stanford University, Stanford, California 94305. M. Lee is now with Deutsche Forschungsanstalt für Luft- und Raumfahrt, Pfaffenwaldring 38-40, D-7000 Stuttgart 80, Germany.

Received 29 April 1992.

0003-6935/93/275379-18$06.00/0.

signals can be related to the ratio of the initial-state populations, which can be converted to temperature with an assumption of a Boltzmann population distribution in the ground state. There have been a number of previous studies on the application of PLIF to 2-D thermometry. Cattolica and Stephenson[7] measured the temperature field in a steady premixed CH_4/air flat flame with two-line PLIF of OH. One-line NO PLIF has been applied by Seitzman *et al.*[8] to the measurement of temperature in a rod-stabilized fuel-lean CH_4/air flame with flow-stopping temporal resolution. Lee *et al.*[9] measured 2-D temperature fields in a laminar heated jet with one-line PLIF of O_2. Recently several applications of PLIF thermometry have been presented. Ni-Imi *et al.*[10] have used two-line PLIF of I_2 to measure temperature in a low-density supersonic underexpanded jet. Hartfield *et al.*[11] have applied one-line PLIF of I_2 to the measurement of the temperature field in a supersonic Laval nozzle. Paul *et al.*[12] have used single-shot two-line PLIF of OH to perform temperature measurements in laminar and turbulent flames. Palmer *et al.*[13] and McMillin *et al.*[14,15] have measured temperature fields in supersonic flows by use of PLIF of NO.

The extension of PLIF thermometry to methods that use NO is important for a number of reasons. First, NO (along with its chemical product NO_2) is one of the most important pollutant species. In addition the natural presence of NO in many flows of interest (e.g., flames and hypersonic flows) implies that no seeding of the flow may be required. Finally, the thermal stability of NO means that it can be used for thermometry over a wide temperature range, unlike other species such as OH (which is only present in significant concentrations above ~1000 K) or biacetyl and I_2 (which are unstable at elevated temperatures). Single-point LIF of NO has been applied to the study of a variety of flows, including flames[16–24] and wind-tunnel flows.[25,26] Also, PLIF of NO has been used for a wide range of flow measurements, including planar velocimetry in an underexpanded jet,[27] species imaging in an internal combustion engine,[28] visualization of mixing in supersonic transverse jet injection,[29] vibrational relaxation behind a planar shock,[30] and flow visualization in a supersonic shear layer.[31]

This survey indicates that the application of PLIF to temperature measurements has been fairly limited. In addition, some of these studies have used OH, which is only found at elevated temperatures in reacting flows, or I_2, which is highly reactive and unstable at high temperatures and must be seeded into the flowfield. Thus the need exists for further development of PLIF thermometry techniques. In this paper we provide an overview of PLIF thermometry, as well as demonstrations of the one-line and two-line NO PLIF techniques for 2-D temperature measurements. Multilevel rate equation models applicable to analysis of NO fluorescence are also presented.

Theory of Laser-Induced Fluorescence

Overview

In a laser-induced fluorescence experiment, a laser is tuned in frequency to an optically allowed absorption transition in an atomic or molecular species of interest. Following excitation from a lower to an upper energy state, the excited-state molecules can relax through several paths. Deexcitation processes may include collisional quenching, stimulated emission, spontaneous emission (also called radiative decay or fluorescence), rotational energy transfer (RET) and vibrational energy transfer, predissociation, and photoionization. Many studies have been performed on the modeling of energy transfer in LIF by use of rate equations.[3,32–43] The simplest model that has been developed is the two-level model, in which the only energy states of importance are the laser-coupled states. Subsequently, more complex models have been developed to allow inclusion of important energy transfer processes such as RET. Accurate prediction of the fluorescence signal requires the development of multilevel rate equation models, which in turn requires detailed examination of the spectroscopy of the species of interest.

Spectroscopy of NO

The NO transitions that have been examined most extensively for LIF studies are the $A\,^2\Sigma^+–X\,^2\Pi$ (0, 0), $B\,^2\Pi–X\,^2\Pi$(7, 0), and $D\,^2\Sigma^+–X\,^2\Pi$ (0, 1) bands. The $A–X$ (0, 0) band can be excited with a frequency-doubled dye laser at 226 nm, whereas the $B–X$ (7, 0) and $D–X$ (0, 1) bands can be pumped with an argon fluoride (ArF) excimer laser at 193 nm.[23] A comparison of these transitions is summarized in Table 1.

This comparison illustrates the advantages of excitation of the $A–X$ (0, 0) band for quantitative LIF studies. The spectroscopy of the $A–X$ (0, 0) band has been thoroughly studied, and extensive data are available on important parameters such as line positions,[44] linewidths,[45,46] quenching cross sections,[47,48]

Table 1. Comparison of Three Rovibronic Transitions of NO for LIF Studies

Characteristic	$A–X$ (0, 0)	$D–X$ (0, 1)	$B–X$ (7, 0)
$f(v', v'')$	3.8×10^{-4}	3.3×10^{-3}	7×10^{-5}
Excitation wavelength	226 nm	193 nm	193 nm
Accessible transitions	All J''	$J'' = 15.5–46.5$	$J'' = 23.5–34.5$
Excitation from $v'' = 0$?	Yes	No	Yes
Linewidths	+[a]	–[b]	–
Line positions	+	–	–
Quenching	+	–	–
Applicable for low temperature	Yes	No	No
Overlap with O_2 transitions	No	Yes	Yes

[a] Comprehensive data are available.
[b] Data are incomplete.

and RET rates.[49,50] The data on the *B–X* (7, 0) and *D–X* (0, 1) transitions are less comprehensive. In addition, the oscillator strength for the *A–X* (0, 0) band[51] ($f = 3.8 \times 10^{-4}$) is greater than the oscillator strength for the *B–X* (7, 0)[51,52] band ($f = 7 \times 10^{-5}$), and at low temperatures the smaller oscillator strength of the *A–X* (0, 0) band compared with the *D–X* (0, 1) band[51,52] ($f = 3.3 \times 10^{-3}$) is offset by the higher population in $v'' = 0$ compared with $v'' = 1$. Also, the tuning range of the narrow-band ArF laser (~1 nm) limits the rotational levels that can be accessed in the *D–X* (0, 1) band ($J'' = 15.5$–46.5) and the *B–X* (7, 0) band ($J'' = 23.5$–34.5).[23] In contrast the ability to excite the entire manifold of rotational levels enables *A–X* (0, 0) excitation across a wide range of temperatures and permits the development of more sensitive thermometry strategies. For qualitative studies (such as flow visualization), the *D–X* (0, 1) and *B–X* (7, 0) transitions may be superior because of the higher available laser energy at 193 nm (~100 mJ) compared to 226 nm (~1 mJ). However, the increased laser energy at 193 nm may also lead to deviations from the weak excitation limit, and care must be taken to avoid saturation effects. In addition, the presence of O_2 transitions at 193 nm[23,53] can complicate the interpretation of the fluorescence signal in flows where both NO and O_2 are present. Thus, in general, the desire for quantitative LIF measurements dictates the use of the *A–X* (0, 0) transition.

The NO LIF in the *A–X* (0, 0) band can be accurately analyzed by extending the well-known four-level model for LIF[36–38,41] to a five-level model,[53] shown in Fig. 1. The RET has been modeled by use of the approach of Berg and Shackleford,[36] in which all energy states that are not directly coupled by the laser excitation are grouped into bath levels. Thus, in the lower state, RET from bath level 4 to level 1 replenishes the population of the laser-excited state, whereas in the upper-state RET acts to drain the population from the laser-populated state 2 to the bath level 3, delaying the onset of saturation. In addition, radiative decay and collisional quenching are assumed to occur to a fifth level (state 5) that is not collisionally or radiatively coupled to the lower energy levels during the laser pulse. This is an accurate model for energy transfer in NO for the following reasons: first, the majority of the excited molecules decay to vibrational levels in the *X* state other than the initial pumped level[54]; second, vibrational energy transfer in NO is slow compared with a typical laser-pulse duration of ~20 ns.[55,56] The rate equations for the five-level model are

$$dN_1/dt = (-b_{12}I_\nu - R_{14})N_1 + b_{21}I_\nu N_2 + R_{41}N_4, \quad (1)$$

$$dN_2/dt = b_{12}I_\nu N_1 - (b_{21}I_\nu + A_{25} + Q_{25} + R_{23})N_2 + R_{32}N_3, \quad (2)$$

$$dN_3/dt = R_{23}N_2 - (A_{35} + Q_{35} + R_{32})N_3, \quad (3)$$

$$dN_4/dt = R_{14}N_1 - R_{41}N_4, \quad (4)$$

$$dN_5/dt = (A_{25} + Q_{25})N_2 + (A_{35} + Q_{35})N_3. \quad (5)$$

The rates for stimulated emission and absorption are denoted by $b_{ij}I_\nu$, where b_{ij} (cm^2 cm^{-1} J^{-1}) represents the Einstein B coefficients and I_ν is the spectral intensity of the laser (J cm^{-1} s^{-1}); Q_{ij} (s^{-1}) is the collisional quenching rate, and A_{ij} (s^{-1}), the Einstein

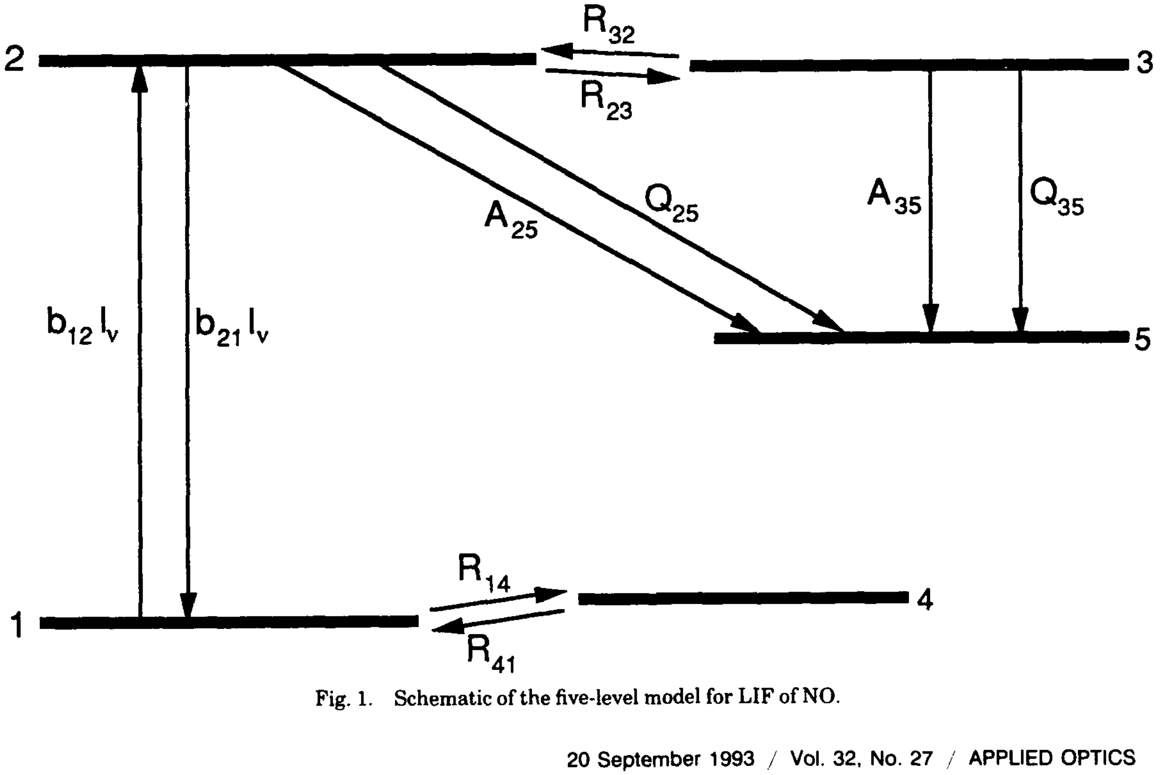

Fig. 1. Schematic of the five-level model for LIF of NO.

A coefficient, is the spontaneous emission rate. The RET rates are denoted by R_{ij} (s^{-1}). The subscripts ij (e.g., $b_{12} = b_{ij}$) indicate that i is the initial state in the energy-transfer process and that j is the final state. Note that the collisional quenching and radiative decay rates from the upper states 2 and 3 into the lower states 1 and 4 are assumed to be negligible.

The RET process is modeled[36] by assuming that the ratio of transfer rates between level 1 and the ground state bath level 4 is equal to the initial Boltzmann fraction in the pumped state, i.e.,

$$R_{41}/R_{14} = N_1{}^0/N_4{}^0. \tag{6}$$

The RET between levels 2 and 3 is modeled in the same way, i.e.,

$$R_{32}/R_{23} = N_1{}^0/N_4{}^0. \tag{7}$$

This approximation yields the LIF signal in the limit of maximum RET (i.e., the RET will not be faster than the values predicted by this model).

The rate equations can be simplified by examining the energy-transfer rates for NO. The radiative decay rate does not vary significantly in the upper state, and so the Einstein A coefficients can be assumed to be constant ($A_{25} = A_{35} = A$). In addition, in recent studies[47,48,57] researchers have observed no significant variation in collisional quenching cross section with rotational level, and so it can be assumed that both the laser-populated level and the upper bath level have the same collisional quenching rate ($Q_{25} = Q_{35} = Q$).

In general, time-dependent analysis of this system of rate equations is required to analyze the LIF signal. A computer program[53] has been written to calculate the temporal variation of the NO fluorescence signal. However, in some cases full numerical analysis is unnecessary, and the rate equations can be solved explicitly. In the limit of weak laser excitation (i.e., the ground-state population is not significantly perturbed), the fluorescence emission rate simplifies to

$$S_f(t) \sim N_1{}^0 b_{12} I_\nu A/(A + Q), \tag{8}$$

which is identical with the result that has been developed previously for the simple two-level model.[3] Note that this result is valid in cases in which the spontaneous emission rates and the collisional quenching rates do not vary significantly in the upper state. In cases where these rates do vary in the upper state (e.g., for OH), the derived result is more complex but has the same basic form. Note also that for narrowband fluorescence collection, processes that transfer molecules out of the detection bandwidth (such as RET) act as additional loss mechanisms for the fluorescence signal.

For strong laser excitation the analysis is generally more complex, but two regimes can be examined. In the first regime, all energy-transfer processes (including RET) are slow compared with the stimulated absorption and emission rates, and no significant RET occurs over the time scale of the laser pulse. In this case, the bath levels do not play a significant role in the energy transfer during the laser excitation, and the fluorescence signal can be determined explicitly by use of the two-level model in two limits. In the first limit, the fluorescence lifetime is short compared with the laser-pulse duration, τ, and the fluorescence signal can be modeled by

$$S_1 \sim N_1{}^0 A\tau b_{12}/(b_{12} + b_{21}), \tag{9}$$

because the fraction of the fluorescence signal emitted after cessation of the laser pulse is insignificant. Note that in this expression, the steady-state fluorescence emission rate has been temporally integrated to yield the fluorescence signal. In the second limit, the fluorescence lifetime is not negligible compared with the laser-pulse duration, and thus the fluorescence after the end of the laser pulse must also be considered. The fluorescence that is emitted after the end of the laser pulse can be written as

$$\begin{aligned} S_2 &\sim N_2{}^{\mathrm{end}}[A/(A + Q)] \\ &= [N_1{}^0 b_{12}/(b_{12} + b_{21})][A/(A + Q)]. \end{aligned} \tag{10}$$

If we combine Eqs. (9) and (10), the total fluorescence is

$$S_{\mathrm{total}} = S_1 + S_2 \sim [N_1{}^0 b_{12}/(b_{12} + b_{21})]\{A\tau + [A/(A + Q)]\}. \tag{11}$$

Note that this expression is valid provided that the absorption transition is saturated at the end of the laser pulse. Also note that in this case the fluorescence signal is dependent on the collisional quenching rate, even though the absorption transition is saturated during the laser pulse. However, if the detection system is temporally gated to detect only the portion of the fluorescence that is emitted during the laser pulse, Eq. (9) can be used to describe the fluorescence signal, even if the signal emitted after the end of the laser pulse is significant.

In the second regime of strong excitation, the RET and/or collisional quenching rates are not negligible with respect to the laser excitation rate. In this case, saturation may or may not be reached because of the rapid energy transfer. Thus a full time-dependent analysis must be used to evaluate the fluorescence signal in this limit.

Many NO lines actually consist of pairs of transitions originating from the same lower state into two different upper states. Modeling of these overlapped line pairs requires the addition of a sixth level to the five-level model.[53] The additional absorption transition acts to increase the transfer rate of molecules out of the ground state, thus leading to more rapid depletion of this state. The rate equations for the six-level model are similar to the equations derived for the five-level model, and these equations can be examined in the weak and strong excitation limits.

For weak excitation, the six-level model also reduces to the solution given by the two-level model. In the case of strong excitation, the analysis is complicated by the presence of two transitions with different oscillator strengths originating from the same lower state. In the limit that both transitions saturate and the stimulated emission rate dominates the energy transfer, the model of saturated fluorescence developed previously can again be used. However, if either transition is only partially saturated, or if other energy-transfer processes are rapid with respect to the laser excitation rate, a full time-dependent model must be analyzed.

Finally, it should be noted that rate equation analyses often include two assumptions about the laser spectral intensity I_ν. First, it is assumed that the laser has a uniform temporal profile with a characteristic duration given by τ. In this case, the total laser intensity is

$$I = E/A\tau, \tag{12}$$

where E is the laser energy and A is the cross-sectional area of the beam. In the weak excitation limit, this assumption causes no error. However, in the strong excitation limit temporal variations in the laser intensity may lead to deviations from saturation. In this case, the assumption of a temporally uniform laser pulse may lead to errors in the prediction of the fluorescence signal, and time-dependent analyses are required for accurate modeling.

It is also typically assumed that the laser linewidth is much broader than the absorption linewidth, and so the spectral intensity I_ν is approximated as

$$I_\nu = I/\Delta\nu_L, \tag{13}$$

where $\Delta\nu_L$ is the laser linewidth. However, in general this simplification is not necessary. Instead, the overlap between the absorption line and the laser line can be explicitly evaluated by including the overlap integral between the two line shapes,[26] and so I_ν is defined as

$$\begin{aligned} I_\nu &= I\int_{-\infty}^{\infty} \phi(\nu, \nu_0, P, T) g(\nu, \nu_L, \Delta\nu_L)\mathrm{d}\nu \\ &= IG(\nu_L, \nu_0, P, T, \Delta\nu_L), \end{aligned} \tag{14}$$

where $\phi(\nu, \nu_0, P, T)$ is the absorption line-shape function centered at ν_0, $g(\nu, \nu_L, \Delta\nu_L)$ (in inverse wave numbers), is the laser line-shape function centered at ν_L, and $G(\nu_L, \nu_0, P, T, \Delta\nu_L)$ (in inverse wave numbers) is the line-shape overlap integral. In this formulation the integrals of the laser and absorption line-shape functions over all frequencies are normalized to unity. It will be shown below that assuming $G(\nu_L, \nu_0, P, T, \Delta\nu_L) \approx 1/\Delta\nu_L$ can lead to significant errors in prediction of the variation of the fluorescence signal as a function of pressure and temperature.

A comparison of the rates for the various energy transfer processes for a typical PLIF experiment is illustrative. A mixture of 0.25% NO in air at 295 K and 1 atm has been examined, and the laser source is assumed to have an energy of 3.0 mJ/pulse, a pulse duration of 20 ns, a Gaussian lineshape with $\Delta\nu_L \approx 0.6\ \mathrm{cm}^{-1}$, and a cross-sectional area of $\sim 5\ \mathrm{cm} \times 100\ \mu\mathrm{m}$. The RET rates for NO in the A state were obtained from Ebata *et al.*,[50] and identical rates are used for modeling of lower-state RET. The collisional quenching cross sections of Raiche and Crosley[47] were used. The Einstein B coefficient for excitation of the $Q_2(7)$ line is $b_{12}[Q_2(7)] = 224\ \mathrm{cm}^2\ \mathrm{cm}^{-1}/\mathrm{J}$. The relevant energy-transfer rates are $Q \sim 6 \times 10^8\ \mathrm{s}^{-1}$, $A \sim 5 \times 10^6\ \mathrm{s}^{-1}$, $R_{14} \sim 1 \times 10^{10}\ \mathrm{s}^{-1}$, and $b_{12}[Q_2(7)] \cdot I_\nu \sim 1 \times 10^9\ \mathrm{s}^{-1}$. Thus $R_{14} > b_{12}[Q_2(7)] \cdot I_\nu > A, Q$, and so RET acts to prevent saturation of the transition, enabling application of the weak excitation limit for analysis of the fluorescence signal.

Temperature Measurements with LIF–NO One-Line Thermometry

In the limit of weak laser excitation, the NO fluorescence emission rate is accurately described by Eq. (8). The signal can be reduced to a function of temperature alone if one of two sets of conditions is valid. The first set of conditions specifies that χ_{NO} is constant and that the flow is isobaric. In this limit the fluorescence signal can be written as

$$S \sim [F_{v''J''}(T)/T][A/(A + Q)]G(T). \tag{15}$$

Assuming that the collisional quenching is much faster than the spontaneous emission ($Q \gg A$) and the quenching cross section is not a function of temperature (i.e., $Q \sim P/T^{1/2}$), the fluorescence signal can be reduced to

$$S \sim [F_{v''J''}(T)/T^{1/2}]G(T). \tag{16}$$

The second set of conditions requires that χ_{NO} is constant, $Q \gg A$, and the collision width must be negligible (i.e., $\Delta\nu_{\mathrm{laser}} \gg \Delta\nu_c$ or $\Delta\nu_D \gg \Delta\nu_c$). In this case the fluorescence signal can again be described by Eq. (16), assuming that the quenching cross section is independent of temperature. If either of these two sets of conditions is valid, the fluorescence signal can be reduced to a function of temperature alone. Note that single-line thermometry can only be applied in nonreacting flows or in reacting flows where the seed species has constant concentration (e.g., NO in fuel-lean flames). In addition, this technique has limited applicability in nonisobaric flows. These constraints limit the utility of NO single-line PLIF for thermometry, but this method is advantageous because it permits a direct measurement of temperature on a single-shot basis with a single laser and detector.

Temperature Measurements with LIF–NO Two-Line Thermometry

In the weak or strong excitation limits, the ratio of the fluorescence signals resulting from the excitation of two NO transitions can be written as

$$\text{Ratio} \sim [F_{v''J''}(T)]_1/[F_{v''J''}(T)]_2 \sim f(T). \qquad (17)$$

Thus the signal ratio is solely dependent on the ratio of the initial-state populations, which is a function of temperature alone. Note that this derivation assumes that the overlap integrals for the two lines have identical pressure and temperature dependences. In the intermediate regime between strong and weak excitation, the transitions are partially saturated and Eq. (17) cannot be used to model the fluorescence signal ratio. If the degree of saturation were precisely the same for both lines, the signal ratio could be approximated by the ratio of state populations, but in general varying saturation effects can lead to errors in two-line thermometry measurements and should be avoided if possible.

The two-line thermometry technique has several advantages over other approaches. Using the ratio of the fluorescence signals to determine temperature minimizes measurement uncertainties that are due to variations in quenching cross section, species mole fraction, and pressure. As a result, the two-line method can be applied to a wide range of flows, including reacting and supersonic flows. In addition, two-line thermometry is applicable in either the weak or the strong excitation limits. However, this technique also has important limitations. In particular, in studies of rapidly varying flows, the use of two excitation sources and two detection systems is required for acquiring flow-stopping measurements. Thus the experimental requirements for instantaneous two-line measurements are more extensive than for one-line measurements.

NO One-Line Thermometry

Introduction

As discussed above, in isobaric flows with constant NO mole fraction, the NO fluorescence signal can be reduced to a function of temperature alone, enabling application of the one-line thermometry technique. A schematic of the experimental facility used to generate a flow of this type is shown in Fig. 2. An 8-mm-i.d. electrically heated torch (Sylvania SGH114372) was mounted within a 7.5-cm-i.d. tube. Gas flowed through the torch and exited with a temperature ranging from 295 to 1200 K. A shroud flow of the same mixture as the torch flow was used to maintain a constant gas composition throughout the measurement region.

A standard experimental arrangement[58] was used for the PLIF studies. The beam from an excimer-pumped dye laser (Lambda Physik EMG 160/FL 3002) was doubled in BBO to excite transitions in the A–X (0, 0) band of NO at 226 nm. The laser beam was formed into a thin sheet with the combination of a spherical lens (1-m focal length) and a cylindrical telescope (−12.5-mm and 50-cm focal lengths), and this sheet was propagated along the center line of the torch flow. The resulting fluorescence was collected at right angles to the path of laser propagation with a Cassegrainian lens ($f/1.2$, 95-mm focal length) and detected with an image-intensified CCD camera (Amperex NXA1061). The intensifier was tempo-

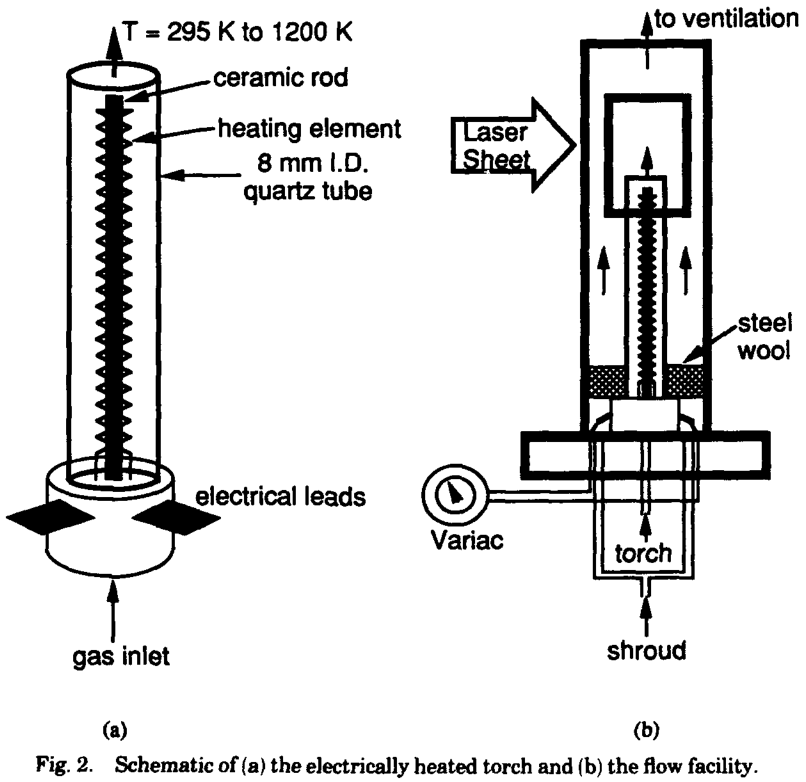

(a) (b)

Fig. 2. Schematic of (a) the electrically heated torch and (b) the flow facility.

rally gated (duration ~1 μs) to detect the entire fluorescence decay. The influence of elastic scattering of the laser light was examined by acquiring images of the flow without NO seeding and was observed to be negligible.

A gas mixture of 0.25% NO + 5% O_2 + 94.75% N_2 was chosen for two reasons. A low NO concentration was used to minimize attenuation of the laser sheet. In addition, for the conditions of this experiment, the electronic quenching rate of NO by N_2 was negligible, and so 5% O_2 was seeded into the flow to ensure that collisional quenching dominated the deexcitation from the A state ($A \sim 5 \times 10^6\ \mathrm{s}^{-1}$, $Q \sim 2 \times 10^8\ \mathrm{s}^{-1}$ at 295 K and 1 atm). The flow rate through the torch was 7.2 standard liters per minute (slpm), the shroud flow rate was 50.8 slpm, and the resulting torch and shroud velocities were 2.4 m/s and 0.2 m/s, respectively. Thus the torch's Reynolds number based on jet diameter was 1200 at 295 K and 160 at 1000 K.

In the limit of weak laser excitation, the LIF signal can be analyzed with

$$S_f \sim [F_{v''J''}(T)/T^{1/2}]G(T). \qquad (16)$$

Criteria for selection of an appropriate absorption transition for one-line thermometry include sensitive and monotonic temperature dependence of the fluorescence signal, sizable fractional population over the temperature range of interest (for maximization of the fluorescence signal), and negligible overlap with neighboring lines. Equation (16) illustrates that the fluorescence signal will tend to decrease as temperature increases because of the $T^{1/2}$ dependence. Thus the temperature sensitivity of the fluorescence signal will be maximized by selecting a transition with a fractional population that also decreases with increasing temperature. In addition, to maximize the fractional population over the temperature range of interest (295 K to ~1000 K), an appropriate absorption transition will be the line with a lower state that has a maximum population at 295 K. An examination of the NO A–X (0, 0) spectrum[44] illustrates that the $Q_2(7)/F_{12}(7)$ line pair is an appropriate choice for single-line thermometry, because the $N'' = 7$ level is the most highly populated state at room temperature, and this transition is separated from nearby lines by at least 2.4 cm^{-1}.

Calculation of the line-shape overlap integral requires knowledge of the laser linewidth. The laser linewidth at 226 nm has been measured[53] with a fixed-gap air-spaced étalon (Tec Optics) to be ~0.6 cm^{-1}, and the laser line shape can be approximated by a Gaussian. The laser linewidth has been observed to vary by as much as ±10% from shot to shot, and the laser position can vary by ~0.02 cm^{-1}. The laser line shape can be combined with the NO Doppler width, collision width, and collision shift to calculate the temperature dependence of the overlap integral. The Doppler width of NO at 226 nm is

$$\Delta\nu_D = 0.1(T/295)^{1/2}\ \mathrm{cm}^{-1}. \qquad (18)$$

The gas mixture in this experiment is predominantly N_2, and thus the pressure broadening of NO is dominated by NO–N_2 collisions. Chang *et al.*[46] have shown that the collision width and shift for NO broadening by N_2 are given by

$$\Delta\nu_c = 0.583P(295/T)^{0.75}\ \mathrm{cm}^{-1}, \qquad (19)$$

$$\text{Collision shift} = -0.18P(295/T)^{0.56}\ \mathrm{cm}^{-1}, \qquad (20)$$

where P is the pressure (atm). The overlap integral has been calculated on the basis of the assumption that the laser is tuned to absorption linecenter at 295 K and that the collision shift results in detuning of the laser at elevated temperatures. The result (plotted in Fig. 3) illustrates that the overlap integral varies by ~34% (from 0.76 to 1.02 cm) for temperatures ranging from 295 to 1100 K. Thus an assumption of a constant overlap integral will lead to errors in the predicted variation of the fluorescence signal with temperature.

The overlap integral can be combined with the Boltzmann fraction for the $Q_2(7)/R_{12}(7)$ transition to compute the variation of the NO LIF signal with temperature. The results of this calculation are shown in Fig. 4. Examination of this plot indicates that the signal varies monotonically by a factor of ~3 over the temperature range of interest. Single-point measurements of NO LIF have been acquired and are plotted in Fig. 4, and the good agreement between the calculation and measurements confirms the accuracy of the modeling.

Saturation effects in NO LIF have been examined by measuring the variation in the temporally integrated fluorescence signal with increases or decreases in laser intensity. A single-point LIF saturation measurement was performed at 295 K and 1 atm for the selected gas mixture and the $Q_2(7)/R_{12}(7)$ transition, and the results are plotted in Fig. 5, along with

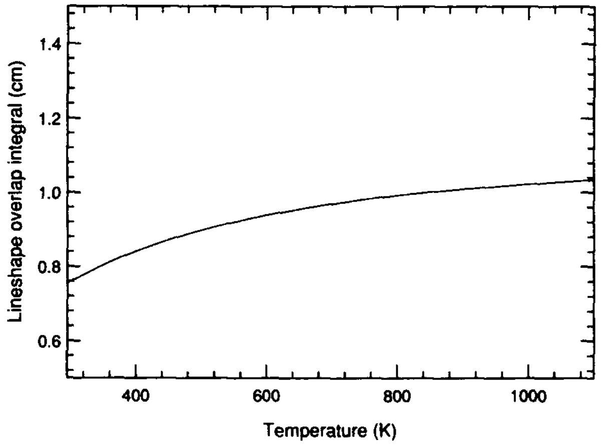

Fig. 3. Variation of the line-shape overlap integral from 295 to 1100 K for NO at 1 atm. The laser linewidth is 0.6 cm^{-1}, and the laser line shape is Gaussian. It is assumed that the laser is tuned to the center of the absorption line at 295 K, and this calculation includes the effect of the collision shift of the absorption line with respect to the laser line at elevated temperatures.

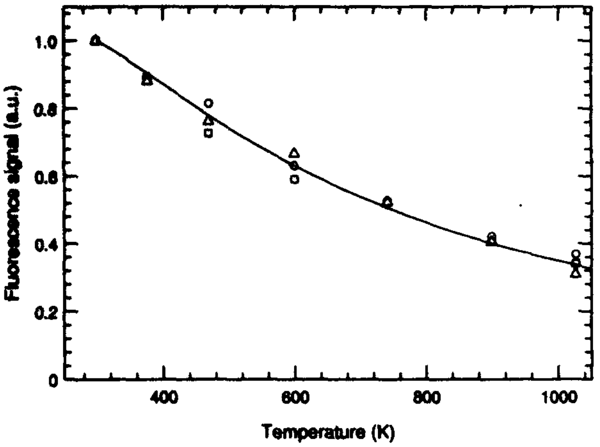

Fig. 4. NO fluorescence signal as a function of temperature for excitation of the $Q_2(7)/R_{12}(7)$ line. The solid line is a theoretical calculation of the fluorescence signal variation, and the data points are LIF measurements. The data were acquired in three separate sets, and each data set is normalized to unit value at 295 K. The gas mixture is 0.25% NO + 5% O_2 + 94.75% N_2.

calculations from the six-level model for NO LIF. The sheet intensity was varied with UV neutral density filters (Esco Corp.) and was determined by measuring the laser-pulse energy, beam height, and beam width and combining these parameters with calculations of the line-shape overlap integral. Combining typical laser parameters (~ 0.5 mJ/pulse, 5-cm height, ~ 300-μm width) with an overlap integral of ~ 0.75 cm leads to a peak laser intensity of ~ 0.0025 J cm/cm^2. Examination of the result in Fig. 5 illustrates that no significant saturation effect is observed for laser intensities of this magnitude, and thus the weak excitation limit is valid for analysis of the LIF signal. These results also show that the laser intensity could be increased (with a corresponding increase in signal) without incurring significant saturation effects.

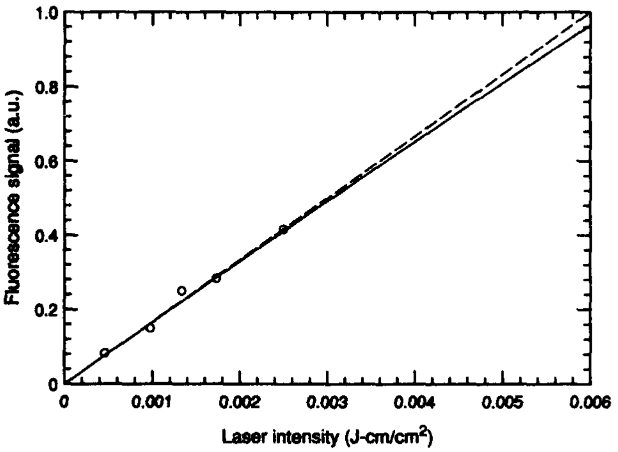

Fig. 5. NO LIF measurements and rate equation calculations of saturation effects at 295 K for a mixture of 0.25% NO + 5% O_2 + 94.75% N_2. The results of the rate equation calculations are denoted by the solid line, and the dashed line denotes linear fluorescence. The LIF measurements are represented by the data points and are normalized at the maximum laser intensity. The laser sheet intensity in this experiment is ~ 0.0025 J cm/cm^2.

Additional measurements (not presented here) that were performed at higher laser intensities indicate that saturation effects in NO LIF are accurately predicted by the simple five- and six-level models presented above.[53] The accuracy of these simple models eliminates the necessity for development of more complex multilevel models for NO LIF.

PLIF Imaging of Temperature

Single-shot and 100-frame-average PLIF images were acquired at two vertical positions above the exit of the torch. The imaged regions are 25 mm wide × 28 mm tall, and the first region (the lower view) extended from 2 mm below to 26 mm above the torch exit, whereas the second region (the upper view) extended from 24 mm to 52 mm above the torch exit. The 100-frame-average images of the laser sheet distribution were acquired by operating the torch and shroud flows without applying voltage to the torch and imaging the fluorescence from the uniform field of NO. The PLIF images were corrected for variations in the laser sheet spatial distribution and the camera background.

The PLIF images have been converted into 2-D images of temperature by calibrating the fluorescence signal with the known temperature at one point in the flowfield (measured with a thermocouple). Errors can be incurred if the temperature at the calibration point is varying, and thus calibration in the edges of the jet where mixing between the hot and cold fluid occurs is not appropriate. It appears that the shroud region would be the preferred calibration point, because the signal is maximum in this location. However, wide temperature variations (~ 350 ± ~ 50 K) resulting from the heating of the shroud gas as it flows over the exterior of the torch make this region inappropriate for calibration. Thus points along the jet centerline have been chosen for calibration, because the temperature is essentially invariant in this region. The images in the lower view are calibrated at a point 1 cm above the exit of the torch, and the calibration point for the upper-view images was 3 cm above the exit. The resultant PLIF images of temperature are shown in Fig. 6. Note that the single-shot images display significant flow structure, whereas the averaged images only show a monotonic variation in temperature from the centerline to the shroud. This comparison illustrates the importance of acquiring flow-stopping data to observe the complex fluid dynamics.

Radial profiles of temperature were taken from the averaged PLIF images at y = 10 mm and 20 mm in the first viewed region [Fig. 6(a)], and at y = 30, 40, and 50 mm in the second viewed region [Fig. 6(b)]. The profiles are plotted in Fig. 7, along with profiles acquired by translating a Pt/Pt-10%Rh thermocouple (3-mil bead) radially across the torch flow and averaging 20 readings at each location. The thermo-

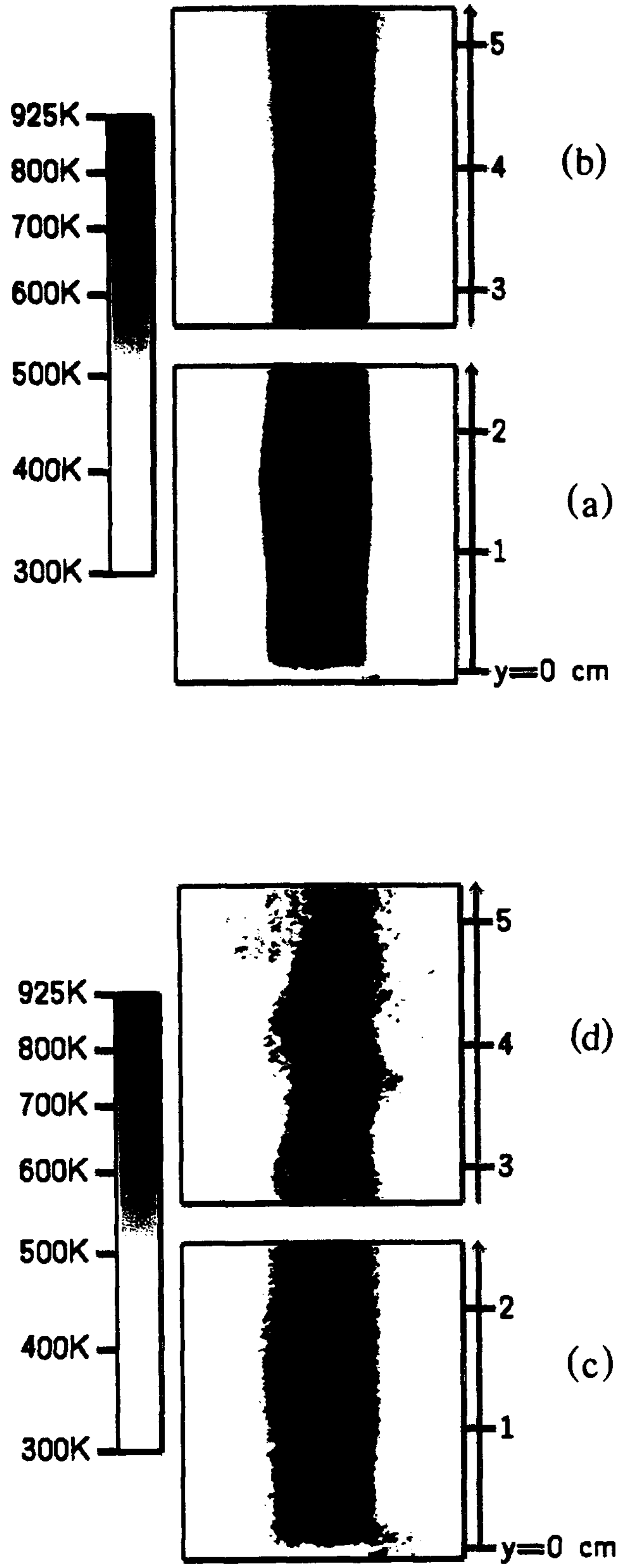

Fig. 6. PLIF images of temperature. The gray color bar indicates the temperature scale. (a) 100-frame-average image, $y = -2$ to 26 mm; (b) 100-frame-average image, $y = 24$ to 52 mm; (c) single-shot image, $y = -2$ to 26 mm; (d) single-shot image, $y = 24$ to 52 mm.

couple data have been corrected for radiation losses, and the error bars on the data correspond to twice the standard deviation of each measurement. The discrepancy between the two measurements is <40 K in all cases.

Previous studies of axisymmetric jets[59] have determined that a region of potential flow (termed the potential core) is present in the center of the jet near the jet exit. The mixing of the jet with the freestream causes a reduction in the size of this region until approximately five diameters downstream of the exit, at which point the potential core ends and the flow is fully established. The radial temperature profiles in Fig. 7 clearly illustrate the presence of this conical potential flow region extending from the jet exit to ~ 40 mm downstream, corresponding to roughly five jet diameters.

The accuracy of the one-line thermometry technique can be examined by analyzing the sources of measurement error. Sources of error include variations in the collisional quenching rates, incorrect calibration of the PLIF images, variations in the laser line shape, and random noise in the images. Estimates indicate that the error resulting from quenching is $<5\%$, primarily because of uncertainty in the quenching cross-section data. Errors in calibration of the images are estimated to be $\sim 1\%$ or less, because of the stability of the flow at the calibration points in the potential core. Laser line-shape effects (including variations in linewidth, line position, and line shape) are estimated to cause a maximum error of $\sim 6\%$, and averaging of the data will reduce this error to $\sim 2\%$.

The primary source of random error in this experiment is the shot noise of the measurement. The varying signal level throughout the images results in variations in the signal-to-noise ratio (SNR), and an examination of the PLIF images shown in Fig. 6 shows a SNR ranging from ~ 7 (in the core of the jet) to ~ 10 (in the shroud region) for the single-shot images and ~ 70 (in the core) to ~ 100 (in the shroud) for the 100-frame-average images. The images are processed with 100-frame-average images of the laser sheet profile and background, which have SNR's of ~ 70–100, and each image is calibrated against the signal at one point in the core of the flow. Thus the random error resulting from shot noise is $\sim 14\%$ to 20% for the single-shot image and $\sim 2\%$ for the average image.

From these results we estimate that the single-shot PLIF temperature measurements have a maximum error of $<12\%$ because of systematic effects and $<20\%$ because of random error, whereas the average measurements have a maximum systematic error of $<8\%$ and a random error of $\sim 2\%$. The systematic error in these measurements could be reduced with more precise data on collisional quenching rates and careful monitoring of the laser parameters from shot to shot with an étalon. In addition, the application of lasers with broader or narrower line shapes will

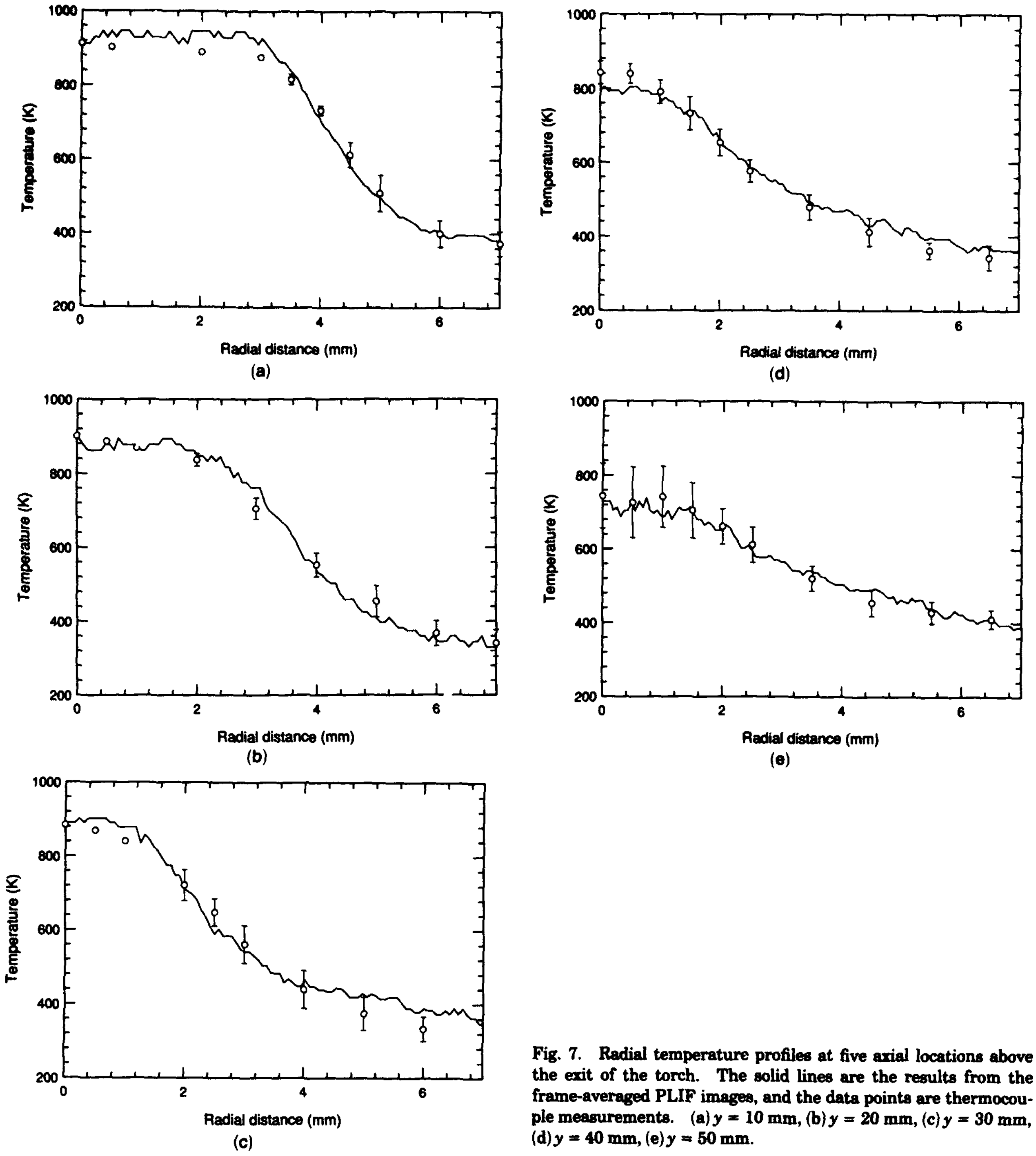

Fig. 7. Radial temperature profiles at five axial locations above the exit of the torch. The solid lines are the results from the frame-averaged PLIF images, and the data points are thermocouple measurements. (a) $y = 10$ mm, (b) $y = 20$ mm, (c) $y = 30$ mm, (d) $y = 40$ mm, (e) $y = 50$ mm.

also reduce the measurement error. The use of broader lasers is constrained by several factors, including reduced signal levels because of decreased laser intensity, the possibility for unwanted excitation of neighboring absorption transitions, and limited flexibility in laser linewidths, particularly at frequency-doubled wavelengths.

Reduction of the random error requires an increase in the fluorescence signal, which can be achieved in a number of ways. The saturation measurement presented in Fig. 5 illustrates that the laser intensity can be increased considerably without introducing significant nonlinearity into the measurement. In addition, the signal can be increased by reducing the O_2 mole fraction, thus decreasing the collisional quenching rate. This may result in a more complex dependence of the fluorescence signal on temperature because of the temperature dependence of the N_2 quenching cross section,[48] but this variation can be accounted for. An increase in the NO mole fraction will also result in an improvement in SNR, but it may not be practical because of increasing optical attenuation.

NO Two-Line Thermometry

Introduction

The NO two-line thermometry technique has been demonstrated in an underexpanded jet flow. This flow is useful for the development of measurement methods for a number of reasons. The wide variations in pressure, temperature, and velocity throughout the flowfield represent a strenuous test for diagnostic techniques. In addition, this flow has been well studied, and the flow properties can be calculated along the jet center line by use of correlations[60] or throughout the flowfield with a method-of-characteristics solution.[13]

A schematic of the underexpanded jet is shown in Fig. 8. Gas flows from a high-pressure reservoir into a low-pressure background region, and for pressure ratios above ~4–5, the barrel shock structure[60] is formed. Within the barrel shock, the gas undergoes an isentropic expansion, resulting in decreases in pressure, temperature, and density, and increases in Mach number and velocity. This expansion is bounded in the axial direction by a normal shock (termed the Mach disk), and in the radial direction by incident shocks. The flow within the barrel shock is steady.

A schematic of the experimental facility is shown in Fig. 9. A mixture of 1% NO in air flowed from the reservoir (P_{res} = 630 Torr) through a 1.8-mm-diameter nozzle into the background region (P_{back} = 10 Torr), which was maintained at low pressure through continuous evacuation. The pressure ratio of 63:1 corresponded to a distance from the jet exit to the Mach disk of $x_M/D = 5.3$.[60] The Mach number in this flow varied from $M = 1$ at the nozzle exit to $M = 6.5$ at the Mach disk, and the pressure and temperature decreased from 330 to 0.25 Torr and from 250 to 30 K, respectively.

The beam from a doubled excimer-pumped dye laser (Lambda Physik EMG 203/FL 2002) was sequentially tuned to excite two different rotational transitions in the A–X (0, 0) band of NO at 226 nm. The ~3-mJ laser beam was formed into a 100-μm-thick × 10-mm-high sheet with a 50-cm spherical lens and two cylindrical lenses (50 mm negative and 500 mm positive), and the sheet propagated through the flowfield along the center line of the underexpanded jet. The resulting fluorescence was detected with the same imaging system used in the one-line experiment. The PLIF images resulting from excitation of each of the two NO lines were acquired following tuning of the laser to each transition, and the two images were processed to determine the temperature variation throughout the flowfield.

Selection of appropriate transitions for two-line thermometry measurements requires consideration of several criteria. The chosen transitions should be isolated from other lines and should originate from initial states with a population ratio that is a strong function of temperature over the temperature range of interest. In addition, the signal in each image must be sufficiently large to avoid errors resulting from poor SNR, and the fluorescence signal variation in each image must not exceed the dynamic range of the detection system.

Rate equation modeling (discussed below) illustrates that for $x/D < 1.5$, typical laser sheet intensities result in partial saturation of the absorption transitions. However, beyond $x/D \approx 1.5$ the low density in this flow results in reduced collisional quenching and RET rates (at $x/D = 2$, $Q \sim 10^7\ \text{s}^{-1}$, $R \sim 1.5 \times 10^8\ \text{s}^{-1}$; at $x/D = 5$, $Q \sim 9 \times 10^5\ \text{s}^{-1}$, $R \sim 1.3 \times 10^7\ \text{s}^{-1}$), leading to complete saturation of the NO fluorescence. In addition, because collisional quenching is slow compared with the laser-pulse duration, a simple two-step model for the fluorescence

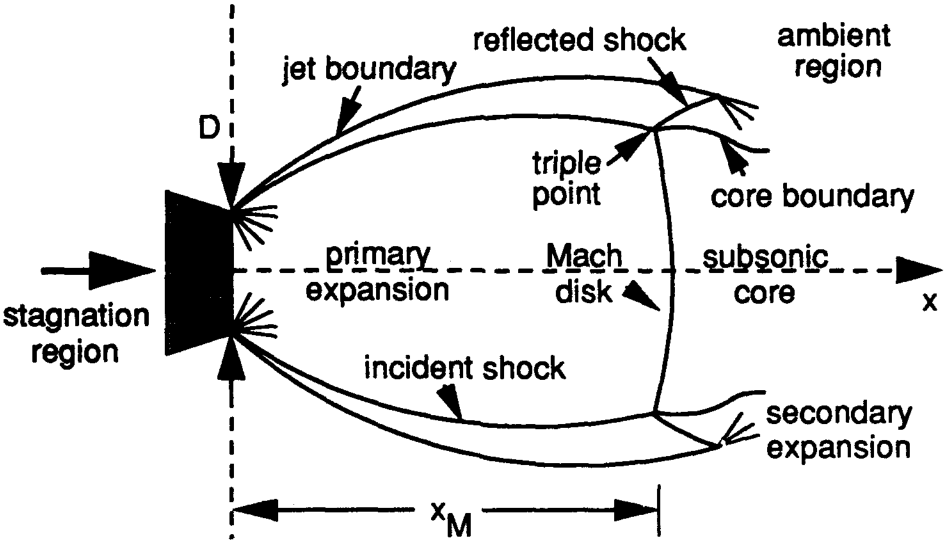

Fig. 8. Schematic of the barrel shock flow structure.

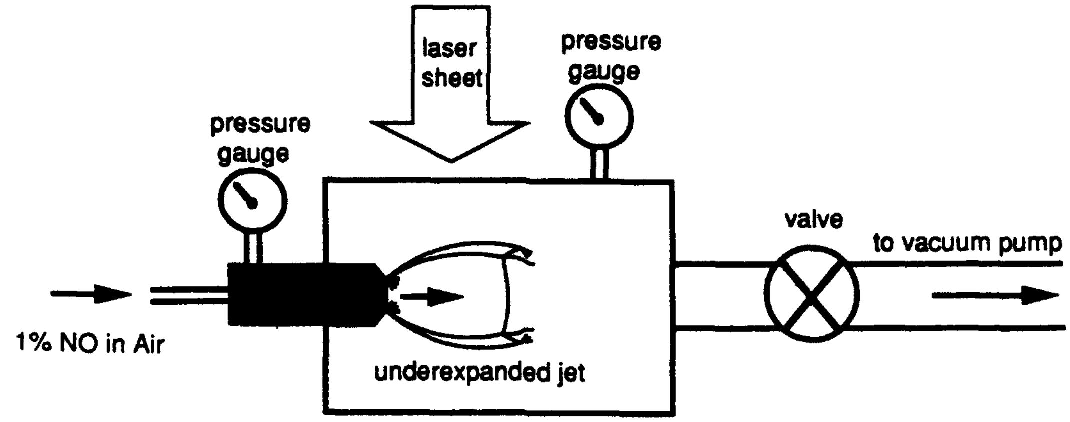

Fig. 9. Schematic of the underexpanded jet flow facility.

was used. As discussed previously, in the limit of strong excitation the fluorescence signal will reduce to

$$S_{\text{total}} \sim [N_1^0 b_{12}/(b_{12} + b_{21})]\{A_{21}\tau + [A_{21}/(A_{21} + Q_{21})]\}. \tag{11}$$

Because the fluorescence signal is related to density, near the Mach disk the signal will be low (because of the decreased density) unless the fractional population in the absorbing state is relatively high [i.e., $F_{v''J''}(T)$ is very large]. Thus the choices for appropriate transitions for a two-line temperature measurement in this flow are limited to relatively low-lying rotational levels, because the rotational populations in the two initial states must be maximized at low temperatures. However, if transitions originating from the two lowest rotational levels (i.e., $N'' = 0$, and $N'' = 1$) are chosen to maximize the fluorescence signal, the signal ratio will not be a very sensitive function of temperature because of the small energy spacing between these levels. The solution to this tradeoff is to select one line that originates from the lowest possible rotational level and then select another line that provides enough signal to obtain a reasonably high SNR but also has a sizable rotational level spacing. The dynamic range of the measurement system should also be considered in this analysis, because errors resulting from detector saturation will occur if the range of signal variation throughout the flowfield exceeds this dynamic range.

An examination of the NO spectra indicates that the lowest accessible rotational level is the $N'' = 0$, $J'' = 1/2$ level in the $X\,^2\Pi_{1/2}$ electronic state of NO. Three transitions [$Q_1(0)$, $R_1(0)$, and $R_{21}(0)$] originate from this level. The $Q_1(0)$ line is partially overlapped by several lines, including $P_1(17)$, $Q_1(4)$, and $P_2(25)$, and the $R_1(0)$ line is partially overlapped by $Q_1(6)$ and $Q_2(18)$. In contrast, the $R_{21}(0)$ line is only overlapped by the $P_1(19)$ line, and for the range of temperatures encountered in this experiment, the contribution of the latter line to the fluorescence signal is negligible. Thus the $R_{21}(0)$ line is an appropriate choice for excitation of a low-lying rotational level.

For selection of the second transition, the variation in signal throughout the flowfield has to be predicted and compared with the detection system dynamic range. In addition, the temperature dependence of the Boltzmann fraction for each transition has to be calculated to determine the sensitivity of the signal ratio to temperature. The nominal dynamic range of the Amperex CCD camera system is ~80–200,[61] and for the experiments performed here, this dynamic range was reduced considerably because of fixed-pattern noise in the camera. An appropriate choice for the second excitation line is $P_1(3)$, and a prediction of the fluorescence signal variation, modeled by $N_T F_{v''J''}(T)\{A_{21}\tau + [A_{21}/(A_{21} + Q_{21})]\}$, as a *function of center line distance for the* $R_{21}(0)$ *and* $P_1(3)$ transitions (shown in Fig. 10) illustrates that no errors should be incurred because of saturation of the detection system. The temperature sensitivity of the signal ratio can be illustrated by plotting the Boltzmann fraction ratio of the two lines as a function of temperature. Examination of the result (shown in Fig. 11) indicates that over the temperature range of interest (30–100 K, corresponding to $x/D = 1.5$–5.3) the population ratio is a monotonic and sensitive function of temperature. Thus the

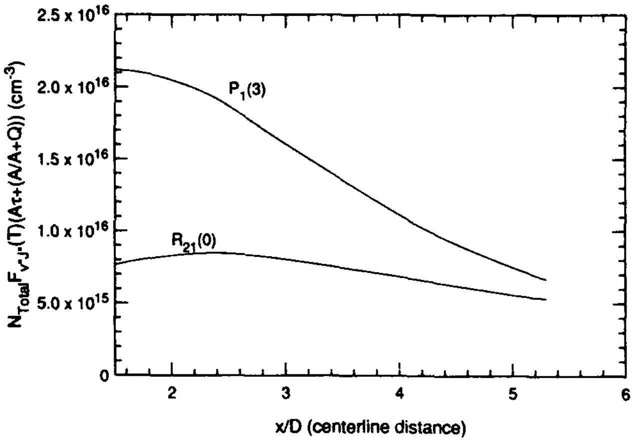

Fig. 10. Plot of $N_T F_{v''J''}(T)\{A_{21}\tau + [A_{21}/(A_{21} + Q_{21})]\}$ as a function of center line distance from $x/D = 1.5$ to $x/D = 5.3$ for the $R_{21}(0)$ and $P_1(3)$ lines.

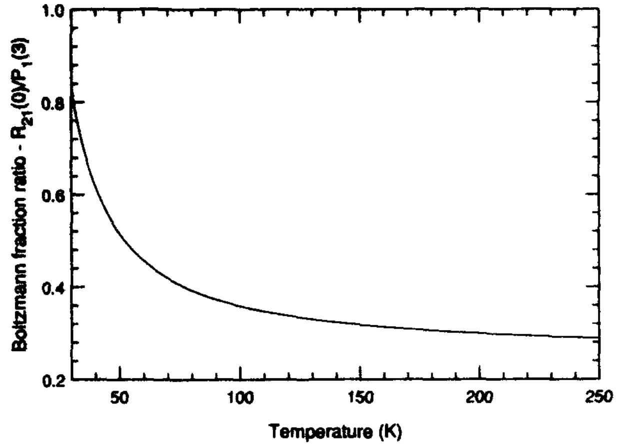

Fig. 11. Variation of the Boltzmann fraction ratio for the $R_{21}(0)$ and $P_1(3)$ transitions as a function of temperature.

excitation of this pair of lines is a viable strategy for two-line thermometry.

The five-level model for NO LIF has been used to analyze saturation effects for excitation of the $R_{21}(0)$ and $P_1(3)$ lines. Calculations have been performed for temperatures and pressures corresponding to the physical conditions at the axial locations $x/D = 1, 2, 3, 4$, and 5 along the center line of the flow, permitting examination of the onset of saturation as a function of axial position. Fig. 12 illustrates the results of these calculations for the $R_{21}(0)$ transition [the results for the $P_1(3)$ transition are similar]. The estimated laser intensity in this experiment is ~0.375 J-cm/cm^2, corresponding to a laser-pulse energy of 3 mJ in a 100 μm × 10 mm sheet and an overlap integral of ~1.25 cm. These results demonstrate the growing importance of saturation effects as the flow propagates downstream and the onset of complete saturation (to within <5%) for $x/D > 1.5$.

PLIF Imaging of Temperature

Figure 13 displays 50-frame-average PLIF images acquired following excitation of the $R_{21}(0)$ and $P_1(3)$ lines. The flow moves from left to right, and the imaged region is 15 mm × 20 mm. A comparison of the signal variation throughout these two images illustrates the temperature sensitivity of the measurement. The $R_{21}(0)$ image displays a slowly decreasing signal level from the nozzle exit to the Mach disk, whereas the $P_1(3)$ image shows a more rapid decrease in signal as the Mach disk is approached. In both images, the fluorescence signal is quite low in the background region outside the barrel shock because of the combination of high temperature (295 K) and moderate pressure (10 Torr). The signal persists in the shear layer because of the low temperature (~100 K) combined with the moderate pressure (roughly equal to the background pressure) in this region.

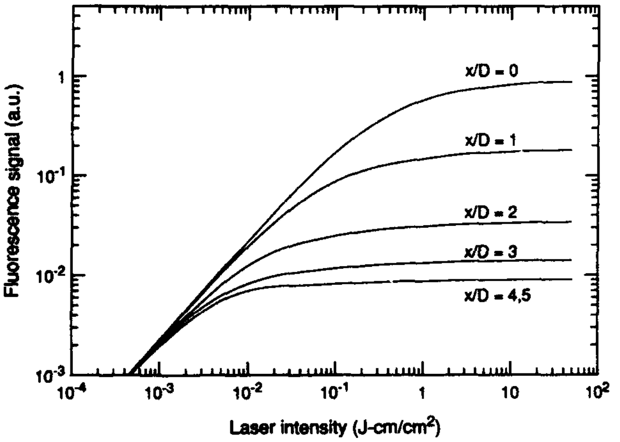

Fig. 12. Fluorescence signal versus laser intensity at five axial locations $x/D = 0, 1, 2, 3, 4$, and 5, for excitation of the $R_{21}(0)$ transition. The laser intensity in this experiment was ~0.375 J cm/cm^2.

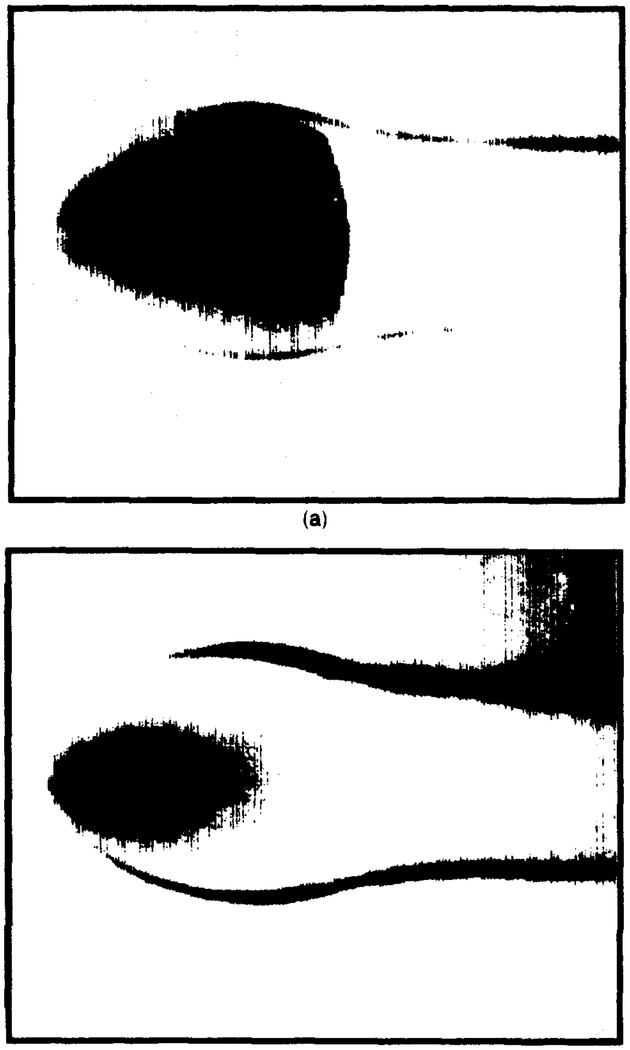
(a)

(b)

Fig. 13. 50-frame-average PLIF images acquired following excitation of the $R_{21}(0)$ and $P_1(3)$ lines. (a) $R_{21}(0)$, (b) $P_1(3)$. The images are displayed with a gray color scale, where white indicates no signal and black indicates the maximum signal.

Several forms of image processing are performed to extract temperature from these images. Fixed-pattern noise is removed by spatially filtering the images, background frames are subtracted, and the effects of asymmetry resulting from velocity-induced Doppler shifts are reduced by averaging the images about the jet center line. Note that removal of the fixed-pattern noise through subtraction of background images was not possible because of the tendency for the noise to drift temporally and spatially.[53] Note also that corrections for spatial variations in the laser sheet intensity are unnecessary because of the saturation of the absorption transition. The ratio of the processed images results in an image that is a relative measure of temperature. The ratio image can then be calibrated at any point in the flowfield to determine the absolute temperature, because the temperature can be accurately predicted at all points. We have chosen to calibrate the image against the centerline temperature at a point in the barrel shock just before the Mach disk, because measurement errors resulting from deviations from saturation are minimized. At this point in the flowfield, the temperature is 31 K. The resultant temperature image is shown in Fig. 14. Note that although the image does extend from $x/D = 0$ to $x/D = 5.3$, the two-line temperature measurement is inaccurate for $x/D < 1.5$, because deviations from complete saturation in this region result in errors in the interpretation of the fluorescence signal.

The PLIF image of temperature in Fig. 14 has the expected characteristics. There is a monotonic decrease in temperature from the jet exit to the Mach disk. The temperature drops rapidly near the jet exit, and then more slowly as the Mach disk is approached. As we move radially away from the center line, the temperature decreases slowly, and at the edges of the barrel shock the temperature gradient is large. The temperature profile along the center line of the jet can be compared with the results from the correlation of Ashkenas and Sherman.[60] The comparison is shown in Fig. 15 and shows good agreement for $1.5 \leq x/D \leq 5.3$. The measurement agrees with the calculation to within ±6 K and ±9%.

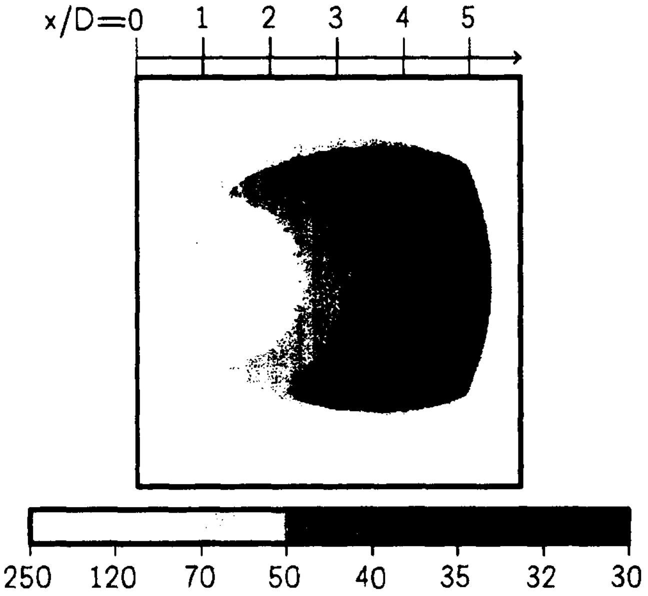

Fig. 14. PLIF image of temperature. The gray color bar indicates the temperature scale. The two-line temperature measurement is valid for $x/D > 1.5$.

Radial temperature profiles from the PLIF image can be compared with profiles calculated with a method-of-characteristics code.[13] The results of the comparison at axial locations $x/D = 2$, 3, 4, and 5 are shown in Fig. 16. Good agreement between the measured and calculated temperature profiles is observed, except for some deviation near the edge of the barrel shock at small x/D values ($x/D = 2$ and 3). In this region, the measured temperature is larger than the predicted temperature by as much as ~30%. There are two potential reasons for this error. First, a slight misalignment of the camera or laser sheet with respect to the flowfield can lead to deviations when the images are processed. In addition, spatial filtering of the images to remove the camera pattern noise can lead to errors in regions of high temperature gradient. Spatial filtering acts to alter the slope of the gradient, underpredicting the temperature at some locations and overpredicting it at others.

Other sources of systematic error in this experiment include the contribution of overlapped spectral features and variations in laser sheet intensity. The $R_{21}(0)$ line overlaps with the $P_1(19)$ line, and the $P_1(3)$ line overlaps with the $P_1(14)$ line. Because the $P_1(14)$ and $P_1(19)$ transitions originate from relatively elevated rotational levels, they are expected to contribute significant fluorescence signal at moderate-to-high temperatures, but the effects of these overlaps should be small at low temperatures. A calculation of NO absorption line strengths shows that at $T = 98$ K (corresponding to $x/D = 1.5$) the signal from excitation of the $P_1(19)$ line is less than 0.2% of the $R_{21}(0)$ signal, and the $P_1(14)$ line contributes <3% of the $P_1(3)$ signal. In addition, the contribution of these transitions decreases rapidly with decreasing temperature, and so the effect of the overlapping transitions on this temperature measurement should be negligible.

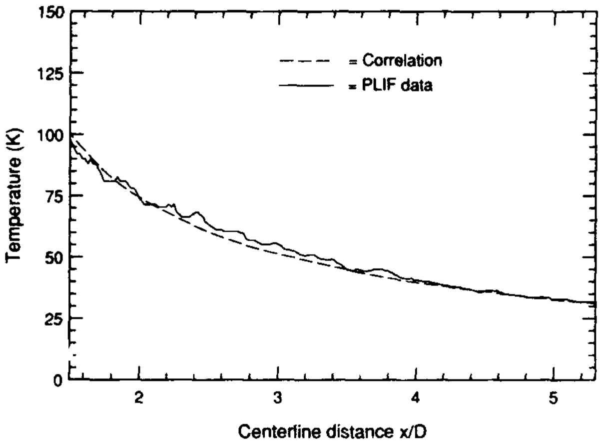

Fig. 15. Comparison between center line temperature profiles measured from the PLIF image in Fig. 14 and calculated with the correlation of Ashkenas and Sherman.[60]

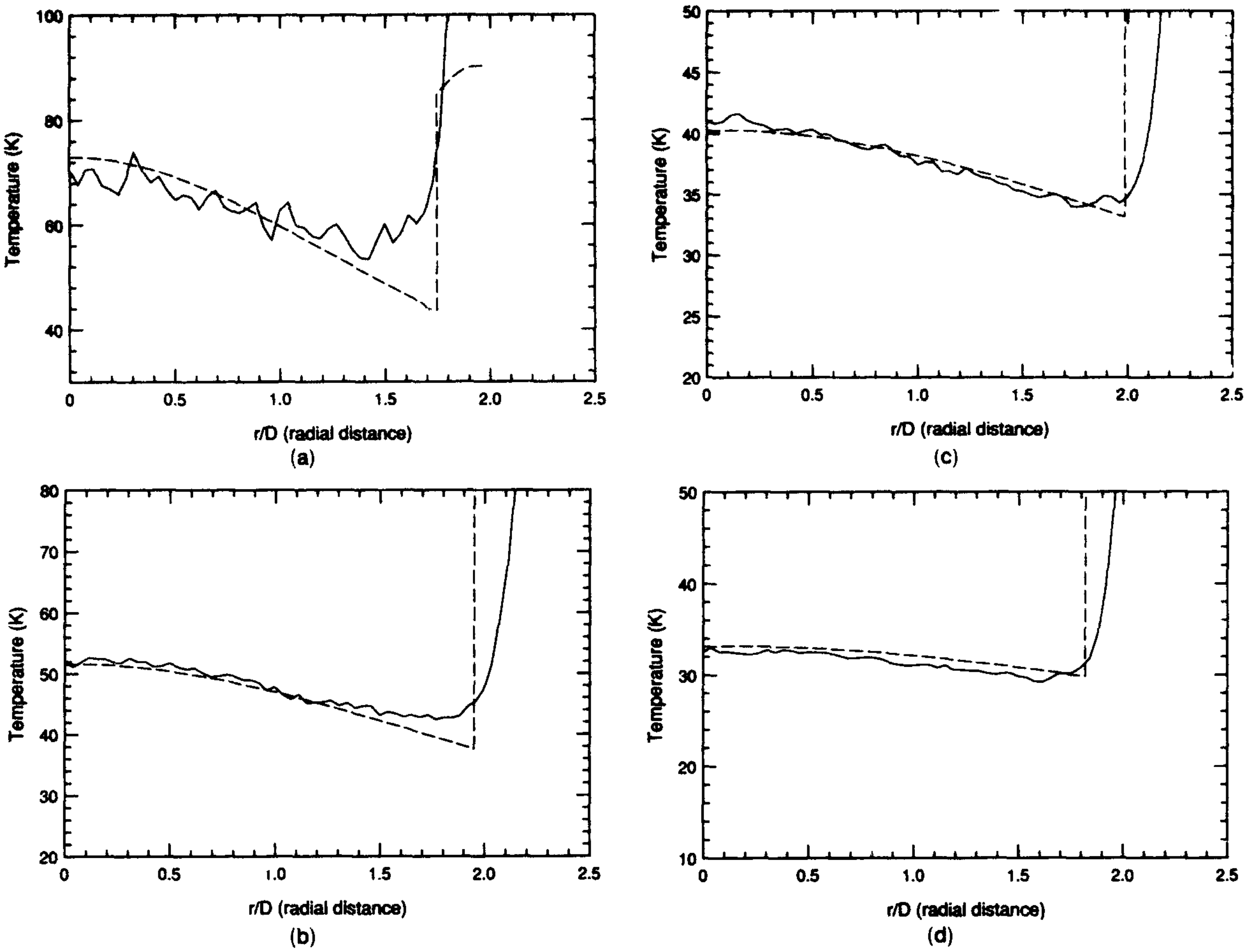

Fig. 16. Comparison between radial temperature profiles measured from the PLIF image in Fig. 14 and calculated with an MOC code.[13] The solid lines represent the PLIF data, and the dashed lines represent the MOC calculations. (a) $x/D = 2$; (b) $x/D = 3$; (c) $x/D = 4$; (d) $x/D = 5$.

Variations in the spatial profile of the laser sheet can cause deviations from saturation. The sheet profile was ~ 10 mm long and had a roughly Gaussian distribution, and the region of the flow from $x/D = 1.5$ to 5.3 was ~6 mm long. The laser sheet was centered at $x/D \sim 2$ to align the most energetic portion of the sheet with the region of the flow where deviations from saturation were most likely to occur (i.e., small x/D). Thus the laser intensity was estimated to vary from a maximum at $x/D = 2$ to 94% of maximum at $x/D = 1.5$ and 46% of maximum at $x/D = 5.3$. Variations of this magnitude cause insignificant deviations from saturation, and thus errors resulting from the spatial nonuniformity of the laser sheet should be negligible. Saturation was experimentally verified by varying the laser sheet intensity and observing minimal changes in the PLIF signal.

The signal variation throughout the barrel shock results in a variation in SNR (and thus in random error) in the images. The raw PLIF image of the $P_1(3)$ line has an SNR (neglecting fixed-pattern noise) of ~ 75 to 1 near the jet exit and ~ 25 to 1 at the Mach disk, whereas the raw image of the $R_{21}(0)$ line has a SNR of ~ 50 to 1 near the exit and ~ 25 to 1 near the Mach disk. The spatial filtering of the images acts to increase this SNR by a factor of ~ 2. The resultant SNR of the ratio image (computed from the square root of the sum of the squares of the error in each image) is ~ 80 to 1 near the jet exit and ~ 35 to 1 at the barrel shock. Thus the random error in the fluorescence signal ratio varies from ~ 1.5% (at small x/D) to ~ 3% (at large x/D). The resultant estimate for the random error in the temperature measurement is ~ 2 K at $x/D = 1.5$ and ~ 1 K at $x/D = 5.3$, corresponding to 2% and 3% errors, respectively.

The error analysis presented above shows that the minimum error in the temperature measurement is ~ 3% near the Mach disk along the jet center line, and the error is larger near the jet exit and near the edges of the barrel shock. In future experiments, systematic errors can be decreased if the following steps are taken:

1. Averaging the images about the center line of the jet to remove the velocity-induced Doppler shift leads to errors. The effect of the Doppler shift can be minimized with more accurate tuning of the laser

wavelength (e.g., by pressure tuning) and shot-to-shot monitoring of the laser line shape with an étalon. Broadening of the laser linewidth will also reduce the influence of this effect.

2. Fixed-pattern noise is generated in the camera readout by imbalances in the gains and offsets of the three output amplifiers. Removal of this noise requires spatial filtering of the PLIF images, which can lead to measurement errors. Pattern noise can be significantly reduced by carefully adjusting the camera before data acquisition. Unfortunately the spatial and temporal drift of the noise makes elimination of this noise source difficult. One solution to this problem is the use of a camera that has only a single output amplifier. In such a device, no fixed-pattern noise is generated.

3. The slight misalignment of the flowfield with respect to the laser–camera system results in significant measurement errors near the edges of the barrel shock when the images are processed to remove the effects of Doppler shifts. These deviations can be removed through careful alignment of the imaged region with a focusing target. In measurements where two cameras are used (e.g., an instantaneous two-line thermometry experiment), the cameras have to be carefully indexed, and the images should be processed to remove residual distortions.

Extension to Other Flow Studies

Application of the one- and two-line NO LIF thermometry techniques to more complex flow environments requires consideration of several factors. Variations in pressure, temperature, and chemical composition (such as those encountered in flames or wind tunnel flows) can complicate the prediction and analysis of fluorescence signals. In addition, in studies of rapidly varying flows, the necessity for acquisition of single-shot measurements can lead to errors that are reduced in time-averaged measurements. Potential sources of uncertainty include fluctuations in NO mole fraction, collisional quenching rates and collision widths; temporal, spatial, and spectral variations of the laser; inaccurate calibration of the fluorescence signal; and decreased signal because of reduced NO concentrations and increased quenching rates.

As discussed above, the one-line thermometry technique is highly sensitive to changes in the physical composition of the gas. Variations in quench rates and linewidths will increase the measurement error, and in flows where the NO mole fraction fluctuates, the one-line technique cannot be used. In contrast, when the two-line technique is applied, ratioing of the fluorescence signals, combined with the relatively small variations in the collisional quenching cross sections and collision-broadening coefficients throughout the $A(v' = 0)$ level of NO, will tend to minimize the influence of these variations. Thus for temperature measurements in complex flows (particularly in chemically reacting flows), the two-line thermometry method will be preferred.

Pulsed dye lasers have several advantages for PLIF studies, including a wide range of accessible wavelengths, narrow linewidths ($\Delta\nu_L \sim 0.1\text{–}1.0\ \mathrm{cm}^{-1}$), and relatively high power. Unfortunately variations in laser parameters can lead to measurement errors. First the laser line shape often consists of several competing spectral modes, and the distribution of energy within these modes can vary during the laser pulse and from pulse to pulse. In cases where the laser and absorption linewidths are of the same order, laser line-shape fluctuations may have a significant effect on the fluorescence signal, particularly for single-shot measurements. This error can be reduced by use of a laser with a linewidth that is much broader or narrower than the absorption line. In cases where this is not possible, the laser line shape should be monitored with an étalon. This étalon can also be used to check the tuning and stability of the laser wavelength. Second, as discussed above, temporal variation of the laser energy can lead to errors in cases where saturated fluorescence is used. Rate equation modeling and saturation measurements can assist in analyzing the magnitude of this effect. Third, the spatial variation of the laser sheet should be measured by projecting the sheet onto a linear or 2-D array, or by acquiring images of a uniform field (e.g., by using PLIF or Rayleigh scattering).

Calibration of the PLIF signal (or signal ratio in the two-line technique) is necessary to convert the measured fluorescence signal into temperature. The accuracy of the temperature measurement is limited by the accuracy of this calibration. Calibration of the measurements in this study was straightforward because the flows that were examined were steady, and because the temperature at any point could be calculated (in the supersonic jet) or measured with a thermocouple (in the laminar heated jet). Alternative calibration techniques (required in more complex flows) include simultaneous measurement of the temperature at a single point in the flowfield with another method (e.g., absorption spectroscopy or coherent anti-Stokes Raman spectroscopy) or measurement of the fluorescence signal from a reference cell containing a known concentration of NO. Careful monitoring of experimental parameters (in particular, the detector sensitivity and the laser energy, line shape, and spatial profile) can also be used to directly determine the calibration constant.

In the studies performed here, gas mixtures with large NO mole fractions and small quantities of quenching species were used to maximize the fluorescence signal. In flows where the NO mole fraction is smaller (e.g., flames), the decreased NO concentration will result in reduced fluorescence signals. In addition, the fluorescence signal will also be decreased by increased concentrations of rapid quenchers such as H_2O or CO_2. Increases in laser intensity can compensate for decreases in the fluorescence signal but may lead to the onset of saturation effects. Linearity of the fluorescence signal can be accurately evaluated by use of the five- and six-level models we have presented here and, in addition, should be checked with saturation measurements.

Conclusions

One-line and two-line thermometry techniques based on PLIF of NO have been applied to planar measurements of temperature. The one-line technique provides a simple method for acquiring flow-stopping (single-shot) measurements with a single laser and detection system, but the applicability of this technique is limited. In contrast the NO two-line technique can be used in a wide range of flows, but two measurements are required to determine temperature. The development of multilevel rate equation models has enabled analysis of energy transfer in NO LIF and examination of the onset of saturation effects. Finally the availability of comprehensive spectroscopic data on the NO A–X (0, 0) band system permits accurate prediction of NO fluorescence signals.

This research was supported by the U.S. Air Force Office of Scientific Research, Aerospace Sciences Directorate, with Julian Tishkoff as technical monitor.

References

1. M. L. Elder and J. D. Winefordner, "Temperature measurements in flames—a review," Prog. Anal. At. Spectrosc. **6,** 293–427 (1983).
2. N. M. Laurendeau, "Temperature measurements by light-scattering methods," Prog. Energ. Combust. Sci. **14,** 147–170 (1988).
3. A. C. Eckbreth, *Laser Diagnostics for Combustion Temperature and Species* (Abacus, Kent, England, 1988).
4. R. L. McKenzie, "Progress in laser-spectroscopic techniques for aerodynamic measurements—an overview," presented at the American Institute of Aeronautics and Astronautics Twenty-Ninth Aerospace Sciences Meeting, Reno, Nevada, 7–10 January 1991.
5. M. B. Long, P. S. Levin, and D. C. Fourguette, "Simultaneous Two-dimensional mapping of species concentratoin and temperature in turbulent flames," Opt. Lett. **10,** 267–269 (1985).
6. D. C. Fourguette, R. M. Zurn, and M. B. Long, "Two-dimensional Rayleigh thermometry in a turbulent nonpremixed methane–hydrogen flame," Combust. Sci. Technol. **44,** 307–317 (1986).
7. R. J. Cattolica and D. A. Stephenson, "Two-dimensional imaging of flame temperature," in *AIAA Progress in Aeronautics and Astronautics,* J. R. Bowen, N. Manson, A. K. Oppenheim, and R. I. Soloukhin, eds. (American Institute of Aeronautics and Astronautics, New York, 1984), Vol. 95, pp. 714–721.
8. J. M. Seitzman, G. Kychakoff, and R. K. Hanson, "Instantaneous temperature field measurements using planar laser-induced fluorescence," Opt. Lett. **10,** 439–441 (1985).
9. M. P. Lee, P. H. Paul, and R. K. Hanson, "Quantitative imaging of temperature fields in air using planar laser-induced fluorescence of O_2," Opt. Lett. **12,** 75–77 (1987).
10. T. Ni-Imi, T. Fujinoto, and N. Shimizu, "Method for planar measurement of temperature in compressible flow using two-line laser-induced iodine fluorescence," Opt. Lett. **15,** 918–920 (1990).
11. R. J. Hartfield, Jr., S. D. Hollo, and J. C. McDaniel, "Planar temperature measurement in compressible flows using laser-induced iodine fluorescence," Opt. Lett. **16,** 106–108 (1991).
12. P. H. Paul, U. E. Meier, and R. K. Hanson, "Single-shot, multiple-camera planar laser-induced fluorescence imaging in gaseous flows," presented at the American Institute of Aeronautics and Astronautics Twenty-Ninth Aerospace Sciences Meeting, Reno, Nevada, 7–10 January 1991.
13. J. L. Palmer, B. K. McMillin, and R. K. Hanson, "Planar laser-induced fluorescence imaging of underexpanded free jet flow in a shock tunnel facility," presented at American Institute of Aeronautics and Astronautics Twenty-Second Fluid Dynamics, Plasma Dynamics and Lasers Conference, Honolulu, Hawaii, 24–26 June 1991.
14. B. K. McMillin, J. L. Palmer, and R. K. Hanson, "Two-dimensional temperaturements of shock tube flows using planar laser-induced fluorescence imaging of nitric oxide," presented at American Institute of Aeronautics and Astronautics Twenty-Second Fluid Dynamics, Plasma Dynamics and Lasers Conference, Honolulu, Hawaii, 24–26 June 1991.
15. B. K. McMillin, J. L. Palmer, and R. K. Hanson, "Temporally resolved, two-line temperature imaging of NO temperature in a transverse jet in supersonic cross flow," Appl. Opt. (to be published).
16. D. R. Grieser and R. H. Barnes, "Nitric oxide measurements in a flame by laser fluorescence," Appl. Opt. **19,** 741–743 (1980).
17. C. Morley, "The mechanism of NO formation from nitrogen compounds in hydrogen flames studied by laser fluorescence," in *Eighteenth Symposium (International) on Combustion* (Combustion Institute, Pittsburgh, Pa., 1981), pp. 23–32; Combust. Flame **47,** 67–81 (1982).
18. J. F. Verdieck and P. A. Bonczyk, "Laser-induced saturated fluorescence investigations of CH, CN, and NO in flames," in *Eighteenth Symposium (International) on Combustion* (Combustion Institute, Pittsburgh, Pa., 1981), pp. 1559–1566.
19. M.-S. Chou, A. M. Dean, and D. Stern, "Laser induced fluorescence and absorption measurements of NO in NH_3/O_2 and CH_4/air flames," J. Chem. Phys. **78,** 5962–5970 (1983).
20. G. Kychakoff, K. Knapp, R. D. Howe, and R K. Hanson, "Flow visualization in combustion gases using nitric oxide fluorescence," AIAA J. **22,** 153–154 (1984).
21. M. Alden, H. Edner, and S. Wallis, "Simultaneous spatially resolved NO and NO_2 measurements using one- and two-photon laser-induced fluorescence," Opt. Lett. **10,** 529–531 (1985).
22. R. J. Cattolica, J. A. Cavolowsky, and T. G. Mataga, "Laser-fluorescence measurements of nitric oxide in low-pressure H_2/O_2/NO flames," in *Twenty-Second Symposium (International) on Combustion* (Combustion Institute, Pittsburgh, Pa., 1988), pp. 1165–1173.
23. A. M. Wodtke, L. Huwel, H. Schlüter, H. Voges, G. Meijer, and P. Andresen, "High-sensitivity detection of NO in a flame using a tunable ArF laser," Opt. Lett. **13,** 910–912 (1988).
24. U. Westblom and M. Alden, "Simultaneous multiple species detection in a flame using laser-induced fluorescence," Appl. Opt. **28,** 2592–2599 (1989).
25. K. P. Gross and R. L. McKenzie, "Measurements of fluctuating temperatures in a supersonic turbulent flow using laser-induced fluorescence," AIAA J. **23,** 1932–1936 (1985).
26. K. P. Gross, R. L. McKenzie, and P. Logan, "Measurements of temperature, density, pressure, and their fluctuations in supersonic turbulence using laser-induced fluorescence," Exp. Fluids **5,** 372–380 (1987).
27. P. H. Paul, M. P. Lee, and R. K. Hanson, "Molecular velocity imaging of supersonic flows using pulsed planar laser-induced fluorescence of NO," Opt. Lett. **14,** 417–419 (1989).
28. P. Andresen, G. Meijer, H. Schlüter, H. Voges, A. Koch, W. Hentschel, W. Opperman, and E. Rothe, "Fluorescence imaging inside an internal combustion engine using tunable excimer lasers," Appl. Opt. **29,** 2393–2404 (1990).
29. M. P. Lee, B. K. McMillin, and R. K. Hanson, "Planar fluorescence imaging of a transverse jet in a supersonic crossflow," J. Prop. Power **8,** 729–735 (1992).
30. B. K. McMillin, M. P. Lee, and R. K. Hanson, "Planar

laser-induced fluorescence imaging of shock-tube flows with vibrational nonequilibrium," AIAA J. **30,** 436–443 (1991).

31. N. T. Clemens, P. H. Paul, M. G. Mungal, and R. K. Hanson, "Scalar mixing in the supersonic shear layer," presented at American Institute of Aeronautics and Astronautics Twenty-Second Fluid Dynamics, Plasma Dynamics and Lasers Conference, Honolulu, Hawaii, 24–26 June 1991.
32. E. H. Piepmeier, "Theory of laser saturated atomic resonance fluorescence," Spectrochim. Acta Part B **27B,** 445–452 (1972).
33. J. W. Daily, "Saturation effects in laser-induced fluorescence spectroscopy," Appl. Opt. **16,** 568–571 (1977).
34. J. W. Daily, "Saturation of fluorescence with a Gaussian laser beam," Appl. Opt. **17,** 225–229 (1978).
35. R. P. Lucht and N. M. Laurendeau, "Two-level model for near saturated fluorescence in diatomic molecules," Appl. Opt. **18,** 856–861 (1979).
36. J. O. Berg and W. L. Shackleford, "Rotational redistribution effect on saturated laser-induced fluorescence," Appl. Op. **18,** 2093–2094 (1979).
37. C. Chan and J. W. Daily, "Laser excitation dynamics of OH in flames," Appl. Opt. **19,** 1357–1367 (1980).
38. R. P. Lucht, D. W. Sweeney, and N. M. Laurendeau, "Balanced cross-rate model for saturated molecular fluorescence in flames using a nanosecond pulse length laser," Appl. Opt. **19,** 3296–3300 (1980).
39. A. J. Kotlar, A. Gelb, and D. R. Crosley, "A multilevel model of response to laser-fluorescence excitation in the hydroxyl radical," in *Laser Probes for Combustion Chemistry,* D. R. Crosley, ed., Vol. 134 of ACS Symposium Series (American Chemical Society, Washington, D.C., 1980), pp. 137–144.
40. D. Stepowski and M. J. Cottereau, "Time-resolved study of rotational energy transfer in $A\,^2\Sigma^+$ ($\nu' = 0$) state of OH in a flame by laser induced fluorescence," J. Chem. Phys. **74,** 6674–6679 (1981).
41. R. Cattolica, "OH rotational temperature from two-line laser-excited fluorescence," Appl. Opt. **20,** 1156–1166 (1981).
42. D. H. Campbell, "Collisional effects on laser-induced fluorescence measurements of hydroxide concentrations in a combustion environment. 1: effects for $\nu' = 0$ excitation," Appl. Opt. **23,** 689–703 (1984a).
43. D. H. Campbell, "Collisional effects on laser-induced fluorescence measurements of hydroxide concentrations in a combustion environment. 1: effects for $\nu' = 1$ excitation," Appl. Opt. **23,** 1319–1327 (1984b).
44. J. R. Reisel, C. D. Carter, and N. M. Laurendeau, "Einstein coefficients for rotational lines of the (0, 0) band of the NO $A\,^2\Sigma^+ – X\,^2\Pi$ system," J. Quant. Spectrosc. Radiat. Transfer **47,** 43–54 (1992).
45. L. G. Dodge, J. Dusek, and M. F. Zabielski, "Line broadening and oscillator strength measurements for the nitric oxide $\gamma(0, 0)$ band," J. Quant. Spectrosc. Radiat. Trans. **24,** 237–249 (1980).
46. A. Y. Chang, M. D. DiRosa, and R. K. Hanson, "Temperature dependence of collisional broadening and shift in the NO A–X (0, 0) band in the presence of argon and nitrogen," J. Quant. Spectrosc. Radiat. Transfer **47,** 375–390 (1991).
47. G. A. Raiche and D. R. Crosley, "Temperature dependent quenching of the $A\,^2\Sigma^+$ and $B\,^2\Pi$ states of NO," J. Chem. Phys. **92,** 5211–5217 (1990).
48. M. C. Drake and J. W. Ratcliffe, "High temperature quenching cross sections for nitric oxide laser-induced fluorescence measurements," J. Chem. Phys. **98,** 3850–3865 (1993).
49. A. S. Sudbo and M. M. T. Loy, "Measurement of absolute state-to-state rate constants for collision-induced transitions between spin-orbit and rotational states of NO ($X\,^2\Pi$, $v = 2$)," J. Chem. Phys. **76,** 3646–3654 (1982).
50. T. Ebata, Y. Anezaki, M. Fujii, N. Mikami, and M. Ito, "Rotational energy transfer in NO ($A\,^2\Sigma^+$, $\nu = 0$ and 1) studied by two-color double-resonance spectroscopy," Chem. Phys. **84,** 151–157 (1984).
51. K. P. Huber and G. Herzberg, *Constants of Diatomic Molecules* (Van Nostrand Reinhold, New York, 1979).
52. R. W. Nicholls, "Franck–Condon factors to high vibrational quantum numbers IV: NO band systems," J. Res. Nat. Bur. Stand. Sect. A **68,** 535–540 (1964).
53. M. P. Lee, "Temperature measurements in gases using planar laser-induced fluorescence imaging of NO and O_2," Ph.D. dissertation (Stanford University, Stanford, Calif., 1991).
54. D. R. Crosley, Molecular Physics Laboratory, SRI International, Menlo Park, Calif., 94025 (personal communication, March 1991).
55. K. L. Wray, "Shock-tube study of the vibrational relaxation of nitric oxide," J. Chem. Phys. **36,** 2597–2603 (1962).
56. R. L. Taylor, M. Camac, and R. M. Feinberg, "Measurements of vibration–vibration coupling in gas mixtures," in *Eleventh Symposium (International) on Combustion* (Combustion Institute, Pittsburgh, Pa., 1967), pp. 49–65.
57. I. S. McDermid and J. B. Laudenslager, "Radiative lifetimes and electronic quenching rate constants for single-photon-excited rotational levels of NO ($A\,^2\Sigma^+$, $\nu' = 0$)," J. Quant. Spectrosc. Radiat. Trans. **27,** 483–492 (1982).
58. R. K. Hanson, J. M. Seitzman, and P. H. Paul, "Planar laser-fluorescence imaging of combustion gases," Appl. Phys. B **50,** 441–454 (1990).
59. N. Rajaratnam, "Turbulent jets," in *Developments in Water Science,* V. T. Chow, ed. (Elsevier, New York, 1976), Vol. 5.
60. H. Ashkenas and F. S. Sherman, "The structure and utilization of supersonic free jets in low density wind tunnels," in *Rarefied Gas Dynamics,* J. H. de Leeuw, ed. (Academic, New York, 1966), Vol. 2, pp. 84–105.
61. J. M. Seitzman, "Quantitative applications of fluorescence imaging in combustion," Ph.D. dissertation (Stanford University, Stanford, Calif., 1991).

a reprint from Applied Optics

Absorption measurements of water-vapor concentration, temperature, and line-shape parameters using a tunable InGaAsP diode laser

M. P. Arroyo and R. K. Hanson

A tunable diode laser diagnostic based on spectrally resolved laser absorption has been developed to detect water vapor. The system uses a distributed feedback InGaAsP diode laser, emitting at ~ 1.38 μm. The diode laser is tuned in wavelength by modulation of the current, resulting in 1-cm^{-1} tuning at 80-Hz repetition rate. The directly measured absorption spectra yield values for water-vapor concentration and temperature, as well as a collision-broadening line shape. To our knowledge, we accurately determined required data for H_2O line strengths and self-broadening coefficients for several spectral lines in a static cell filled with pure water vapor. The temperature and concentration of the water vapor present in laboratory room air and in the postflame gases above a methane–air flat flame burner have also been measured. These results agree well with calculated values and independent measurements.

Key words: Diode laser, spectroscopy, water, absorption, linewidth, line strength.

Introduction

Measurements of water vapor are generally relevant to combustion, propulsion, and aerodynamic facilities, since water vapor can be related to performance parameters such as extent and efficiency of combustion, propulsion efficiency, and heat release. The development of a nonintrusive technique for monitoring H_2O based on high-resolution absorption spectroscopy is especially valuable, as it may provide a means of simultaneously measuring multiple parameters including concentration, temperature, pressure, and even velocity, since all these parameters affect the position and shape of individual absorption lines.[1-3] The use of tunable semiconductor diode lasers for this spectroscopic technique is attractive, as these lasers are compact, rugged, cost effective, compatible with optical fiber transmission, and simple to operate. These lasers are narrow-linewidth light sources whose wavelength can be tuned easily by changing the laser temperature and injection current.

Room-temperature-operated GaAlAs and InGaAsP diode lasers now provide access to the near-IR region of the optical spectrum, generally between ~0.7 and 1.6 μm, with GaAlAs lasers providing the shorter wavelengths and InGaAsP the longer wavelengths. Several coincidences with absorption bands of interesting species have been pointed out.[4] Some monitoring of O_2,[3,5] NO_2,[6] and H_2O[7,8] with GaAlAs diode lasers and HCN,[9] CO and CO_2,[10] HCl[11] and H_2O[12,13] with InGaAsP diode lasers has been reported already.

The emphasis in previous water-vapor papers[7,12,13] has been mostly on frequency-modulation detection strategies suited for very low absorption ($<0.1\%$) in connection with trace gas detection applications. In that case the feature of central interest is the magnitude of the line-center absorption over a fixed path length. However, accurate characterization of the shape of the absorption features is more complex, with frequency-modulation detection strategies, because of the mathematical transform that relates the actual line shape to the wave form observed. This problem is particularly acute for doublets, triplets, and other cases of overlapping lines, which are common features in the water-vapor spectrum. Since our interest is focused on quantitatively measuring concentrations, temperature, pressure, and even velocity, of water vapor at high temperatures, a wavelength-modulation technique with direct absorption detection is used. The laser-wavelength-modulation technique as it will be described here involves tuning the wavelength of a single-mode probe laser across one or more closely spaced spectral lines of the water vapor and directly monitoring the resultant absorp-

---

The authors are with the High Temperature Gasdynamics Laboratory, Department of Mechanical Engineering, Stanford University, Stanford, California 94305-3032.

Received 14 September 1992.
0003-6935/93/306104-13$06.00/0.

tion spectra. The tuning range of the probe must be sufficiently large to resolve the scanned lines completely in a single sweep. Good temporal resolution will be possible if the tuning is fast enough.

The water-vapor absorption lines previously used in diode laser measurements lie near 820 mm (Refs. 7, 8) or 1.3 μm (Refs. 12, 13); the emphasis has been on room-temperature detection, although activity has recently been initiated in other laboratories to measure water at higher temperatures.[13] These lines are generally too weak for monitoring water in transient high-temperature flows in laboratory facilities. We have calculated that the strongest absorption lines of water vapor occur between 1.35 and 1.41 μm at room temperature and somewhat beyond these limits (1.34–1.46 μm) at 1500 K, the line intensities being between 100 and 1000 times stronger than those at 820 nm and 1.30 μm.[14] Thus it is clear that water-vapor measurements in high-temperature, laboratory-scale flows should preferably be done at longer wavelengths. Unfortunately the long-wavelength diode laser market is dominated by the telecommunications industry, which seeks to avoid any light losses that are due to absorption. Thus diode lasers are available mostly at 1310 ± 30 nm and 1550 ± 30 nm, and it is hard to find lasers outside these ranges. This is particularly true for the single-mode [distributed feedback (DFB)] lasers needed for spectroscopic measurement, as the wavelength dispersion in the manufacturing process of this type of lasers is narrower than in the multimode (Fabry–Perot) lasers. We are hopeful that the increasing scientific demand for spectroscopic applications of diode lasers will increase the range of wavelengths available in the near future.

The measurements presented here were performed with a DFB diode laser operating near 1385 nm. Experiments in a static cell, in laboratory room air, and in the postflame gases above a methane–air flat-flame burner have been carried out. Temperatures and water concentrations were inferred from Voigt fits of the absorption profiles for several absorption lines.

Measurement Technique

The measurement technique is based on the absorption of monochromatic near-IR laser radiation by water vapor. As is well known, the transmission of a probe beam of light through a uniform absorbing medium follows the Beer–Lambert relation,

$$\tau(\nu) = I(\nu)/I_0 = \exp[-k(\nu)L], \qquad (1)$$

where $\tau(\nu)$ is the transmissivity at frequency ν, I_0 is the incident intensity of the probe beam, $I(\nu)$ is the intensity at frequency ν observed after propagation through a length L of the absorbing medium, and $k(\nu)$ is the spectral absorption coefficient (reciprocal centimeters). The absorption coefficient can be expressed as

$$k(\nu) = P_{\text{abs}} S(T, \nu_0) \phi(\nu - \nu_0), \qquad (2)$$

where P_{abs} is the partial pressure of the absorbing species (atmospheres), $S(T, \nu_0)$ is the line strength of the transition centered at ν_0 ($\text{cm}^{-2}\text{atm}^{-1}$), and $\phi(\nu - \nu_0)$ is the line-shape function (centimeters). The line-shape function depends on temperature through the Doppler broadening and on both pressure and temperature through the collision (or pressure) broadening. The line-shape function is usually expressed in terms of a Voigt profile characterized by a parameter a, which is given by

$$a = (\ln 2)^{0.5} \gamma_c / \gamma_d, \qquad (3)$$

where γ_c and γ_d are the collision and Doppler half-widths (HWHM), respectively. The Doppler half-width is well known and can be calculated as

$$\gamma_d = 3.581 \times 10^{-7} (T/M)^{0.5} \nu_0, \qquad (4)$$

where T is the temperature (kelvin) and M is the molecular weight (atomic mass unit) of the absorber. The collision half-width has to be measured experimentally and depends not only on the absorbing molecules but also on the temperature, pressure, and composition of the gas.

Line strengths and positions for water vapor at room temperature have been taken from the HITRAN database,[15] a line-by-line compilation of spectral parameters, which contains line parameters on numerous water-vapor absorption bands at 296 K. The line strengths at any other temperature T may be calculated from

$$\begin{aligned} S(T, \nu_0) = {} & S(T_0, \nu_0)(T_0/T)[Q(T_0)/Q(T)] \\ & \times [1 - \exp(-hc\nu_0/kT)] \\ & \times [1 - \exp(-hc\nu_0/kT_0)]^{-1} \\ & \times \exp[-(hcE''/k)(1/T - 1/T_0)], \end{aligned} \qquad (5)$$

where $T_0 = 296$ K, h is Planck's constant (erg s), k is Boltzmann's constant (ergs per degree kelvin), c is the speed of light (centimeters per second), ν_0 is the resonant frequency of the line, E'' (reciprocal centimeters) is energy of the lower state of the transition (also taken from the HITRAN database), and $Q(T)$ is the rovibrational partition function. When we use the rigid-rotor, harmonic-oscillator model, the partition function can be given by[16]

$$\begin{aligned} Q(T) = {} & 0.5[(\pi/ABC)(kT/hc)^3]^{0.5} \\ & \times [1 - \exp(-hc\nu_1/kT)]^{-1} \\ & \times [1 - \exp(-hc\nu_2/kT)]^{-1} \\ & \times [1 - \exp(-hc\nu_3/kT)]^{-1}, \end{aligned} \qquad (6)$$

where A, B, and C are the three rotational constants of an asymmetric top rotor, 27.0, 14.4, and 9.4 cm^{-1} for water,[16] respectively and ν_1, ν_2, and ν_3 are the three fundamental vibration frequencies, 3657.05, 1594.75 and 3755.93 cm^{-1},[17] respectively.

The spectral regions accessed by the near-IR semiconductor diode lasers contain many water-vapor absorption bands that are overtones or combinations of the fundamental modes. In addition the high-temperature spectra in this region contain hot bands, which are absorption bands originating from excited vibrational levels rather than from ground level. The strongest band at long wavelengths is the $\nu_1 + \nu_3$ band with a band intensity of 6.431×10^{-19} cm mole^{-1}, at 296 K, and a peak line strength of 0.52 and 0.016 cm^{-2}atm^{-1} at 296 K and 1500 K, respectively. At shorter wavelengths the strongest band is the $2\nu_1 + \nu_2 + \nu_3$, which is ~1000 times weaker than the $\nu_1 + \nu_3$ band. The analysis of the line strength of the individual lines within the $\nu_1 + \nu_3$ band at room temperature (296 K) and at high temperature (1500 K) (Fig. 1) shows that the lines are much weaker at 1500 K than at low temperatures, but the range of wavelengths containing lines with similar strength is wider at 1500 K than at 296 K. It can also be seen that the lines can be grouped into three primary branches, i.e., the P, Q, and R branches, according to the change in the rotational quantum number, which occurs in the transition.

The strategy for measuring the temperature of the gas is based on the intensity ratio of two absorption lines, which is given by

$$R = S(T_0, \nu_1)/S(T_0, \nu_2) \times \exp[-(hc/k)(E_1'' - E_2'')(1/T - 1/T_0)]. \quad (7)$$

Thus, for a given pair of lines the intensity ratio is a function of temperature only. For convenience, the two lines (1 and 2) are labeled so as to keep the intensity ratio between 0 and 1.[2] The sensitivity of this ratio to temperature can be obtained by differentiating equation [Eq. (7)]. It can be seen that the peak sensitivity for a specific pair of lines occurs at

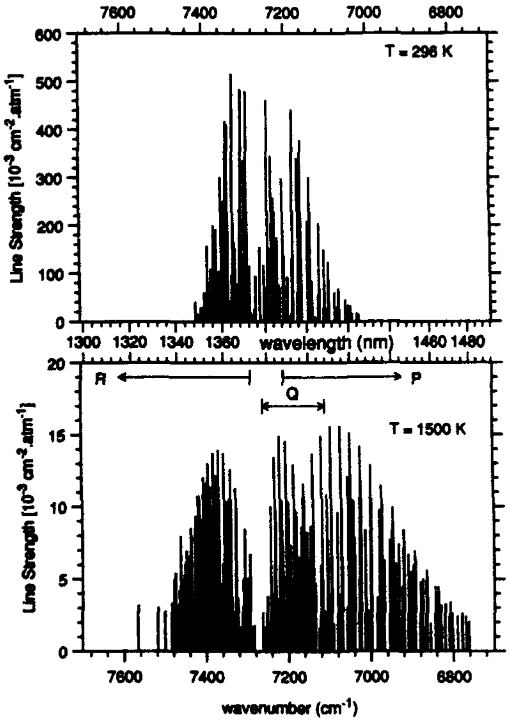

Fig. 1. Line position and strength for the $\nu_1 + \nu_3$ band at 296 and 1500 K.

$$T = (hc/2k)(E_1'' - E_2'') = 0.72\Delta E'', \quad (8)$$

where T is in kelvins and $\Delta E''$ in reciprocal centimeters. However, if the intensity ratio R reaches unity for a lower temperature, $T_{R=1}$, the maximum sensitivity will be at this temperature. Nevertheless, the most sensitive line pair for a certain range of temperatures does not correspond necessarily to a line pair with a relative maximum in that range as the actual sensitivity depends also on the ratio of the transition probabilities of both lines.

The partial pressure of water vapor can be obtained from Eqs. (1) and (2) if the temperature, line strength, and path length are known. If the total pressure P is also known, we can obtain the mole fraction of water vapor, X, since

$$X = P_{\text{abs}}/P. \quad (9)$$

Experimental Details

Diode Lasers

The diode lasers used for the present experiments are DFB InGaAsP diode lasers from Anritsu Corporation, in an open-chip carrier configuration. The distributed feedback structure constrains the laser to operate in a single longitudinal mode (single frequency). At a driving current of 70 mA at 25 °C, the diode lasers nominally provide an output power of 5 mW at a wavelength of 1384 nm. The diode laser controller is the new compact ILX Lightwave LDC-3722 system, which includes temperature and current control in the same package. The open-chip carrier laser is bonded with thermal epoxy to a copper block with a thermistor imbedded in it. The copper block is pressed against a thermoelectric heat pump by two nylon screws. Both the thermistor and the heat pump are driven by the laser controller system.

A complete characterization of the laser diodes has been made using a Jarrell-Ash 0.5-m monochromator, modified to produce sweeps across a small range of wavelength in real time. This is done by mounting a mirror in the optical path upstream of the output slit. The mirror is attached to a galvanometer, which oscillates at frequencies near 1 kHz. The mirror diverts the light out of the side of the monochromator where a slit and a detector are placed. With this system we have easily confirmed that the side-mode suppression ratio (SMSR) of the diode laser, defined as

$$\text{SMSR} = -10\log(I_s/I_m), \quad (10)$$

where I_m is the peak intensity of the main mode and I_s is the peak intensity of the strongest side mode, is better than 50 dB between the threshold current (~27 mA at 25 °C) and 100 mA. We have also observed that the spectrum above this current is asymmetric, with only one side mode occurring. This side mode becomes more important as the current is increased. Thus at 110 mA we measured a SMSR of 20 dB, while at 120 mA we measured only 10 dB.

Figure 2 shows the instrument-broadened spectrum of the laser diode at 20 °C for several driving currents. The original time scale of the horizontal axis has been transformed into a relative wavenumber scale. To calibrate this transformation, the spectrum of the laser light at 120 mA was recorded driving the monochromator with its motor at a speed of 100 nm/min and the mirror still. Then, the same spectrum was recorded with the mirror oscillating sinusoidally at ~1 kHz. By comparing the position of the two peaks in both recordings and taking into account the sinusoidal motion of the mirror, the transformation relation can be obtained. It can be seen that the peak wavelength and the peak intensity change with current. As is well known, they change with temperature also. The peak intensities have been observed to change linearly with current over a small range of current. The measured tuning rates for these lasers are 0.107 nm/° C (−17 GHz/° C) and 0.007 nm/mA (−1 GHz/mA).

The range of absolute wavelengths, which can be tuned continuously by varing the laser temperature, is obtained for each specific laser by measuring the absorption in a room air optical path between the laser and the detector. The laser is operated at a constant current, and the wavelength tuning is done by varying the laser temperature. The water-vapor absorption lines are easily observed, and their known relative intensities and positions permit easy identification of the lines that are being observed. Figure 3 shows the calculated absorption coefficient in the range of wavelengths emitted by our laser diode with the lines that have been probed in the present experiments. The absorption coefficients at a temperature typical of a flame is also shown for comparison. The spectroscopic parameters of the probed lines are listed in Table 1.[15] We note that more than 100 transitions are tabulated in HITRAN for this range of wavelengths and that only the strongest ones have been listed in Table 1. We evaluated the broadening parameter a at the laboratory room air and the methane–air flame conditions existing in our experiments by using the theoretical linewidth calculations of Delaye *et al.*[18]

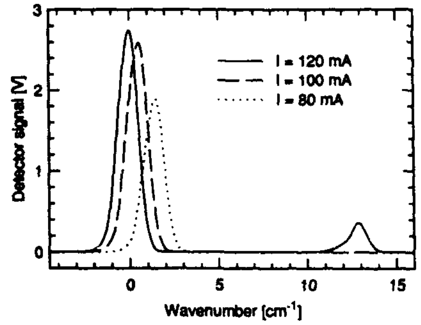

Fig. 2. Diode laser spectrum at three injection currents. The spectral linewidth is much larger than the laser linewidth because of instrument broadening.

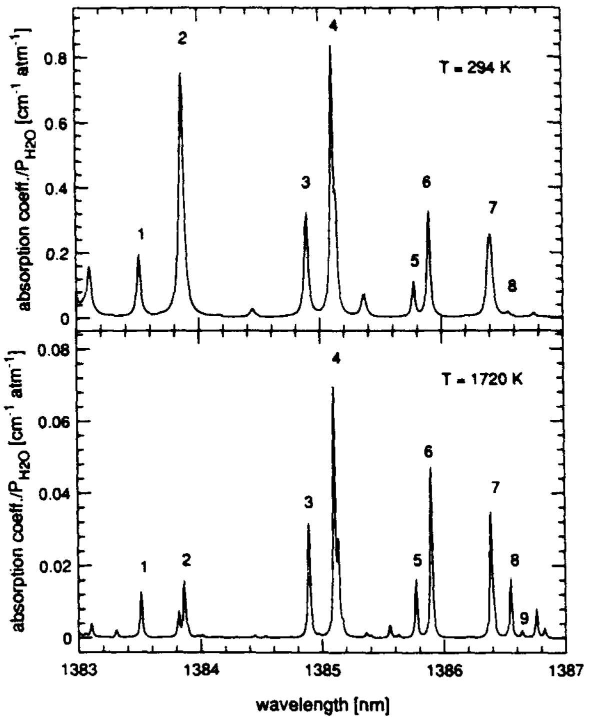

Fig. 3. Calculated absorption at T = 294 K, x_{H_2O} = 0.0146 (laboratory room air, top panel) and at T = 1720 K, x_{H_2O} = 0.158 (methane–air flame, bottom panel) for the spectral region of the diode laser.

Wavelength-Modulation Technique

In the present experiments the laser was modulated with a triangular function (~80 Hz frequency and 35-mA amplitude) superimposed on a mean current 65 mA. This means that the current ranges from 30 to 100 mA, where the laser operates single mode. The amplitude of the modulation is large because of the limited current tuning rate of the InGaAsP diode lasers. This large-modulation amplitude implies a large modulation in the output power of the laser. The tuning capabilities at different frequencies and amplitudes are reported in Fig. 4. They have been measured by modulating the diode laser at frequencies as high as 2 kHz and amplitudes as high as 40 mA. The increase of tuning range with amplitude is almost linear, although the slope decreases slowly with increasing amplitude. The decrease in tuning range with increasing frequency is a well-known feature of diode lasers. This decrease is substantial even at relatively low frequencies (as high as 1 kHz), which is why the present experiments have been done at a relatively low modulation frequency.

Figure 5 shows a schematic diagram for the direct absorption detection employed in the flame experiments. The output of the laser diode is collimated by a 6-mm focal length lens, with f-number = 1 and a broadband antireflecting coating to reduce back reflec-

Table 1. Spectroscopic Parameters for the Strongest Water Lines between 1383 and 1387 nm[a]

			$T = 294$ K		$T = 1720$ K								
Line	λ (nm)	ν (cm^{-1})	$10^4 S$ ($cm^{-2}\,atm^{-1}$)	a	$10^4 S$ ($cm^{-2}\,atm^{-1}$)	a	E'' (cm^{-1})	J'	k_a'	k_c'	J''	k_a''	k_c''
1	1383.512	7227.983	522.822	6.90	20.134	1.41	383.843	4	3	2	4	3	1
2	1383.819	7226.380	2.034	6.17	10.134	1.32	1581.336	10	4	6	10	4	7
2	1383.887	7226.024	1594.826	8.79	14.234	1.33	23.794	0	0	0	1	0	1
2[b]	1383.894	7225.987	0.201	6.78	3.643	1.30	1899.008	12	4	8	11	4	7
3	1384.891	7220.787	181.155	7.69	5.292	1.41	315.779	4	2	3	4	2	2
3	1384.899	7220.741	414.052	7.03	26.486	1.39	508.812	5	3	3	5	3	2
4	1385.107	7219.658	1736.739	5.45	102.138	1.29	488.108	4	4	0	4	4	1
4	1385.139	7219.491	5709.642	5.45	33.563	1.29	488.134	4	4	1	4	4	0
4[b]	1385.174	7219.311	1.249	5.27	4.077	1.28	1477.298	10	5	5	9	5	4
5	1385.773	7216.190	147.704	5.78	16.862	1.34	610.114	5	4	1	5	4	2
6	1385.899	7215.534	741.312	5.78	71.617	1.34	610.341	5	4	2	5	4	1
7	1386.390	7212.979	295.092	5.93	51.657	1.34	756.725	6	4	2	6	4	3
7	1386.411	7212.868	676.899	8.16	11.089	1.40	173.365	3	1	3	3	1	2
8	1386.550	7212.144	20.967	6.20	16.223	1.33	1122.709	8	4	4	8	4	5
9	1386.645	7211.653	0.003	7.44	2.859	1.25	2918.244	14	5	9	14	5	10

[a] The parameter a is evaluated for $P = 1$ atm, at the laboratory room air conditions ($T = 294$ K) and at the methane–air flame conditions ($T = 1720$ K). 1 atm = 760 torr.

[b] These lines correspond to the $2\nu_2 + \nu_3$ band. All the other lines correspond to the $\nu_1 + \nu_3$ band.

tions into the cavity laser. A first glass plate, used as a beam splitter, sends part of the beam through a low-finesse solid étalon of 2-GHz spectral range and onto detector D_3, providing a measurement of the change in relative wavelength during tuning. The rest of the beam is passed through the postflame gases above a premixed methane–air flat-flame burner. Approximately 10% of the beam is split off both before and after passing above the burner and is monitored on a pair of detectors (D_1 and D_2), that are optically balanced by variation of the beam-splitter angles. The detectors used are germanium photodiodes (EG&G J-16-18A-R01M) mounted in amplifier–filter packages, which give a low-pass cutoff frequency (−3 dB) of 90 kHz and a responsivity of 28 V/mW at 1.38 μm. We recorded the étalon signal I_3, the reference signal I_1, the transmitted signal I_2, and the absorption signal ($I_{\mathrm{dif}} = I_1 - I_2$) with digital storage oscilloscopes. The absorption signal was first passed through a differential amplifier with a gain factor of 20 and a bandwidth of 100 kHz.

The burner is a rectangular water-cooled flat-flame burner with a fine-mesh metal honeycomb burner surface, which measures 3 cm × 9 cm. Gas flows of methane and compressed air were conducted to the burner through calibrated rotameters. Equivalence ratios of 0.82 (fuel lean) were used in these experiments. The probe beam was directed across the long dimension of the burner. A shroud of nitrogen N_2 was used along the long dimension on both sides of the burner to stabilize the flame. Measurements

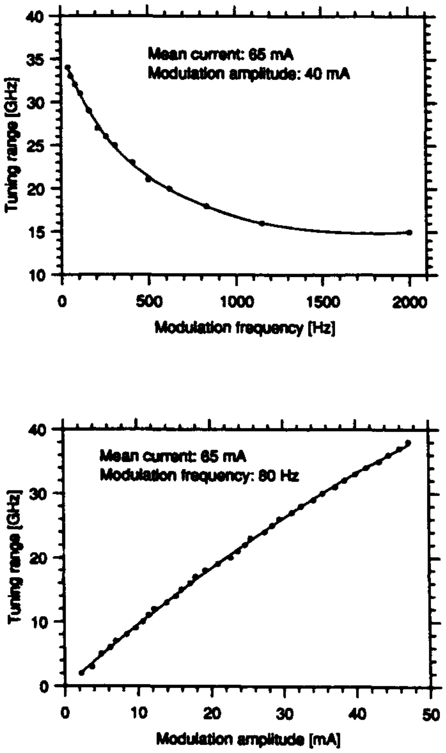

Fig. 4. Tuning capabilities of the diode laser ($T_{\mathrm{laser}} = 20$ °C).

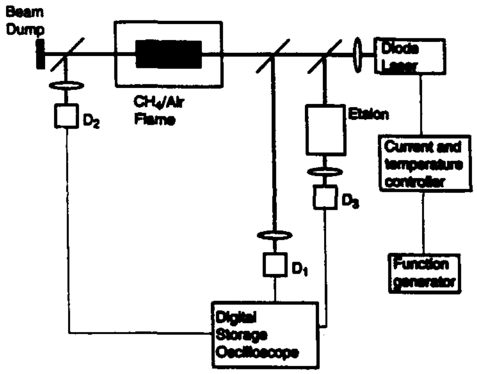

Fig. 5. Experimental schematic for the experiments in a flame.

were made ~5 mm above the burner surface along the burner centerline.

We measured the temperature profile along the probe path with Pt/Pt-Rh10% thermocouples, corrected for radiation losses. The temperature of the postflame gases was found to be 1720 K, stable within 20 K along most of the length. The temperature dropped sharply, over a distance of ~3 mm, at both ends of the observation path.

In the experiments in the flame the path lengths from the laser to both detectors, L_1 and L_2, are carefully matched in such a way as to have $L_2 = L_1 + L_f$, where L_f is the length of the flame. In these experiments, $L_1 = 71.2$ cm, $L_2 = 80.2$ cm, and $L_f = 9$ cm, with the beam splitter placed 22.7 cm from the laser.

In the cell experiments the flame was replaced by a 15-cm-long sample cell that contains glass windows. The cell has two sidearms, one leading to a pressure gauge (MKS Baratron 227 AHS) and vacuum system, the other to a flask containing water vapor at room temperature. Water vapor was introduced into the cell from the evaporated distilled water contained in the flask. The maximum water vapor pressure obtained in this way was ~21 Torr, corresponding to a measured room temperature 296 K. Laser, detectors, and optics are enclosed in a nitrogen-purged area to prevent absorption by room air. Further precautions were also taken by matching carefully the path lengths L_1 and L_2 in such a way as to have $L_2 = L_1 + L_c$, where L_c is the length of the cell.

In the experiments in room air, no flame or cell was placed between the beam splitters, and the étalon was situated at the end of the optical path (instead of the beam dump). A neutral-density filter was used to decrease the back reflections from the étalon into the diode laser. The lengths used were $L_1 = 26$ cm and $L_2 = 134.5$ cm. The absorption signal recorded by the oscilloscope was $I_{\text{div}} = (I_1 - I_2)/I_1$ (instead of $I_1 - I_2$). This signal was the output of a divider circuit, which also allowed electronic variations in the signal from detector D_1 to balance it perfectly with the signal from detector D_2. This setup permitted analysis of the absorption profiles for three different path lengths (L_1, L_2, and $L_1 - L_2$).

An example of the experimental traces obtained in this last case is shown in Fig. 6, which corresponds to four repeated scans of the 5–6 line pair (at 1385.773 and 1385.899 nm, respectively). The two panels on the top show the transmission signals, I_1 and I_2, through path lengths of $L_1 = 26$ cm (the upper record) and $L_2 = 134.5$ cm (the lower record), as recorded with detectors D_1 and D_2, respectively. The third panel shows the signal $I_{\text{div}} = I_1 - I_2/I_1$, as recorded from the divider output. The divider output voltage ranges from 0 (for $I_1 = I_2$) to 10 V (for $I_2 = 0$). The absorbance $[k(\nu)\Delta L]$ for a path length $\Delta L = L_2 - L_1 = 108.5$ cm can be inferred from the divider signal. The bottom panel shows the étalon trace as recorded by detector D_3.

The signal from detector D_1 clearly shows the line 6 feature, while line 5 is barely seen because of its smaller absorbance. Both lines are more pronounced for longer path lengths, as in the signal from detector D_2. Nevertheless, the signal from the divider provides a sensitive way to detect even smaller absorbances. The étalon trace shows that the length of the scan is 38 GHz. This scan is fully recorded in the ramp-up of the triangle function, where 19 fringes can be seen clearly, while part of it (~4 GHz) is missed in the ramp down, where only 17 fringes can be seen. The other two fringes occur in the lower-laser-power end of the scan This also implies phase variation between the current (or output power) and the emission wavelength modulations. This effect has been observed to be important for frequencies >100 Hz.

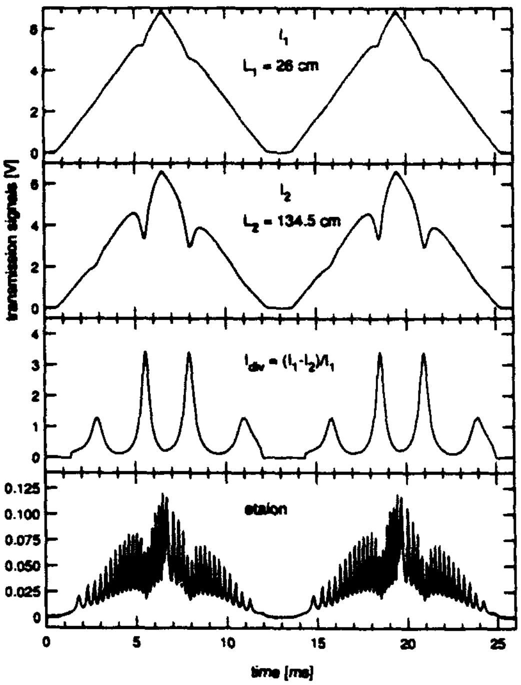

Fig. 6. Raw data trace showing absorption scans of the lines 5–6 of H_2O in laboratory room air with $T = 294$ K ($T_{\text{laser}} = 40$ °C).

Reduction of the Profiles

The first step in the analysis of the recorded absorption signals is to convert its time scale into an optical frequency scale. This conversion is obtained from the étalon signal (Fig. 7). It is clear that the peaks of the étalon signal are not equidistant in time, which shows that the time dependence of the laser frequency is not quite linear; we used a fifth-order polynomial to fit the peak positions. The residual shows that the differences found between the measured and the fitted peak positions are smaller than 0.1 GHz.

In the analysis of the data recorded from the experiments in air the absorbance from the I_1 and I_2 signals was calculated as $k(\nu)L = -\ln[I(\nu)/I_0]$, where the reference signal I_0 was assumed to be linear and was calculated from each recorded signal. The absor-

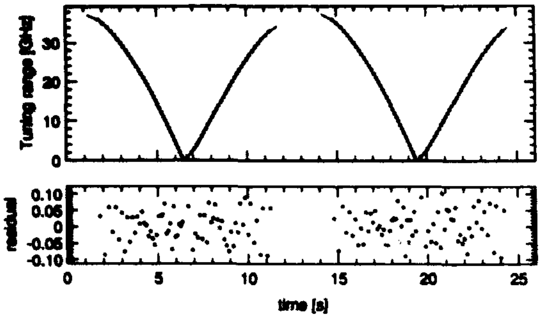

Fig. 7. Fitting of the peak positions in the étalon signal shown in Fig. 6.

bance for the ΔL path length was calculated from the I_1 and I_2 signals as $k_{21}(\nu)\Delta L = -\ln[I_2(\nu)/I_1(\nu)]$ and from the divider signal as $k_{\text{div}}(\nu)\Delta L = -\ln[1 - I_{\text{div}}(\nu)]$. The absorbance was then normalized to unity at the largest peak, namely $(kL)_{\text{peak}}$, and the location corresponding to zero frequency was set at this maximum. These normalized experimental profiles were then fitted to a set of line shapes (Voigt profiles) whose intensity ratio is a function of temperature as in Eq. (7). The fitting procedure minimizes the integrated squared difference between the experimental profile and a calculated profile with the same area. The fit was first optimized with respect to the shift in frequency of each profile from zero with an assumed temperature and a given a Voigt parameter. The fit was then optimized with respect to temperature (through the intensity ratio) with the best-fit a Voigt parameter determined at each temperature. Once the best-fit a parameter and temperature were determined, the fit of the shift was reoptimized. If there was appreciable change in this fit, the iteration procedure was repeated.

Figure 8 shows the reduced profiles corresponding to the first pair of absorption features in Fig. 6. The residuals show the difference between the data and the best-fit Voigt profile. The experimental profiles, and more clearly the residuals, are seen to be noisier at lower laser wavelengths (higher laser frequency emission). This noise is due to either fluctuations in the laser output power (which is due to fluctuations in its driving current) or the intrinsic noise of the detector. These fluctuations are small enough not to be seen on the direct signal (Fig. 6). Nevertheless, the division by the reference signal I_0 to obtain the absorbance profile makes them more noticeable as it changes the scale of the plot. This effect is, of course, more important at lower values of the reference signal than at higher values. As is well known, it is also more important when the absorbance signal is lower (compare normalized signals from detectors D_1 and D_2). When the I_1 and I_2 signals are divided, after being simultaneously recorded, the noise that is due to fluctuations in the laser output power should cancel, but the detector noise will still remain. This can be seen in Fig. 8c, which shows a residual noise of the same order of magnitude as the residual from the detector D_2 signal, but for a smaller absorbance.

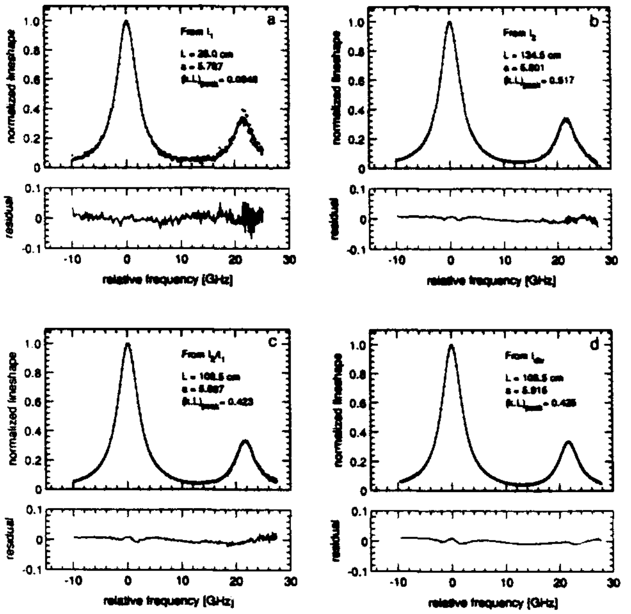

Fig. 8. Reduced profiles and residuals from the data of Fig. 6 ($\nu_0 = 7215.534$, $\Delta\nu = 21.6$ GHz).

The divider signal (Fig. 8d) shows a less noisy residual, which is due to the cancellation of the laser noise and the effective reduction in the detector noise as the absorption signal uses the whole voltage range of the detector.

Even though, in theory, the divider signal is the only signal we need to analyze to obtain the absorbance in a path length ΔL, in practice the signals from detectors D_1 and D_2 need to be recorded, too. Practical problems with the divider signal arise from the fact that signals from detector D_1 and D_2 have to be balanced perfectly. Any small dc offset between both signals or any small difference in their amplifier gain will give an absorbance signal with the baseline displaced and even tilted, which cannot be fitted accurately. We observed that a dc offset of 50 mV (1% of the full range voltage for detector D_1 and D_2 signals) noticeably tilts the baseline as it makes a bigger change in the low than in the high wavelength absorbance signal obtained. The difference in the gain of the detector signals can be easily corrected afterward as it only displaces the absorbance signal without tilting it. Several ways to determine when the balance is perfect have been tried, but none are fully satisfactory. For example, the detector signals can be perfectly balanced in a range of wavelengths where the absorption is negligible. However, when the laser temperature is changed to tune to another wavelength range, the signals do not remain balanced. We also tried to observe the wings of the divider signal and have them approach zero in a symmetric manner. Nevertheless, as the time-to-wavelength transformation is not linear, and we cannot tune far enough in the wings of the lines, this procedure did not work perfectly either. Thus we need to record the signals from detectors D_1 and D_2 as well. In our data reduction the divider signal is analyzed when-

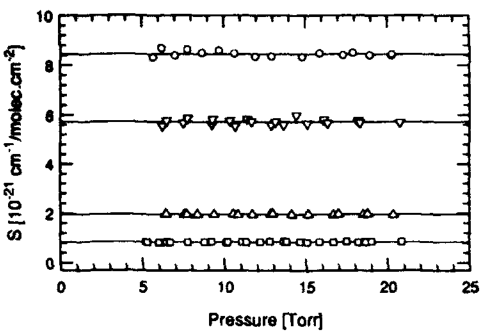

Fig. 9. Measured strengths for four different spectral lines. The horizontal lines represent the average values for each data set. These values and the wave numbers of the lines are listed in Table 2, together with the symbols used in the figure.

ever possible; otherwise, the direct signals from detectors D_1 and D_2 are used.

The absorption coefficient obtained from the four experimental profiles analyzed gives a mean value of 3.83×10^{-3} cm^{-1} with the value from the signal I_1 being 7% lower than the values from the other three normalized profiles (which agree within 1% of each other). The a parameter obtained from data in Fig. 8 is 5.85, with all the data agreeing within 1%. The intensity ratio for this fitting was kept constant at ⅓ as both lines have exactly the same energy E''.

Results and Discussion

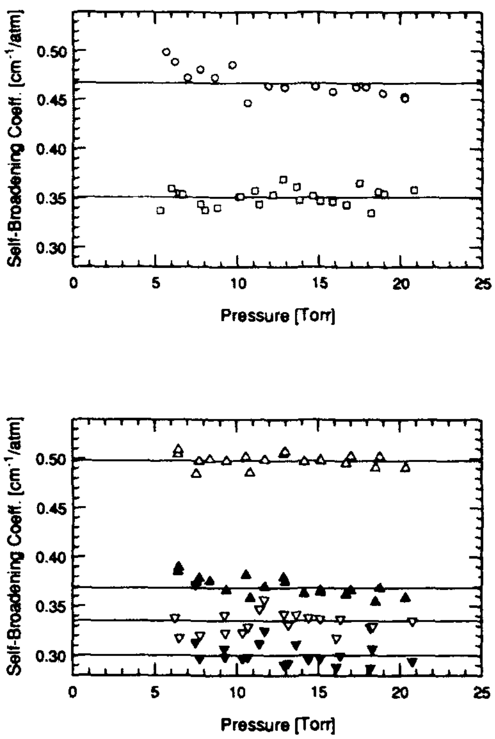

Fig. 10. Measured self-broadening coefficient for the same lines represented in Fig. 9. The horizontal lines represent the average value for each data set. These values and the wave number of each line are listed in Table 2, together with the symbols used in the figure.

Experiments in a Cell

In these experiments we probed all the strongest lines accessible with the diode laser. Data have been taken with undiluted water vapor in the cell at total pressures as high as the saturated water vapor pressure (21 Torr at 296 K). For each line, the amount of water vapor in the cell was increased to the saturated pressure and then decreased in steps of ~ 1 Torr, with data being taken at every step. Values of line strength S and collision (or self-broadening) half-width were computed for each data point from the a parameter of the Voigt fit and the peak absorbance of the signal, through Eqs. (2) and (3). Although measurements at pressure as low as 1 Torr were taken, we found that the lowest-pressure data were prone to errors because of the presence of a small quantity (of the order of tenths of Torr) of air in the cell. We found that the linewidth calculations were also prone to errors at the lowest pressures since the collision broadening was much smaller than the Doppler broadening (a parameters of the order of 0.1). Thus the data presented are limited to pressures higher than 5 Torr.

The line-strength results are plotted in Fig. 9 for

Table 2. Line Parameters Obtained from Absorption Data Acquired in a 15-cm-Long Static Cell at $T = 296$ K

		Relative Frequency (GHz)			$10^{21}S$ (cm^{-1}/mole cm^{-2})			$\gamma_{0\text{self}}$ (cm^{-1}/atm)		
Line	ν (cm^{-1})	Ref. 20	Ref. 15	Measured	Measured	Ref. 15	Ref. 19	Measured	Ref. 15	Ref. 18
1	7227.983	0.0	0.0	0.0	1.76	2.10	1.90	0.386	0.370	0.380
2 (○)	7226.024	0.0	0.0	0.0	8.44	6.33	8.63	0.467	0.452	0.404
3	7220.787	1.32	1.35	1.40	0.923	0.726	0.935	0.484	0.439	0.437
3	7220.741	0.0	0.0	0.0	2.10	1.67	2.25	0.425	0.430	0.404
4 (▽)	7219.658	0.0	0.0	0.0	5.72	7.00	6.08	0.335	0.383	0.314
4 (▼)	7219.491	−3.19	−5.01	−3.21	1.91	2.30	2.12	0.300	0.439	0.314
5 (□)	7216.190	21.33	19.68	21.62	0.840	0.707	0.808	0.351	0.345	0.337
6	7215.534	0.0	0.0	0.0	2.57	3.00	2.64	0.375	0.342	0.337
7 (△)	7212.979	1.95	3.33	2.04	0.978	1.20	1.01	0.369	0.423	0.357
7 (▲)	7212.868	0.0	0.0	0.0	1.96	2.70	2.06	0.498	0.500	0.445
8	7212.144	−22.24	−21.72	−22.44	0.0956	0.0863	0.0934	0.380	0.329	0.355

The symbols correspond to those used in Figs. 9 and 10.

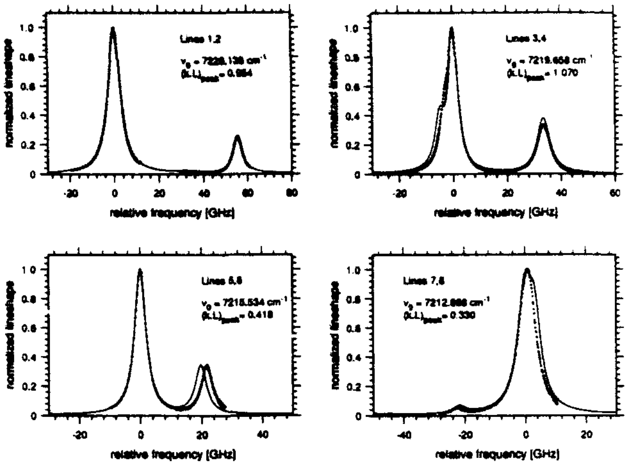

Fig. 11. Experimental (dots) and calculated (solid curve) normalized profiles for the lines probed in the experiments in room air. Theoretical conditions are as follows: T = 294 K, x_{H_2O} = 0.0146, P = 1 atm, L = 108.5 cm.

four of the lines studied. The overall scatter is quite low, and very precise (to within 1.5%) S values are obtained by averaging the data points. These averages are shown as the solid lines in Fig. 9 and are listed in Table 2.

We calculated values of the self-broadening coefficient, $\gamma_{0self} = \gamma_c/P_{abs}$, by using the water-vapor pressure measured for each data point. The resulting γ_{0self} values, plotted in Fig. 10, display a higher overall scatter than the line-strength measurements. This scatter may be due to the low a parameters (less than 1) of the lines at the studied pressures. This means that a small change in the baseline position implies a bigger change in the half-width of the line than in the total integrated absorptivity of the signal. In fact, it can be clearly seen from the plots that when there are two transitions involved in the same line (lines 4 and 7) there is a correlation between the deviation of both lines from the average value. The precision of the γ_{0self} measurements obtained by averaging the data points is better than 3%. These averages, shown as solid lines in the plots, are listed in Table 2.

We estimate the absolute accuracies of the S and the γ_{0self} values in Table 2 to be within 3% and 5%, respectively, taking into account the measurement precision, the overall signal processing system, and the absolute pressure and temperature measurement accuracies.

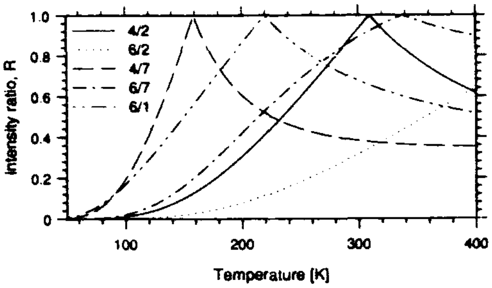

Fig. 12. Intensity ratio versus temperature for selected low-temperature line pairs.

Table 2 compares the experimental values of the measured lined parameters with the values listed in the most recent update (1992) of the HITRAN data base,[15] with the theoretical linewidth calculations by Delaye *et al.*[18] and with some recent measurements by Toth.[19] As a by-product of our Voigt-fitting procedure, we have also obtained the relative frequency (i.e., frequency difference) of some line-pair peaks. These values are also listed in Table 2 and are compared with the HITRAN data base and some measurements by Flaud *et al.*[20] Better agreement is found with this latter source.

The lines strengths listed in the 1992 HITRAN data base[15] differ by ~20% from our measured values, which we believe are accurate to within the stated 3% error bars. We note that similar discrepancies have been found by other workers,[8] although for lines from a different band. Better agreement is found with the line strengths measured by Toth,[19] although almost all of his values are slightly higher (between 1% and 10%) than ours.

The self-broadening coefficients in the HITRAN listing are obtained from measurements of corresponding lines in the 720-nm region by Grossmann and Browell.[21] The Delaye *et al.*[18] values are based on an approximation valid for low rotational quantum numbers. The vibration–rotation interaction is ne-

Table 3. Line Parameters Obtained from Absorption in a 108.5-cm Path Length in Laboratory Room Air at T = 294 K

Line	ν (cm^{-1})	Relative Frequency (GHz)	$k(\nu_0)L$	R	a	$100(a - a_{th})/a_{th}$ Ref. 18	Ref. 15	x_{H_2O} (%)
1	7227.983	0.0	0.234	1.	6.80	−1.3	4.9	1.39
2	7226.024	0.0	0.949	1.	8.50	−3.4	2.1	1.40
3	7220.787	1.26		0.440	7.52	−2.1	11.2	
3	7220.741	0.0	0.372	1.	7.18	2.3	4.5	1.38
4	7219.658	0.0	1.128	1.	5.39	−1.2	−25.5	1.53
4	7219.491	−3.2		0.333	5.39	−1.2	−25.5	
5	7216.190	21.6		0.333	5.86	1.3	6.2	
6	7215.534	0.0	0.430	1.	5.86	1.3	2.9	1.47
7	7212.979	1.5		0.433	6.45	8.7	13.3	
7	7212.868	0.0	0.362	1.	8.78	7.6	7.4	1.57
8	7212.144	−23.0		0.0465	8.77	41.4	44.2	

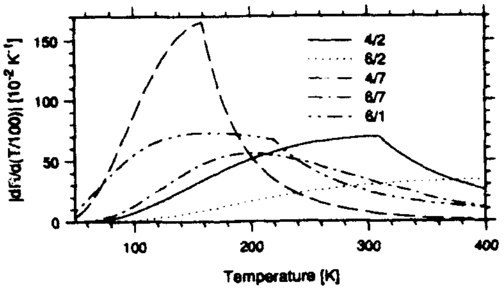

Fig. 13. Sensitivity of intensity ratio to temperature for the low-temperature line pairs of Fig. 12.

glected in these calculations. At wavelengths near 820 nm, some measurements made by Goldstein *et al.*[8] agree with both the theoretical values of Delaye *et al.*[18] and the measurements by Grossmann and Browell. However, in our case the data in the HITRAN listing are more than 10% higher than the theoretical values of Delaye *et al.*, with our measurements agreeing better (within 4%) with the first source than with the second one (~ 10% positive differences).

These discrepancies between tabulated or previous data and our measurements are sufficient to warrant further experimental investigation of these and other water lines in the $\nu_1 + \nu_3$ band.

Experiments in Room Air

The experimental normalized profiles for all the lines probed in these experiments are shown in Fig. 11 for a path length of 108.5 cm and a measured temperature of 294 K. The profiles calculated using the HITRAN data base are also plotted for comparison.

Table 3 summarizes the line parameters obtained in our experiments. We note that the measured *a* parameters agree quite well with calculations from Ref. 18 and data from the HITRAN data base,[14] with the only exception being line 8. This can be because line 8 is much weaker than line 7 and close enough to overlap with it. Thus line 8 is much more affected than line 7 by any small error in the baseline of the absorption data. The mole fraction has been obtained, assuming $T = 294$ K, from the peak absorbance and the intensity of the strongest transitions, as measured in our previous experiments. The mean value, calculated from all the lines probed, is 0.0146, which implies a relative humidity of 60%. All the inferred values agree within 5%. We note that the temperature needs to be known before the mole fraction can be calculated. The accuracy of this temperature has to be higher for the lines with a strong dependence on temperature but can be relaxed somewhat for the lines with a weak dependence. We calculate that within a range of 50 K around 300 K the intensities of lines 3 and 4 change less than 6%, as they reach their maximum intensities at ~ 300 K. Lines 5 and 6 exhibit a maximum similar to that of lines 3 and 4 but near 350 K. Thus these lines are suitable for measuring mole fractions at low temperatures.

Table 4. Selected Line Pairs for H_2O Thermometry at Low Temperatures

Lines	$\Delta E''$ (K)	T_{low} (K)	T_{high} (K)	$T = 294$ K R	 100 dR/dT	$R_{meas.}$	$T_{infer.}$
4/2	670	150	1070	0.891	0.688	0.967	305
6/2	845	215	1425	0.300	0.292	0.313	299
4/7	450	85	385	0.376	0.079	0.400	279
6/7	630	135	625	0.854	0.351	0.810	278
6/1	325	85	1020	0.724	0.272	0.661	306

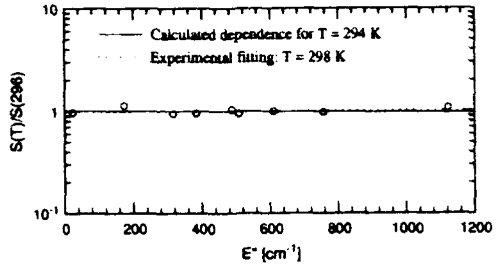

Fig. 14. Measured line intensity versus E'' at room temperature.

Of all the lines accessible with the diode laser, only pairs 5–6 and 7–8 can be tuned simultaneously in the

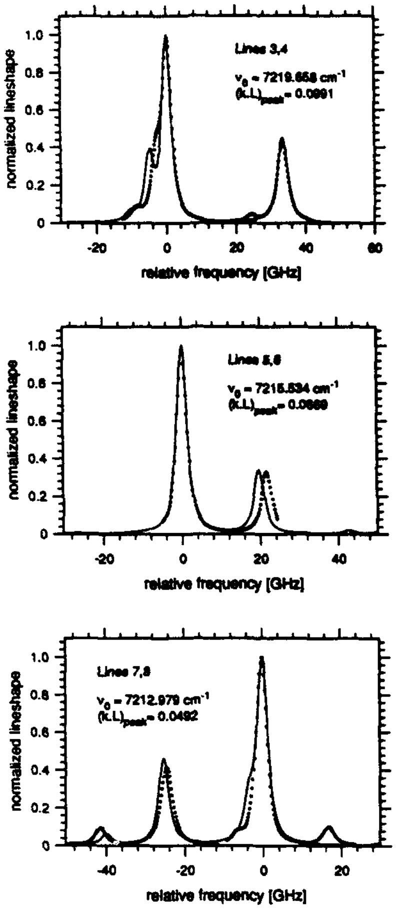

Fig. 15. Experimental (dots) and calculated (solid curve) normalized profiles for the lines probed in the experiment in a methane–air flame. Theoretical conditions are as follows: $T = 1720$ K, $x_{H_2O} = 0.158, P = 1$ atm, $L = 9$ cm.

Table 5. Line Parameters Obtained from the Absorption in a 9-cm Path Length in a Fuel Lean ($\phi = 0.82$) Methane–Air Flame at $T = 1720$ K[a]

Line	ν (cm^{-1})	Relative Frequency (GHz)	$k(\nu_0)L$	R	a	$100(a - a_{th})/a_{th}$ Ref. 18	x_{H_2O} (%)
3	7220.787	1.26		0.15	2.90		
3	7220.741	0.0	0.0368	1	1.47	6.1	18.1
3	···	−8.9		0.08	1.45	···	*
4	7219.658	0.0	0.0829	1	1.31	1.2	16.3
4	7219.491	−3.2		0.33	1.31	1.0	
4	7219.311	−9.0		0.06	1.30	1.8	
5	7216.190	21.6		0.33	1.32	−1.4	
6	7215.534	0.0	0.0602	1	1.32	−1.4	17.0
7	···	16.9		0.12	1.40	···	*
7	7212.979	0.0	0.0470	1	1.10	−18.0	16.9
7	7212.868	−1.5		0.25	1.15	−17.7	
7	···	−6.8		0.06	1.30	···	*
8	7212.141	0.0	0.0183	1	1.60	20.8	19.8
9	7211.653	−16.8		0.2	1.40	12.4	

[a] Asterisks denote lines not tabulated in the HITRAN database.

same sweep. Pair 5–6 is not good for T measurements, as both transitions have the same low energy E'', and so their ratio is independent of T. Pair 7–8 could be good for T measurements because of the difference in E'' of the transitions involved. The drawback is that there are many components of these lines: at least three at room temperature, and more as temperature increases. Furthermore, at room temperature and $P = 1$ atm (760 Torr), the weaker line of the pair is obscured by the wings of the stronger line, making an accurate measurement of the intensity ratio difficult. If we take $R = 0.1$ and $dR/dT = 0.01/100$ K as the lower limit criteria,[2] this line pair should be good for T measurements between 450 K and 1500 K, but with a low sensitivity ($<0.04/100$ K). We also considered the possibility of using the intensity ratio of two lines, which are not close together. The line pairs giving the highest ratio and sensitivity are plotted in Figs. 12 and 13. Table 4 list their constants, where T_{low} and T_{high} indicates the range of temperatures where $R \geq 0.1$ and $dR/dT \geq 0.01/100$ K. The temperature inferred from all these pairs compares well with the measured value of 294 K (agreement better than 5%).

The temperature inferred from the linear fitting of $S(T)/S(296)$ versus E'' (Fig. 14) for all the lines measured is 298 K, which also compares well with the measured temperature.

Experiments in a Flame

The normalized experimental profiles for all the lines probed in these experiments are shown in Fig. 15. The profiles calculated from the HITRAN data base and broadening parameters from Ref. 18 are also plotted for comparison. Table 5 summarizes the line parameters obtained in our experiments. Apart from the same differences in line positions observed at room temperature, we also observe some features that are not included in the HITRAN data base, probably corresponding to hot-band transitions. We obtained the mole fraction assuming $T = 1720$ K. The mean value, obtained from all the lines measured, is 0.171, which agrees within 8% with the calculated value of 0.158, corresponding to a $\phi = 0.82$ methane–air flame.

The temperature has been inferred from the linear fitting of $S(T)/S(296)$ versus E'' (Fig. 16) for all the lines probed in these experiments. The value obtained is 1915 K, which is slightly higher than the measured value. We note that the slope of the linear fitting is dominated by the line with biggest E'' (line 8). Thus, if we assume that the ratio $S(T)/S(296)$ is 10% smaller than the present value, the linear fitting will give a temperature of 1710 K, in better agreement with the measured temperature value. The change in the ratio $S(T)/S(296)$ can be explained by errors in the line strength at 296 K or by the presence of a high E'' line blended with line 8 and not tabulated in the data base. Since we do not believe there is such a big error in our measurement of the line strength at 296 K for this line, and taking into account that the a parameter obtained for line 8 in this flame experiments is bigger than expected, it is quite likely that a high-E'' line not tabulated in the data base could be blended with line 8.

The line pairs with the best sensitivity at the flame temperature are 8–7, 8–14, and 7–4. All of these can provide the temperature with an accuracy of ~200 K if the intensity ratio is measured to within 0.01. This low sensitivity, together with the possible error in the strength of line 8, as remarked in the previous

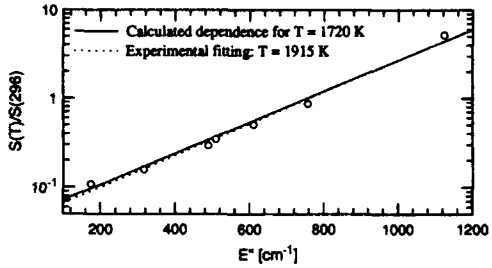

Fig. 16. Measured line intensity versus E'' at high temperature.

paragraph, could explain that the temperatures inferred from these line pairs (2980, 2760, and 2280 K respectively) are quite far from the measured value.

More accurate measurements would be possible if line pairs with better sensitivity were available. This means that line pairs with bigger $\Delta E''$ and ratios nearer to 1 should be looked for. An analytical search of the theoretical water vapor spectra showed that there are several such line pairs near 1.40 μm. Unfortunatley, these wavelengths, to our knowledge are not yet commercially available in DFB lasers, although they may be in the future. At the present, a good alternative to DFB lasers are FP lasers modified with a short external cavity,[22] which can force the laser to emit in a single mode.

Conclusions

A wavelength-modulated diode laser has been used to detect water vapor at room temperature and in a flame by means of spectrally resolved line-of-sight absorption. The simplicity of the optical setup makes such a diagnostic easy to implement in studies of combustion flows where water vapor is one of the primary species. The system could be coupled with fiber optics to probe remote environments.

Temperature and water concentrations, as well as water line parameters, have been inferred from the directly measured absorption spectra. Line parameters for several spectral lines have been obtained for water-vapor pressures as high as 20 Torr at T = 296 K, with an absolute accuracy of 5% or better. Temperature has been obtained from the intensity ratio of a pair of lines. In the range of wavelengths available in the present experiments, there are only a few line pairs close enough to be recorded simultaneously, but their sensitivity to temperature is small. Thus we also demonstrated the technique with several line pairs not simultaneously tuned. Temperatures inferred in this way were in close agreement with the temperature measured in laboratory room air. At higher temperature the agreement with radiation-corrected thermocouple measurements was not good, since the sensitivity of the line pairs to temperature and their fractional absorptions were quite low. More accurate measurements of temperature will be obtained when diode lasers become available at other wavelengths. Future work will focus on the region around 1.4 μm, which looks promising for high-temperature measurements. An effort to apply our current diode laser to mass and momentum flux measurements is also in progress.

This research was sponsored by the U.S. Air Force Office of Scientific Research, Aerospace Sciences Directorate, with Julian Tishkoff as technical monitor. M. P. Arroyo was partially supported by the Spanish Government under the Fullbright Program.

References

1. E. C. Rea and R. K. Hanson, "Rapid laser-wavelength modulation spectroscopy used as a fast temperature measurement technique in hydrocarbon combustion," Appl. Opt. **27**, 4454–4464 (1988).
2. A. Y. Chang, M. D. DiRosa, D. F. Davidson, and R. K. Hanson, "Rapid tuning cw laser technique for measurements of gas velocity, temperature, pressure, density, and mass flux using NO," Appl. Opt. **30**, 3011–3022 (1991).
3. L. C. Philippe and R. K. Hanson, "Tunable diode laser absorption sensor for temperature and velocity measurements of O_2 in air flows," in *Technical Digest, Twenty-Ninth Aerospace Sciences Meeting* (American Institute of Aeronautics and Astronautics, Washington, D.C., 1991), paper 91-0360.
4. D. T. Cassidy, "Trace gas detection using 1.3-μm InGaAsP diode laser transmitter modules," Appl. Opt. **27**, 610–614 (1988).
5. D. M. Bruce and D. T. Cassidy, "Detection of oxygen using short external cavity GaAs semiconductor diode lasers," Appl. Opt. **29**, 1327–1332 (1990).
6. W. Length and H. Gehrtz, "Sensitive detection of NO_2 using high-frequency heterodyne spectroscopy with a GaAlAs diode laser," Appl. Phys. Lett. **47**, 1263–1265 (1985).
7. L.-G. Wang, D. A. Tate, H. Riris, and T. F. Gallagher, "High-sensitivity frequency-modulation spectroscopy with a GaAlAs diode laser," J. Opt. Soc. Am. B **6**, 871–876 (1989).
8. N. Goldstein, S. Adler-Golden, J. Lee, and F. Bien, "Measurement of molecular concentrations and line parameters using line-locked second harmonic spectroscopy with an AlGaAs diode laser," Appl. Opt. **31**, 3409–3415 (1992).
9. H. Sasada and K. Yamada, "Calibration lines of HCN in the 1.5-μm region," Appl. Opt. **29**, 3535–3547 (1990).
10. D. T. Cassidy and L. J. Bonnell, "Trace gas detection with short-external-cavity InGaAsP diode laser transmitter operating at 1.58 μm," Appl. Opt. **27**, 2688–2693 (1988).
11. A. C. Stanton and J. A. Silver, "Measurements in the HCL 3 ← 0 band using a near-IR InGaAsP diode laser," Appl. Opt. **27**, 5009–5015 (1988).
12. C. B. Carlisle and D. E. Cooper, "Tunable diode laser frequency modulation spectroscopy through an optical fiber: high sensitivity detection of water vapor," Appl. Phys. Lett. **56**, 805–807 (1990).
13. A. C. Stanton, D. S. Bomse, and J. A. Silver, "A nonintrusive diagnostic for water vapor in high temperature flow fields," Tech. Rep. R90-01, for National Aero-Space Plane Joint Program Office AFSC/NAC (Southwest Sciences, Inc., Santa Fe, N.M., 1991).
14. M. P. Arroyo and R. K. Hanson, "Tunable diode laser absorption technique for detection of water vapor in aerodynamic flows," in *Technical Digest, Thirtieth Aerospace Sciences Meeting* (American Institute of Aeronautics and Astronautics, Washington, D.C., 1992) paper 92-0510.
15. HITRAN data base, 1992 ed. (Digital Product Section, National Climatic Center, National Oceanic and Atmospheric Administration, Federal Building, Asheville, N. C. 28801).
16. G. Herzberg, *Molecular Spectra and Molecular Structure II. Infrared and Raman Spectra of Polyatomic Molecules* (Van Nostrand Reinhold, New York, 1945).
17. L. S. Rothmann, R. R. Gamache, A. Goldman, L. R. Brown, R. A. Toth, H. M. Pickett, R. L. Poynter, J.-M. Flaud, C. Camy-Peyret, A. Barbe, N. Husson, C. P. Rinsland, and M. A. H. Smith, "The HITRAN Database: 1986 edition," Appl. Opt. **26**, 4058–4097 (1987).
18. C. Delaye, J.-M. Hartmann, and J. Taine, "Calculated tabulations of H_2O line broadening by H_2O, N_2, O_2, and CO_2 at high temperature," Appl. Opt. **28**, 5080–5087 (1989).
19. R. A. Toth, Jet Propulsion Laboratory, 4800 Oak Grove Drive, Pasadena, Calif. 91109 (personal communication, 1992).
20. J. M. Flaud, C. Camy-Peyret, and J. P. Maillard, "Higher

ro-vibrational levels of H_2O deduced from high resolution oxygen-hydrogen flame spectra between 2800–6200 cm^{-1}," Mol. Phys. **32**, 499–521 (1976); C. Camy-Peyret, J. M. Flaud, and J. P. Maillard, "Higher ro-vibrational levels of H_2O deduced from high resolution oxygen-hydrogen flame spectra between 6200 and 9100 cm^{-1}," Mol. Phys. **33**, 1641–1650 (1977).

21. B. E. Grossmann and E. V. Browell, "Spectroscopy of water vapor in the 720-nm wavelength region: line strengths, self-induced pressure broadenings and shifts, and temperature dependence of linewidths and shifts," J. Mol. Spectrosc. **136**, 264–294 (1989); "Water-vapor line broadening and shifting by air, nitrogen, oxygen, and argon in the 720-nm wavelength region," J. Mol. Spectrosc. **138**, 562–595 (1989).
22. B. F. Ventrudo and D. T. Cassidy, "Operating characteristics of a tunable diode laser absorption spectrometer using short-external-cavity and DFB laser diodes," Appl. Opt. **29**, 5007–5013 (1990).